THE ATLAS GLOBAL FEATURE EXTRACTOR

AND

A MEASUREMENT OF ELECTROWEAK W BOSON PRODUCTION

IN ASSOCIATION WITH JETS IN PROTON-PROTON COLLISIONS

USING THE ATLAS DETECTOR

Gregory Myers

Submitted to the faculty of the Graduate School

in partial fulfillment of the requirements

for the degree

Doctor of Philosophy

in the Department of Physics,

Indiana University

August 2023

Accepted by the Graduate Faculty, Indiana University, in partial fulfillment of the
requirements for the degree of Doctor of Philosophy.

Doctoral Committee

_____

Sabine Lammers, PhD (Chair)

_____

Harold Evans, PhD

_____

Radovan Dermisek, PhD

_____

Gerardo Ortiz, PhD

August 9th, 2023

Dedicated to my parents,

Brent and Jemma Myers

Acknowledgments

"*We are who we are because somebody loved us.*" – Cornel West

In the spirit of this quote, first I would like to thank my full family, by birth and by law and love, for their support. Throughout my life, my family (my parents especially) have encouraged me to think freely and explore my interests. I will acknowledge people who have had a formative influence on me in roughly chronological order. But let me thank now my brother, Jef, for letting me borrow his copy of Stephen Hawking's *The Universe in a Nutshell* which kick-started my interest in high energy physics. At risk of not mentioning someone by name, let me just thank Uncles: Dean, Mark, and Bob, Aunts: Jan, Barbara, Cathy, Cindy, and Deb, cousins and extended family: Rob, Andy, Mary-Jemma, Mark Jr., Trent, Luke, Morgan, Spencer, Tegan, Jimmy, Ezra, Elliot, and Lucia. Christine and Jackie Schliefer as well as Iris and Mabel Schliefer-Myers have also been influential to me throughout the course of my PhD.

I would like to acknowledge my grandparents: Dot and Bill Myers who were a formative force on me growing up. Dot always wanted a doctor in the family – though probably not what she was thinking, I now tick that box. Unfortunately, I never met my other set of grandparents: James and Virginia Rumple, but I know that a piece of them lives on through me. I hope that the work detailed here honors their memory as well as that of Dot and Bill.

My first real foray into studying physics was in high school. I thought that if I could learn about acoustics and recording technology, I could make my bands sound better.

volume with stories of how you have all helped and inspired me, but I will spare us all the embarrassment. So let me just say thank you.

Gregory Myers

THE ATLAS GLOBAL FEATURE EXTRACTOR

AND

A MEASUREMENT OF ELECTROWEAK W BOSON PRODUCTION IN

ASSOCIATION WITH JETS IN PROTON-PROTON COLLISIONS USING THE

ATLAS DETECTOR

The development, commissioning, and operation of ATLAS Global Feature Extractor (gFEX) trigger system is presented. In addition, a measurement of electroweak W boson production in association with jets in proton-proton collisions at $\sqrt{s} = 13$ TeV using data collected by the ATLAS detector, corresponding to 139 fb^{-1} is presented. A fiducial cross-section of $\sigma_{\text{fiducial}}^{\text{EWKW}} = 936 \pm 171(\text{stat} + \text{syst}) \pm 84(\text{th.})$ fb for the electroweak W production processes in the $W \rightarrow \ell\nu$ channel is measured, where ℓ is either an electron or muon. This measurement is found to be in good agreement with the Standard Model prediction of $959 \pm 64(\text{stat} + \text{syst}) \pm 116(\text{th.})$ fb, as given by the Powheg generator.

Contents

List of Tables

List of Figures

List of Acronyms

ATCA Advanced Telecommunications Computing Architecture. 49, 52–56, 63–65

AXI Advanced Extensible Interface. 63

BCID Bunch Crossing Identifier. 67, 78, 88, 90, 92

BCR Bunch Counter Reset. 66, 82, 83, 88, 91

BNL Brookhaven National Laboratory. 61

BSM Beyond the Standard Model. 22, 57

CP Cluster Processor. 46

CRC Cyclic Reduncancy Check. 69

CSC Cathode-Strip Chamber. 40, 43

CTP Central Trigger Processor. 44, 45, 54, 66, 67, 82, 91

DCS Detector Control System. 63–65

DMA Direct Memory Access. 79

DSID ATLAS Dataset Identifier. 192

ECR Event Counter Reset. 66, 67, 82, 83

eFEX Electromagnetic Feature Extractor. 46, 49, 52, 53, 80, 84, 174

EFT Effective Field Theory. 22, 162

EMB Electromagnetic Barrel Calorimeter. 34, 43

EMEC Electromagnetic End-Cap Calorimeter. 34, 43, 72

EWK-W electroweak-induced W boson production in association with jets. 23, 100–105,
107, 111–114, 116, 119, 120, 123, 128, 141, 142, 148, 158, 160–165, 192, 195

Chapter 1

Introduction

The Standard Model of particle physics has successfully described many orders of magnitude of physical phenomena. It is arguably our best understanding of the quantum world; however, it is known to be incomplete. An obvious omission is gravity, but there are more elements to our universe for which we currently have no suitable explanation substantiated by experimental evidence – particulate dark matter, dark energy, the small but non-zero neutrino mass, and matter/anti-matter asymmetry to name a few.

On the path towards a full description of the fundamental physics that defines our universe, we use the technology available, innovating where possible, to reduce the world to fundamental building blocks. This work describes my contributions to these efforts, and is organized as follows.

First, I will discuss the theoretical background required to understand scattering in terms of quantum field theory. Next, I will describe the local symmetries that seem to be manifest in our universe and cast the players which act out their stories under these symmetries. Then I will mention briefly some hints of physics beyond the understanding of our current Standard Model. All of this takes place in chapter 2. The description of an experimental setup used to probe this fundamental physics follows in chapter 3, where the Large Hadron Collider (LHC) and ATLAS detector are described. A short digression into the world of ATLAS trigger and data acquisition follows in chapter 4 and chapter 5 where I describe my contributions to the detector upgrade efforts. Finally, chapter 6 explains the landscape of electroweak measurements and my contribution to

the measurement of one class of electroweak processes accessible to collider experiments in the LHC era. Figure 1.1 shows a summary of the Standard Model measurements using the ATLAS detector to date to illustrate the breadth of physics available to study using this experiment and the predictive power of the Standard Model over many orders of magnitude.

The two prongs of effort presented in this text: work on the ATLAS trigger and the measurement of electroweak physics may seem at first to be disparate endeavors. But as I will explain, the two bases of knowledge are becoming increasingly intertwined as collider experiments push to higher energy and higher luminosity.

A final, perhaps pedantic, note on grammar: I will interchangeably use the royal "we" and colloquial "I" pronouns. When using "we" I attempt to pay homage to the titanic efforts of my peers and those who came before me, while also making the reader complicit in my assumptions. Whether using "we" or "I," any errors in this text belong solely to me.
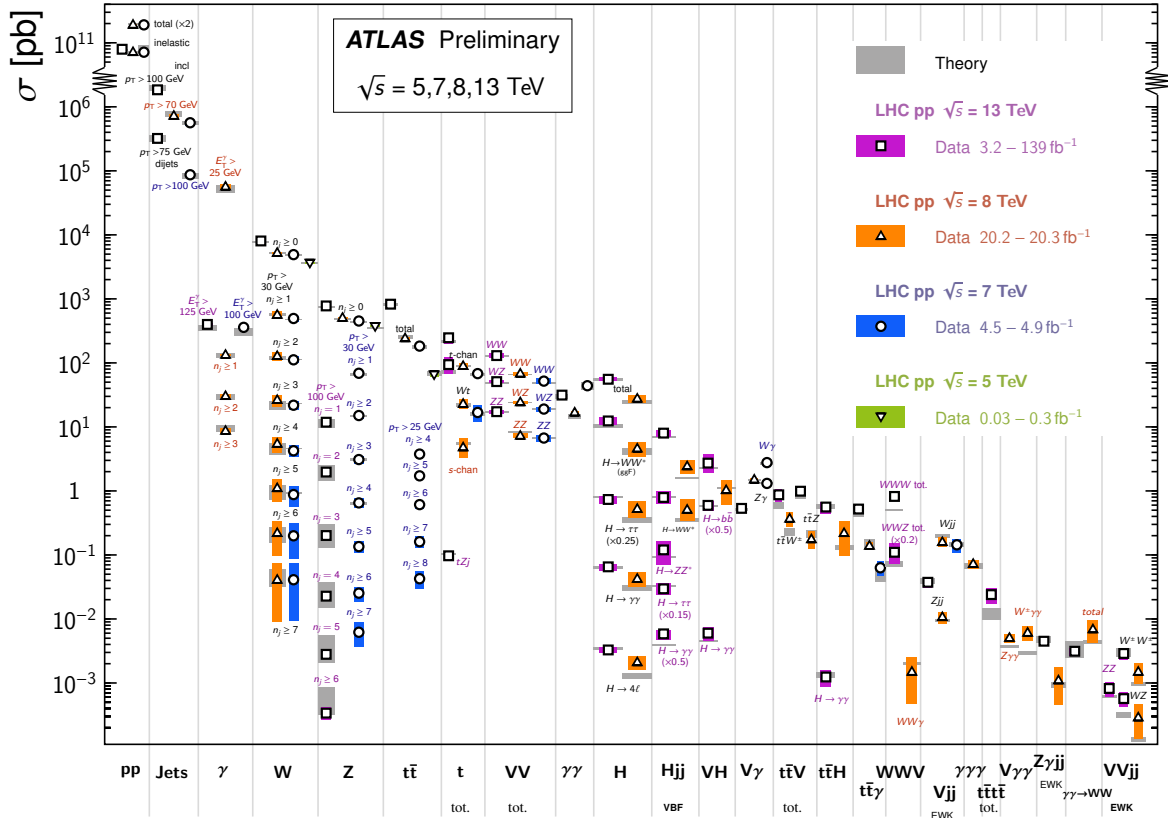
Figure 1.1: A summary of ATLAS Standard Model cross-section measurements versus theoretical predictions [17].

Chapter 2

Theoretical Background

2.1   Formalism

For thousands of years, humans have envisioned a theoretical framework which describes our universe as a composite system built from a set of irreducible building blocks – the term "atom" originates from the Greek word for "uncuttable." In the mid 19th century, evidence began to emerge for microscopic objects perhaps fitting this role. As the modern reader knows, these atoms were not the end of the story, and our journey into the subatomic world continues to this day. The language used to describe the frontier of our now subatomic understanding has evolved considerably and merits some brief discussion here. Much of this section is a summary without proof of results detailed in [61, 68].

2.1.1   Foundation in Quantum Field Theory

Unless otherwise stated, I will work in natural units where $\hbar = c = 1$. It is easy to see in these units that lengths may be measured in units of inverse energy. Thus, to probe small length scales, high energy particles will be needed. This will require a relativistic description of quantum mechanics. Historically, several attempts were made to reconcile these paradigms, but arguably the most fruitful begins with considering *fields* (as opposed to individual particles). These fields are then quantized, and out of this comes a description of multi-particle states and a mechanism by which we employ (in some cases) perturbative expansion to calculate measurable quantities.

We begin by considering a set of fields and their action, S. This is related to a Lagrangian density, $\mathcal{L}$, which can be a function of one or more of these relativistic fields,

ϕ and their first derivatives $\partial_\mu \phi$ as shown in Equation 2.1.

$$S = \int \mathcal{L}(\phi, \partial_\mu \phi) \, d^4 x \tag{2.1}$$

The Lagrangian density will often be referred to as simply, "the Lagrangian" from here onward, as it is a common convention to do so; however, the Lagrangian density is in reality related to the familiar Lagrangian by integral over the three spatial dimensions. And in analogy to the prescription in classical mechanics, the principle of least action allows us to derive the Euler-Lagrange equations of motion for these relativistic fields:

$$\partial_\mu \left(\frac{\partial \mathcal{L}}{\partial (\partial_\mu \phi)} \right) - \frac{\partial \mathcal{L}}{\partial \phi} = 0 \tag{2.2}$$

Again, in analogy with classical mechanics, we can relate the Lagrangian density to a Hamiltonian density, $\mathcal{H}$, by defining the canonical momenta, π, as shown below.

$$\pi(x) \equiv \frac{\partial \mathcal{L}}{\partial \dot{\phi}(x)} \tag{2.3}$$

$$\mathcal{H} = \pi(x)\dot{\phi}(x) - \mathcal{L} \tag{2.4}$$

Then we promote π and ϕ to operators, derive canonical commutation relations, and use these relations to construct creation and annihilation operators that let us express any final state of arbitrary particle number as a time-ordered product of creation and annihilation operators acting on the ground state. Making this more concrete, we can calculate the Green's function for this theory by considering the propagation of one ground state field excitation from coordinate y to coordinate x:

$$D_F(x - y) = \langle 0|T\phi(x)\phi(y)|0\rangle \tag{2.5}$$

The T above denotes the time-ordering of the ϕ operators, with the latest appearing farthest to the left. This D_F in fact retains the name propagator hereafter. Wick's theorem allows us to express an arbitrary time-ordered product of ϕ differing in spatial coordinates by a sum of propagators.

Ultimately, what we are after to calculate observable quantities is a way to predict the probability of any final state given an initial state. For this, we can substitute those states, $|i\rangle$ and $|f\rangle$ into Equation 2.5 to study $\langle i|T\phi(x)\phi(y)|f\rangle$. To calculate quantities of this type, we make use of the Feynman rules for the theory considered. These rules are specific to the fields and interactions considered, and they help to organize the infinite sums required in calculating the propagation from point y to point x in an interacting theory.

2.1.2 Scattering

Scattering experiments involve preparing a system in a known initial state $|i\rangle$, allowing the particles in this state to interact, evolving them to some final state $|f\rangle$. The projection of $\langle f|i\rangle$ is related to what is experimentally measured. We express these initial and final states in a convenient basis, say momentum eigenstates $|k\rangle$, while encapsulating the interaction physics in a unitary operator known as the scattering S-matrix, $\mathcal{S}$. This matrix must have the property that it reduces to the identity matrix in the case where the initial and final state do not interact, and therefore it has the form given in Equation 2.6, where we have defined the matrix, $\mathcal{T}$, to encapsulate the purely interacting terms.

$$\mathcal{S} = \mathbb{1} + i\mathcal{T} \tag{2.6}$$

Going one step further, 4-momentum conservation requires that $\mathcal{T}$ always contain a term enforcing this: $(2\pi)^4\delta^4(k_{\text{in}} - k_{\text{out}})$. Factoring this item out from the interactions lets us define the invariant matrix element $\mathcal{M}$ as in Equation 2.7.

$$\langle k_{\text{out}}|i\mathcal{T}|k_{\text{in}}\rangle = (2\pi)^4\delta^4(k_{\text{in}} - k_{\text{out}}) \cdot i\mathcal{M}(k_{\text{in}} \rightarrow k_{\text{out}}) \tag{2.7}$$

Now that we have a prescription for calculating the expectation value of final states given initial states in a relativistic quantum field theory, one might ask how this relates to something that can be measured in the laboratory. For this, we introduce the concept of a *cross-section*, denoted by σ. Given two beams of colliding particles, one of type a and the other of type b, this σ is intrinsic to the particles themselves and is related to the beam parameters as shown in Equation 2.8.

$$N_{\text{events}} = \frac{\sigma N_a N_b}{A} \tag{2.8}$$

Here the constituent terms are:

- N_{events}: the number of events expected to be produced from the process described by σ

- N_a and N_b: the number of a- and b-type particles in their respective beams

- A: the mutual area of the beams exposed to one another, orthogonal to their respective momentum axes

Using what we have developed so far, consider the case of two particles colliding, where the initial state and final state both contain two particles. The momentum of the initial state is: $k_1 + k_2$, which is equal to the final state momentum $k_1' + k_2'$ when 4-momentum is conserved. In this case, the differential scattering cross-section can be computed by Equation 2.9:

$$d\sigma = \frac{1}{4|\mathbf{k_1}|_{\text{CM}}\sqrt{s}} |\mathcal{M}|^2 \, d\Upsilon_{n'}(k_1 + k_2) \tag{2.9}$$

Where $d\Upsilon_{n'}$ is the Lorentz-invariant phase space measure for n' particles:

$$d\Upsilon_{n'}(k) = (2\pi)^4 \delta^4 \left(k - \sum_{i=1}^{n'} k_i' \right) \prod_{j=1}^{n'} \frac{d^3 k_j'}{(2\pi)^3 2k_j^{0'}} \tag{2.10}$$

From this, we can extract scattering cross-sections that can then be compared to those measured in experiment. In addition, the tools presented here can be generalized to give predictions about a great many configurations of underlying fields with more or less exotic mathematical properties.

One complication is that in many theories, practical calculations involve infrared and/or collinear divergences, which must be dealt with. A common tool is the renormalization of the couplings in the theory. A parameter μ is introduced such that these divergences are canceled out at the expense of having the coupling depend on this parameter. Then the value of μ must be chosen carefully so that the calculation of interest is perturbative as well as physical in the regime under analysis. This will be relevant again in chapter 6.

2.1.3 Gauge Theory and Lie Groups

Gauge symmetry will play an important role in understanding the modern formulation of particle physics, and so it merits a bit of discussion here. Gauge symmetry is the invariance of the Lagrangian under certain local transformations which belong to a Lie Group. A Lie Group is composed of a continuously generated group of unitary operators that act on quantum states such that the infinitesimal group elements can be written as in Equation 2.11, where g are the infinitesimal group elements, α are the group coefficients, and T^a are the generators of the group.

$$g(\alpha) = \mathbb{1} + i\alpha^a T^a + \mathcal{O}(\alpha^2) \tag{2.11}$$

The general property of group closure requires that the set of generators, T^a, must span the space of infinitesimal group transformations. And so the commutator of any two generators must be itself a linear combination of generators, such as is shown in Equation 2.12. The vector space spanned by these generators along with the operation of commutation is called the Lie Algebra of the group.

$$\left[T^a, T^b\right] = i f^{abc} T^c \tag{2.12}$$

These f^{abc} are known as structure constants. Groups which have $f^{abc} \equiv 0$ are called Abelian, whereas groups with any non-zero structure constants are called non-Abelian. Given that Abelian groups must have the commutator of any generators vanish, this means that these generators are the rather simple set of 1×1 matrices, represented by a single complex phase shift of the form $e^{i\phi}$. These properties in application to our quantum states of interest define what is known as the *Unitary Group* of order 1, denoted as $U(1)$.

This concept of invariance under certain local gauge transformations was encountered first in classical electromagnetism, where it was noticed that transforming the vector potential by adding any curl-less vector field would leave the magnetic field invariant [56]. This invariance has its roots in the $U(1)$ gauge structure of electromagnetism and the associated conservation of the $U(1)$ charge. In fact, Noether's Theorem [54] relates the existence of invariance under a local symmetry to the existence of an associated conservation law. In the case of electromagnetism, this is precisely the conservation of the familiar electric charge. The power of Noether's Theorem is not confined to the specific case of $U(1)$; indeed, it applies to any continuously generated symmetry.

What in the next section will turn out to be quite interesting is the description of the class of non-Abelian Lie Groups known as *Special Unitary Groups*. A Special Unitary Group of order N is denoted as $SU(N)$. Since $U(1)$ commutes with all other unitary transformations, it is customary to remove this subgroup when considering $SU(N)$. Then the generators of $SU(N)$ are the set of $N \times N$ unitary matrices with determinant 1. The removal of the $U(1)$ subgroup makes them traceless, leaving $N^2 - 1$ linearly independent matrices as the set of generators. As such, the fundamental representation of $SU(N)$ is an $N-$dimensional complex vector. For $N > 2$, this complexity leads to the existence of an additional adjoint representation [61]. What will become important shortly is the nature of the representation of a group. Quoting directly from [68], "A representation of a compact non-abelian group is a set of finite-dimensional hermitian matrices T_k^a that obey the same commutation relations as the original generator matrices T^a."

The ecosystem of group-theoretical tools extends well beyond the two classes discussed above and is interesting in its own right. For now, we have a sufficient background to formulate the modern view of the Standard Model of particle physics.

2.2 The Standard Model

The Standard Model of particle physics brings together the matter and interactions observed in experiment thus far. It consists of matter particles which are fermions and force carrying particles which are bosons. For the moment, our understanding of the origin of the matter content of the standard model is rather limited – asking where it comes from is much like asking, "Why do we exist?" So the matter content is taken from experimental evidence and is written in terms of representations of gauge groups which define the interactions of the matter fermions. The bosonic content observed in the laboratory arises from the gauge structure of the theory itself and is said to mediate these interactions.

Additionally, it seems that our universe comes with a massive scalar field, the Higgs field, which at low energies, exhibits spontaneous symmetry breaking – a process by which the true symmetry of the theory is broken, and the low energy observations differ from those at higher energy. This will be discussed in more depth during the description of the Higgs sector in subsection 2.2.1.

Theoretically, these constituents are described by three fermionic representations of the underlying symmetry groups $SU(3) \times SU(2) \times U(1)$. A summary of the fields and their representations is found in Table 2.1.

Field	SU(2) Components	SU(3)	SU(2)	U(1)
Q	$\begin{pmatrix} u \\ d \end{pmatrix}_L \begin{pmatrix} c \\ s \end{pmatrix}_L \begin{pmatrix} t \\ b \end{pmatrix}_L$	3	2	$\frac{1}{6}$
u	$(u_L)\,(c_L)\,(t_L)$	$\bar{3}$	1	$-\frac{2}{3}$
d	$(d_L)\,(s_L)\,(b_L)$	$\bar{3}$	1	$\frac{1}{3}$
L	$\begin{pmatrix} \nu_e \\ e \end{pmatrix}_L \begin{pmatrix} \nu_\mu \\ \mu \end{pmatrix}_L \begin{pmatrix} \nu_\tau \\ \tau \end{pmatrix}_L$	1	2	$-\frac{1}{2}$
e	$(e_L)\,(\mu_L)\,(\tau_L)$	1	1	1
G_μ^α	$-$	8	1	0
W_μ^α	$W_\mu^1, W_\mu^2, W_\mu^3$	1	3	0
B_μ	B_μ	1	1	0
ϕ	$\begin{pmatrix} H + v \\ \phi^0 \end{pmatrix}$	1	2	$-\frac{1}{2}$

Table 2.1: The field content of the Standard Model – the $SU(2)$ components are listed explicitly in the second column, since they will play a role in explaining how to construct the particle content which can be currently observed from these fields. The right-most columns list the representation in each symmetry group realized by each field. The right-most column is the bare $U(1)$ charge on each field.

These fields form the basis which gives rise to the particle contend of the Standard Model observed in the lab, directly or indirectly. This set of fundamental particles is presented in usual fashion in Figure 2.1. The subject of the next sections is precisely how these particles arise from the fundamental fields.
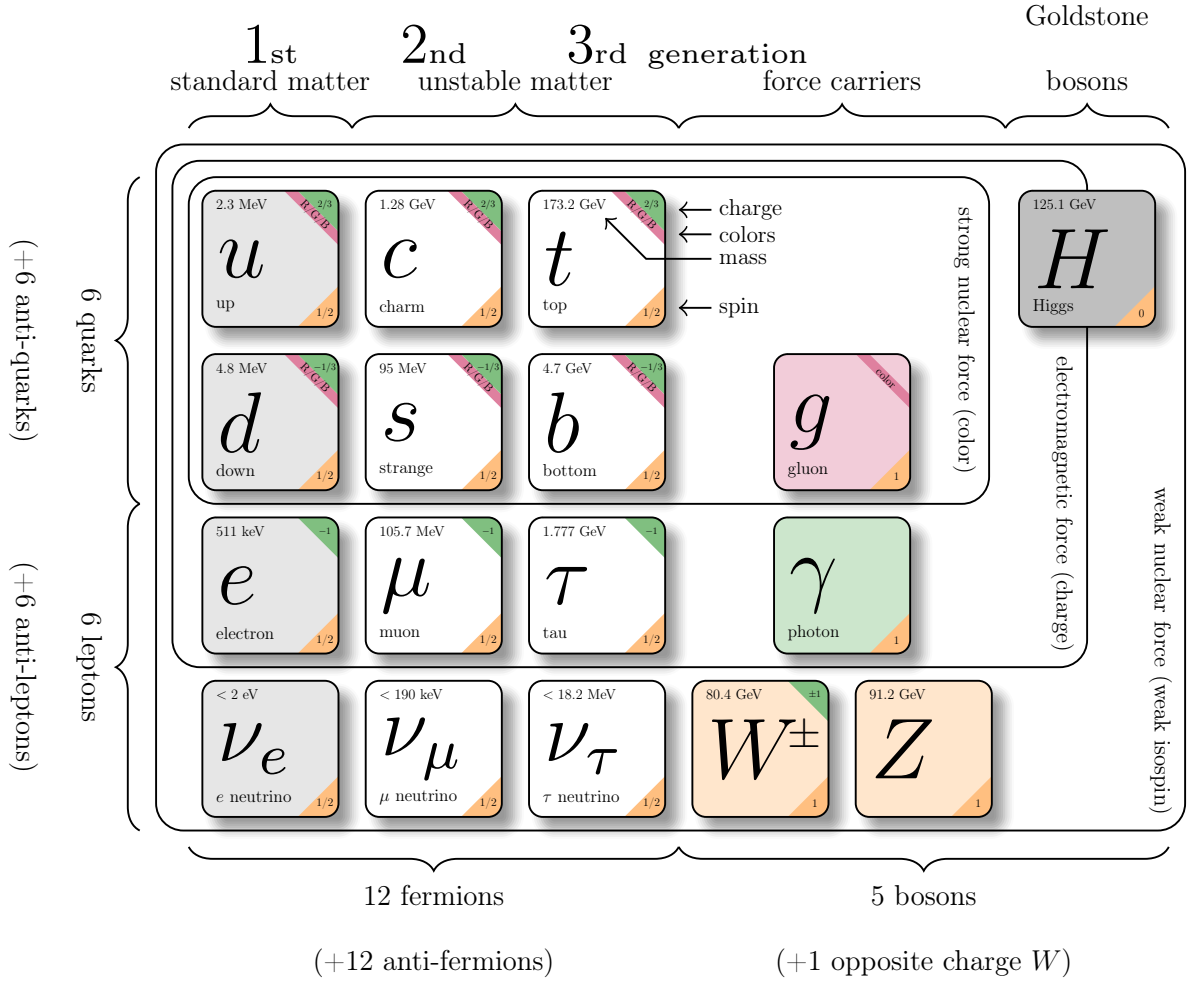
Figure 2.1: The Standard Model of Particle Physics (adapted from the diagram by Carsten Burgard [4])

2.2.1 The Higgs Sector

Beginning by considering the complex scalar field ϕ in the $(1, -\frac{1}{2})$ representation of $SU(2) \times U(1)$. The covariant derivative of ϕ is:

$$(D_\mu \phi)_i = \partial_\mu \phi_i - i \left[g_2 W_\mu^a T^a + g_1 B_\mu Y \right]_i^j \phi_j \tag{2.13}$$

$$\text{where } T^a = \frac{1}{2}\sigma^a \text{ and } Y = -\frac{1}{2}\mathbb{1}$$

Now suppose that ϕ has a potential of the form [69]:

13

$$V(\phi) = -\frac{\lambda^2 v^2}{2}\left(\phi^\dagger\phi\right) + \frac{\lambda^2}{2}\left(\phi^\dagger\phi\right)^2 \tag{2.14}$$

A global transformation can be made to bring the vacuum expectation value completely into the first component of ϕ, such that:

$$\langle 0|\,\phi\,|0\rangle = \frac{1}{\sqrt{2}}\begin{pmatrix} v \\ 0 \end{pmatrix} \tag{2.15}$$

Then a Lagrangian representing bosonic mass terms can be written and diagonalized by defining:

$$\theta_\mathrm{W} := \tan^{-1}(g_1/g_2) \tag{2.16}$$

$$c_\mathrm{W} := \cos\theta_\mathrm{W} \tag{2.17}$$

$$s_\mathrm{W} := \sin\theta_\mathrm{W} \tag{2.18}$$

$$W_\mu^\pm := \frac{1}{\sqrt{2}}\left(W_\mu^1 \mp iW_\mu^2\right) \tag{2.19}$$

$$Z_\mu := c_\mathrm{W}W_\mu^3 - s_\mathrm{W}B_\mu \tag{2.20}$$

$$A_\mu := s_\mathrm{W}W_\mu^3 - c_\mathrm{W}B_\mu \tag{2.21}$$

$$
\begin{aligned}
\mathcal{L}_\mathrm{mass} &= -\frac{1}{8}g_2^2 v^2 \begin{pmatrix} 1 & 0 \end{pmatrix}\begin{pmatrix} \frac{1}{c_\mathrm{W}}Z_\mu & \sqrt{2}W_\mu^+ \\ \sqrt{2}W_\mu^- & - \end{pmatrix}^2\begin{pmatrix} 1 \\ 0 \end{pmatrix} \\
&= -M_W^2 W^{+\mu}W_\mu^- - \frac{1}{2}M_Z^2 Z^\mu Z_\mu
\end{aligned}
\tag{2.22}
$$

As can be seen from Equation 2.22, the $W^\pm$ and Z bosons have acquired masses: $M_W = \frac{g_2 v}{2}$ and $M_Z = \frac{M_W}{c_\mathrm{W}}$ respectively, the photon A_μ has remained massless. The

masses of the W and Z bosons are measured experimentally to be $M_W = 80.377 \pm 0.012$ GeV and $M_Z = 91.1876 \pm 0.0021$ GeV [69]. This gives a value for the weak mixing angle, evaluated at M_Z in the $\overline{\text{MS}}$ renormalization scheme, of $\sin^2 \theta_{\text{W}} = 0.23121(4) \pm 1.7 \times 10^{-4}$ [69]. In addition, the form of the Higgs potential $V(\phi)$ gives a mass term $M_H = \sqrt{2\lambda}v$ arising from the Higgs self-coupling. The Higgs mass has been measured experimentally to be 125.25 ± 0.17 GeV [69]. This mass along with the vacuum expectation value of $v \approx 246.22$ GeV gives $\lambda \simeq 0.13$ [69].

For the quark and lepton fields, represented by left-handed Weyl spinors, there is no gauge group singlet contained in any product of their representations, and so a mass term cannot be written in this way. However, a Yukawa coupling to the Higgs field is allowed. And the transformation of the Higgs field is made as was done previously. For the leptons, this takes the form:

$$\mathcal{L}_{\text{Yukawa}} = -y\epsilon^{ij}\phi_i L_j e + \text{h.c.} \tag{2.23}$$

$$= -\frac{1}{\sqrt{2}}y(H + v)(L_2 e)$$

$$= -\frac{1}{\sqrt{2}}y(H + v)\bar{\mathcal{E}}\mathcal{E}$$

Where we have defined $\mathcal{E}$ as the Dirac field for the electron, which has acquired mass of $M_e = \frac{yv}{\sqrt{2}}$, while the $\mathcal{N}$ field representing the neutrino has remained massless. The definitions of these Dirac fields are shown in Equation 2.24 and Equation 2.25. There are no other gauge invariant terms involving L or e that have mass-dimension 4 or less [68]. Experimentally measured, each generation of charged lepton is more massive than the last: $M_e \simeq 511$ keV, $M_\mu \simeq 106$ MeV, and $M_\tau \simeq 1777$ MeV [69]. One interpretation of this mass hierarchy given the relation of the coupling y to the lepton mass is that the

more massive leptons couple more strongly to the Higgs field. Though, there is currently no theoretical explanation for the numerical values of the lepton (or any fermion) masses in the Standard Model. These remain free parameters in the model which are measured experimentally.

$$\mathcal{E} := \begin{pmatrix} e \\ e^{\dagger} \end{pmatrix} \tag{2.24}$$

$$\mathcal{N} := \frac{1}{2}(1 - \gamma_5)L = \begin{pmatrix} \nu \\ 0 \end{pmatrix} \tag{2.25}$$

For the quark fields, much of the same logic applies as for the leptons. There is no way to construct a gauge group singlet from the product of their representations, but we are permitted to write a Yukawa term of the form:

$$
\begin{aligned}
\mathcal{L}_{\text{Yukawa}} &= -y_1 \epsilon^{ij} \phi_i Q_{\alpha j} d^{\alpha} - y_2 \phi^{\dagger i} Q_{\alpha i} u^{\alpha} + \text{h.c.} \tag{2.26} \\
&= -\frac{1}{\sqrt{2}} y_1 (H + v)(Q_{\alpha j} d^{\alpha}) - \frac{1}{\sqrt{2}} y_2 (Q_{\alpha j} u^{\alpha}) \\
&= -\frac{1}{\sqrt{2}} y_1 (H + v) \bar{\mathcal{D}}^{\alpha} \mathcal{D}_{\alpha} - \frac{1}{\sqrt{2}} y_2 (H + v) \bar{\mathcal{U}}^{\alpha} \mathcal{U}
\end{aligned}
$$

As in the case of the leptons, we have defined Dirac fields $\mathcal{U}_{\alpha}$ and $\mathcal{D}_{\alpha}$, but here both objects have acquired masses of $M_d = \frac{y_1 v}{\sqrt{2}}$ and $M_u = \frac{y_2 v}{\sqrt{2}}$. These are identified as the up and down-type quarks, respectively. Their Dirac field components are defined below in Equation 2.27 and Equation 2.28.

$$\mathcal{U}_{\alpha} := \begin{pmatrix} u_{\alpha} \\ u_{\alpha}^{\dagger} \end{pmatrix} \tag{2.27}$$

$$\mathcal{D}_{\alpha} := \begin{pmatrix} d_{\alpha} \\ d_{\alpha}^{\dagger} \end{pmatrix} \tag{2.28}$$

In addition to the couplings to fermions and weak bosons, the kinetic term in the Lagrangian for the Higgs allows for triple and quartic self-coupling. The full set of these interactions of the Higgs boson with the other Standard Model particles are summarized in Figure 2.2.
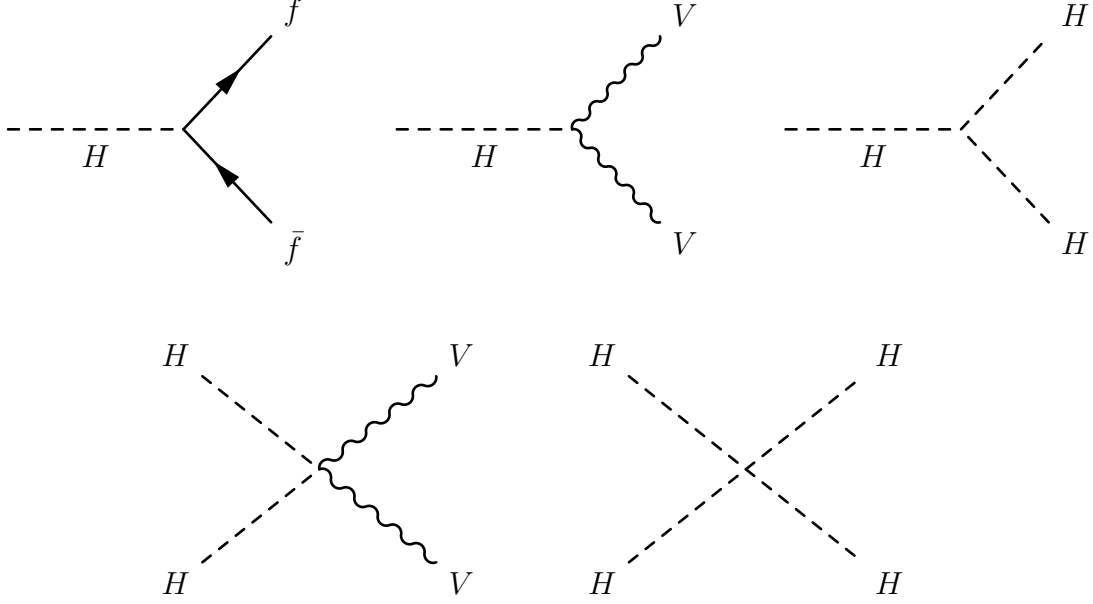
Figure 2.2: Vertices involving the Higgs boson, allowed by the Standard Model. Here, f is any fermion, and V is either $W^\pm$ or Z boson (as allowed by charge conservation).

2.2.2 The Electroweak Sector

Having understood the origin of boson and charged fermion masses and explored the landscape of Higgs interactions, we now turn to the interactions involving the $W^\pm$ and Z bosons. Expressing the kinetic term of the fermion Lagrangian now in terms of $W_\mu^\pm$ and Z_μ, and first considering the leptons, we have couplings to the electroweak bosons:

$$\mathcal{L}_{\text{Int}} = \frac{1}{\sqrt{2}} g_2 W_\mu^+ J^{-\mu} + \frac{1}{\sqrt{2}} g_2 W_\mu^- J^{+\mu} + \frac{e}{s_{\text{W}} c_{\text{W}}} Z_\mu J_Z^\mu + e A_\mu J_{\text{EM}}^\mu \tag{2.29}$$

Here e is the unit of electric charge on the electron, and we have defined:

$$J^{+\mu} := \bar{\mathcal{E}}_L \gamma^\mu \mathcal{N}_L \tag{2.30}$$

$$J^{-\mu} := \bar{\mathcal{N}}_L \gamma^\mu \mathcal{E}_L \tag{2.31}$$

$$J_Z^\mu := J_3^\mu - s_W^2 J_{EM}^\mu \tag{2.32}$$

$$J_3^\mu := \frac{1}{2}\bar{\mathcal{N}}_L \gamma^\mu \mathcal{N}_L - \frac{1}{2}\bar{\mathcal{E}}_L \gamma^\mu \mathcal{E}_L \tag{2.33}$$

$$J_{EM}^\mu := -\bar{\mathcal{E}}_L \gamma^\mu \mathcal{E}_L \tag{2.34}$$

A completely parallel derivation exists for the interaction of the quarks with the electroweak gauge bosons, substituting $\mathcal{E}$ with $\mathcal{D}$ and $\mathcal{N}$ with $\mathcal{U}$, also updating the unbroken $U(1)$ charges according to $Q = T^3 + Y$, such that $J_{EM}^\mu := +\frac{2}{3}\bar{\mathcal{U}}_L \gamma^\mu \mathcal{U}_L - \frac{1}{3}\bar{\mathcal{D}}_L \gamma^\mu \mathcal{D}_L$.

Also, as in the case of the Higgs field, the kinetic term of the electroweak Lagrangian allows for triple and quartic boson self-interactions. The full set of electroweak vertices is shown below in Figure 2.3.
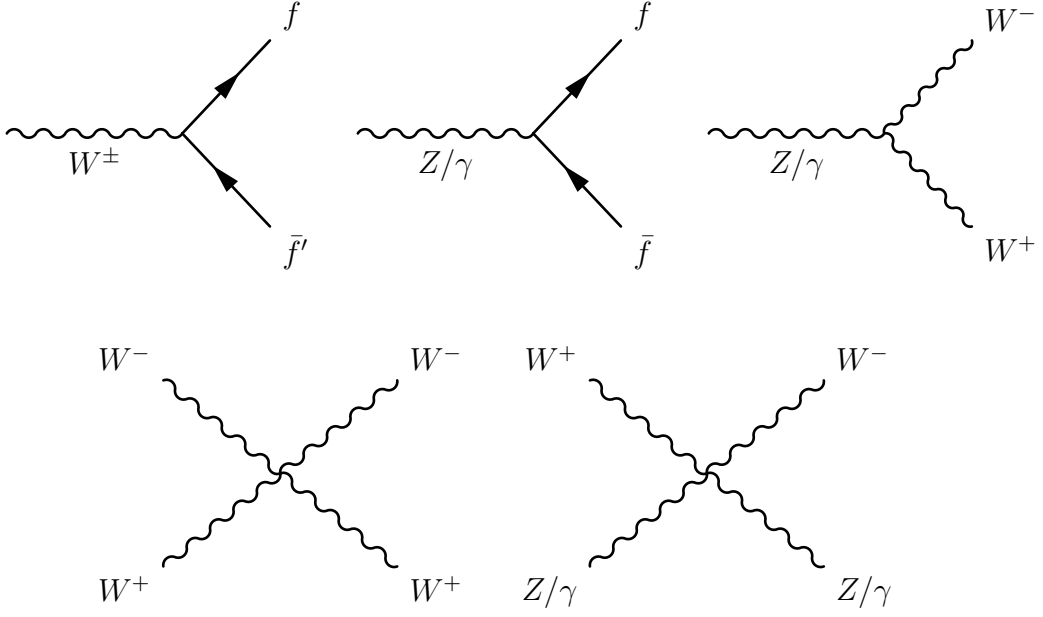
Figure 2.3: Vertices allowed by the Standard Model containing a W or Z boson

The associated couplings are $g_{Wff} = \frac{e}{\sin\theta_{\mathrm{W}}}$, $g_{\gamma ff} = e$ [68], $g_{Zff} = \frac{e}{\sin\theta_{\mathrm{W}}\cos\theta_{\mathrm{W}}}$, $g_{WW\gamma} = e$, $g_{WWZ} = e\cot\theta_{\mathrm{W}}$ [1], $g_{WWWW} = \frac{e^2}{2\sin^2\theta_{\mathrm{W}}}$, $g_{WWZ\gamma} = e^2\cot^2\theta_{\mathrm{W}}$, and $g_{WWZZ} = e^2\cot^2\theta_{\mathrm{W}}$ [62]. One interesting note, is that the $W^{\pm} \to f\bar{f}'$ vertex is the only vertex in the standard model which connects $\mathcal{D}$ and $\mathcal{U}$-type or $\mathcal{N}$ and $\mathcal{E}$-type fermions. In addition, the generations of fermions can be connected by the $W^{\pm} \to f\bar{f}'$ vertex. In the case of the quarks, the fact that there are two Yukawa couplings introduces an added complexity that the weak eigenstates of the quarks need-not in general be the same as the mass eigenstates. This amounts to a unitary transformation of the charged currents: $J^{+\mu} := \bar{\mathcal{D}}_{LI}(V^{\dagger})_{IJ}\gamma^{\mu}\mathcal{U}_{LJ}$ and $J^{-\mu} := \bar{\mathcal{U}}_{LI}V_{IJ}\gamma^{\mu}\mathcal{D}_{LK}$. This transformation V is known as the Cabibbo–Kobayashi–Maskawa (CKM) matrix, shown in Equation 2.35. It depends on three angles $\theta_1, \theta_2, \theta_3$ and one phase δ, which have been measured experimentally and can be found in [69]. In the expression below, c_i and s_i are shorthand for $\cos\theta_i$ and $\sin\theta_i$ respectively.

$$V = \begin{pmatrix} c_1 & s_1 c_3 & s_1 s_3 \\ -s_1 c_2 & c_1 c_2 c_3 - s_2 s_3 e^{i\delta} & c_1 c_2 s_3 + s_2 s_3 e^{i\delta} \\ -s_1 s_2 & c_1 s_2 c_3 + c_2 s_3 e^{i\delta} & c_1 s_2 c_3 - c_2 s_3 e^{i\delta} \end{pmatrix} \tag{2.35}$$

2.2.3 The QCD Sector

The $SU(3)$ charge has historically been called "color charge" in analogy with the three primary colors red, green, and blue and their combinations which can result in a colorful combination or colorless combination (singlet). Thus, this sector of the Standard Model goes by the name of Quantum Chromodynamics (QCD).

The expanded terms of the QCD Lagrangian are shown below in Equation 2.36 [62]. The first line represents the kinetic term that gives rise to the propagators. The second line is the color interaction between the quarks and gluons, where $T_a = \frac{\lambda_a}{2}$, and λ_a are the Gell-Mann matrices. The third line is the interaction of the gluons with one another. The sums run over i, where i denotes flavor (u, d, s, c, b, t).

$$\begin{aligned} \mathcal{L}_{\text{QCD}} = &-\frac{1}{4} \left(\partial^\mu G_a^\nu - \partial^\nu G_a^\mu \right) \left(\partial_\mu G_\nu^a - \partial_\nu G_\mu^a \right) + \sum_i \bar{Q}_i^\alpha \left(i \gamma_\mu \partial_\mu - m_i \right) Q_i^\alpha \\ &- g_s G_a^\mu \sum_i \bar{Q}_i^\alpha \gamma_\mu \left(T_a \right)_{\alpha\beta} Q_i^\beta \\ &- \frac{g_s}{2} f^{abc} \left(\partial^\mu G_a^\nu - \partial^\nu G_a^\mu \right) G_\mu^b G_\nu^c - \frac{g_s^2}{4} f^{abc} f_{ade} G_b^\mu G_c^\nu G_\mu^d G_\nu^e \end{aligned} \tag{2.36}$$

Thus, the allowed pure-QCD vertices in the standard model are shown in Figure 2.4. The value of the single coupling constant $\alpha_s \equiv \frac{g_s^2}{4\pi}$ measured at $s = M_Z$ is $\alpha_s = 0.1179(9) \pm 0.0076$ [69].
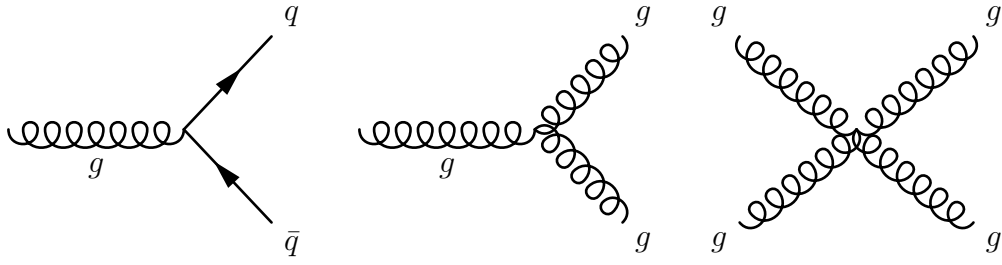
Figure 2.4: QCD vertices allowed by the Standard Model – g here is denoting a gluon

There are several notable properties of QCD, one being that only color singlet states are observed in nature to date. Also, when renormalizing QCD, it is evident that the coupling strength is larger at low energies, and therefore quarks and gluons become confined in hadrons and mesons. This is in fact true of QCD, while not true for the electroweak interactions where the underlying symmetry is broken.

This confinement leads to many difficulties in the lab, since the quarks and gluons themselves can only ever be indirectly measured. Furthermore, if one wants to study high energy proton-proton interactions for example, the initial momentum states of the constituent objects (primarily two up quarks, one down quark, and a soup of gluons) are not known with certainty. The content and momentum states of the internal constituents of the proton are estimated in this case by Parton Distribution Functions (PDFs) as a function of momentum transfer.

2.3   Physics Beyond the Standard Model

There are many notable phenomena which have been observed experimentally for which the Standard Model currently offers no explanation. The omission of gravity is perhaps most glaringly obvious. In addition, there is no suitable candidate for particulate dark matter, no explanation for the experimentally observed, non-zero neutrino mass, and

no explanation for the mass hierarchy or content of families of quarks and leptons. Also, from the Standard Model point of view, the neutrinos are massless; however, it is known from neutrino oscillation observations that the neutrinos have a very small but explicitly non-zero mass. All of these observations require explanations Beyond the Standard Model (BSM).

In the modern era, there is a lack of observations in collider experiments that are in tension with the Standard Model (though some do exist, [7, 46]). In light of this, another method to explore the possible BSM landscape is to do a blanket search using an Effective Field Theory (EFT) built from all allowed operators of appropriate mass dimension. Experimentalists can then measure processes and observables which may have contributions from BSM operators. And in the absence of the detection of new physics, this allows for constraint of the energy scale at which new physics can exist.

This EFT approach begins by considering the hypothesis that the Standard Model measured so far is a low energy approximation of a more fundamental theory. Therefore, at some higher energy, Λ, cracks in the Standard Model could appear. These deviations could take the form of altering the couplings of the fields. And so we can write the full Lagrangian as:

$$\mathcal{L}_{\text{SM}} = \mathcal{L}_{\text{SM}}^{(4)} + \frac{1}{\Lambda} \sum_k C_k^{(5)} Q_k^{(5)} + \frac{1}{\Lambda^2} \sum_k C_k^{(6)} Q_k^{(6)} + \mathcal{O}\left(\frac{1}{\Lambda^3}\right) \tag{2.37}$$

Where the $\mathcal{L}_{\text{SM}}^{(4)}$ term is the renormalizeable Standard Model Lagrangian containing the familiar terms described in section 2.2. The $C_k^{(n)}$ are the dimension-n couplings (dimensionless Wilson coefficients), and the $Q_k^{(n)}$ are the dimension-n operators [48]. If these dimension-$n > 4$ terms are manifest in nature, this could show up in collider experiments as anomalous couplings between the known Standard Model fields.

We are working towards a measurement of the electroweak-induced W boson production in association with jets (EWK-W) processes in chapter 6, which involves one aptly named Vector Boson Fusion (VBF)-W process. This VBF-W process contains the WWV vertex, which could be affected by any of the terms in the dimension-6 effective Lagrangian shown in Equation 2.38. Any anomalous excess or deficit in the EWK-W production cross-section could hint at non-zero values for one or more of these terms.

$$
\mathcal{L}_{\mathrm{EFT}}^{WWV} = -ig_{WWV} \left[g_1^V V^\mu \left(W_{\mu\nu}^- W^{+\nu} - W_{\mu\nu}^+ W^{-\nu} \right) + \kappa_V W_\mu^+ W_\nu^- V^{\mu\nu} + \frac{\lambda_V}{m_W^2} V^{\mu\nu} W_\nu^{+\rho} W_{\rho\mu}^- \right]
$$
$$
+ ig_{WWV} \left[\frac{\tilde{\kappa}_V}{2} W_\mu^- W_\nu^+ \epsilon^{\mu\nu\rho\sigma} V_{\rho\sigma} + \frac{\tilde{\lambda}_V}{2m_W^2} W_{\rho\mu}^- W_\nu^{+\mu} \epsilon^{\nu\rho\alpha\beta} V_{\alpha\beta} \right] \qquad (2.38)
$$

Whether any of the these terms are manifest in nature remains to be seen. And so, with the potential to discover new insight into the nature of the universe, we now turn our attention to the experimental setup for such a measurement.

Experimental Background

3.1 CERN and the LHC

At the energy frontier as the world's highest energy hadron collider, the aptly named LHC is the latest extension of the vast accelerator complex housed at CERN, situated outside of Geneva, straddling the border between France and Switzerland. An outline of the CERN accelerators and subsystems is shown in Figure 3.1.
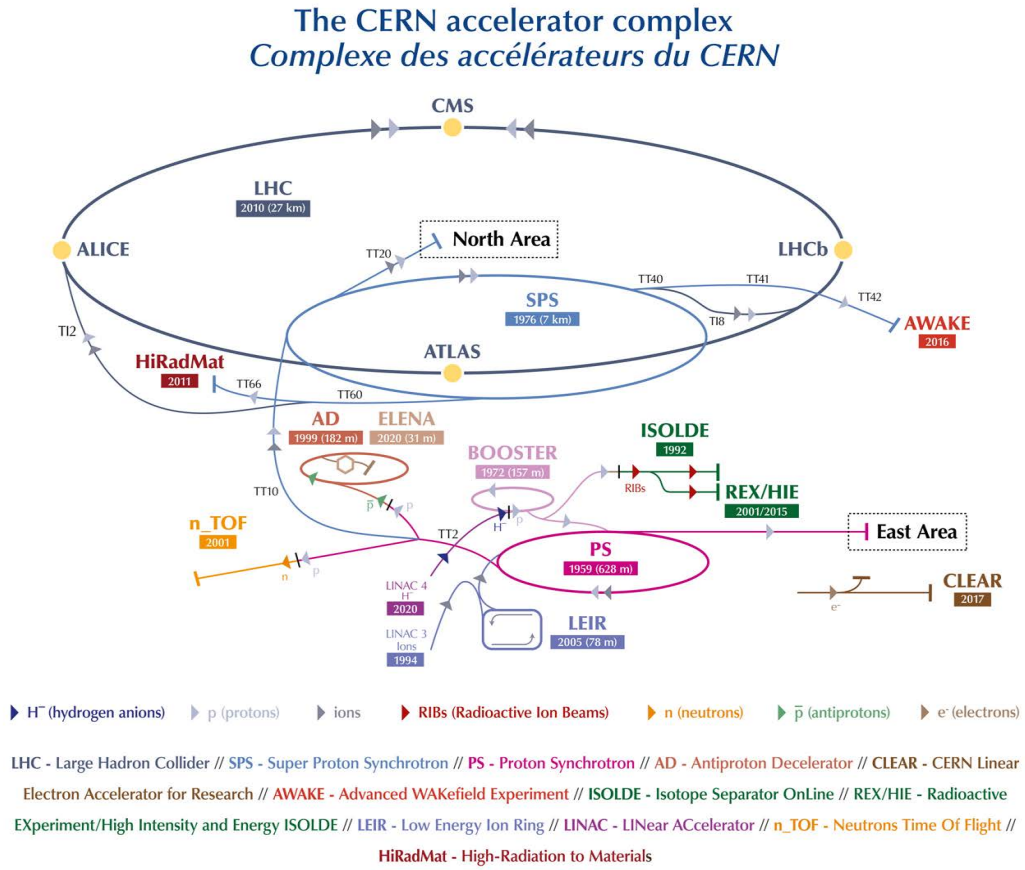
Figure 3.1: The CERN accelerator complex during the LHC Run 3 period [52]

As can be seen in Figure 3.1 the LHC is the final stage in the accelerator chain. The origin of the particles which find themselves in the LHC depends on their type. During Run 3, protons destined for the LHC originate from Linear Accelerator (LINAC) 4, as H^- anions with center of mass energy of about 160 MeV, which are then stripped of their electrons before exiting. For about 40 years prior to Run 3, LINAC 2 was used as the first acceleration stage, accelerating bare protons to about 50 MeV. Passing next through the Proton Synchrotron Booster (PSB), the protons reach an energy of about 2 GeV en route to the Proton Syncrhotron (PS). The PS further increases the energy to about 26 GeV. The PS then injects the particles into the Super Proton Synchrotron (SPS), which feeds them into the LHC at an injection energy of 450 GeV. From there, the LHC further increases the particle energies. During Run 2, the proton-proton beams maintained a center of mass energy of 13 TeV (6.5 TeV per beam). Currently, in Run 3, this has increased to 13.6 TeV (6.8 TeV per beam).

In addition to protons, heavy ions such as lead nuclei can be injected into the machine. Heavy ions which find themselves in the LHC come initially from LINAC 3 and are then injected into the Low Energy Ion Ring (LEIR), where their energy is stepped from 4.2 MeV to 72 MeV per nucleon before injection into the PS. The PS increases the energy to roughly 6 GeV. From there the heavy ions also pass through the SPS, exiting with about 177 GeV and into the LHC where the lead-lead beams in Run 2 were accelerated to 2.76 TeV each.

It is worth emphasizing that the work described in this document pertains mainly to proton-proton collisions, data, and the physics therein. Though there is obviously overlap in the physics as well as in the challenges of recording and analyzing both sets of data, the heavy ion program is not considered in the remainder of the text unless explicitly

invoked. In addition, the abundance of high energy particle beams allows for the study of phenomena from antimatter to exotic radio-isotopes to new accelerator research and development. Some of these peripheral accelerator-related experiments housed at CERN are shown in Figure 3.1.

The LHC itself inhabits the tunnel which was formerly the home of the Large Electron Positron Collider (LEP) and is about 27 kilometers in circumference. The LHC consists of two beam pipes through which like-charge high energy particles circulate in opposite directions. Radio frequency (RF) cavities accelerate the beams by applying a 400.8 MHz alternating electric field of about 5 MV/m. The alternating electric field also has the effect of packing the constituent particles into bunches longitudinally, with a minimum temporal bunch spacing of about 25 ns. For a given bunch position, the revolution frequency is 11.245 kHz. These parameters give a harmonic number of 3564 possible bunch positions around the LHC ring. During an LHC proton fill, a maximum of 2808 positions can be populated by proton bunches containing about 10^{11} protons per bunch. The empty positions and specific filling scheme are chosen to balance the load on the machine – and also by requirement provide space for an "abort gap" of 3 μs which allows the time required to build up the nominal field of the LHC dump kicker magnet. This magnet initiates the mechanism by which the LHC can be emptied of particles by diverting the beams into designated fixed targets housed at LHC point 6 which are designed to safely absorb the $\sim 10^2$ MJ stored in each beam [43].

The particle bunches are made to cross paths at 4 interaction points around the LHC ring with a frequency of 40 MHz. Each interaction point is surrounded by large particle detectors: ATLAS, CMS, ALICE, and LHCb. These detectors are designed to measure the properties of radiation emanating from collisions during these bunch crossings in

the hope of using this information to divine the underlying physics driving the particle interactions [43]. A graphical layout of the LHC is shown in Figure 3.2.
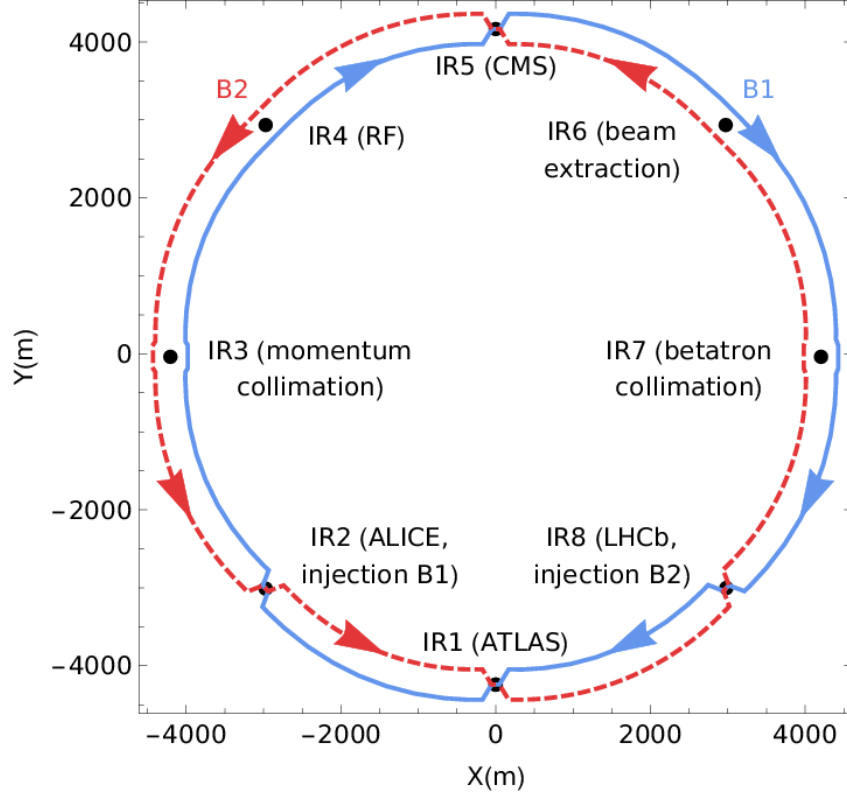
Figure 3.2: The orientation of beams and points of interest around the LHC ring [36]

The proton-proton collisions per second is commonly referred to as the instantaneous luminosity, L, and is a function of several beam-related parameters shown in Equation 3.1 from [43].

$$L = \frac{N_b^2 n_b f_{\text{rev}} \gamma_r}{4\pi \epsilon_n \beta^*} F \tag{3.1}$$

In this expression, the meaning of each parameter is defined below:

- N_b is the number of particles per bunch

27

- n_b is the number of bunches per beam

- f_{rev} is the revolution frequency

- γ_r is the relativistic gamma factor

- ϵ_n is the normalized transverse beam emittance

- β^* is the beta function at the collision point

- F is the geometric luminosity reduction factor due to the crossing angle at the collision point

At the beginning of an LHC fill, the instantaneous luminosity can reach about 10^{34} cm^{-2} s^{-1}. As the bunches cross and collisions occur between constituent particles, the number of particles per bunch and thus the instantaneous luminosity decreases. Once the quality of the beams significantly degrade due to these collisions, a decision is made by the LHC operators to dump the beams, and the LHC is refilled. Typically, LHC fills last for $\mathcal{O}(\text{hours})$, and refilling takes about 1-2 hours before the stable colliding beams are realized again after the beams have been dumped. During physics running, this procedure is repeated many times in order to accumulate data for the experiments to analyze.

The number of times a specific event is expected to occur per unit time is then related to the cross-section for the event times the luminosity (Equation 3.2).

$$N_{\mathrm{event}} = L\sigma_{\mathrm{event}} \tag{3.2}$$

As discussed in chapter 2, there is a procedure to calculate σ_{event} for processes which one would like to study. Then the task becomes accumulating enough events of a given type to be able to test hypotheses against the measured data. This broaches the topic

of recording the data from LHC collisions. For that, we turn our focus to the ATLAS detector, one of the two general purpose particle detectors at the LHC. It is the largest collider detector ever built, and its description follows in the next section.

3.2   The ATLAS Detector

The ATLAS detector sits at interaction point 1 on the LHC ring, near the main entrance to the CERN Meyrin site, approximately 100 meters underground. ATLAS is one of two general purpose detectors at the LHC, the other being CMS. ATLAS is designed to have acceptance covering almost the full azimuthal angle. It is symmetric with respect to the beam pipe axis and allows for detection of particles at very small angles off this axis in both forward and backward directions.

ATLAS is composed of several sub-detectors, designed to measure specific properties of radiation emitted from collisions. Working outward from the interaction point, these sub-detector systems are: the Inner Detector (ID), the calorimeters, and the muon system. Also, the infrastructure to identify interesting collisions and read out data exists both on and off detector and goes by the name Trigger and Data Acquisition (TDAQ). Figure 3.3 shows an overview of the detector technologies that comprise ATLAS, and Figure 3.4 shows examples of several different types of radiation passing through these systems.
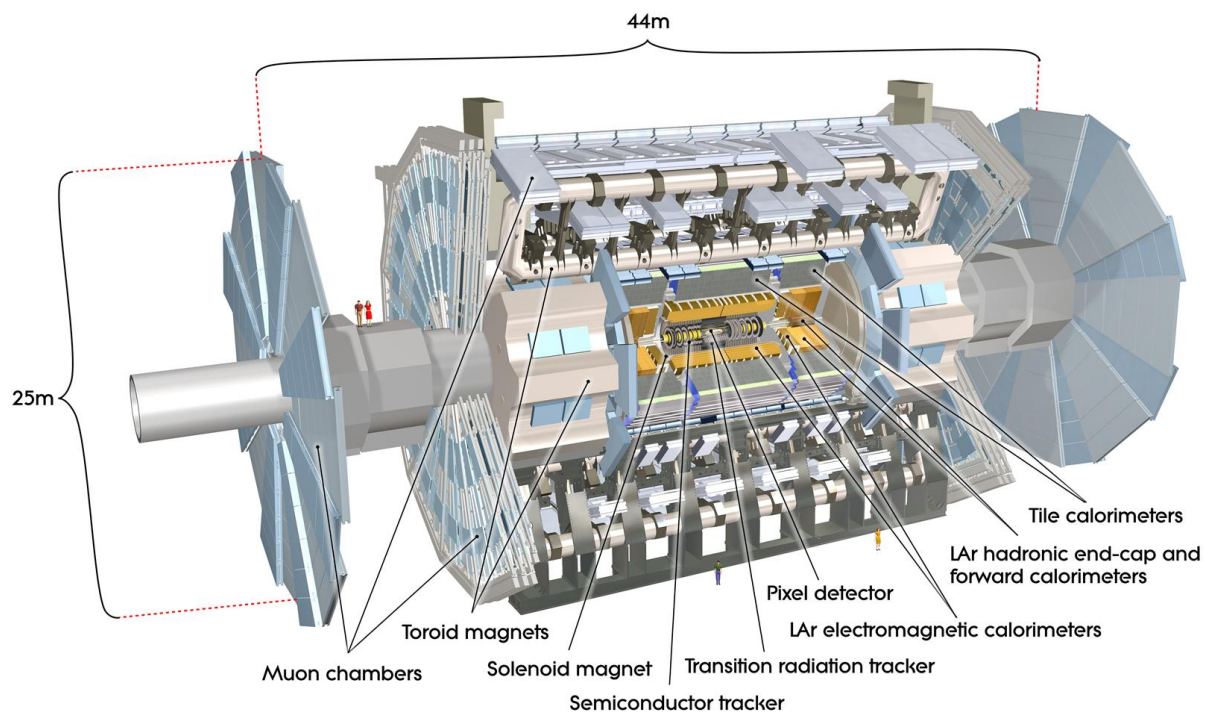
Figure 3.3: The ATLAS detector [60]
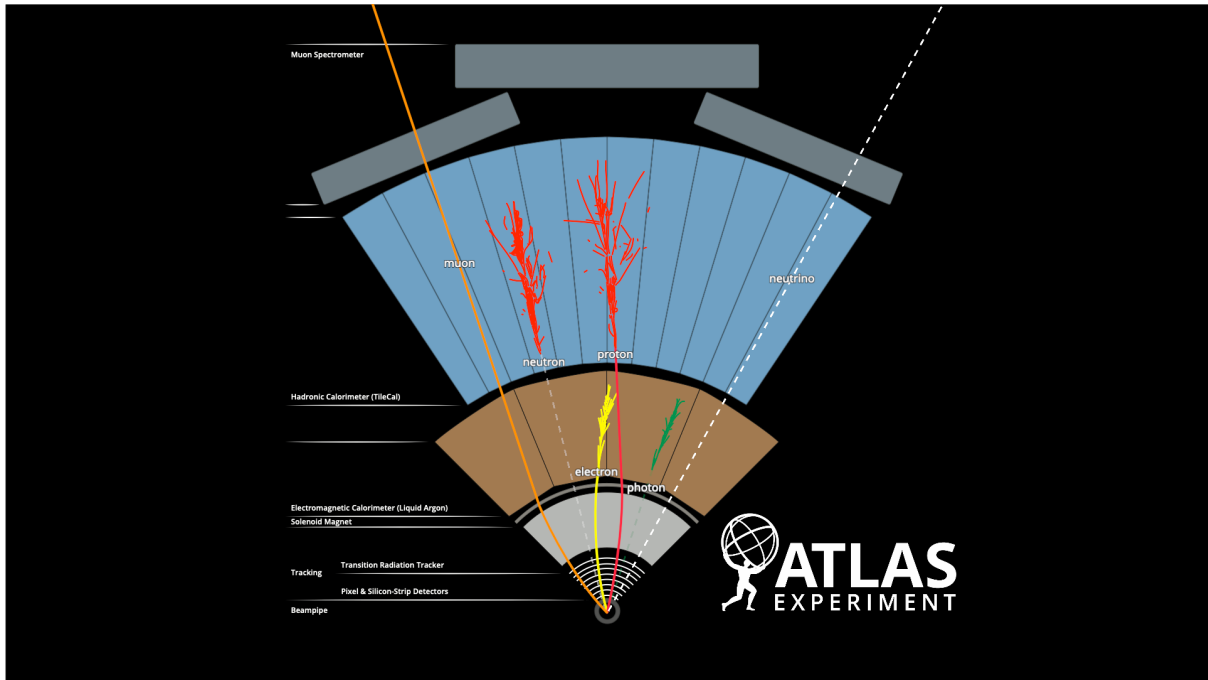
Figure 3.4: The passage of various types of radiation through the ATLAS detector [51]

The coordinate system used by ATLAS and each of the sub-detectors are described in more detail below. Much of the information in this section comes from [11] unless otherwise noted.

3.2.1 Coordinate System

ATLAS uses a right-handed coordinate system with the beam pipe running along the z-axis, and the positive x-axis pointing towards the center of the LHC ring. The positive y-axis then points up from the LHC tunnel towards the earth's surface. Pseudorapidity, η, is commonly used in place of unscaled polar angle, θ, due to its invariance under

Lorentz boosts. The definition of η in terms of θ is shown in Equation 3.3.

$$\eta = -\ln\left[\tan\left(\frac{\theta}{2}\right)\right] \tag{3.3}$$

For massive objects the rapidity, y, is used in place of pseudorapidity. The expression for a massive object's rapidity in terms of its energy and momentum components is shown in Equation 3.4.

$$y = \frac{1}{2}\ln\left(\frac{E + p_z}{E - p_z}\right) \tag{3.4}$$

This expression for y collapses to that of η for massless objects and objects whose total energy is much greater than their rest mass, such that $E \approx |\vec{p}|$.

The azimuthal angle is denoted by $\phi \in [0, 2\pi]$. The axes and common coordinates are shown in Figure 3.5.
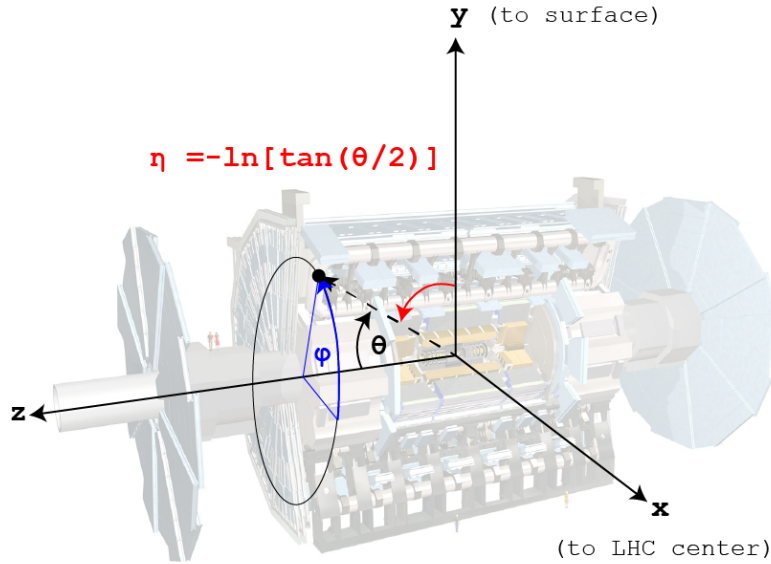
Figure 3.5: The ATLAS coordinate system

3.2.2 Inner Detector

The ID sits closest to the beam pipe, starting at a distance of 5 centimeters, extending radially approximately 1 meter. The ID measures charged particle trajectories, referred to hereafter as "tracks". Particle tracks are used for two very important purposes. The first is to determine the location of primary and secondary vertices in a collision, and the second is to determine each charged particle's momentum. In order to make precise momentum measurements, the ID is immersed in a 2 T solenoidal magnetic field.

The innermost sensors are silicon pixels and the Semiconductor Tracker (SCT) made of silicon micro-strips. Both provide discrete spatial measurements at very high resolution. The pixel system consists of 1744 sensors, each of which are 250 μm thick oxygenated n-type wafers with readout pixels implanted on the n^+ side of the wafer [10, 11]. The nominal pixel size is $50 \times 400 \mu m^2$. Each of the 1744 sensors in the pixel system has 46080 readout channels. The SCT system consists of 15912 sensors which are classic p-in-n technology with AC-coupled readout strips.

The Transisiton Radiation Tracker (TRT) begins at a radial distance of about 0.5 meters from the beam pipe. It is designed to provide continuous tracking at less material per point and cost than the higher precision pixel and SCT systems [10] by exploiting the transition radiation given off by electromagnetically charged particles as they traverse its straw tubes immersed in primarily xenon gas. The TRT consists of about 300,000 polyimide drift tubes (straws) each 4 mm in diameter in a mixture of xenon (70%), carbon dioxide (27%), and O_2 (3%). The straw cathode is operated at -1530 V. Electrically charged particles traveling through the TRT will ionize the gas mixture, resulting in detection via measured straw current. Particles traverse a minimum of 36 straws when passing through the TRT [10, 11].
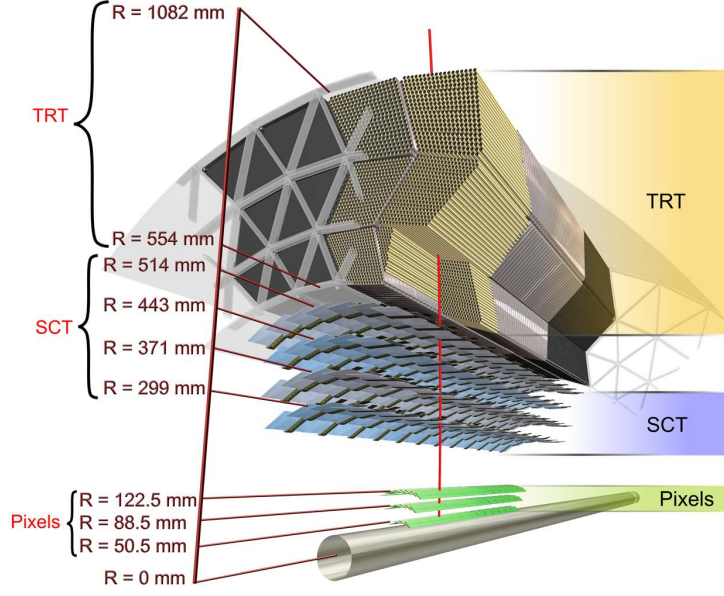
Figure 3.6: The radial arrangement of the ATLAS ID [58]

3.2.3 Calorimetry

The purpose of the calorimeter is to stop as much radiation as possible emanating from the collision point, and thereby measure its energy. ATLAS uses two technologies for calorimetry: Liquid Argon (LAr) and Scintillating Tile (Tile). In the barrel region ($|\eta| < 1.6$), the innermost layer is the LAr Electromagnetic Barrel Calorimeter (EMB) and the outermost layer is Tile hadronic calorimeter. From $|\eta| \in [1.5, 3.2]$ we have both electromagnetic and hadronic LAr calorimeters – the LAr Electromagnetic End-Cap Calorimeter (EMEC) and Hadronic End-Cap Calorimeter (HEC). Note that there is an overlap of the HEC and Tile extended barrel system from $|\eta| \in [1.5, 1.6]$. From $|\eta| > 3.2$ there is reduced spatial granularity, and the region is collectively referred to as the Forward Calorimeter (FCAL). The FCAL extends from $|\eta| = 3.2$ up to roughly the

full calorimeter acceptance of $|\eta| \sim 4.9$. For reference, $|\eta| = 4.9$ corresponds to about $0.9°$ off of the beam axis [11]. Figure 3.7 shows the layout of these calorimeters.
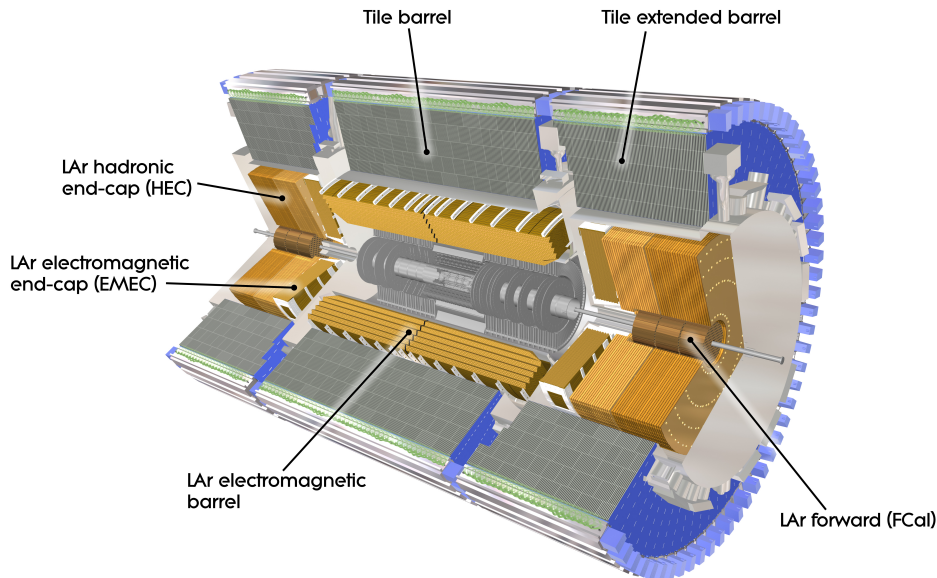
Figure 3.7: The ATLAS calorimeter system [57]

For the electromagnetic calorimeters, liquid argon is the active material, cooled to $-184°$C to remain liquid. Electrons and photons ionize the liquid argon and also lose energy due to cascades of bremsstrahlung initiated by interaction with the passive material, lead in this case. Ultimately, many lower energy electron/positron pairs are created that drift toward the cell anode/cathode under the presence of the high voltage. The resulting electrical pulse is then sampled and transmitted by on-detector electronics. Using the amplitude and temporal location of the peak of these pulses along with calibration data, an energy can be associated with the radiation that passed through the cell. As can be seen in Figure 3.4, tracking information from the IDs combined with the electromagnetic

calorimeter energy is needed to most precisely differentiate electrons and photons [8, 11].

In terms of hadronic calorimeters, the Tile calorimeter uses steel as an absorber and scintillator as the active material. The choice of technology for the Tile calorimeter was motivated by limiting the radiation leakage into the muon system (also called *punch-through*) as well as by keeping the material cost of the system manageable, given the large volume required at this detector radius [9]. The LAr hadronic end caps function in similar fashion to the previously described LAr technology; however, in this case, copper is used as the passive material [8].

The FCAL begins about 4.7 m from the interaction point, due to its position at high $|\eta|$. The small angles and proximity to the beam pipe subjects the FCAL to high particle flux. This consideration resulted in a design with very small LAr gaps surrounding electrode rods centered in tubes oriented parallel to the beam pipe. It is segmented into three layers. The first of which is the electromagnetic FCAL, or FCAL1, using copper as the passive material. The next two layers are the hadronic FCAL2 and FCAL3, both using sintered tungsten as the passive material [8, 11].

Figure 3.8 shows the cumulative distribution of calorimeter material in terms of interaction lengths as a function of pseudorapidity.
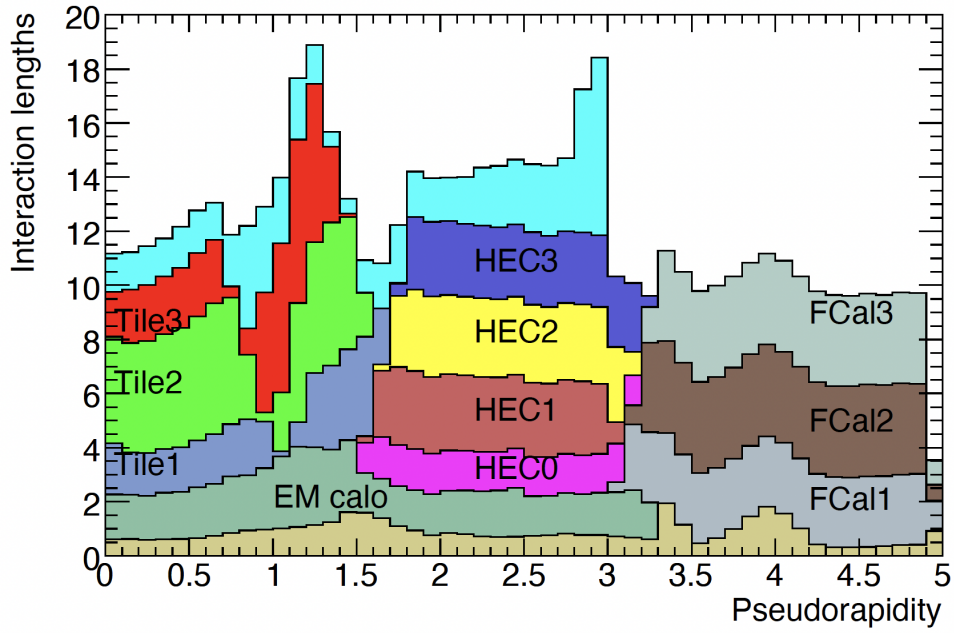
Figure 3.8: The cumulative material distribution of the ATLAS calorimeters as a function of pseudorapidity (η), the unlabeled light-brown component at the bottom of the figure represents the ID, and the unlabeled top layer of blue displays the first active layer of the Muon Spectrometer (MS). [11]

The spatial resolution in $\eta - \phi$ space varies as a function of η, sub-system, and radial distance from the interaction point. In the barrel, the LAr calorimeters are segmented into four transverse layers: pre-sampler, and layers 1, 2, and 3 (sometimes called front, middle, and back), each with further segmentation in $\eta - \phi$. Figure 3.9 shows this segmentation. The Tile calorimeter exists as a self-supporting structure with steel and scintillator interleaved. In the Tile calorimeter, the $\eta - \phi$ segmentation is both coarser and more regular than that of the LAr calorimeter. The energies measured by Tile are considered to logically fall within 0.1×0.1 regions in $\Delta\eta \times \Delta\phi$. The region representing the transverse sum of information contained in this $\eta - \phi$ boundary is given the name "Trigger Tower."
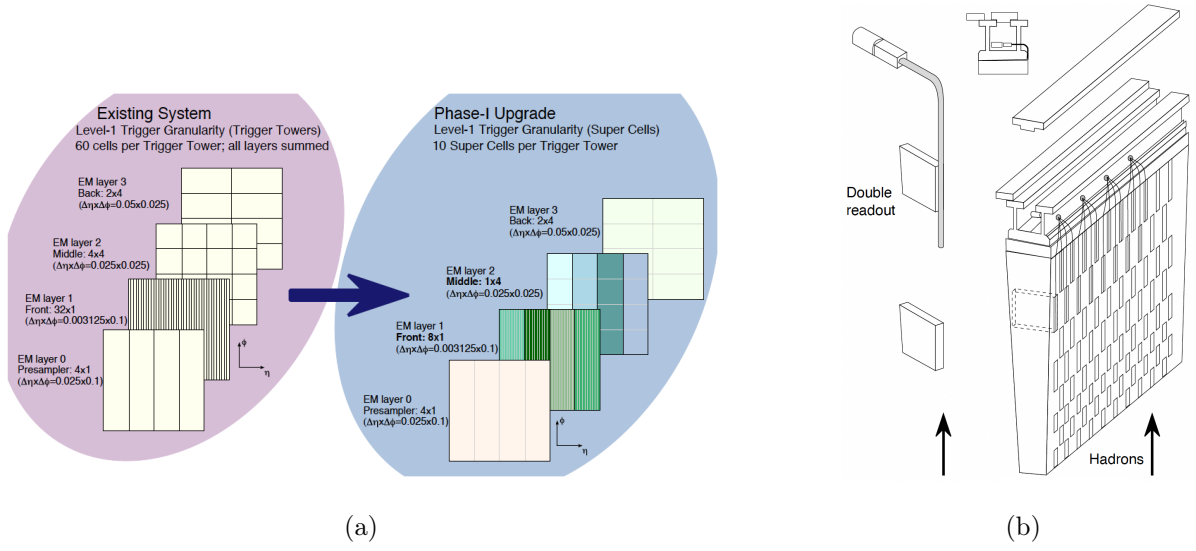
Figure 3.9: The ATLAS barrel calorimeter cell geometry for LAr EMB (a) and Tile (b) calorimeters (adapted from [32] and [9] respectively). The Tile granularity is a roughly uniform 0.1×0.1 in $\Delta\eta \times \Delta\phi$.

An extensive upgrade of the ATLAS calorimeter system was undertaken during Long Shutdown 2. More details of the upgrade efforts can be found in chapter 4 and chapter 5. A more detailed view of the LAr cells in the barrel region is shown below.
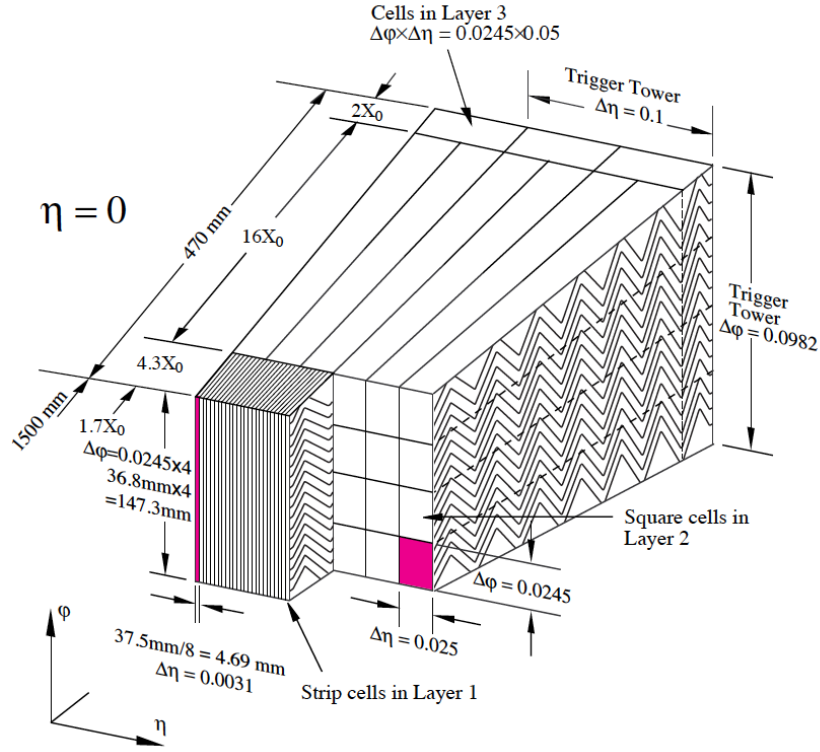
Figure 3.10: The ATLAS LAr calorimeter cell overview

3.2.4 Muon System

Since muons are about 200 times more massive than electrons, they are less affected by bremsstrahlung, earning them the title of minimum-ionizing particles. They escape the ID and calorimeters, leaving only subtle signatures in each. The purpose of the muon system is to measure the momentum of the charged particles (predominantly muons) exiting the barrel and end-cap calorimeters with greater accuracy than can be achieved using the limited information from the ID and calorimeter. To that end, a 0.5 T magnetic field is applied by superconducting air-core toroid magnets in the barrel, and a 1 T magnetic field is applied by two end-cap toroid magnets. The curvature of the muon trajectory combined with precise knowledge of the magnetic field can then be used to calculate the momentum of the muon. For ATLAS, the muon system performance benchmark is a

resolution within 10% for a muon with $p_T = 1$ TeV.

The muon system consists of several technologies. Monitored Drift Tube (MDT) chambers are used to make precision momentum measurements up to $|\eta| < 2.7$. Cathode-Strip Chambers (CSCs) are also used for this purpose in a small portion of the forward region $(2 < |\eta| < 2.7)$. In order to trigger on muon tracks, a system of fast triggering chambers is used, capable of sending tracking information within a few tens of nanoseconds after the passage of a particle. In the barrel region $(|\eta| < 1.05)$ Resistive Plate Chambers (RPCs) provide this service, while in the end-cap $(1.05 < |\eta| < 2.4)$ Thin Gap Chambers (TGCs) are used. Figure 3.11 shows the layout of these components during Run 2. An extensive upgrade to the end-cap "small wheels" was undertaken for Run 3. In this work, the Run 2 configuration is considered by default unless explicitly mentioning Run 3.
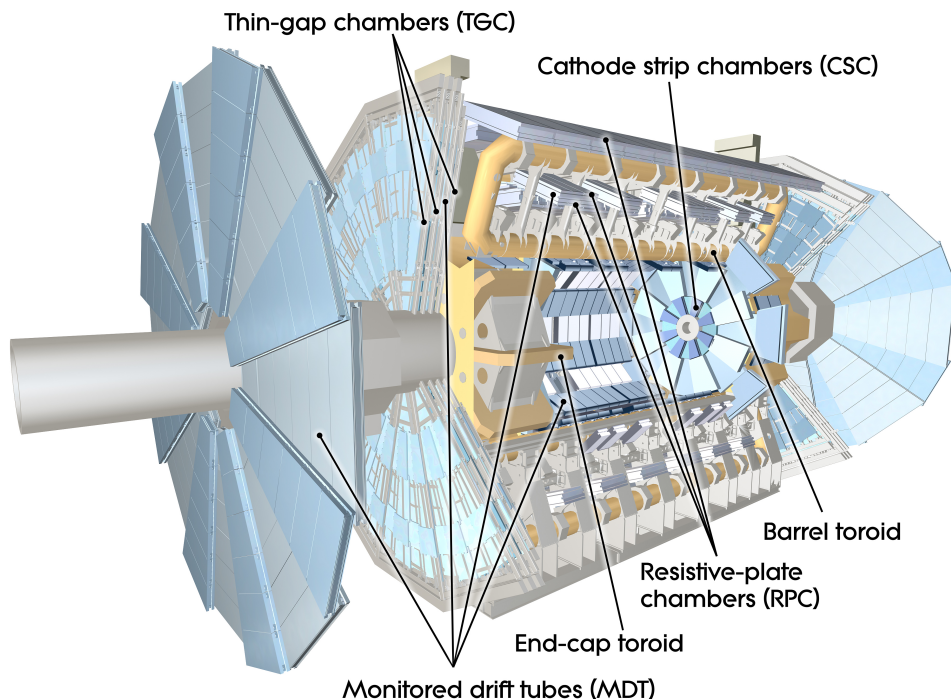
Figure 3.11: The ATLAS muon system [59]

3.2.5 Trigger and Data Acquisition

High energy hadron collisions create a very busy environment for a general purpose detector such as ATLAS. In order to cope with this challenge and maintain sensitivity to interesting physics, ATLAS employs a multi-stage trigger system consisting of three levels of event selection: Level-1 (L1), Level-2 (L2), and the event filter. The latter two stages are collectively referred to as the High Level Trigger (HLT) [11].

The L1 trigger consists of custom electronics and high speed connections. It uses reduced granularity and a subset of detectors (RPC, TGC, and all calorimeters) to make fast decisions on which events to pass on to the HLT. Throughout Run 2, the L1 trigger operated up to the designed maximum trigger rate of 100 kHz, a reduction by a factor of 400 from the 40 MHz bunch crossing frequency provided by the LHC [11].

The HLT is seeded by Region of Interests (RoIs) designated by the L1 trigger and uses commercially available computing and networking resources. Algorithms running in the HLT use the full granularity of the calorimeters and muon system, as well as data from the ID. The event rate out of the HLT is around 200 Hz, with an average processing time around 4 seconds per event [11].

During the recent Long Shutdown 2 (LS2), from late 2018 to the Spring of 2022, the trigger system underwent major upgrades. A detailed discussion of the Level 1 Calorimeter Trigger (L1Calo) and its most recent upgrade can be found in chapter 4, with a specific focus on one processor module, the Global Feature Extractor (gFEX) in chapter 5.

All the aforementioned detector subsystems work together to identify and trigger the recording of luminosity relating to physics processes that demand study. A practical example of the instantaneous luminosity delivered by the LHC and that recorded by ATLAS during one LHC fill is shown in Figure 3.12 alongside the total integrated luminosity to

date delivered to and recorded by ATLAS.
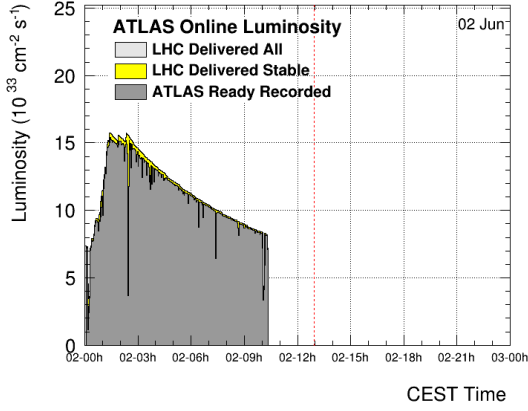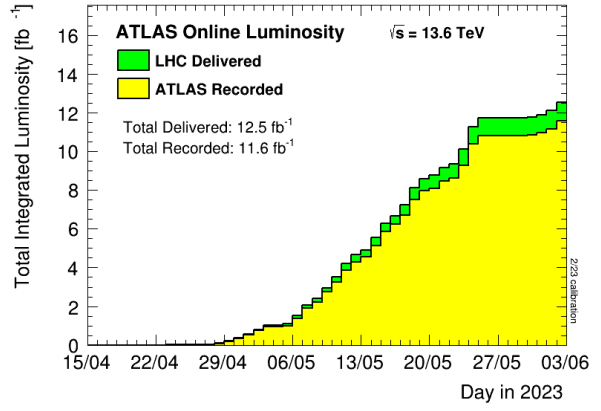
(a)   (b)

Figure 3.12: A recent summary of luminosity delivered to and recorded by ATLAS: Figure (a) shows the instantaneous luminosity delivered and recorded by ATLAS on June 2nd, 2023. The red dashed line represents the time the image was generated. Figure (b) shows the total integrated luminosity delivered to and recorded by ATLAS in the year to date 2023 at the time of this writing.

One physics analysis using 139 fb^{-1} of data recorded by ATLAS from 2015-2018 is the subject of chapter 6. Before discussion of this analysis, let us consider the upgrade work to boost the performance of the ATLAS trigger for Run 3, which follows in the next two chapters.

To conclude this chapter, Table 3.1 shows the sub-systems discussed and their associated dimensions in radial and η coordinates.

Sub-Detector	Sub-System	Approximate Radial Distance From Beam Pipe (m)	$|\eta|$ Range
Inner Detector	Pixel	0.05-0.12	0-2.5
	SCT	0.30-0.51	0-2.5
	TRT	0.55-1.08	0-2.5
Calorimter	EMB	1.15-2.25	0-2.5
	EMEC	0.33-2.25	2.5-3.2
	Tile	2.28-4.25	0-1.6
	HEC	0.33-2.03	1.5-3.2
	FCAL	0.07-0.45	3.1-4.9
Muon Spectrometer	RPC	4.5-11	0-1.05
	MDT	4.5-11	0-2.7*
	TGC	1.5-12	1.05-2.4
	CSC	0.88-2.8	2.0-2.7

Table 3.1: ATLAS sub-detector radial and η coverage (*except in the innermost EMEC layer, where the coverage is limited to $|\eta < 2.0)$

Chapter 4

The ATLAS Level 1 Calorimeter Trigger

4.1 Triggering ATLAS

As mentioned in the previous chapter, the ID has very granular information which is critical in the offline reconstruction, but it is currently too computationally cumbersome to contribute to the ATLAS level 1 trigger decision. And so the calorimeter and muon systems form the primary level 1 triggers. The current industry of identifying interesting calorimeter signatures is confined to electron-finding, tau-finding, jet-finding, and finding missing transverse energy. Ideally, the level 1 trigger accepts the best candidates for events of each type, thereby reducing the rate at which the more computationally expensive HLT algorithms must process data. At the same time, the level 1 trigger must not throw away interesting events through inefficiencies or lack of acceptance.

Also, the continuous flow of data requires that there are no bottlenecks in the data collection process. Thus, the level 1 system must operate at a fixed latency so as not to introduce further dead time into the data taking. And so the trigger system is synchronized to the LHC clock, the detector data flows through the processor modules with fixed latency, and once the trigger conditions are met, a Level 1 Accept (L1A) signal is issued from the Central Trigger Processor (CTP), signaling that all detector modules should read out their data for the accepted bunch crossing.

In summary, the proton bunches collide in the center of ATLAS. The radiation excites the electronics in the various sub-detectors. The calorimeter and muon systems process signals in real time and use low-latency processors to delineate interesting bunch crossings

from boring ones. Then, once an interesting bunch crossing is identified, this decision is propagated to the CTP, which issues an L1A signal that triggers all the sub-detectors to read out their data. This process continues *ad infinitem* while the LHC is running.

4.2   L1Calo Architecture
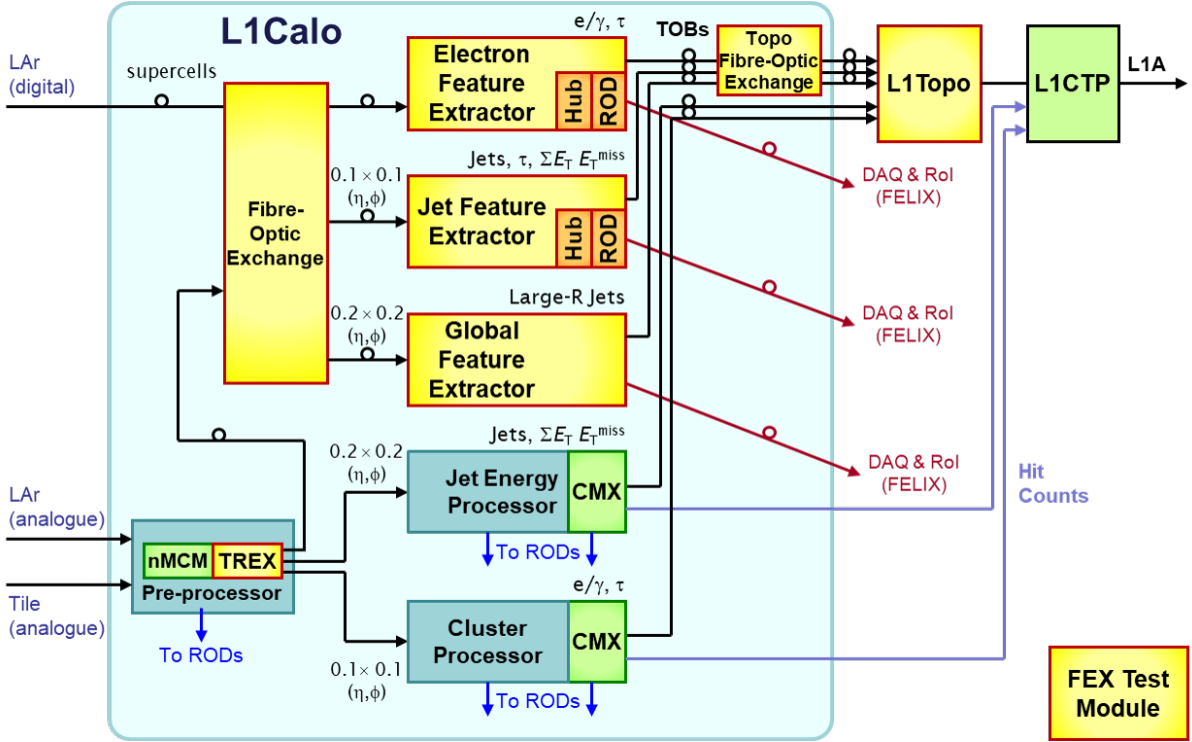
Figure 4.1: Overview of the L1Calo system at the beginning of LHC Run 3 (updated figure from [12]).

L1Calo is designed to identify high energy electrons, photons, taus, jets, and $E_{\mathrm{T}}^{\mathrm{miss}}$ at level 1 using calorimeter data. As viewed from the level 1 perspective, electrons and photons leave very similar signatures (more details of the differentiation of these objects using the HLT can be found in subsection 6.2.1).

Electron, photon, and tau identification makes use of granular calorimeter elements to pass along information about spatial isolation and hadronic energy fraction in local

clusters of energy. These properties are used to discriminate these EM objects from jets. The level 1 EM trigger objects are then used by the HLT as a seed object or RoI, around which more computationally intensive measurements can be done. The fine granularity and seeding require a dedicated system to handle this heavy processing. The legacy system, used for Run 1 and Run 2 of the LHC, uses the Cluster Processor (CP) for this. The upgrade system uses primarily the Electromagnetic Feature Extractor (eFEX) for this purpose.

Jet and $E_\mathrm{T}^\mathrm{miss}$ identification in ATLAS are event-level quantities and do not seed RoIs in the HLT. The jets represent local maxima of energy in the $\eta - \phi$ space of the calorimeter. The $E_\mathrm{T}^\mathrm{miss}$ is constructed from the negative vector sum of all energy deposited in the calorimeter. The $E_\mathrm{T}^\mathrm{miss}$ (sometimes refered to as missing transverse momentum) is then the vector that points opposite the direction of any positive imbalance of energy. The Jet Energy Processor (JEP) modules carry out these computations in the legacy system. The Jet Feature Extractor (jFEX) and gFEX are responsible for jet and $E_\mathrm{T}^\mathrm{miss}$ finding in the upgrade system.

Additionally, the Level 1 Topological Trigger Module (L1Topo) was added in Run 2 to profit from the combination of signatures from multiple systems, and new L1Topo boards will carry out this task in the upgrade system.

The eFEX and the jFEX can be thought of as analogous to the CP and JEP modules of the legacy system, whereas the gFEX extends this architecture to increase the acceptance of events containing very energetic, Lorentz-boosted bosons or decay products of new heavy particles. These boosted object decays typically result in larger radius jets ($R \sim 1.0$ or larger) than those initiated by QCD processes ($R \sim 0.4$), and additionally possess multiple hard cores within the jet radius. Therefore, the combination of large-radius jet

finding and jet substructure information at level 1 is crucial to ensure that these events are triggered [12].

Operationally, the legacy system and the upgrade system run in parallel until the commissioning of the phase-1 upgrade is complete. This provides the opportunity to smooth the transition from legacy to upgrade trigger items. As the modules are commissioned, the upgrade system will take over the duty of triggering ATLAS, and the associated legacy trigger items will be disabled [12]. And so a detailed description of the legacy system will shortly become unnecessary (and is not discussed here in detail) as we now look toward the future and the operation of the phase 1 upgrade.

4.3 L1Calo Phase-1 Upgrade

Upstream of L1Calo, the LAr calorimeter processors have also undergone extensive upgrade to send more granular information than previously possible. The legacy system used analogue Low-Voltage Differential Signaling (LVDS) signals sent by the calorimeter, whereas the phase 1 upgrade uses digital signals sent via optical fiber. The calorimeter modules sending information to the FEXes are the Liquid Argon Trigger Object Mezzanine (LATOME) for LAr and the Tile Rear Extension (TREX) for Tile. Figure 4.2 shows a schematic outline of the data paths in the phase 1 upgrade system. A brief description of each module follows here.
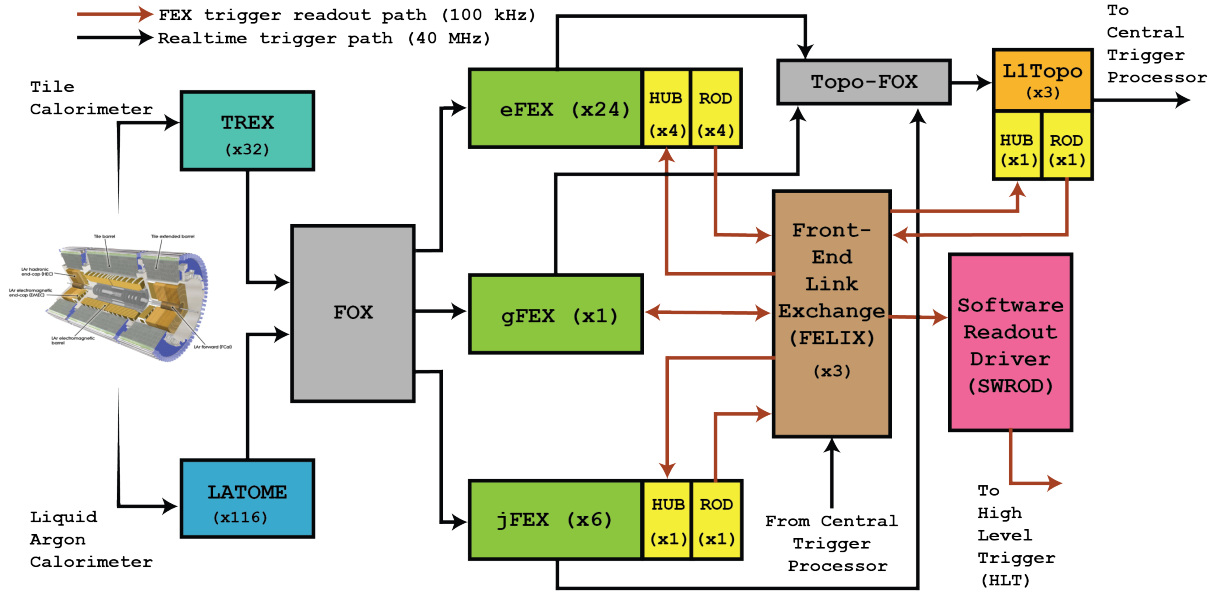
Figure 4.2: The L1Calo Phase-1 upgrade architecture

4.3.1 LATOME and TREX

The LATOME module falls outside the scope of L1Calo and therefore is not discussed in detail here. Much more information can be found in [30]. The TREX technically belongs to L1Calo; however, its purpose in Run 3 is covered in other documents – simplifying a bit, that is, to digitize the signals sent by the Tile calorimeter and interface with the digital readout chain [49]. The primary focus here is to discuss the L1Calo FEX processor systems and L1Topo. This follows in the subsequent sections. Details of the calorimeter input data formats which are sent to the FEX modules can be found in Appendix A. The output of these modules passes through a passive fiber optic patch box known as the Fiber Optic Exchange (FOX), which duplicates channels where needed and reorders the channels into appropriate fiber bundles for input into the FEX systems.

4.3.2 eFEX

The eFEX system is designed to take over the electron, photon, and tau-lepton iden-tification from the legacy system within $|\eta| < 2.5$. To that end, eFEX employs 24 1u Advanced Telecommunications Computing Architecture (ATCA) modules. The modules inhabit two ATCA shelves, each of which is equipped with two readout and timing hub modules (HUBs) and hosting two Readout Driver modules (RODs) which distribute the Trigger and Timing Control (TTC) signals to the eFEX as well as aggregate the readout data from the eFEX modules. Each module processes EM and hadronic signals in order to calculate E_{T} and the quantities listed in Equation 4.1, in $\eta \times \phi = 0.3 \times 0.3$ sliding windows that run by 0.1 in both η and ϕ, such that neighboring windows can overlap [63]. The granularity of the electromagnetic calorimeter as seen by eFEX is shown in Figure 4.3. At larger radius than layer 4, the hadronic calorimeter contributes E_{T} with a granularity of $\eta \times \phi = 0.1 \times 0.1$.
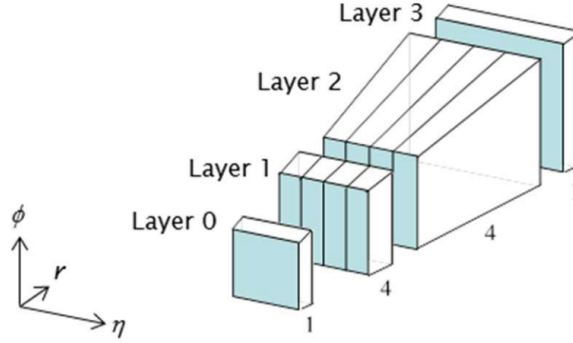
Figure 4.3: eFEX electromagnetic calorimeter input granularity [64]

The electron and photon seed finding algorithm compares the sum of energy in layer 2 in the core area against nearest neighbors. If a core region is a local maximum, then a Trigger Object (TOB) is formed. An example of this seed finding is shown in Figure 4.4.

49
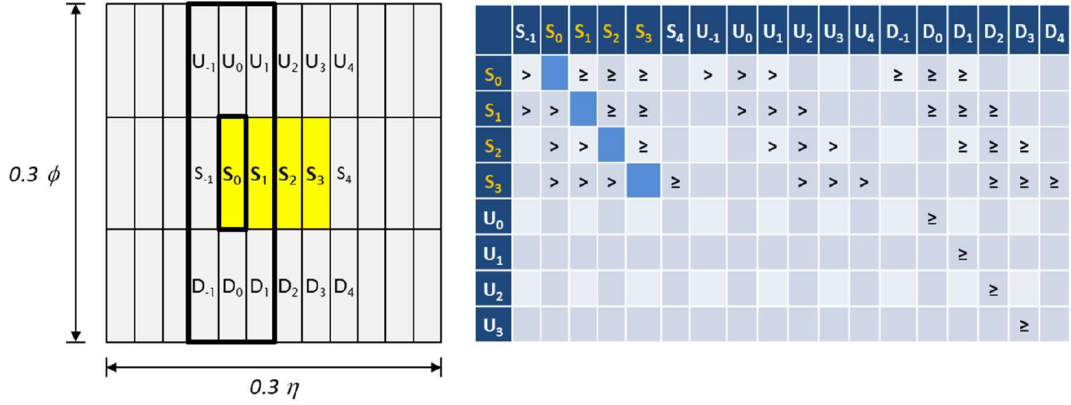
Figure 4.4: eFEX electron/photon seed finding example [64]

Once a TOB is formed, E_{T} and three isolation quantiles are calculated:

$$E_{\mathrm{T}}^{\mathrm{TOB}} = E_{3\times 2}^{(1+2)} + E_{1\times 2}^{(3)} \tag{4.1}$$

$$C_\eta = \frac{E_{3\times 2}^{(2)}}{E_{7\times 3}^{(2)} - E_{2\times 3}^{(2)}} \tag{4.2}$$

$$W_s^2 = \frac{\sum\limits_{i\in\text{layer 1}} E_i^{(1)}(i - i_{\max})^2}{\sum\limits_{i\in\text{layer 1}} E_i^{(1)}} \tag{4.3}$$

$$D_{\mathrm{Had}} = \frac{E_{3\times 2}^{(1+2)} + E_{1\times 3}^{(3)}}{E_{3\times 3}^{(\mathrm{Had})}} \tag{4.4}$$

Here the notation $E_{n\times m}^{(\text{layer})}$ is denoting the $n\times m$ supercells in a given layer, and $(i - i_{\max})$ is the distance of the ith cell to the seed. Thresholds on the quantities in Equation 4.1 are determined by data analysis to optimize the performance of the trigger.

For the tau identification, a similar procedure is carried out. First, a local maximum search performed in towers built from all layers of the electromagnetic and hadronic supercells. Next, a "little" seed finding algorithm searches the supercells in layer 2. An

example of this is shown in Figure 4.5.
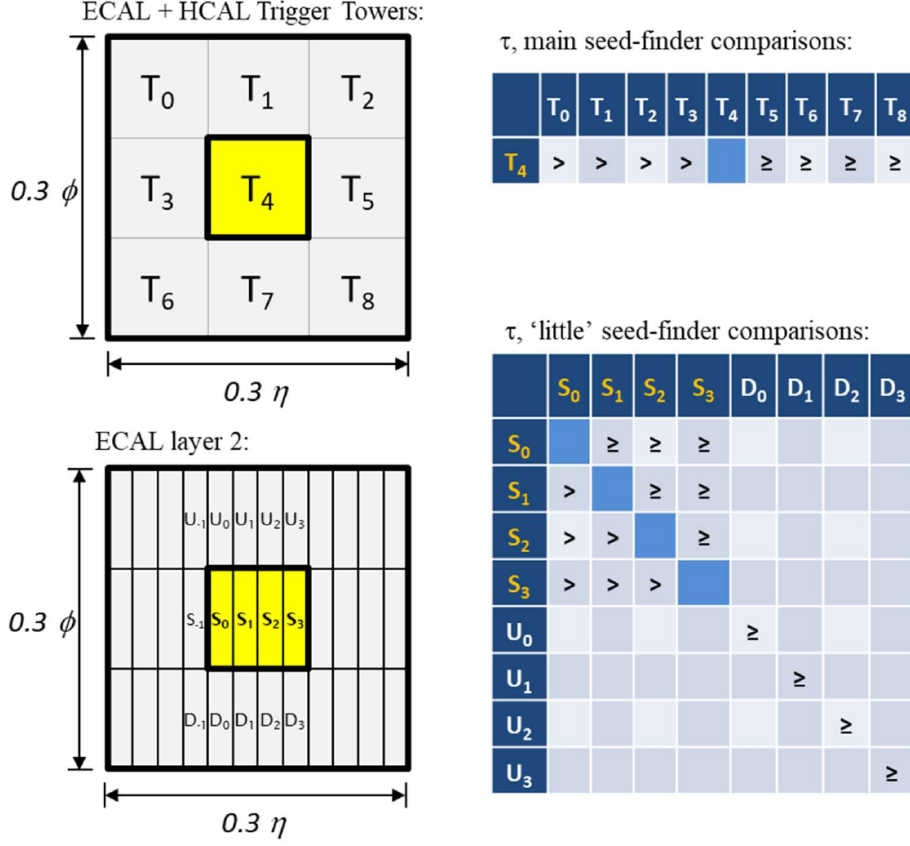
Figure 4.5: eFEX tau-lepton seed finding example [64]

Upon the identification of a tau seed, a TOB is formed, and the E_{T} and T_η quantity are calculated as shown in Equation 4.5. Thresholds are determined for these quantities to optimize the trigger performance.

$$E_{\mathrm{T}}^{\mathrm{TOB}} = E_{5\times2}^{(1+2)} + E_{3\times2}^{(0+3)} \tag{4.5}$$

$$T_\eta = \frac{E_{3\times2}^{(2)}}{E_{9\times3}^{(2)} - E_{2\times3}^{(2)}} \tag{4.6}$$

In addition, a BDT based tau-lepton identification algorithm has been implemented

51

for eFEX and relies on similar shower shape information. This algorithm is currently under development and integration into the eFEX system.

As of the time of this writing, the eFEX has taken over the electron, photon, and tau identification for L1Calo, and the associated legacy trigger items have been decommissioned.

4.3.3 jFEX

The jFEX system consists of six 2u modules which cover the full ϕ range from $|\eta| < 4.9$, housed in one ATCA shelf. Four modules process data from the central region of the calorimeter ($|\eta| \leq 3.2$) and two modules process the forward region ($3.2 < |\eta| < 4.9$). As in the eFEX system, the jFEX modules interface with two HUB/ROD modules for TTC and readout purposes. The jFEX small-radius jet-finding and $E_{\mathrm{T}}^{\mathrm{miss}}$-finding is analogous to the legacy architecture, while the tau and large radius jet computations are have been updated for Run 3. Several sliding window algorithms of various window size run in parallel to achieve this. The jet-finding process considers the sums of E_{T} around a given trigger tower (0.1×0.1 in $\eta \times \phi$) and comparing it to its eight nearest neighbors. If the E_{T} of this tower is a local maximum, then it becomes a jet candidate. Around any jet candidate, a larger sum is performed. The small radius jets are approximately 0.4×0.4 in $\eta \times \phi$, and large radius jets can be formed up to a potential size of 2.2×2.2 in $\eta \times \phi$. The structure of a jFEX small radius jet is shown in Figure 4.6.
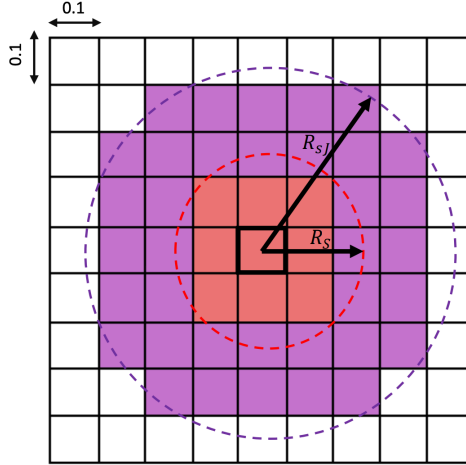
Figure 4.6: jFEX jet structure, showing the 3×3 seed and the $R \sim 0.4$ small radius jet (figure by Niklas Schmitt).

The tau objects are calculated up to $|\eta| < 2.5$ using a similar algorithm along with shower shape information to calculate two quantities for a tau TOB: $E_{\mathrm{T}}^{\mathrm{core}}$ - the energy of in the cone $R < 0.2$ around the center of the seed, and $E_{\mathrm{T}}^{\mathrm{iso}}$ - the energy in the ring of $0.2 < R < 0.4$ around the center of the seed. There is also the future possibility to include forward electron identification ($2.3 < |\eta| < 4.9$).

For the $E_{\mathrm{T}}^{\mathrm{miss}}$ calculation, an average energy per unit area, ρ, is calculated as the truncated mean of all towers passing given upper and lower thresholds. The vector sum of the tower E_{T} is accumulated and finally, ρ is subtracted. The $E_{\mathrm{T}}^{\mathrm{miss}}$ x- and y-components are then taken to be the negative of the ρ-subtracted sums.

4.3.4 gFEX

The gFEX is a single ATCA module which is designed to trigger on large radius jets and $E_{\mathrm{T}}^{\mathrm{miss}}$. The gFEX is described in its own dedicated chapter (chapter 5), and so I defer most details until then. In the context of L1Calo as a whole, the gFEX noticeably differs from the eFEX and jFEX in several physical ways, one being that it is a single module.

Another is that the gFEX interfaces directly with the Front End Link Exchange (FELIX) and does not employ HUB or ROD modules. The gFEX extends the architecture of the legacy system, implementing several novel physics algorithms.

4.3.5   L1Topo

The L1Topo in the Phase-1 upgrade is composed of three 2u ATCA modules, which share many design similarities with the jFEX. It is designed to intake trigger objects from the various level 1 modules, compute relevant quantities related to the trigger decision, and then transmit the appropriate bits to the CTP in order to trigger the event. The triggers may be issued based on threshold of TOB E_T for example, or in the case of jets and leptons, the multiplicity of the TOBs with E_T above a threshold. The L1Topo also receives information from the level 1 muon system for combination with L1Calo derived quantities [34].

4.3.6   HUB/ROD

The HUB module is a 1u ATCA board which hosts a ROD card on-board. The HUB portion of the electronics receives TTC information via connection with a FELIX card and distributes this timing information to the ROD and to the modules in its host shelf through the ATCA back-plane. The ROD aggregates the fragments of readout data from the modules in its host shelf, and sends this data to FELIX upon receipt of an L1A.

4.3.7   FELIX and SWROD

The FELIX was designed as a multipurpose router of sorts, designed to interface with many different frontend technologies in ATLAS and transceive their Input/Output (I/O) across the threshold of custom electronics to commercial PC systems [47].

The FELIX receives data from the front-end modules and passes this data over a Peripheral Component Interconnect Express (PCIe) bus in a commercial host PC. Then this data is sent over the network via netio application to a Software Readout Driver (SWROD) client, which aggregates the data for transmission to the HLT [50].

4.4 The L1Calo Surface Test Facility

The L1Calo Surface Test Facility (STF) is a test stand heavily used to aid in developing firmware and software for the Phase-1 upgrade. This test stand exists on top of the CERN test bed and uses both net-booted and local-boot machines. There are three ATCA racks, housing four ATCA shelves. At least one of each Phase-1 upgrade module finds its home here, as well as three FELIX cards each housed in a commercial host PC, and a dedicated SWROD PC. A version of the L1Calo online software is configured to run here to facilitate testing of software and firmware updates before installing them in the production system.

Chapter 5

The Global Feature Extractor

5.1   gFEX Design
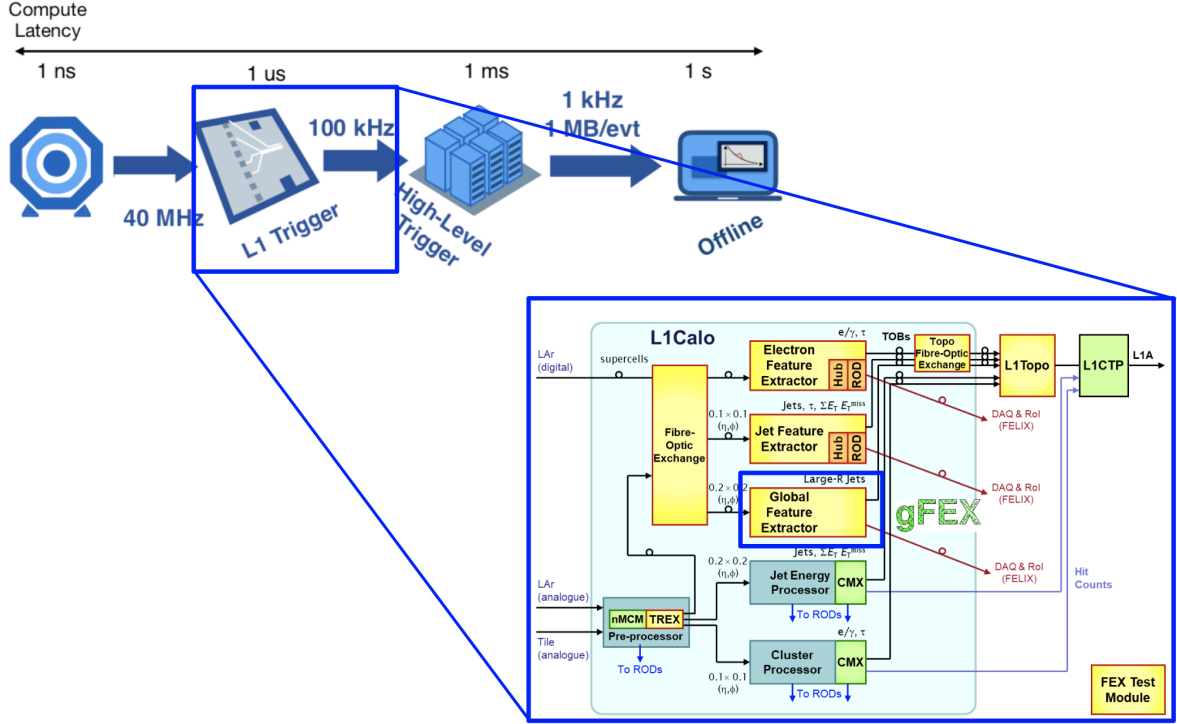
Figure 5.1: gFEX in the context of the ATLAS trigger

Extending the architecture of L1Calo of Runs 1 and 2, the gFEX aims to increase the Level 1 trigger sensitivity to interesting physics channels while coping with the higher pileup environment of Run 3 and beyond.

The full gFEX system is made up of a single ATCA board which processes the full $\eta - \phi$ range of the entire calorimeter. Considering the full expanse of the calorimeter on one gFEX board allows for novel calculation of global quantities such as missing transverse energy and total energy. The $E_\mathrm{T}^\mathrm{miss}$ trigger can be used to search for events producing

neutrinos as well as more exotic events where new physics could produce stable particles which escape detection, such as those predicted in dark matter, SUSY, and BSM Higgs models. The gFEX aims to improve upon the Level 1 $E_{\mathrm{T}}^{\mathrm{miss}}$ trigger from the previous runs, which is essential to make this trigger robust against higher pileup [33]. The design of the $E_{\mathrm{T}}^{\mathrm{miss}}$ algorithm is inspired by the work in [3].

The gFEX is also designed to trigger on large and small radius jets, offer insight into large radius jet substructure. This allows the gFEX to characterize topologies which result in collimated decay products, such as boosted hadronic final states and energetic boson decays. These large radius jets improve upon the legacy level 1 trigger, which is only able to identify local energy maxima in comparatively smaller regions of interest [33]. The predicted gain in trigger efficiency versus the legacy system as the number of constituent sub-jets increases can be seen in Figure 5.2.
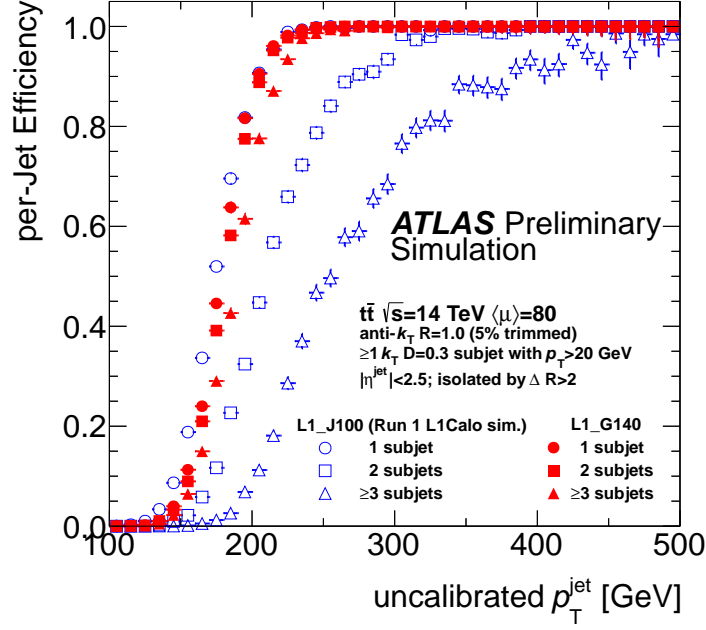
Figure 5.2: Expected gFEX large radius jet trigger efficiency (per-jet) as a function of offline jet p_T and number of constituent sub jets [2].

5.1.1 Hardware

The gFEX board is a 26 layer Printed Circuit Board (PCB) housing 3 Xilinx™ Virtex™ Ultrascale+™ (vu9p) processor FPGAs (pFPGAs) and 1 Xilinx Zynq™ Ultrascale+ (zu19) hybrid System on Chip (SoC) and FPGA programmable logic. Avago™ miniPODs™ provide optical to electrical signal conversion for low latency I/O. On-board the FPGA chips, Multi-Gigabit Transceivers (MGTs) take the electrical input from the miniPODs and perform the high speed serial to parallel data conversion. TOBs are also transmitted to L1Topo via the output channels of the MGTs and miniPODs. There are also miniPODs dedicated to both sending and receiving data from the FELIX. The gFEX-side receives Gigabit Transceiver protocol (GBT) formatted data from the FELIX while transmitting, so-called "Full-Mode" data. The gFEX receives data from the calorimeters

and transmits trigger objects to L1Topo at 11.2 Gbps [33]. The interface to the FELIX (both transmitters and receivers) operates at 9.6 Gbps. The Full-Mode protocol refers to the gFEX-to-FELIX transmission of 8b10b encoded data at the full user bandwidth of 9.6 Gbps. This is in contrast to GBT encoded data, which reduces the useable bandwidth to a maximum user payload of 7.68 Gbps. This reduction comes from the usage of GBT data frame bits used to fulfill the requirement that the GBT protocol be radiation hard [47]. This radiation hardness is less important for the gFEX, as it operates in a low radiation environment. Nevertheless, the gFEX receivers conform to this standard GBT protocol as implemented by the FELIX.

The 8b/10b encoding scheme maps 8-bit data characters onto 10-bit characters. This encoding serves to balance the number of sequential 1s or 0s in a data transmission, aiding in clock recovery and synchronization between transmitter and receiver by ensuring that regular transitions occur in a given data line. By nature of this encoding scheme, there are more 10-bit characters than 8-bit characters. These extra 10-bit values are used as control characters, also known as K-characters. One of these K-characters, known as K28.5, is used by the gFEX input from the calorimeters to denote the start/end of a data frame and is therefore used in the timing synchronization of these links, which will be discussed later.

In addition to I/O with external devices, the gFEX has several dedicated lines which transmit high-speed data for inter-FPGA communication, allowing the large-radius jet algorithm to consider jets which represent regions that can cross pFPGA boundaries. These lines operate at a high data rate, transmitting partial sum information within each bunch crossing to neighboring devices. Also, the pFPGAs maintain connections with the Zynq in order to facilitate the readout upon receipt of an L1A, the realtime calculations

of global quantities such as E_T^{miss}, and also the control and monitoring of the pFPGAs themselves.

The full set of these main I/O connections, both internal and external, is summarized in Figure 5.3.
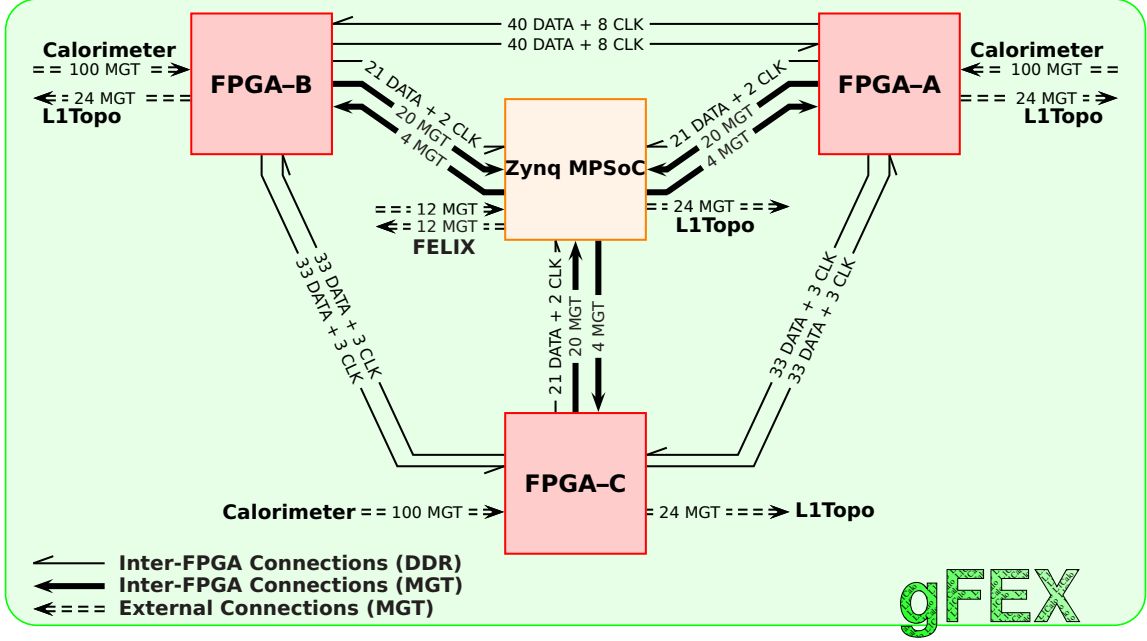
Figure 5.3: gFEX FPGA connections [33]

The optical connections to gFEX which transmit and receive data are summarized in Table 5.1. There are two 48-channel fiber bundles input to each pFPGA from the calorimeters, as well as 4 spare fiber channels. Transmission to L1Topo on the real-time path occurs through 24 fiber channels per pFPGA, grouped into 48-channel output connections. One 24-channel connector handles both the transmitter and receiver fibers connected with the FELIX. Internally, these multi-fiber bundles are broken out into 12 channels by custom fiber assemblies, which route these sets of 12 fibers into dedicated miniPODs.

Connector Number	Connector Name	Type	Fiber Channels
1	MTP48-RX-A-L		48
2	MTP48-RX-B-L		48
3	MTP48-RX-A-R		48
4	MTP48-RX-B-R	receive	48
5	MTP48-RX-C-R		48
6	MTP48-RX-C-L		48
7	MTP12-RX-S		12
8	MTP24-TXRX-Z	receive and transmit	12 RX + 12 TX
9	MTP48-TX-AB	transmit	48
10	MTP48-TX-ZC		48

Table 5.1: gFEX optical connectors

Additionally, the gFEX hardware includes one Universal Asynchronous Receiver/-Transmitter (UART) port, one JTAG port, and two Ethernet ports. The UART port is used mainly to communicate with the Zynq processor system for debugging purposes. The JTAG connection is used for loading firmware onto the FPGA devices, and also to utilize debugging tools such as internal logic analyzers. Finally, there is a Micro SD™ slot which is used to store the disk mounted to run the Zynq operating system.

Brookhaven National Laboratory (BNL) fabricated the prototype and production gFEX boards. The production run consisted of three complete gFEX boards (model names: V4B, V4C, and V4D), and one board using production PCB but hosting only the Zynq FPGA (model name V4A). One complete module is meant for installation in AT-LAS, leaving two complete spares. One spare module is housed at CERN in the STF. The other spare module resides at BNL and is used in testing phase 2 upgrade technol-

ogy. The spare modules can be physically hot-swapped with no need for modification to the firmware or software. This procedure has been successfully exercised several times in the course of commissioning, with a time cost of this kind of physical intervention and subsequent revalidation of the system of about 1 hour.

Figure 5.4 shows two of the gFEX boards, one outside the shelf near the STF, and the other installed in the shelf and operating in the experimental cavern.

(a)   (b)
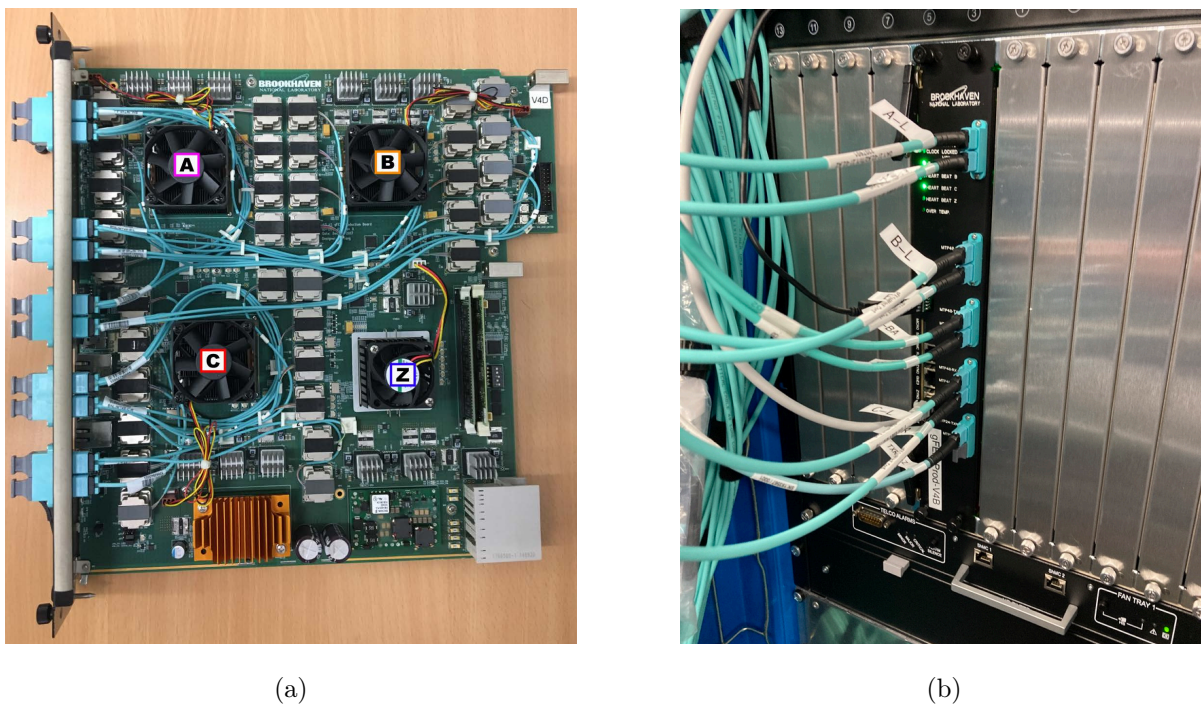
Figure 5.4: The gFEX board outside the shelf near the STF, with FPGA labels super-imposed (a) and the gFEX installed in the shelf near the ATLAS detector (b).

5.1.2 Zynq Processor Operating System

The Zynq processor system is a 64-bit, quad-core, ARM™ Cortex™ CPU on-board the Zynq chip. It runs a custom Linux Operating System (OS), originating from the Open-Embed and Yocto projects, configured for gFEX. The OS can be accessed by standard

network connection, utilizing the gFEX Ethernet port. This OS can interface with the on-board FPGA programmable logic. A firmware design supporting memory mapped registers can then be controlled via direct manipulation of these registers. A custom driver for this memory access runs during normal operation and performs run control and monitoring operations. The pFPGA memory space is accessible via manipulation of status, data, and control registers on the Zynq. The memory access driver uses a "bit-banging" routine to read and write pFPGA memory space, sending and receiving data over a dedicated Advanced Extensible Interface (AXI) bus.

The low-level memory access driver is used by an instance of an event-listener-style server program, called Ironman (based on the `Twisted` python package), which receives commands by communicating with a remote client over standard network connection and TCP or UDP.

In addition, the Zynq must interface with the ATLAS Detector Control System (DCS) which is an industrial control and monitoring system used for all ATLAS sub-detectors. To communicate with DCS, the Zynq OS runs an OPC-UA server. This server polls low-level sensors at regular intervals of about 30 seconds by reading registers on via the gFEX i2c bus. Temperatures, voltages, currents, CPU and disk usage are all published by this server and logged by the client, giving a time history of each point of interest. The DCS client also has access to the ATCA shelf and can control the power state of the gFEX and monitor shelf-related metrics. The majority of the operating system, DCS, and related software is written and maintained by the University of Chicago group.

The realtime processing of the physics quantities of interest is handled by firmware – that is, custom machine code embedded in the FPGA devices to perform high speed computations. The firmware for the gFEX also handles interfacing with external systems

and remote software, and buffering of data, and other on-board low-level tasks.

5.1.3 Firmware

Figure 5.5: The gFEX top level firmware and its interfaces. The fiber counts displayed in red reflect the channel numbers used in the STF
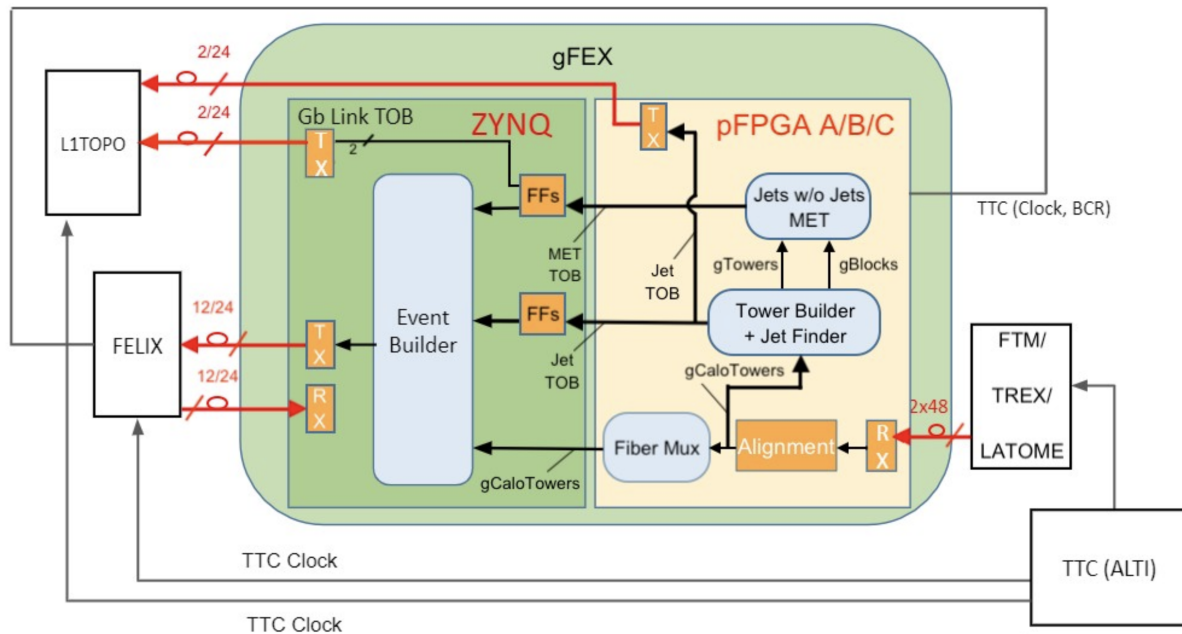
Because of the fast response time required by the ATLAS trigger, the gFEX firmware must do the heavy processing for the system. Thus, the firmware must also allow for sensible control and monitoring. Though there are many requirements and constraints on the gFEX firmware, from the user point of view, there is a logical segmentation of interface and calculation functionality as follows:

1. Interfaces with:

   (a) The host ATCA shelf

   (b) DCS

(c) ATLAS calorimeters

(d) L1Topo

(e) FELIX and SWROD

(f) Trigger menu and run control software

2. Calculation of physics quantities used to generate the triggers for ATLAS:

(a) Small and large radius jet-finding

(b) Calculation of the average event energy per unit area, ρ

(c) $E_{\mathrm{T}}^{\mathrm{miss}}$-finding and calculation of the total E_{T} sum in each event ($\sum E_{\mathrm{T}}$)

The interface with the host ATCA shelf is implemented in dedicated Intelligent Platform Management Controller (IPMC) firmware [42], and the DCS interface has already been summarized in subsection 5.1.2. The remaining user-facing controls and diagnostics are described below. An exhaustive description of the gFEX firmware does not follow here, instead an explanation of the behavior of the user-side interfaces which control and monitor gFEX during nominal physics operation. Figure 5.6 shows a high-level overview of the gFEX firmware.
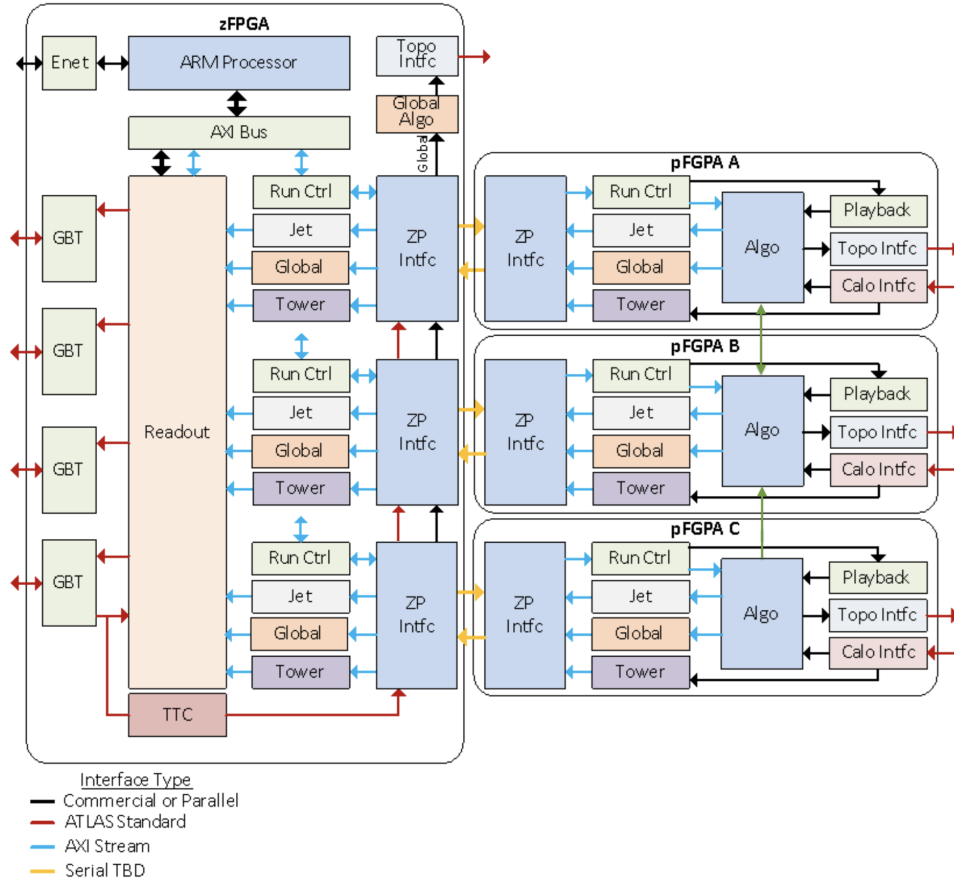
Figure 5.6: An overview of the gFEX firmware (the inter-FPGA communication lines from pFPGA-C to pFPGA-A are not shown).

Clock Recovery and Interface with CTP via FELIX

We will meet the gFEX-FELIX interface again when discussing the readout path. First, the gFEX receiver-side uses the FELIX GBT data header to derive a clock in phase with the CTP. This clock is passed through an `si5345` chip for jitter cleaning. The output of the `si5345` is then used to derive the various clock frequencies needed for gFEX. A graphical representation of this clock tree is shown in Figure 5.7. In addition to providing the master clock, the FELIX also forwards the Bunch Counter Reset (BCR), L1A, and Event Counter Reset (ECR) to the gFEX. The BCR indicates that a module should reset

its bunch counter from 3563 to 0. The bunch counter on board the module is responsible for associating the data from a given collision to the Bunch Crossing Identifier (BCID) given by the CTP. The ECR is a signal that indicates that the local counter keeping track of the number of L1A issued should be changed in the following way: increment the upper 8-bits by 1 and reset the lower 24-bits to 0.
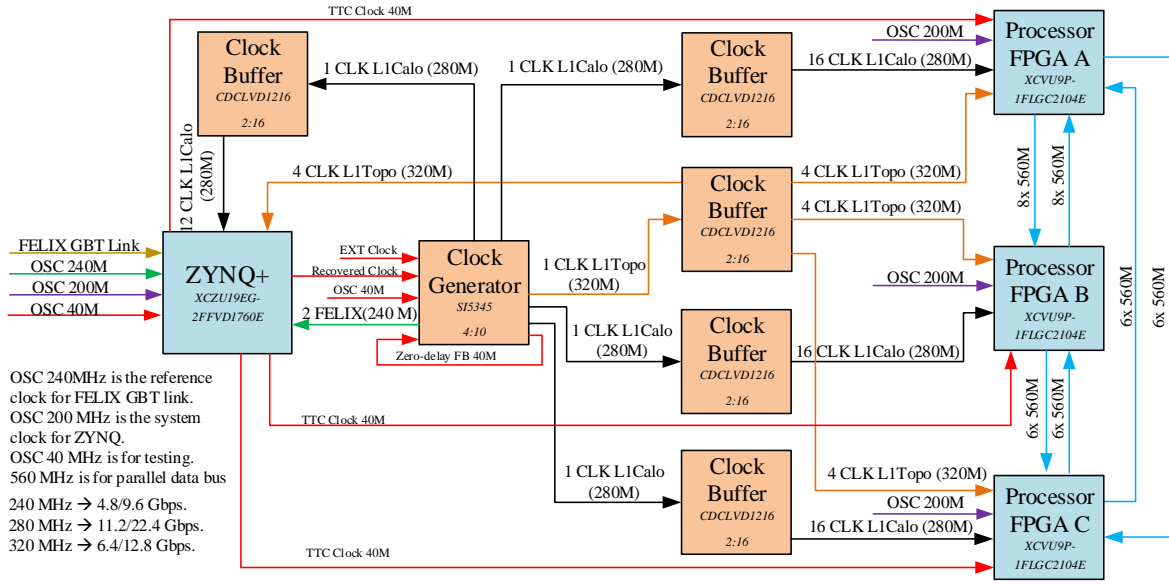
Figure 5.7: The gFEX firmware clock tree, showing the derivation and distribution of the different clock frequencies used throughout the gFEX firmware [33].

Input Fiber Status and Control

In order for the gFEX to properly parse the calorimeter input data for physics use, each incoming data link must be checked for proper behavior and timing. Any unused input channels must be masked such that they do not inject chaotic data into the algorithms. And the input data streams must be properly aligned in time with respect to one another. This last condition ensures that data from the same bunch crossing is being processed at

67

the same time by the physics algorithms on board the gFEX.

The firmware defines registers meant storing status information and writing commands. These are memory locations which a user can read and/or write to in order to monitor and control the operation of gFEX. Each pFPGA's firmware has the following input link status and control registers exposed to the user:

Register Name	Number	Type	Bit-Width (per input fiber)
MGT_ALGN	4		1
CLK_ALGN	25		8
BCID_ALGN	25	read-only	8
MGT_CRCERR	25		8
MGT_LNKERR	25		8
MGT_MASK	4		1
CLK_DLY	25		8
BCID_DLY	25		8
FIB_DSBL	1	read-write	–
ERR_CTR_CLR	4		1
BCID_INIT	1		–

Table 5.2: The gFEX pFPGA input fiber status and control registers.

During operation of the gFEX, it is vital to understand if the system is working as intended. These status and control registers store information about the calorimeter input links and allow a user to judge if they are working properly and control aspects of each link, such as enabling or disabling them or adjusting their relative timing phase. Each block of registers and their intended purpose is explained below.

A status bit for each link denoting whether the K28.5 control character is being received

at regular intervals in the data stream is stored in the `MGT_ALGN` register block. The `MGT_MASK` register allows the user to mask the data coming from any channel, replacing the data payload by zero values, except for bits corresponding to the `BCID_LOW` field. For the masked links, a value can be written to the `BCID_INIT` register in order to change the initial value of `BCID_LOW` in the masked data frames to give a similar value to the `BCID_LOW` in the incoming calorimeter data frames. This setting of the `BCID_LOW` in the masked data frames allows the input alignment and downstream procedures to treat all inputs equally, regardless of input mask configuration, which could change from run to run due to user choice (during testing and commissioning) or, in exceptional cases, front-end module problems.

The `CLK_ALGN` and `BCID_ALGN` blocks are used for measuring the timing phase for each input fiber. The phase can be adjusted, delaying the data in time by writing to the `CLK_DLY` or `BCID_DLY` registers. The total delay (in 280 MHz clock ticks) for any given fiber is the sum of the values in its `CLK_DLY` register and its `BCID_DLY` registers. In the current implementation, the maximum valid input delay is 62 (31+31) of these 280 MHz clock ticks (8 bunch crossings and 6 clock ticks). The alignment procedure is described in greater detail in subsection 5.2.2

The `MGT_CRCERR` registers store the count of Cyclic Reduncancy Check (CRC) errors for each link, summed over all bunch crossings since the last clear command has been issued. Similarly, the `MGT_LNKERR` block stores counts 8b10b out-of-table errors for each link. Both sets of error counters are reset to zero by issuing a clear command – toggling the respective bit in the `ERR_CTR_CLR` register block for a given input fiber.

In order to configure the inputs without disturbing the downstream components (for example, a multiplexer that depends on proper parallel alignment of the input data K28.5

69

characters), an enable/disable mechanism exists for controlling the output of the input fiber data to the downstream components. Once the input masking and alignment is done, the user can change the value of the least significant bit in the FIB_DSBL to enable or disable the output of the fiber data into the downstream components. This enable or disable occurs upon the change of state of this bit, and is not determined by the absolute value of the bit itself.

In addition to what is enumerated above, there are several blocks of read-only registers designed to store the information in the align-frames from each fiber. This allows for online mapping checks using the values in these registers while the production system is running. The description of this mechanism follows later in this chapter, with discussion of the intricacies of the input mapping in subsection 5.1.4.

As a practical example of the utility of these registers, a Pythonic psuedo-code snippet is presented which outlines how one might assess if there is a problem with an input link during normal operation. One complication is that the information stored in these registers is non-trivially arranged with respect to the input fiber number. To find the information for a specific fiber in these register blocks, one can use the following relations to pick out the relevant register and bits (note the difference in bit order between registers with width 1 and width 8):

```python
def get1BitFiberStatusFields(fiberNumber):
    valsPerReg   = 25
    regIndex     = math.floor(fiberNumber / valsPerReg)
    bitWithinReg = fiberNumber % valsPerReg
    bit          = valsPerReg - bitWithinReg - 1
    mask         = 0b1
    return regIndex, bit,  mask

def get8BitFiberStatusFields(fiberNumber):
    valsPerReg      = 4
    regIndex        = math.floor(fiberNumber / valsPerReg)
    byteWitinReg    = fiberNumber % valsPerReg
    lowBitWithinReg = byteWitinReg*8
```

```
14      mask            = 0xFF
15      return regIndex, lowBitWithinReg, mask
```

Here, the `fiberNumber` input parameter is the index of the `shrd_gtrx` vector in the firmware source (unique per pFPGA), which is a remapped vector of the 100 input channels required for optimizing the firmware synthesis. The return values for the above functions can then be used to read or write status and control fields for specific inputs. The following example illustrates how to read the basic link health status fields for the `shrd_gtrx(0)` input:

```
1 # read mgt lock bit:
2 lockIdx, lockBit, lockMask = get1BitFiberStatusFields(0)
3 isLocked = bool((read(MGT_ALGN[lockIdx]) >> lockBit) &
    lockMask)
4 # read error counters:
5 errIdx, errBit, errMask = get8BitFiberStatusFields(0)
6 numErrors  = (read(MGT_CRCERR[errIdx]) >> errBit) & errMask)
7 numErrors += (read(MGT_LNKERR[errIdx]) >> errBit) & errMask)
8 # link is healthy if status bit is 1 and error count is 0:
9 isHealthy = isLocked and (numErrors == 0)
```

Tower Builder

The tower builder firmware resides in each pFPGA and operates mostly independent of direct user control. It begins to process the input data once its input has been enabled using the `FIB_DSBL` mechanism described previously. The tower builder decodes the data frames from the calorimeter, picking out the relevant bits which correspond to gCaloTower (the supercell sums sent to gFEX) energies, saturation bits, etc. It does so using lookup tables which are compile-time constants to populate several arrays which hold gCaloTower energies from different parts of the calorimeter. The input data formats for gFEX are defined in Figure A.3. A given gCaloTower energy is stored in exactly one of the following

71

arrays:

- `etower_data` electromagnetic E_{T} outside the extended region ($|\eta| \notin [2.4, 2.5]$)

- `htower_data`: hadronic E_{T} from Tile or HEC, where the HEC E_{T} is not in the overlapping region ($|\eta| \notin [1.5, 1.6]$)

- `otower_data`: hadronic E_{T} from the HEC which overlaps with Tile ($|\eta| \in [1.5, 1.6]$)

- `xetower_data`: electromagnetic E_{T} in the extended EMEC region ($|\eta| \in [2.4, 2.5]$)

- `xhtower_data`: hadronic energy, extended HEC region ($|\eta| \in [2.4, 2.5]$)

Figure 5.8 shows the break-up of the calorimeter $\eta - \phi$ space into regions processed by each pFPGA and highlights the special regions corresponding to `otower` in orange and `xetower` and `xhtower` in blue.

Once these arrays are filled, the gTower energies are calculated by summing the desired transverse EM and hadronic components while considering the relevant saturation bits for each channel. These gTower energies – the main building blocks on which the gFEX algorithms run – are also stored in on-board playback memory for each device and passed along to the jet finder. More information on the enumeration of these gTowers in each pFPGA can be found in Appendix B.
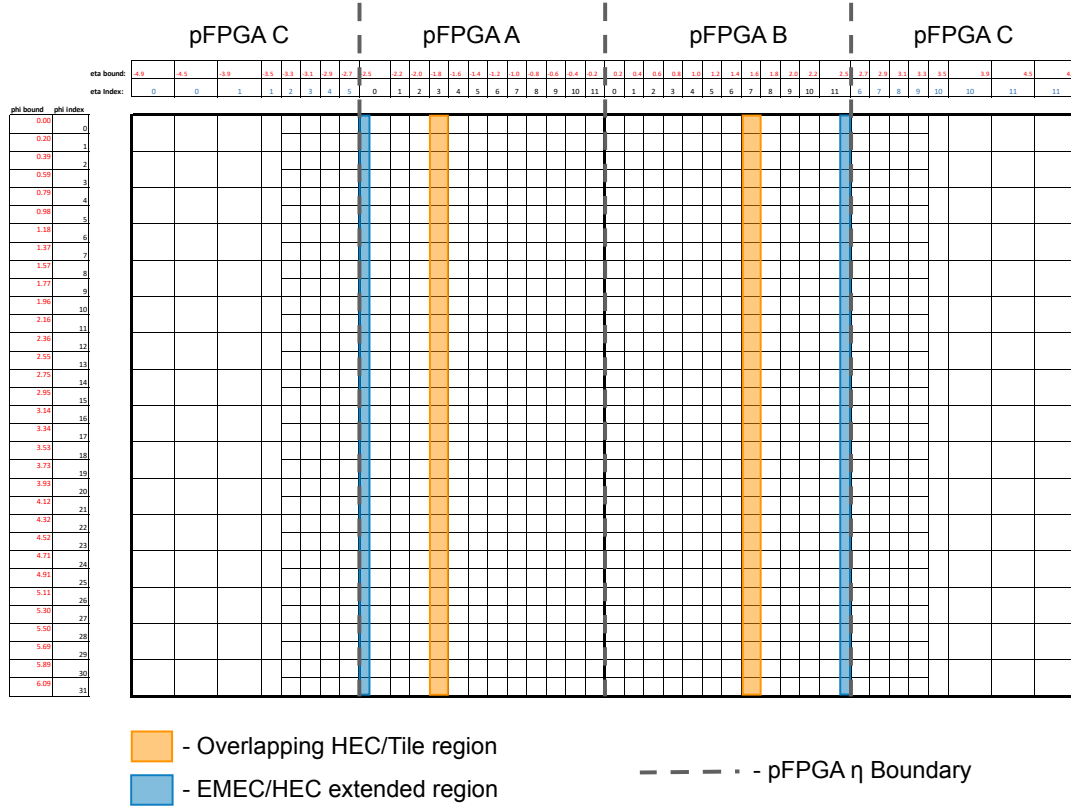
Figure 5.8: gFEX pFPGA η boundaries and special regions

Jet Finder

As previously mentioned, the purpose of the jet finder firmware is to find local maxima in the $\eta - \phi$ distribution of energy in the calorimeter. An additional benefit is the sharing of the calculated sums with the $E_{\mathrm{T}}^{\mathrm{miss}}$ algorithms. The rather complex design of the jet finder firmware is motivated by the need for low latency calculations. Below is the basic outline of the jet finding procedure:

1. The large radius jets are defined by a unique geometric sum of 69 gTowers. The large radius jet energy is calculated for each bunch crossing by summing the energy of the 69 gTowers contained within its boundary. Each pFPGA is logically separated into 64 jet engines, which perform the necessary summing by strategically sharing information with their neighbors. The jet engines cover 6 bins in η and 1 bin in ϕ.

Three examples are shown in Figure 5.9. Here, as seen in the figure, information is shared between neighboring pFPGAs to form the large radius jets.

2. The gBlock - the 3x3 gTower sum - energies are calculated in this process as well. On the pFPGA boundaries, no information is shared between neighboring pFPGAs in this case, and so the gBlocks become 3x2 sums of gTowers in these locations.

3. Two sets of jet TOBs are calculated for each bunch crossing - one set from jet engines 0-31 (η index 0-5) and the other from jet engines 32-63 (η index 6-11). In each set, the highest energy large radius jet with gBlock passing the seed threshold is sent, as well as the two highest energy gBlocks and ρ (the event energy density) within the pFPGA. For each large radius jet, the final energy is the sum of the 69 gTowers with the associated ρ subtracted. For each set in each pFPGA, if there is no gBlock E_T that passes the given seed threshold, then the leading large radius jet E_T is forced to zero for this set in the pFPGA.

4. The jet engines in pFPGA C function only to send information to pFPGAs A and B, and do not contribute to the trigger decision. And while the jet TOBs, large and small radius, are calculated out to $|\eta| < 3.2$, they do not include the FCAL information and do not impact the trigger decision. This architecture choice arises from the exotic geometry of the FCAL, which is more coarse and irregular than the barrel and leads to difficulties in defining consistent gBlock and large-R jet radii across gFEX. In addition, highly energetic particle decays tend to result in more central trajectories, and so the current use-cases for the large-R jet triggers involve primarily pFPGAs A and B.
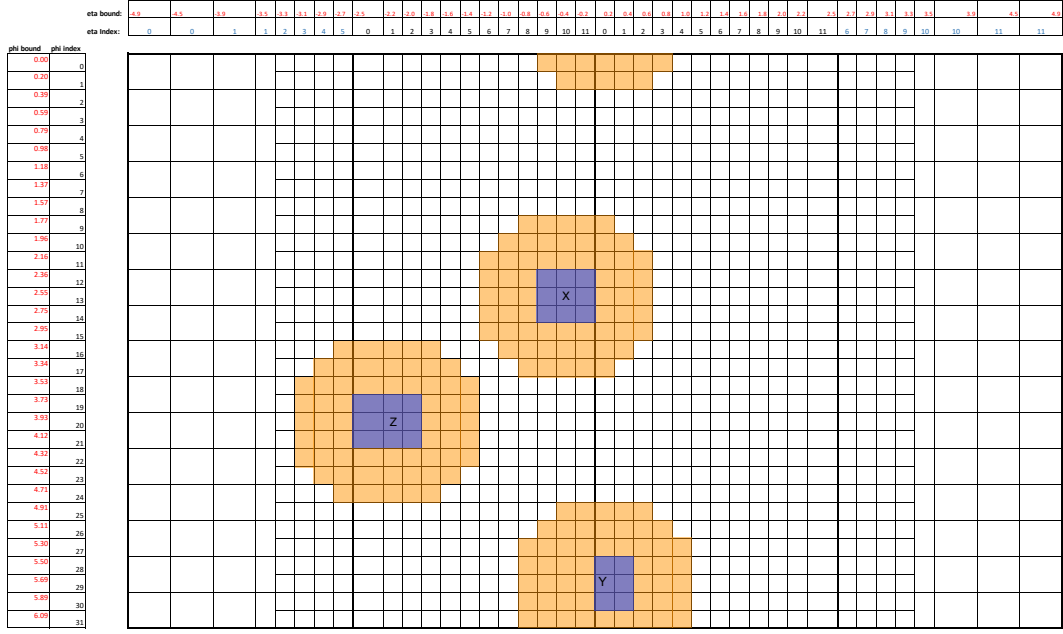
Figure 5.9: A gFEX large radius jet example, where the bold black like represents the geometric pFPGA boundary. X represents the large radius jet and gBlock centered on η bin 10 in engine 45 in pFPGA A. Y represents the large radius jet and gBlock centered on η bin 0 in jet engine 29 in pFPGA B. Z represents a jet centered on η bin 1 in jet engine 20. Large radius jets in pFPGAs A and B receive information from pFPGA C up to $|\eta| < 3.2$, but no jets are seeded in pFPGA C

.

In addition to sharing information between jet engines, the jet finder also sends the gTower and gBlock energies to the $E_{\mathrm{T}}^{\mathrm{miss}}$ algorithms. Since they do not lie on the latency-critical path, these algorithms can wait slightly longer to receive this data in order to profit from reusing the already computed sums.

$E_{\mathrm{T}}^{\mathrm{miss}}$ Finder

The firmware to compute the $E_{\mathrm{T}}^{\mathrm{miss}}$ contains several algorithms. The baseline algorithm for the beginning of Run 3 is the so-called, "Jets without Jets" (JwoJ) algorithm. It is

based on the concepts described in [3]. The procedure by which JwoJ calculates E_T^{miss} is outlined below:

1. For each gTower, consider both the E_T of the gBlock centered on this gTower and the E_T of the gTower itself

2. If the gBlock energy is greater than the specified threshold, add the gTower energy to the hard term `MHT` (both x and y components separated by discrete vector decomposition)

3. If the gBlock energy is less than the specified threshold, add the gTower energy to the soft term `MST` (both x and y components separated by discrete vector decomposition)

4. The E_T^{miss} is the weighted sum of the hard and soft terms, where the weights a and b come from dedicated optimization studies: $E_T^{\text{miss}} = a \cdot \text{MHT} + b \cdot \text{MST}$ (the vector sum of x and y components)

The separation of E_T into hard and soft terms and weighted sum allows us to apply a simple calibration to the E_T^{miss} if needed through the a and b coefficients, which are configurable parameters. This becomes especially useful in the current and future LHC runs as the average number of interactions per bunch crossing increases. The soft term encapsulates the information about the pileup and background noise, while the hard term speaks for the hard scattering processes. Then the two component scaling can be tuned to bring the Level 1 E_T^{miss} closer to the offline E_T^{miss}.

In addition to the baseline algorithm, two more algorithms have been proposed: a noise-cut E_T^{miss} and a $\rho + \text{RMS}$ E_T^{miss}. As of this writing, the noise-cut E_T^{miss} has been implemented, while the $\rho + \text{RMS}$ E_T^{miss} is still in development. The noise-cut E_T^{miss} algorithm reuses modified versions of the JwoJ firmware components to simply perform the vector sum of all gTowers with E_T over a configurable threshold. This threshold is foreseen to be four times the standard deviation of the RMS gTower E_T measured in

minimum bias data. Then, the x and y components of this sum are transmitted as the E_T^{miss} for the event. The ρ + RMS E_T^{miss} functions similarly, placing a three standard deviation threshold on the ρ-subtracted gTower E_T. Provided the resources are available, this third flavor of E_T^{miss} algorithm will be implemented in the future.

One interesting detail about the E_T^{miss} computation (agnostic of choice of algorithm) is that the E_T^{miss} information from each pFPGA must be combined on the Zynq before it is sent to L1Topo on the realtime path. This amounts to an additional vector sum performed on the Zynq and thus requires more checks on data integrity and alignment there.

Zynq Streaming Status and Control

Proper computation of the global E_T^{miss} on the Zynq requires that another timing alignment be performed similar to the one done for the pFPGA inputs, this time aligning the E_T^{miss} information from all the pFPGAs. Since there is buffering and a full event building mechanism in the software portion of the readout chain, the jet information need not be aligned in time across all devices; however, the jet trigger objects from each pFPGA half (jet engines 0-31 and jet engines 32-63) are sent serially in one readout packet per pFPGA. And so the two jet data links from each pFPGA must be pair-wise aligned with one another to receive the correct pairs of jet TOB data frames in each readout packet.

The status and control elements that check the quality of these links and perform their timing alignment are mostly repurposed components from the input status and control firmware. From the user-side, there are a couple of key differences. The first difference is that the E_T^{miss} links are not transmitted via MGT, and as a result, the status bits in

the `MGT_ALGN` are unused for these links. Second, there are 12 pFPGA-to-Zynq links of this type (in contrast to the 100 input links considered for each pFPGA in the previous section), 2 jet and 2 E_T^{miss} links from each pFPGA. Additionally, each pFPGA sends its raw input data to the readout as one large serial data packet per bunch crossing. Since there is only one data packet per bunch crossing, these input data readout links do not require further alignment, and so they are not controlled or considered in this interface.

Event Builder and FELIX Readout

The stream of trigger object data from each bunch crossing, passing through the Zynq streaming status and control interface, is stored in a circular buffer addressed by the bunch crossing ID. Upon receipt of an L1A, the gFEX must send the relevant trigger objects corresponding to the correct bunch crossing to FELIX. And so the triggered BCID is retrieved from the buffer and sent to FELIX. One consideration is the depth of the buffer – too small a buffer would result in incorrect information being sent along the readout path in the event of buffer overflow; therefore, the gFEX buffers a full LHC orbit of data, which allows ample latency for the L1A signal to reach gFEX before an overflow can occur. Additionally, this allows for many contiguous bunch crossings worth of data to be readout at once if desired. The gFEX can be configured to send between 1 and 255 bunch crossings of jet and global TOB data per L1A, provided there is an acceptable gap between L1A signals, such that overlapping data is not requested.

The gFEX sends data via 12 MGT transmitter channels and receives data via 12 MGT receivers. These channels are referred to as "elinks," a term originally denoting a specific lane in the GBT data frame, but also used to describe a complete Full-Mode channel. The data which gFEX transmits is buffered by the FELIX and then transferred across

a PCIe bus, which is read via Direct Memory Access (DMA) by the FELIX software application running on this commercially available host PC. This data is then transferred to the SWROD over a standard high-speed network connection and netio based server-client software applications. The SWROD aggregates all the fragments of data from the gFEX elinks before packaging this data together and sending it downstream to the HLT. This is the basic mechanism by which the collision data as seen by gFEX crosses the threshold from custom electronics to the world of software running on common PCs.

All 12 of the gFEX receiver channels receive an identical copy of the information from FELIX in the form of GBT data frames containing the relevant TTC information. The 12 gFEX transmitters are grouped by data type. The different data types and various identifiers assigned along the data path are shown in the table below:

zFPGA Name	Data Type	Mnemonic	Link ID	Elink ID	Link Number
ttc_tx_data[1]	Global TOB A	GBLA	0x6B1A	0x1C0	7
ttc_tx_data[2]	Jet TOB C	TOBC	0x20BC	0x180	6
ttc_tx_data[3]	Jet TOB B	TOBB	0x20BB	0x140	5
ttc_tx_data[4]	Jet TOB A	TOBA	0x20BA	0x100	4
daq_tx_data[1]	Input Data B	TWRB	0xFEDB	0x280	10
daq_tx_data[2]	Input Data A	TWRA	0xFEDA	0x2C0	11
daq_tx_data[3]	Global TOB C	GBLC	0x6B1C	0x240	9
daq_tx_data[4]	Global TOB B	GBLB	0x6B1B	0x200	8
daq_tx_data[5]	Spare	SPR3	N/A	0x000[*]	0[*]
daq_tx_data[6]	Spare	SPR2	N/A	0x040[*]	1[*]
daq_tx_data[7]	Input Data C	TWRC	0xFEDC	0x080	2
daq_tx_data[8]	Spare	SPR1	N/A	0x0C0[*]	3[*]

Table 5.3: gFEX-to-FELIX elinks in several useful identification schemes. The zFPGA name is related in the firmware source to pins on the Zynq FPGA. The Mnemonic is used in several firmware/software source codes. The link ID is a numeric value included in the gFEX readout header data. The elink ID is used on the FELIX-side as a link identifier, and the link num. is the FELIX Full Mode link number. *Several of the spare link identifiers are reserved, and their correspondence between gFEX and FELIX is only known relative to one another.

The readout of the gFEX input data at the full trigger rate is a unique feature of the gFEX system. The reduced granularity of its calorimeter inputs, relative to eFEX and jFEX, allows the transmission of this raw data at the full designed Run 3 trigger rate requirement of 100 kHz. For reference, one elink corresponding to the input readout from one pFPGA operating at 100 kHz uses a bandwidth of 4.5 Gbps. During testing, this

functionality was verified to operate nominally up to 130 kHz, which corresponds to a bandwidth of about 5.8 Gbps for one elink of this type.

Since the FELIX is designed to be a multipurpose high speed router of sorts, that is, to handle many different use cases inside and outside of ATLAS, the FELIX hardware, firmware, and software require configuration to support the gFEX use case. The `FLX-712` cards can support 24 and 48 channel operating modes, and as such there is some freedom in the on-board fiber routing. In the case of gFEX, one `MTP24` connector is used to carry both sets of 12 channels. These 24 channels are then routed to the miniPODs serviced by one FELIX core design. There is another `MTP24` connector and core device, which is unused in the gFEX case. Next, the Full-Mode firmware flavor provided by the FELIX group is flashed onto the FELIX card. This firmware, specifically the central router, must be configured to specify the data content of its transmitter elinks and enable or disable individual receiver Full-Mode elinks. This elink configuration has the spare elinks coming from gFEX disabled at the FELIX. The remaining 9 gFEX-to-FELIX transmitter links are set to expect Full-Mode data. The 9 active FELIX-to-gFEX links are GBT formatted and set to send the TTC information according to one of several pre-approved formats (`TTC-3` in the nomenclature of [47]). The structure of the general GBT data frame is shown in Table 5.4.

Bits	Field	Description
0-31	FEC	Forward error correction
32-47	E-Group 0	User defined
48-63	E-Group 1	
64-79	E-Group 2	
80-95	E-Group 3	
96-111	E-Group 4	
112-113	IC	Internal Control
114-115	EC	External Control
116-119	Header	GBT header

Table 5.4: The gFEX receiver-side GBT data frame format, as specified in [47]. The "E-group" fields represent the user-configurable data. The right-most bits are the least significant bits. The FEC, IC, and EC bits are unused by the gFEX.

And for the gFEX use case, we have configured the FELIX to have the following signals propagated in each data frame (utilizing only the E-group 0 and zeroing the bits of the unused E-groups):

- L1A: bit 32

- BCR: bit 33

- ECR: bit 34

- Broadcast[2:5]: bits 35-38

- B-Channel: bit 39

The Broadcast[2:5] and B-Channel bits are additional signals that can be sent by the CTP, which are unused in the current gFEX system but may be utilized in the future.

In addition to the TTC bits mentioned above, there is the option to allow the FELIX to control the data flow from the front end via a dedicated XOFF/XON channel in a given GBT link. The XOFF signal is sent by the FELIX to quickly stop the data flow from the front end module when the amount of data stored in the FELIX buffers has reached a defined high-water mark. Once the amount of data in the FELIX buffer has decreased below a defined low-water mark, the FELIX sends an XON signal, telling the frontend to resume the data flow.

As of this writing, this feature is not yet deployed in the gFEX firmware, though there exists a first implementation of the XOFF/XON receiver undergoing testing. In the system design, this feature is a requirement, but it is less critical at the moment since the gFEX FELIX setup includes buffering and watermark settings that result in no data loss during normal running so far in Run 3. On the FELIX-end, specific bits of the GBT frame, bits 32 and 33, are required to transmit the XOFF/XON control characters to gFEX. Thus, the current GBT elink configuration for gFEX has to be modified to move the TTC signals in order to make room for the required XOFF/XON bits. The simplest solution for the definition of the GBT data payload for gFEX in this case then takes the form:

- XOFF/XON: bits 32-33

- L1A: bit 64

- BCR: bit 65

- ECR: bit 66

- Broadcast[2:5] bits 67-70

- B-Channel: bit 71

5.1.4 Input Mapping

A precise understanding of the arrangement of gFEX inputs is key to building and operating the system. Before the construction of the production system, the arrangement of the optical inputs to gFEX was specified in [38]. The LAr and Tile inputs pass through the FOX where specific channels are gathered into the 48-channel fiber bundles meant for gFEX.

In addition to the fiber routing done by the FOX, the gFEX internally contains its own mapping complexities. The MGT connections are defined by pins on the pFPGA chip that are specified in the firmware constraints. The firmware of each pFPGA orders the 100 input data channels in to a vector, termed `AC_Px_MGT_RX`. This 100 element vector is then re-ordered to a configuration that allows for more optimal firmware synthesis. The re-ordered vector is referred to as `shrd_gtrx`. Then a subset of the 100 `shrd_gtrx` channels are selected for use in the physics algorithms: 80 for pFPGAs A and B, and 50 for pFPGA C in the design intended for Run 3.

As mentioned previously, gFEX receives seven 32 bit words per bunch crossing per input fiber. The meaning of these 224 bits is defined by the front end modules. There are two formats of data frames coming from the LATOME modules to gFEX. These formats are described in [30, 49] and displayed in Appendix A. The order of the gCaloTower energies within each data frame is given by configuration files provided by the LAr. These files enumerate which supercells are summed into which gCaloTower. For the data frames arriving from TREX modules, the order of the gCaloTower energies follows the nMCM number and is described in [49]. All of this information is baked into the gFEX firmware at compile time and is encapsulated in the lookup tables of the tower builder.

Though the gFEX receives less granular information than the eFEX and jFEX, a

complete mapping specifies the path of the smallest elements of the digital system through the gFEX. To that end, I have assembled a SQLite database of all supercell and Tile tower elements, as well as the connections and logical names of all data channels input to the gFEX. The purpose of this database is to centralize all the information on the input mapping of the digital system as it relates to gFEX. And then through database query, one can get any desired information about the mapping or programmatically generate the firmware source for the mapping elements of the gFEX tower builder.

When connecting the system for the first time in the late summer of 2021, the one of the natural first step after checking the input miniPOD light levels is attempting to confirm that the input channels are arranged as expected. To do this, a novel method was developed prior to installation. This mapping check involves the gFEX firmware decoding the alignment frames from the LATOME and TREX modules and storing the metadata found inside these data frames. Then the stored values are exposed to the user through register blocks, and so the user can check online the set of module, FEX, and fiber identifiers stored in these registers against the values expected by the gFEX firmware and make a determination of the correctness of the channel routing. This work was completed shortly after installation and all the inputs were confirmed to be in the correct order upstream of gFEX before Run 3 data taking began.

5.2 Online Control and Monitoring Software

The online control and monitoring software is responsible for the configuration of the L1Calo system during ATLAS data taking, as well as providing shift crews and experts with the real time health and coherency of the system. The architecture of this software is rooted in LHC Runs 1 and 2, and it was extended to accommodate the new feature

extractor systems in Run 3. The same software environment configures and monitors the legacy L1Calo systems and the new Phase-1 upgrade systems until the decommissioning of the legacy L1Calo hardware, foreseen in mid Run 3. What follows in this section is a description of the gFEX-specific control and monitoring software in the L1Calo online environment.

5.2.1 Run Configuration

The ATLAS trigger and data acquisition systems are controlled by a finite state machine from the ATLAS control room. The whole of the ATLAS detector is configured and set to record data by TDAQ software under the control of the shift crew in the control room. The shift crew ensures that ATLAS and its subsystems are configured and working properly before the LHC produces stable, colliding beams of protons. The gFEX receives commands from the TDAQ software as mentioned previously via standard UDP/TCP network packets. This procedure operates similarly in the production system and the STF test rig.

5.2.2 Input Alignment

After the application of the desired input mask, the timing skew of the inputs must be addressed. At the data rate of 11.2 Gbps, the gFEX receives seven 32-bit data words per bunch crossing from each link to the calorimeter. The gFEX physics algorithms require that all the seven word input data frames are aligned in time before the data can be further processed. Since the gFEX receives inputs from the entire calorimeter, signals arrive at gFEX after traversing various data paths through different front-end module and over different physical distances. This introduces timing skew among gFEX inputs. In addition, there is a latency uncertainty due to transceiver uncertainty associated with

each transmitter sending data to gFEX. This transceiver latency uncertainty is small but generally non-deterministic. Examples of this skew for several inputs, masked and from LATOME modules, are shown in Figure 5.10 as measured in the STF test rig. During the system configuration at the beginning of each physics run, the gFEX runs a dynamic input alignment algorithm to account for this timing skew. Details of the gFEX input alignment procedure are described below.

(a) pFPGA-A
`shrd_gtrx(0)` fiber
(masked)

(b) pFPGA-A
`shrd_gtrx(91)` fiber
(LATOME)

(c) pFPGA-B
`shrd_gtrx(0)` fiber
(masked)

(d) pFPGA-B
`shrd_gtrx(70)` fiber
(LATOME)
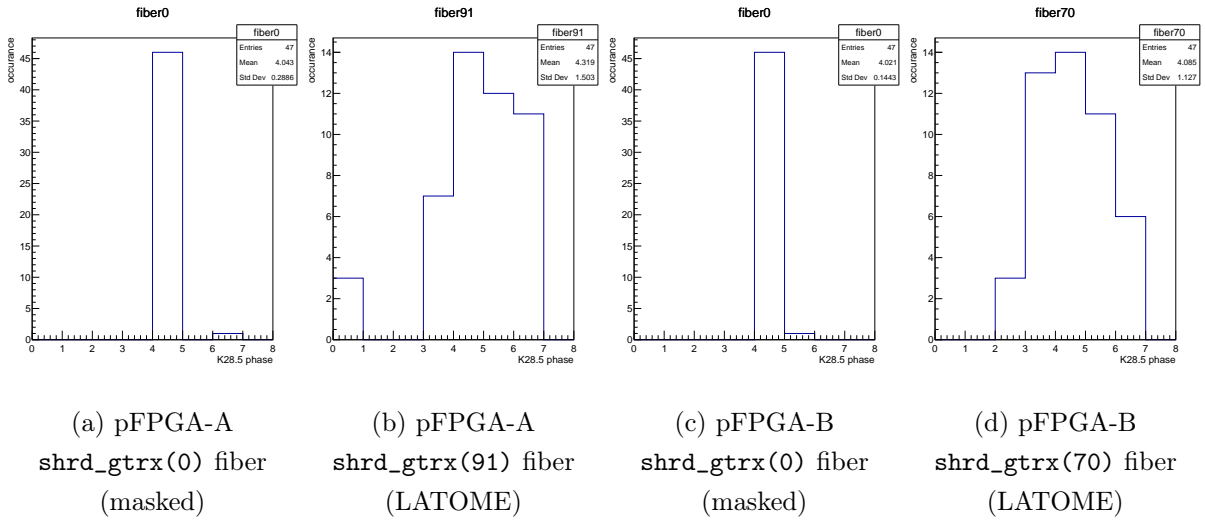
Figure 5.10: Several examples of input fine timing phase measurements over 47 successive resets of LATOME transmitters and then the gFEX receivers, performed in the STF test stand. Two fibers from pFPGAs A and B are shown. The K28.5 phase is shown on the x-axis in units of 280 MHz clock ticks modulo 7. The number of system resets resulting in this phase is shown on the y-axis

In order to provide system flexibility, the input alignment procedure is carried out by software control interfacing with status and control registers which expose input timing information to the user.

1. For each incoming fiber data stream to a pFPGA:

87

- Serial data is received from front end as 7×32-bit words per 40 MHz bunch crossing, one 32-bit word per 280 MHz clock

- A 3-bit counter increments at 280 MHz, synchronized to the FELIX-side BCR distributed to each pFPGA from the Zynq

- Upon receipt of the K28.5 comma character, the value of this counter is stored in a register (in the read-only `CLK_ALGN` block previously described). This value is the fine alignment phase.

- An 8-bit BCID is calculated using a BCR derived from the low 7 bits of the BCID in the data frame (`BCID_LOW`) as they transition `0xDEB` → `0x000` - this is a calorimeter-side BCR. This value is stored in a register (in the read-only `BCID_ALGN` block previously described) and is termed the coarse alignment phase.

2. The 3-bit fine alignment phases are read back and compared across all inputs.

3. We find the maximum value stored by the 3-bit counters observed over all inputs - this is the slowest fiber and used as reference

4. A delay is calculated and applied individually to each fiber such that all fibers have their comma characters aligned with the reference fiber (these delays are written to the read-write `CLK_DLY` block).

5. Finally, the above steps 3-4 are repeated, this time considering the 8-bit coarse phase values and applying delays to earlier-arriving inputs until their BCID phase aligns with the latest arriving input (these delays are written to the read-write `BCID_DLY` block).

In practice, the fine and coarse delays are set in units of 280 MHz clock ticks, and there is no difference in the application of the delays between the two stages. For example, it is possible to delay data by 1 bunch crossing by writing a value of `0x7` to the fine delay register or the coarse delay register for that fiber. In the current design, a maximum value of `0x1f` (31 decimal) can be written to a delay register of either type. As mentioned previously, this sum of delays takes on a maximum value of 8 bunch crossings and 6 clock

ticks. This comfortably accommodates the designed maximum output skew of 3 bunch crossings specified by the LATOMEs and allows headroom for alignment with TREX data. There is no specification for the maximum skew for the TREX data relative to the LATOME data; however, in practice, the data arriving from the Tile calorimeter is observed to be comparably timed to the LAr barrel modules.

This gFEX input alignment procedure is shown schematically for two fibers in the timing diagrams of Figure 5.11.
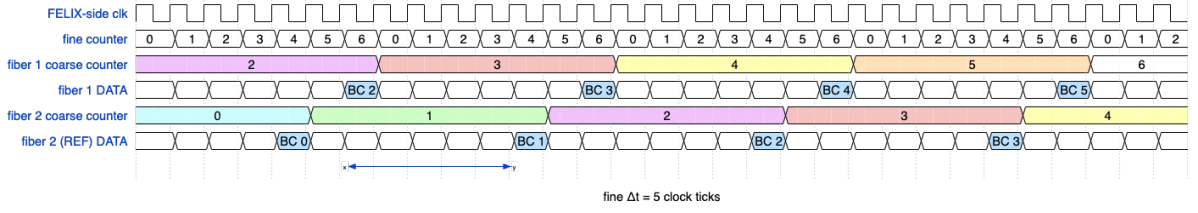
(a) Before fine alignment:

Fiber 2 is the latest arriving data and used as the reference fiber
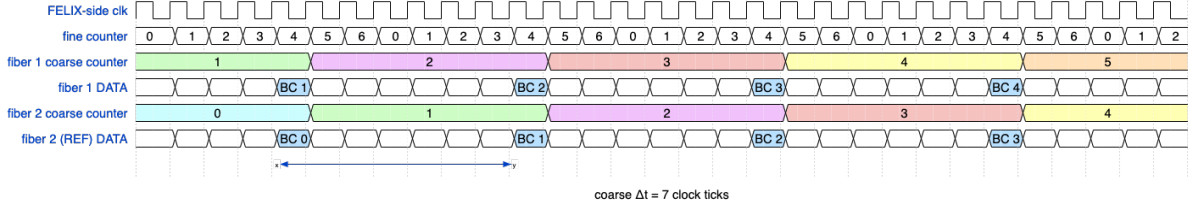
(b) After fine alignment:

A 5 tick delay has been applied to fiber 1 such that the data frame boundaries are aligned between both fibers
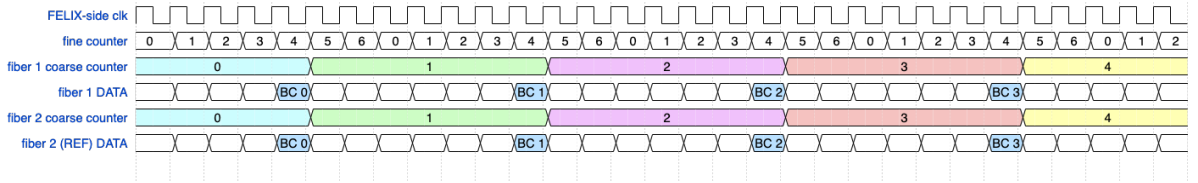
(c) After coarse alignment:

An additional 7 tick delay has been applied to fiber 1 such that the frame boundary and BCIDs match between the two fibers

Figure 5.11: A two-fiber example of the steps involved in performing the gFEX input alignment. The relative phases of two fibers are compared and timing delays applied to the earliest arriving data such that it aligns with the latest arriving data at the end of the procedure.

The software to carry out the delay calculation and application is included in the L1Calo Online software installation, and the input alignment procedure is performed at the beginning of every physics run. In order for the gFEX alignment procedure to result in a deterministic latency (to comply with the ATLAS policy that each subsystem operate

90

at a fixed latency with respect to the LHC BCR distributed by the CTP), one more step is added to the procedure described above. The minimum input delays required to align the gFEX inputs are calculated, and then an offset is added, such that the extra delay applied will absorb any transceiver latency uncertainty from run to run, and the gFEX input phase will remain fixed. These target phase values (one fine and one coarse) are stored in a calibration database and referenced during each call of the alignment procedure. For a sufficiently chosen set of target phases, the dynamic alignment procedure always results in consistent gFEX realtime path latency. For testing purposes, it is also possible to switch the input alignment strategy dynamically by using values for the phase targets. The allowed values and the resulting software behavior is shown in Table 5.5.

Fine Target	Coarse Target	Fine Alignment Strategy	Coarse Alignment Strategy
0x0-0x6	0x0-0xFE	fixed target	fixed target
0xFF	0x0-0xFE	minimum latency	fixed target
0x0-0x6	0xFF	fixed target	minimum latency
0xFF	0xFF	minimum latency	minimum latency
0x7-0xFE	0x0-0xFF	unused	unused

Table 5.5: The range of possible numbers passed as input alignment targets to the gFEX software and the resulting software response. The bottom "unused" row is technically allowed, though it is not advised to be used since it will result in alignment to the fine target modulo 7 and therefore be unnecessarily confusing in practice.

A similar alignment procedure is carried out on-board the Zynq FPGA using the Zynq streaming status and control interface previously described. All the $E_\mathrm{T}^\mathrm{miss}$ links from the pFPGAs (six in total) must be aligned in time, and separately, the pairs of jet links from each pFPGA must be aligned with one another. The same alignment procedure is then

carried out as was done for the calorimeter inputs, though here we need only consider the alignment of the desired sets of links. The relative timing of the sets to one another is not considered, as the data is pulled from the readout buffers based on BCID, and the SWROD will aggregate the event fragments from each of the readout links for each accepted bunch crossing.

5.2.3   Online Monitoring

The existence of dynamic configuration parameters necessitates that these values be monitored over time. There are also many status registers reflecting the operational health of the gFEX at any given time. To track the state of the system over time, the gFEX online software publishes the contents of many of these status and control registers. The registers are polled at a regular interval and the relevant values are then updated in the ATLAS Information Service (IS). These values in IS can be queried by higher level monitoring interfaces, Grafana being one software tool currently used in ATLAS at the time of this writing.

Monitoring these time-series data and having them available via web dashboard interface gives an edge for shift crews and those of us looking to make system improvements. One improvement was the reduction of gFEX latency, achieved by minimizing the total input delays needed. This was done by analyzing the total input delay after reconfiguring the system many times to determine an optimized, conservative alignment target.

5.3   gFEX Validation and Performance

The validation of the gFEX algorithms and the performance of the gFEX system take two main avenues: low-level firmware validation and trigger performance assessment. Logically, the low level firmware is validated before the trigger performance is considered.

What follows here is a summary of the current status of the gFEX jet and $E_{\mathrm{T}}^{\mathrm{miss}}$ algorithm validation and performance.

5.3.1   Jets

The low-level validation of the jet algorithms was undertaken by the University of Oregon group and has been validated for large and small radius jets, comparing firmware output from pFPGAs A and B to the output predicted by software simulation. The outputs from the production system are also by default passed through jet trigger efficiency monitoring software to assess the capability of the gFEX to trigger the desired physics.

As mentioned in chapter 4, the ATLAS jet triggers are event-level triggers. As such, the efficiency of the gFEX jet triggers can be assessed relative to any other event level trigger. The small radius jet trigger efficiency relative to the offline `AntiKtEMPFlowJets` HLT jet trigger, using events triggered at level 1 by a collection of muon trigger items (independent of the jet items), is shown in Figure 5.12.

(a)   (b)
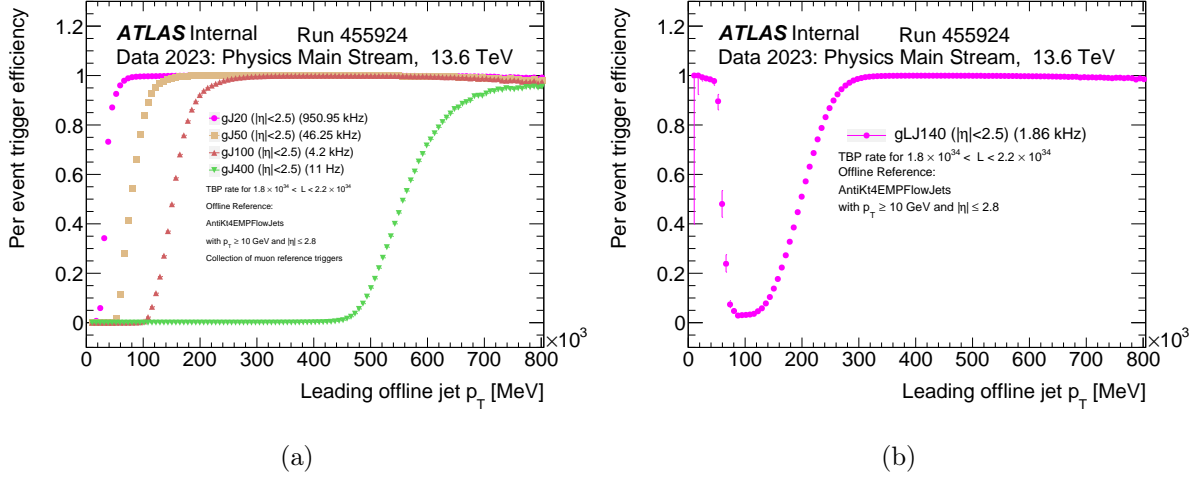
Figure 5.12: gFEX small (a) and primary large (b) radius jet trigger efficiencies for ATLAS run 455924 (July 4th to July 5th, 2023), produced using the utilities in `L1CaloMonitoring` package written by Kristin Dona. The x-axis shows the offline jet p_T calculated by the HLT and the y-axis shows the fraction of events for which the associated level 1 jet trigger was issued. The average trigger rate for each item is also shown. The high efficiency at low large radius jet p_T in (b) is currently under investigation but is hypothesized to come from possible correlation with the muon reference triggers.

5.3.2   Missing Transverse Energy and Total Energy

The low-level functionality of the baseline E_T^{miss} algorithm in each processor FPGA was validated in 2019 using a special test procedure. In order to isolate the E_T^{miss}-specific calculations, several compile-time constants and generics were implemented to disable the Jet Finder firmware block which normally transmits the calibrated gTower and gBlock energies to the JwoJ algorithm. And in its place, a large block RAM is instantiated with a series of test vectors. These test vectors are calibrated gTower and gBlock energies for a sequence of 171 bunch crossings. Once the gFEX is initialized, these inputs are played back to the JwoJ algorithm, and the resulting trigger objects are read out using

the standard readout path. This allows for the hardware output to be directly compared against the expected output.

The initial validation consisted of several tests in which different sequences of input patterns were used. Ultimately, about 10 million bunch crossings of triggered output were recorded to disk and compared against expected values. Perfect agreement is observed in all data recorded. Eighteen bunch crossings of the firmware output versus software prediction are shown in Figure 5.13.
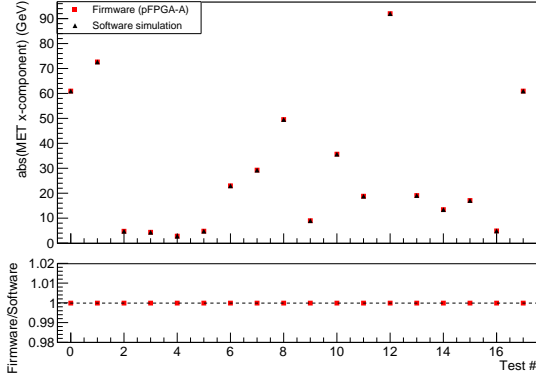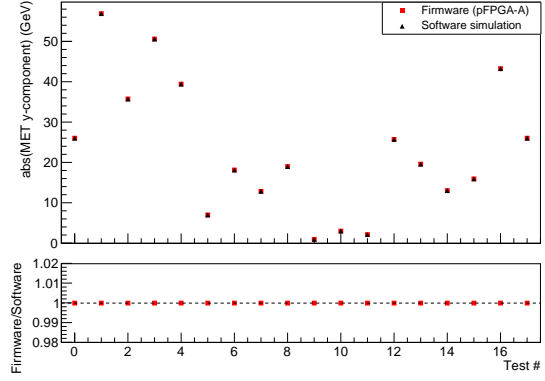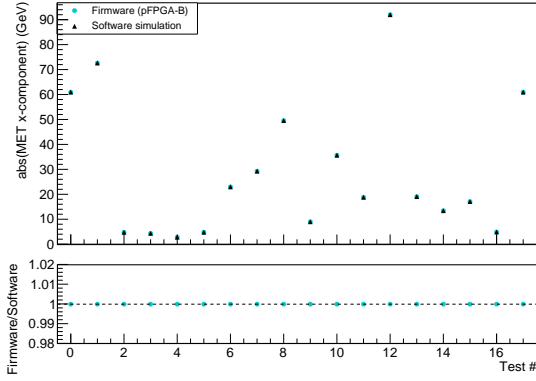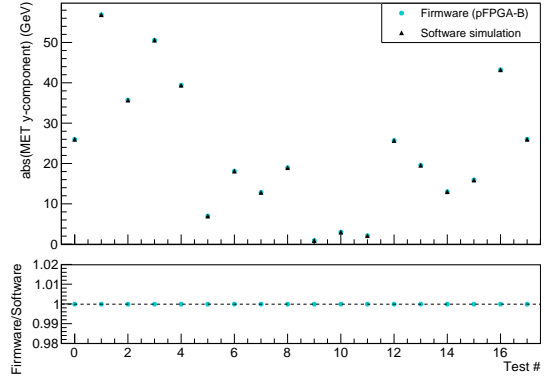
Figure 5.13: Firmware versus software comparison of E_T^{miss} x and y components using gTower and gBlock inputs injected via block RAM playback. Identical input patterns are played back for each pFPGA A and B. pFPGA C firmware was developed later and tested using different inputs due to the difference in gTower granularity.

There are several deficiencies of this method. First, the firmware must be recompiled in order to run this test or change the input test vectors. Second, this test does not include the full data path, though this can be useful when trying to isolate the cause of any disagreement as this test specifically probes the JwoJ arithmetic and follows the resulting trigger objects through the readout. Finally, there are relatively few unique outputs which

can be loaded during one test, and then the user is dependent on the choice of trigger pattern (which is limited in the test rig) in order to observe specific bunch crossings. The more permanent mechanism for testing and validating the algorithm will come in the form of the online software simulation and is currently in development. Nevertheless, this constant input playback test is a useful debugging tool and has also been used in the early stages of validating the alternative noise-cut $E_\mathrm{T}^\mathrm{miss}$ algorithm. Software written by the University of Oregon group currently emulates the $E_\mathrm{T}^\mathrm{miss}$ TOB calculations, and preliminary comparisons with the TOBs from the readout path have taken place, while this software informs the development of the online simulation.

Validation using the full input chain in the production system installed in the ATLAS detector currently yields good agreement between hardware output and the output emulated using the input readout. Such comparisons are shown in Figure 5.14. Given the good agreement observed, the behavior of the gFEX JwoJ $E_\mathrm{T}^\mathrm{miss}$ algorithm is believed to be understood, and pending further optimization based on trigger rate, enabled in ATLAS imminently.
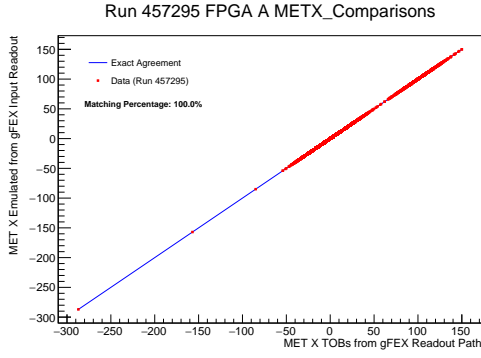
(a) pFPGA-A E_T^{miss} x-component
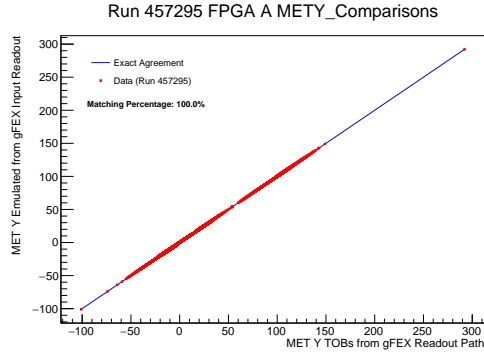
(b) pFPGA-A E_T^{miss} y-component
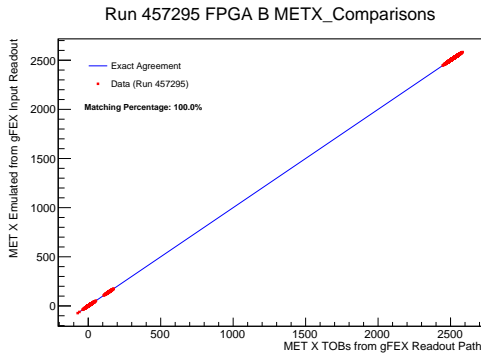
(c) pFPGA-B E_T^{miss} x-component
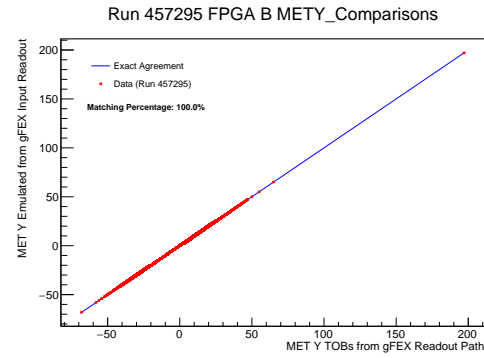
(d) pFPGA-B E_T^{miss} y-component
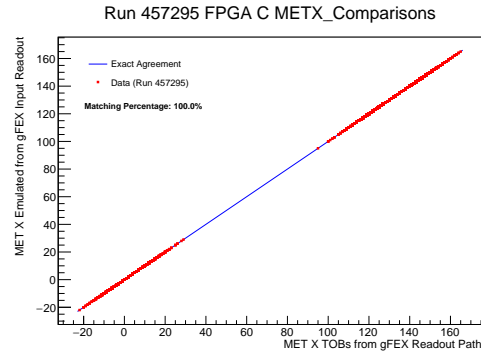
(e) pFPGA-C E_T^{miss} x-component
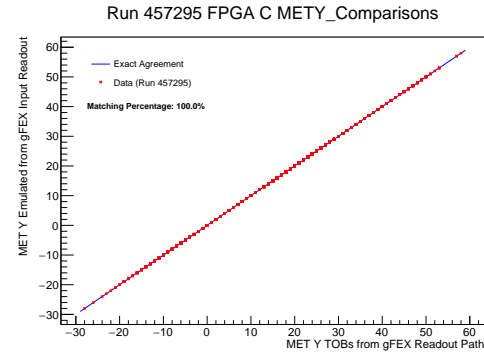
(f) pFPGA-C E_T^{miss} y-component

Figure 5.14: The comparison of firmware TOB output from the readout path versus TOB values emulated using the readout gFEX input data – each of E_T^{miss} x- and y-components within each pFPGA are shown during ATLAS run 457295. Exact agreement is observed in each comparison. These plots were produced using the `gfex_compare` framework, written by Anthony Carroll.

With the gFEX hardware, software, and performance in good shape to increase the level 1 acceptance of interesting jet and $E_\mathrm{T}^\mathrm{miss}$ events, we now turn our focus to a separate line of work using data already recorded during the Run 2 data taking period from 2015-2018. In future measurements of the Run 3 data, we could profit from the gFEX trigger, but to analyze the Run 2 data we will have to rely on the legacy triggers.

Chapter 6

W Boson Production in Association with Jets

6.1 Introduction

As one might imagine, a variety of interesting interactions occur in LHC collisions. The steep running of the QCD coupling relative to electroweak coupling means that at high momentum transfers, the QCD processes diminish while the electroweak processes become more prominent. Despite this relative trend, the QCD processes still dominate at all energies accessible to modern colliders. Currently, the LHC proton-proton collisions at high center of mass energy provide the best available opportunity to measure the properties of electroweak interactions. QCD-induced W boson production in association with jets (QCD-W) is the primary background to any EWK-W measurement at the LHC. As such, to reduce the QCD-W component and the complexity in delineating QCD from electroweak production, only final states where the W boson decays leptonically are considered. Additionally, the electroweak $W \to \tau \nu$ process is not measured directly. The final states considered in this analysis are therefore characterized by the presence of an electron or muon, $E_{\mathrm{T}}^{\mathrm{miss}}$, and two or more jets. Various additional kinematic requirements can be placed on the objects in these events to enhance specific components. Several different kinematic regions are defined for controlling QCD-W background, QCD multijet background, extraction of EWK-W component, and validation.

Previous measurements of electroweak boson production in association with jets have been performed at both ATLAS and CMS. The list below contains these measurements in approximately chronological order for each of the W and Z bosons. The ATLAS

measurements can be seen as well in the introductory plot, Figure 1.1.

- Electroweak Z boson production in association with jets
    - ATLAS at $\sqrt{s} = 8$ TeV [13]
    - CMS at $\sqrt{s} = 8$ TeV [40]
    - ATLAS at $\sqrt{s} = 13$ TeV [15, 27]
    - CMS at $\sqrt{s} = 13$ [44]

- Electroweak W boson production in association with jets
    - CMS at $\sqrt{s} = 7$ [39]
    - CMS at $\sqrt{s} = 8$ [41]
    - ATLAS at $\sqrt{s} =7$ and 8 TeV [16]
    - CMS at $\sqrt{s} = 13$ TeV [45]

This chapter seeks to fill the noticeably missing item of an ATLAS EWK-W measurement at $\sqrt{s} = 13$ TeV. Other electroweak measurements, of vector boson scattering, for example, have recently become feasible as well. These processes are interesting in their own right but beyond the scope of this analysis, and so they are not detailed here.

6.1.1 Electroweak W Boson Production

And example set of EWK-W processes are shown in Figure 6.1. These processes are currently not distinguishable from the other processes with four electroweak vertices and equivalent final states, and so the set of these processes is measured. The VBF processes depicted in the left-most Feynman diagram notably contains the WWZ or $WW\gamma$ vertex, and so measurements of these processes are sensitive to any new physics scenario which could modify the WWZ or $WW\gamma$ couplings. These EWK-W processes also show up

in Higgs analyses as a background, and so independently measuring them is a benefit. Additionally, the EWK-W measurement serves as a testing ground for Monte Carlo (MC) and theoretical tools which attempt to model perturbative QCD in this regime.
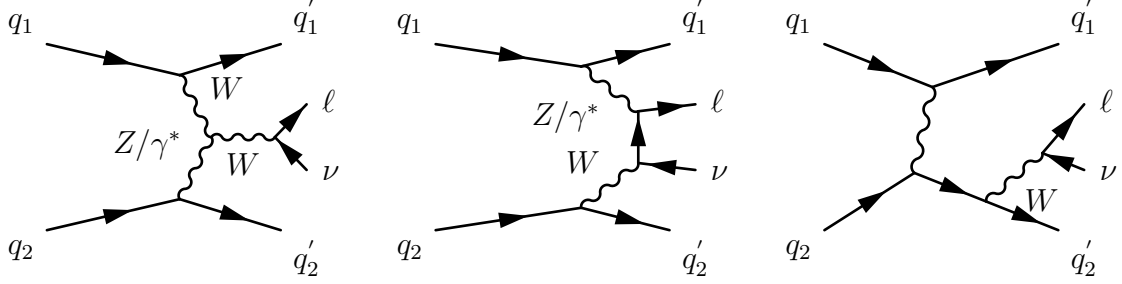
Figure 6.1: Several examples of processes resulting in electroweak W production in association with jets: vector boson fusion (left), multi-peripheral (center), and W bremsstrahlung (right)

Events of this type are characterized by the lack of hadronic activity in the rapidity gap between the two highest p_{T} jets, along with the lepton and $E_{\mathrm{T}}^{\mathrm{miss}}$ inhabiting this rapidity gap [55]. To quantify how close a lepton or jet is to the center of the tag jet rapidity gap, a new observable is defined – centrality. The formula for calculating the centrality of an object is shown in Equation 6.1, where c and y are the centrality and rapidity of the object considered, and y_1 and y_2 are the rapidities of the leading and subleading jets respectively.

$$c = \left| \frac{y - \frac{y_1 + y_2}{2}}{y_1 - y_2} \right| \qquad (6.1)$$
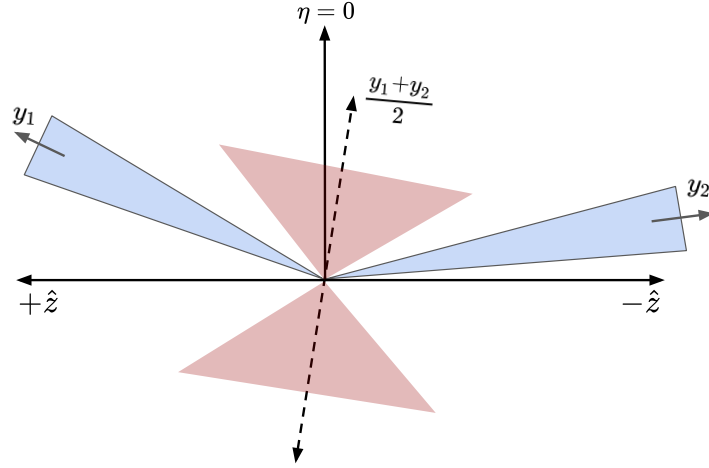
Figure 6.2: A schematic example of the rapidity gap between two jets: the dashed line represents the average rapidity and the light red represents "low" centrality bounds.

The smaller the value of c, the closer an object is to the center of the leading p_T jets' rapidity gap.Figure 6.2 shows an schematic view of the interpretation of centrality. A candidate EWK-W event containing an electron, two high p_T jets, and E_T^{miss}, is shown in several projections of the ATLAS detector in Figure 6.3.
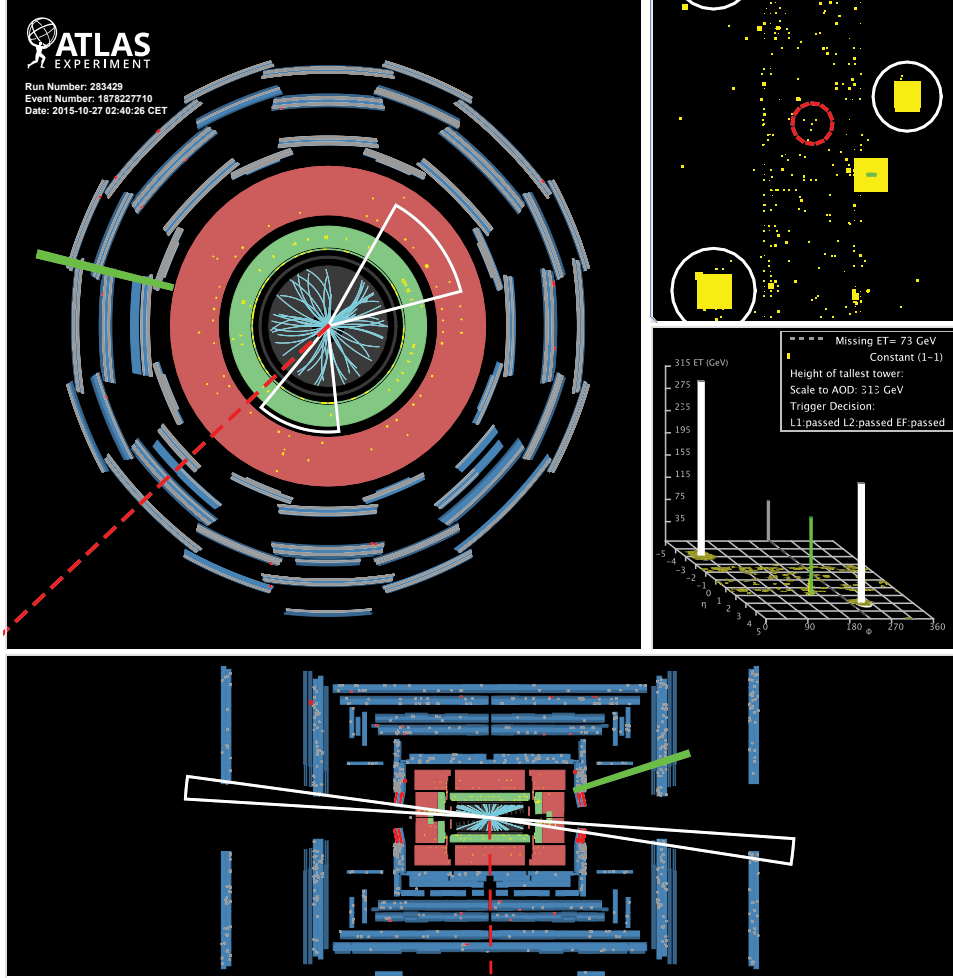
Figure 6.3: A candidate EWK-W event in the ATLAS detector. The top left panel shows the x/y projection. The bottom panel shows the detector $r - z$ projection. The top right shows the calorimeter deposits with η on the horizontal axis and ϕ on the vertical axis. The middle right plot shows this same calorimeter information with energy scale on the z-axis. Jet objects are represented by white cone/circle outlines. An electron object can be seen as a bold green line. And $E_{\mathrm{T}}^{\mathrm{miss}}$ is shown as a dashed line.

6.1.2 QCD Induced W Boson Production Modes

The QCD-W final states appear very similar to the EWK-W final states, especially at the detector level. Several examples of QCD-W processes are shown in Figure 6.4. One

notable difference between the QCD and EWK diagrams is that in the QCD-W case, the final state jets are connected by QCD vertices. This generally leads to much more hadronic activity in the QCD-W events as well as more gluon initiated jets, which tend to have higher particle multiplicity, lower p_{T}, and are less collimated than quark-initiated jets [55, 65]. This also results in more hadronic activity in the rapidity gap between leading p_{T} jets, compared to the EWK-W events.
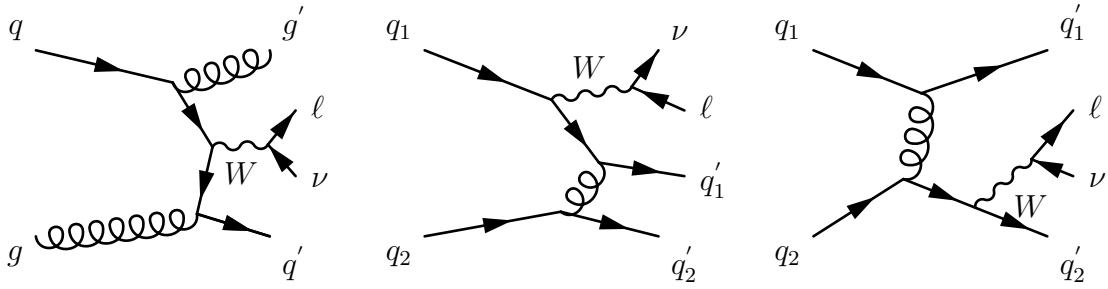
Figure 6.4: Several examples of processes resulting in QCD-W production in association with jets

6.1.3 QCD Multijet Production and Fake Lepton Background

Another background to EWK-W production which merits some discussion is the fake lepton background. Because of the nature of its origin, it historically goes by the name of QCD multijet (or more simply "multijet") background. These are events where jets themselves or energy which should be associated with a jet is reconstructed as a lepton. Two heuristic examples of this are shown in Figure 6.5.
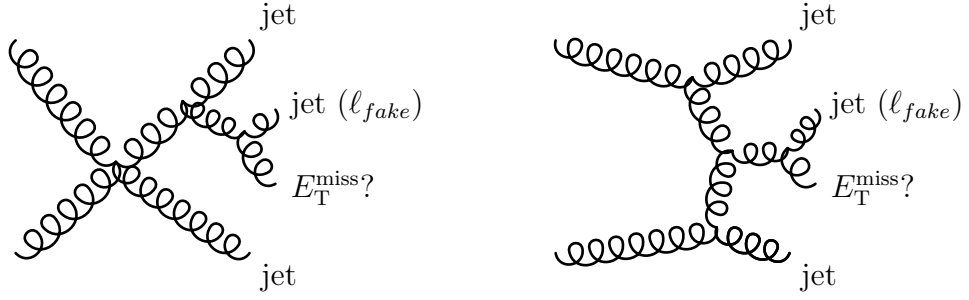
Figure 6.5: Two examples of QCD multijet production which could give rise to fake W candidates

The contribution of these events to the final measurement is about 10% of the QCD-W content; however, this contribution is non-negligible, especially when considering the uncertainties in estimating the contribution of backgrounds of this type. Due to the dependence on detector performance and individual analysis topology, modeling this background in general with Monte-Carlo has so far proved ineffective, and prohibitive numbers of events would need to be generated in order to improve this. And so data-driven methods are employed to estimate this background contribution.

6.1.4   Other Background Processes

Other Standard Model interactions can produce final states which pass the selection cuts for this analysis. One of these backgrounds is the QCD production of a Z boson in association with jets, where detector acceptance and reconstruction results in a final state that ostensibly looks like a single lepton and $E_{\mathrm{T}}^{\mathrm{miss}}$ rather than a lepton-anti-lepton pair from a Z decay. In the same way, diboson production processes are present in the phase space of this analysis. Single-top and $t\bar{t}$ events can result in W boson production as well. Finally, the electroweak production of a Z boson as well as the $W \to \tau\nu$ process are considered as a background.

6.1.5   Analysis Strategy

More details follow in the subsequent sections, but first I will give a high-level outline of the analysis strategy. The analysis presented here seeks to measure the total fiducial cross-section of the EWK-W processes using proton-proton collision data at $\sqrt{s} = 13$ TeV, from the full LHC Run 2 dataset recorded by the ATLAS detector. This dataset contains a total integrated luminosity of 138.9 fb^{-1}.

Collision events are first selected by requiring the assertion of a single-lepton trigger. Next, the raw detector data is processed using ATLAS common reconstruction and calibration procedures to yield physics objects such as electrons, muons, jets, and $E_{\mathrm{T}}^{\mathrm{miss}}$. Kinematic cuts are then applied to these objects in an attempt to carve out a region of phase space where the EWK-W signal is enhanced relative to the backgrounds. Additionally, several orthogonal kinematic regions are used to control the prominent backgrounds.

A data-driven estimate of the multijet background is used, where a template is defined by data-MC in a multijet template construction region. And then an overall normalization is determined by fitting data+MC+multijet in a fit region which contains the bulk of the multijet. The multijet estimate is then frozen as the template shape multiplied by the post-fit normalization.

Finally, the signal and control regions are fitted to extract the EWK-W component, and a total fiducial cross-section in the signal region is computed. One region is not fitted and used as a validation region.

6.2   Detector Object Identification

As mentioned in the previous section, the final states of interest contain a lepton, either electron or muon, $E_{\mathrm{T}}^{\mathrm{miss}}$, and at least two jets. The identification and reconstruction of

each of these objects is described briefly in the subsections below.

6.2.1 Electron and Photon Reconstruction

ATLAS reconstructs electrons and photons within $|\eta| < 2.5$. The following quote taken

from [26] gives a concise introduction to the procedure:

> An electron is defined as an object consisting of a cluster built from energy
> deposits in the calorimeter (super-cluster) and a matched track (or tracks). A
> converted photon is a cluster matched to a conversion vertex (or vertices), and
> an unconverted photon is a cluster matched to neither an electron track nor a
> conversion vertex. About 20% of photons at low $|\eta|$ convert in the ID, and up
> to about 65% convert at $|\eta| \approx 2.3$.

The figure below from [25] shows a schematic view of such $e - \gamma$ radiation passing

through the detector.
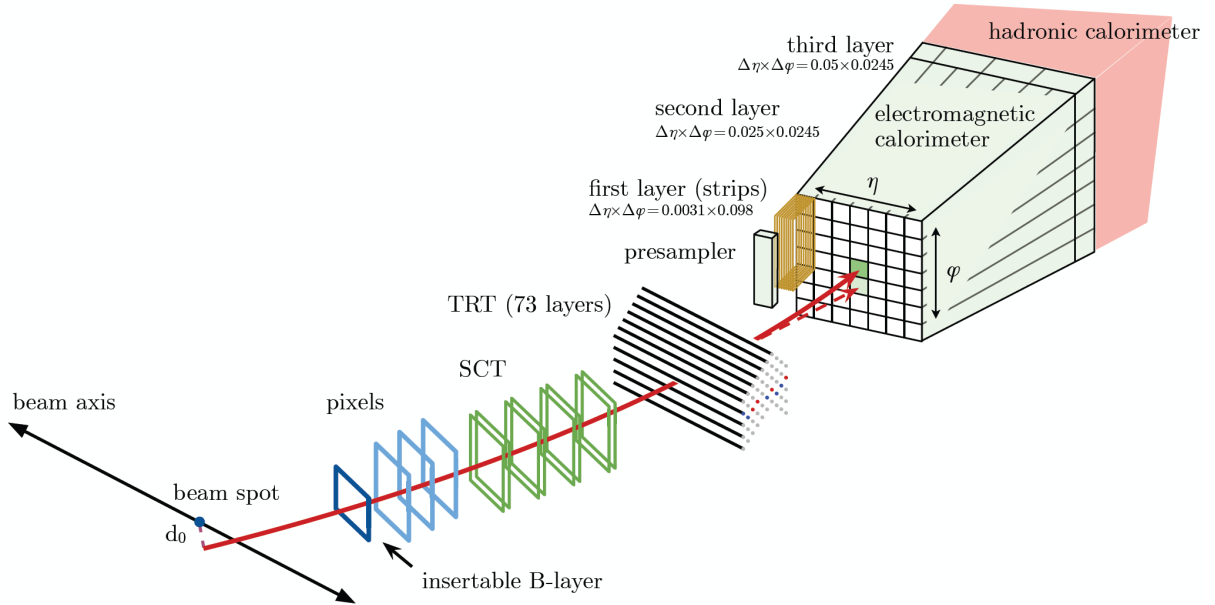
Figure 6.6: Electron and photon schematic trajectory through the ATLAS detector, as depicted in [25]. The solid red curve shows the hypothetical path of an electron, and the dashed red curve shows that of a photon.

The algorithm to construct electron and photon objects considers tracks and sums of cell energies in the calorimeter. It is seeded by level 1 trigger objects to optimize the computational efficiency in the offline reconstruction. The tracks are assembled by considering 'hits' in the ID tracking layers, which are energy depositions from charged particles. These hits are input to an iterative fitting algorithm which groups them to form three-dimensional trajectories and remove any ambiguities, so that a given hit belongs to only one track.

The topo-clusters are sums of energies in the topologically connected cells of the EM and hadronic calorimeters. First proto-clusters are formed by considering cells with energy above a noise threshold, $|\zeta_{\text{cell}}^{\text{EM}}| \geq 4$, where $\zeta_{\text{cell}}^{\text{EM}}$ is defined in Equation 6.2.

$$\zeta_{\text{cell}}^{\text{EM}} = \frac{E_{\text{cell}}^{\text{EM}}}{\sigma_{\text{noise,cell}}^{\text{EM}}} \tag{6.2}$$

Neighboring cells are then added to the proto-cluster if the condition of the adjacent cell is $|\zeta_{\text{cell}}^{\text{EM}}| \geq 2$, and proto-clusters are merged if they contain the same cell with $|\zeta_{\text{cell}}^{\text{EM}}| \geq 2$. Then the boundary of nearest neighbor cells is added to each proto-cluster regardless of energy. Finally, proto-clusters containing two separate cells with $E_{\text{cell}}^{\text{EM}} > 500$ MeV are split into two proto-clusters. Only energy from the EM calorimeter is considered, except in the transition region $1.37 < |\eta| < 1.63$. Here, the energy of the pre-sampler and scintillator between the calorimeter cryostats is referred to as the EM energy, and the fraction of EM energy to the total cluster energy is required to be greater than 50% and the EM energy greater than 400 MeV [26].

The tracks are then matched to the topo-clusters by extrapolating the track from its end-point to the second layer of the calorimeter. If multiple tracks are matched to a topo-cluster, they are ranked, and preference is given to tracks with smaller ΔR to the

topo-cluster. If multiple tracks are matched, and have $\Delta R < 0.01$, then the track with more pixel hits is preferred. The highest ranked track is used to define the reconstructed electron properties. Converted photons are identified by two tracks matched to a topo-cluster containing opposite charge and originating from a common vertex, consistent with a massless particle [26].

The electron and photon reconstruction then proceeds independently by considering super-clusters, which are formed by sorting the initial list of EM topo-clusters by descending E_{T} and iterates over this list, treating each as a seed. An electron seed candidate is required to have $E_{\mathrm{T}} > 1$ GeV and be matched to a track with at least 4 hits in the ID, excluding the TRT. Photon seed candidates are required to have $E_{\mathrm{T}} > 1.5$ GeV, with no requirement on track or vertex matching. Next, satellite clusters are assigned to each seed based on a fixed distance of $\Delta\eta \times \Delta\phi = 0.075 \times 0.125$ around the seed cluster center. For electrons, a cluster is also considered included as a satellite cluster if it falls within $\Delta\eta \times \Delta\phi = 0.125 \times 0.300$ of the seed and its best matched track is also the best matched track for the seed.

Finally, the set of super-clusters for electron and photon candidates is disambiguated according to the criteria in Figure 6.7. Objects which remain ambiguous are left to the individual analysis groups to determine their nature if they are present in a particular measurement.
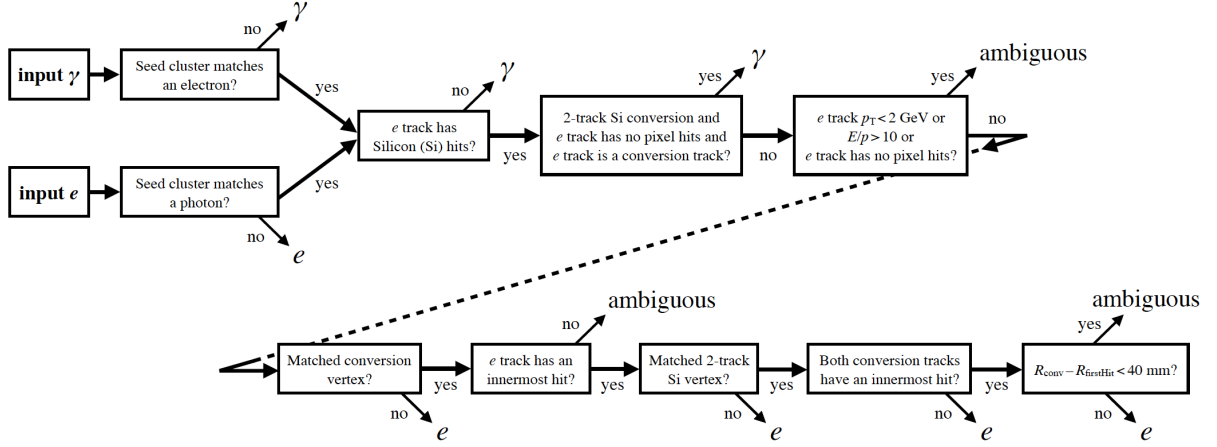
Figure 6.7: Electron and photon disambiguation, as depicted in [26].

The recommendations of the ATLAS EGamma Combined Performance group are applied to the final objects to obtain the nominal calibration as well as systematic variations used to estimate the associated uncertainties, according to the `es2018_R21_v0` model.

In the context of measuring the EWK-W topology, additional requirements are made on the electron objects. For the fiducial measurement regions, the requirements are summarized in section 6.3. Three categories of leptons are defined: signal, and multijet-enriched, and baseline. Table 6.1 defines the qualities of each category. The signal leptons contain the most stringent requirements on the lepton objects, the properties of which are used in the final measurement everywhere except for the multijet/fake lepton estimate. The multijet-enriched leptons are used to form an orthogonal set of events, which allows for a data-driven multijet/fake lepton estimate. The baseline leptons are used to veto events with lepton objects requiring a less stringent set of criteria than the signal leptons.

111

Requirements			
	signal	**multijet-enriched**	**baseline**
Kinematic	$p_\mathrm{T} > 27$ GeV and $|\eta| < 2.47$		
Identification	`Tight`	`Medium`	`LooseBLayer`
Impact parameter	$|d_0^{\mathrm{sig.}}| < 5.0$ $|z_0^{\mathrm{BL}} \sin\theta| < 0.5$ mm	–	$|z_0^{\mathrm{BL}} \sin\theta| < 0.5$
Track isolation **Calorimeter isolation**	$[0, 0.06]$	$[0.08, 0.15]$	–

Table 6.1: Electron object requirements for EWK-W analysis

The track and calorimeter isolation are defined by cuts on variables that are given in Equation 6.3 and Equation 6.4 respectively.

$$\text{Track isolation} := \texttt{ptvarcone30\_TightTTVALooseCone\_pt1000}/p_\mathrm{T}^e \tag{6.3}$$

$$\text{Calorimeter isolation} := \texttt{topoetcone20}/p_\mathrm{T}^e \tag{6.4}$$

The numerator in the track isolation variable corresponds to the sum of track p_T above 1 GeV in a variable size cone radius around the electron, with loose track-to-vertex association. This cone radius goes as $R = 0.3 \times (10 \text{ GeV})/p_\mathrm{T}^e$. The numerator in the calorimeter isolation variable is the sum of topo-cluster E_T in a radius $R = 0.2$ around the electron. In both cases, p_T^e is the p_T of the electron.

6.2.2 Muon Reconstruction

Muons are based on the energy deposited in the detector, consistent with that of a minimum ionizing particle, that is tracking information from the MS and ID primarily. Information in the calorimeter which lies close to the extrapolated track from the ID is

also considered when it is consistent with energy deposition from a minimum ionizing particle [29].

The reconstruction of a track in the MS begins by associating individual straight-line local tracks from hits from individual MS stations. These segments from different stations are combined in to track candidates and required to have their trajectory loosely point back to the interaction point, based on the first order parabolic approximation of muon trajectory bending in the magnetic field. Precision measurements from the bending plane are combined with measurements from the level 1 trigger detectors to build three-dimensional track candidates. Then a global χ^2 fit of the muon trajectory is performed, taking into account possible misalignment and detector effects. Next, using the result of the fit, outlier hits are removed from the track and any hits that were not included in the original track candidate are added. The fit procedure is then repeated using this updated information. The tracks are disambiguated by removing tracks that share a large fraction of hits with higher quality tracks [29]. The fit procedure is performed one last time with a loose IP constraint, and then the resulting trajectory is extrapolated back to the z-axis.

The track from the MS is then matched, if possible, to a track in the ID by a fit considering hits in both systems. If an MS track cannot be sufficiently matched to an ID track, the MS track alone is extrapolated back to the beam line and used in the muon momentum calculation. Energy deposition from the calorimeter is included when the muon ID track extrapolated through the calorimeter passes through cells containing energy deposits consistent with that of a minimum ionizing particle [29].

As in the electron channel, subsequent requirements are made on the muon objects to enhance the population of EWK-W events. These additional requirements are described in Table 6.2.

Requirements			
	signal	**multijet-enriched**	**baseline**
Kinematic	$p_{\mathrm{T}} > 27$ GeV and $|\eta| < 2.5$		
Identification	`Tight`	`Medium`	`Loose`
Impact parameter	$|d_0^{\mathrm{sig.}}| < 3.0$ $|z_0^{\mathrm{BL}} \sin\theta| < 0.5$ mm	–	$|z_0^{\mathrm{BL}} \sin\theta| < 0.5$
Track Isolation	$[0, 0.045]$	$[0.045, 0.35]$	–

Table 6.2: Muon object requirements for EWK-W analysis

The track isolation is defined by a cut on the variable given in Equation 6.5.

$$\text{Track isolation} := (\texttt{ptvarcone30\_TightTTVA\_pt500} + 0.4 \cdot \texttt{neflowisol20})/p_{\mathrm{T}}^{\mu} \quad (6.5)$$

The numerator in the track isolation variable corresponds to the sum of track p_{T} above 0.5 GeV in a variable size cone radius around the muon, with loose track-to-vertex association. This cone radius goes as $R = 0.3 \times (10 \text{ GeV})/p_{\mathrm{T}}^{\mu}$. The `neflowisol20` is a cut on the neural network energy flow in the isolation PFlow algorithm at 0.2, and p_{T}^{μ} is the p_{T} of the muon.

6.2.3 Jet Reconstruction

Jets are formed in ATLAS offline reconstruction by considering the local energy maxima in the radius $R = 0.4$ as identified by the anti-k_t algorithm. The anti-k_t algorithm clusters energy based on an infra-red- and collinear-safe jet convention, where the geometric shape of a jet is not influenced by the low p_{T} emissions in proximity to the hard scattering radiation. It uses a reclustering algorithm that groups energy together based

on the inverse of the squared distance between energy deposits [5]. A strategic combination of calorimeter topo-clusters and charged tracks are used by the particle flow (PFlow) algorithm as input to the anti-k_t algorithm. This improves upon the previous generation of algorithm used in ATLAS, which only used calorimeter topo-clusters. The PFlow algorithm attempts to match well measured tracks to topo-clusters and then the energy of charged particles in the calorimeter is subtracted and replaced by the momentum of the tracks that are matched to those topo-clusters. The jets are retained if, after this subtraction, they have uncalibrated $p_T > 7$ GeV and $|\eta| < 4.5$ [22, 28].

The jet energy scale calibration takes the uncalibrated jet and corrects the four-momentum, jet p_T, energy, and mass to be as close as possible to that of jets reconstructed jet at the particle level. A two-stage pile-up correction is performed, first applying a correction as a function of event pile-up p_T density and jet area and then applying a correction based on pile-up dependence on the average number of interactions per bunch crossing and the number of primary vertices in the event. Next, the four-momentum is adjusted to the particle level energy scale. This is followed by a global sequential calibration to correct for the fact that jets of different particle composition can differ in their transverse energy deposited in the calorimeter. Finally, a residual in-situ calibration is applied only to data, to correct for data/MC differences in the jet response arising from imperfect simulation of both detector materials and physics processes involved [28].

The $R = 0.4$ jets identified by the PFlow anti-k_t algorithm are then subjected to the further requirements in Table 6.3.

Requirements	
Identification	`AntiKt4EMPFlow`
Kinematic	$\lvert\eta\rvert < 4.5$ $p_{\mathrm{T}} > 30$ GeV

Table 6.3: Jet object requirements for EWK-W-W analysis

6.2.4 Overlap Removal

Jets and leptons in proximity to one another are scrutinized to remove objects which may have been improperly reconstructed and duplicated in different lists of reconstructed objects, for example an electron object reconstructed as a jet object or an electron object duplicated in the lists of electrons and the list of jets due to reconstruction ambiguity. The ATLAS standard algorithm to determine which objects to remove is applied [31]. This operates as follows:

- **Electron-jet:**
  - Remove any jet which has $\Delta R(e, j) < 0.2$
  - Remove any electron which has $0.2 < \Delta R(e, j) < 0.4$

- **Muon-jet:**
  - Remove any jet which has $\Delta R(\mu, j) < 0.4$ and less than three associated tracks
  - Remove any muon which has $\Delta R(\mu, j) < 0.4$, where the jet has at least three associated tracks

- **Lepton-lepton:** remove any electron which shares a track with an identified muon

This overlap removal takes place before the objects are passed to the calculation of $E_{\mathrm{T}}^{\mathrm{miss}}$.

6.2.5 Missing Transverse Energy Reconstruction

The reconstruction of E_T^{miss} effectively amounts to summing the transverse energy from the hard-scatter objects and subtracting a soft term, which is the sum of the soft signals consisting of charged particle tracks associated with the primary vertex but not belonging to hard objects. The E_T^{miss} reconstruction follows after the identification and calibration of the objects previously described in the previous subsections, and as a result, changing the object calibration will change the calculation of E_T^{miss}. The overlap removal described previously removes any ambiguity in the objects before the calculation of E_T^{miss} [23, 24]. The calibrated objects are then ordered as: electrons (e), photons (γ), hadronically decaying τ-leptons (τ_{had}), muons (μ), and lastly jets. Then the E_T^{miss} is calculated by considering $p \in \{e, \gamma, \tau_{\text{had}}, \mu, \text{jet}\}$, and then forming the sum as shown in Equation 6.6.

$$\mathbf{E}_T^{\text{miss}} = -\sum_{\substack{\text{selected} \\ \text{electrons}}} \mathbf{p}_T{}^e - \sum_{\substack{\text{accepted} \\ \text{photons}}} \mathbf{p}_T{}^\gamma - \sum_{\substack{\text{accepted} \\ \tau-\text{leptons}}} \mathbf{p}_T{}^{\tau_{\text{had}}} - \sum_{\substack{\text{selected} \\ \text{muons}}} \mathbf{p}_T{}^\mu - \sum_{\substack{\text{selected} \\ \text{jets}}} \mathbf{p}_T{}^{\text{jet}} - \sum_{\substack{\text{unused} \\ \text{tracks}}} \mathbf{p}_T{}^{\text{track}} \tag{6.6}$$

This is explicitly a vector sum with $x - y$ components. From the x and y components of E_T^{miss}, a magnitude and associated ϕ^{miss} can be constructed as shown below.

$$\left| \mathbf{E}_T^{\text{miss}} \right| = \sqrt{\left(E_x^{\text{miss}} \right)^2 + \left(E_y^{\text{miss}} \right)^2} \tag{6.7}$$

$$\phi^{\text{miss}} = \tan^{-1}\left(\frac{E_y^{\text{miss}}}{E_x^{\text{miss}}} \right) \tag{6.8}$$

6.3 Event Selection

Events are selected based on the trigger decision issued by single lepton triggers. Different triggers and configurations cover different time periods during 2015-2018. Table 6.4 shows the set of single lepton triggers considered in this analysis. Several previously unmentioned event properties are considered here. One such quantity is the dijet invariant mass, M_{jj}. This is the invariant mass of the two leading p_{T} jets in an event. Another interesting quantity is the invariant mass of the lepton and $E_{\mathrm{T}}^{\mathrm{miss}}$ system, denoted M_{T}^{W}. This should be equivalent to the mass of the W boson in the event that the lepton and $E_{\mathrm{T}}^{\mathrm{miss}}$ emanate from an on-shell W decay. The JVT and FJVT are denoting jet vertex tagging and forward jet vertex tagging respectively, requiring jets to originate from a location geometrically close to the primary vertex of each event. The b-tagging efficiency refers to the efficiency of the ATLAS detector and software to identify radiation originating from a bottom quark. In general, "jet flavor-tagging" is the term given to attempting to denote certain radiation as arising from a specific flavor of quark.

Lepton Channel	Trigger Name	Period
electron	`HLT_e24_lhmedium_L1EM20VH`	2015
	`HLT_e60_lhmedium`	2015
	`HLT_e120_lhloose`	2015
	`HLT_e26_lhtight_nod0_ivarloose`	2016-2018
	`HLT_e60_lhmedium_nod0`	2016-2018
	`HLT_e140_lhloose_nod0`	2016-2018
muon	`HLT_mu20_iloose_L1MU15`	2015
	`HLT_mu26_ivarmedium`	2016-2018
	`HLT_mu50`	2016-2018

Table 6.4: The set of single lepton triggers used to select events for further analysis.

After passing the level 1 and HLT trigger decisions, events are further filtered according to the series of inclusive requirements as listed in Table 6.5, where the signal region (SR) corresponds to the EWK-W enriched kinematic region and the CR0,1,2 correspond to QCD-W control regions. A Good Run List (GRL) keeps track of data periods which are signed off by data quality inspectors as good for physics analyses, possessing only tolerable defects in data taking. Additional data quality flags exist to delineate individual events which should be discarded.

Requirements		
Data Quality	Fulfills GRL requirements Passes data quality flags ≥ 1 primary vertex and ≥ 2 associated jets	
Lepton Selection	Electrons pass requirements of Table 6.1 Muons pass requirements of Table 6.2 1 signal lepton and no additional baseline lepton Lepton matched to online trigger object	
Jet and $E_{\mathrm{T}}^{\mathrm{miss}}$ Selection	≥ 2 jets fulfilling the requirements of Table 6.3 Jets pass JVT and FJVT $E_{\mathrm{T}}^{\mathrm{miss}} > 30$ GeV $M_{\mathrm{T}}^{W} > 50$ GeV $p_{\mathrm{T}}(j_1) > 80$ GeV $p_{\mathrm{T}}(j_2) > 60$ GeV $M_{jj} > 500$ GeV $|\Delta y(j_1, j_2)| > 2.0$ No event with b-tagged jet	
Signal and Control regions	$N_{\mathrm{leptons}}^{\mathrm{central}}$ where: $c_\ell < 0.4$	$N_{\mathrm{jets}}^{\mathrm{central}}$ where: $c_j < 0.4$
SR	1	0
CR2	0	0
CR1	1	1
CR0	0	1

Table 6.5: Event requirements for EWK-W analysis. The signal and control region requirements are applied after the inclusive requirements listed above.

6.4 Signal and Background Modeling

The object and event selection is applied as previously described. The data events are unweighted, and the MC events are weighted to the data luminosity. Known differences between data and MC related to the efficiency of certain kinematic cuts are corrected by applying scale factors to the MC events. Pileup reweighting of the MC adjusts the event weights based on the number of vertices in the event to correct for different pileup conditions during different data periods and the difference with the generated prediction, which was generated with a fixed pileup configuration before data-taking began. Equation 6.9 shows the expression used to weight each MC sample to the ith data period luminosity.

$$L_{\text{MC}}^i = \left(\frac{\sigma_{\text{generated}} \cdot \text{FilterEfficiency} \cdot \text{kFactor} \cdot w_{\text{MC}} \cdot w_{\text{pileup}}}{N_{\text{generated}}} \right) L_{\text{data}}^i \qquad (6.9)$$

The $\sigma_{\text{generated}}$ is the theoretical cross-section for the generated processes. The FilterEfficiency term adjusts for the efficiency of any event selections applied at the generator level. The kFactor term adjusts the leading order cross-section based on next-to-leading order corrections. The w_{MC} is an event weight given to this event by the generator. The w_{pileup} comes from the previously mentioned pileup reweighting, and $N_{\text{generated}}$ is the number of events generated.

The various weighting parameters are unique to each sample and retrieved using the ATLAS Metadata Interface [18]. The i data periods correspond to 2015, 2016, 2017, and 2018, each with their own pileup profile and L_{data}. The data period luminosities are shown in Table 6.6.

Period	Integrated Luminosity [fb^{-1}]
2015	3.21956
2016	32.9653
2017	44.3074
2018	58.4501

Table 6.6: LHC Run 2 ATLAS integrated data luminosity by data period

The product of object-level scale factors is applied to correct for several quantifiable detector efficiency effects. These scale factors have a mean value of 1 generally speaking. The scale factors applied to each object are:

- Electron
  - Reconstruction efficiency
  - Identification efficiency
  - Isolation working point efficiency (not applied to multijet or baseline electrons)
  - Trigger efficiency

- Muon
  - Identification efficiency
  - Track-to-vertex association
  - Isolation working point efficiency (not applied to multijet or baseline muons)
  - Trigger efficiency

- Jet
  - Jet vertex tagging efficiency
  - Forward jet vertex tagging efficiency

– b-Tagging efficiency

6.4.1   Electroweak W+jets

The EWK-W signal sample containing the VBF-W diagram is modeled by `Powheg` with the `AZNLO` tune and the `NNPDF30NLO` PDF set to generate matrix elements. `Pythia8` with the `CTEQ6L1` PDF set is used for parton showering. These events are NLO in QCD [67].

Two alternative samples are used for comparison with the baseline `Powheg`. One is generated by `Sherpa 2.2.11`. The other is generated by `Herwig7` with matrix elements from `VBFNLO`, which is similar to the `Powheg` configuration.

6.4.2   QCD W+jets

QCD-W events are modeled using the `Powheg` generator with special Born suppression settings to more efficiently populate the phase space considered in this analysis. The standard `Powheg` configuration [6] is modified to include a suppression factor to limit the contribution of events with softer jets in the final state and give preference to events where jets have higher p_{T} and M_{jj} [53]. The suppression factors $F(\Phi_n)$ are given by:

$$F(\Phi_n) = \left(\frac{p_{T_{j_1}}^2}{p_{T_{j_1}}^2 + \Lambda_{p_T}^2} \right) \left(\frac{p_{T_{j_2}}^2}{p_{T_{j_2}}^2 + \Lambda_{p_T}^2} \right) \left(\frac{m_{jj}^2}{m_{jj}^2 + \Lambda_{m_{jj}}^2} \right) \tag{6.10}$$

with $\Lambda_{p_T} = 30$ GeV and $\Lambda_{m_{jj}} = 200$ GeV

Each event is given a weight that is the inverse of $F(\Phi_n)$. The `Powheg` generator can also produce events with negative weight. The final set of events are then culled of any large or spurious weights by assessing the total cross-section uncertainty as a function

123

of the weighted integral of events. The cross-section converges to the expected value within negligible uncertainty when requiring $|W_{\text{MC}}| < 400000$. And so this additional requirement is made on the events in the `Powheg` sample which are used in this analysis.

This `Powheg` sample uses the `AZNLO` tune to generate matrix elements, and `Pythia8` with `CTEQ6L1` PDF set to perform parton showering [6].

The `Powheg` sample is compared against samples produced using two other generators: `Sherpa 2.2.11` [35] and `Madgraph FxFx` [14]. `Powheg` is chosen as the default prediction for the QCD-W contribution based on its superior modeling of the data in the control regions. `Madgraph FxFx` is in good agreement with `Powheg` when $N_{\text{jets}}^{\text{central}} = 0$ but shows an excess of events when $N_{\text{jets}}^{\text{central}} > 0$, as can be seen in Figure 6.8. `Sherpa 2.2.11` has a much harder M_{jj} spectrum than both `Powheg` and `Madgraph FxFx`. Figure 6.9 and Figure 6.10 show the ratio of the three QCD-W samples to data where all other MC contributions have been subtracted from the data, before any fit or data-driven estimate has been performed.

(a) electron channel	(b) muon channel
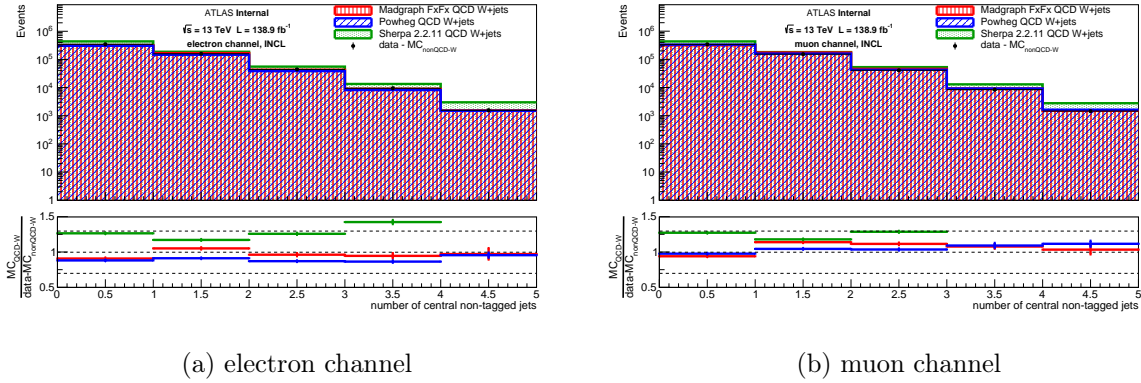
Figure 6.8: QCD-W sample comparison with data of $N_{\text{jets}}^{\text{central}}$ after the subtraction of other MC components. This is before any fitting or multijet estimate has been performed.
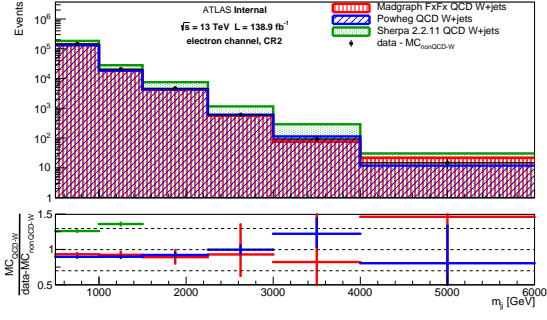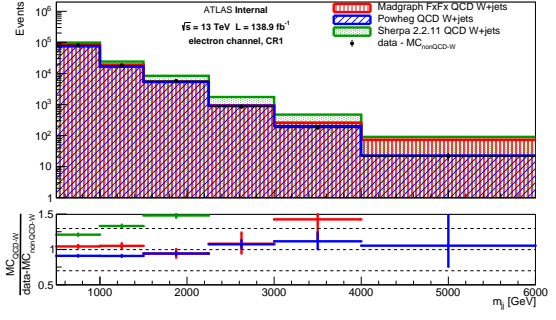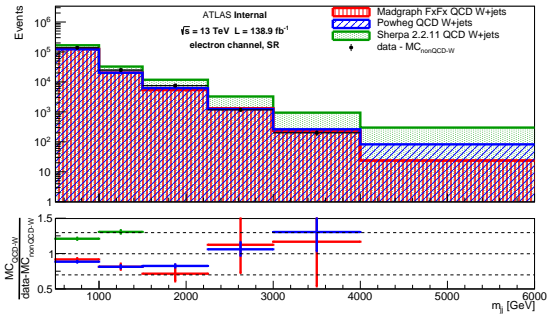
(a) CR2

(b) CR1

(c) SR
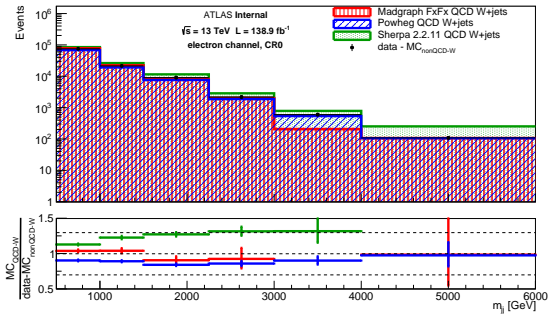
(d) CR0

Figure 6.9: Comparison of QCD-W samples with data in the M_{jj} distributions, electron channel, after the subtraction of other MC components. This is before any fitting or multijet estimate has been performed.
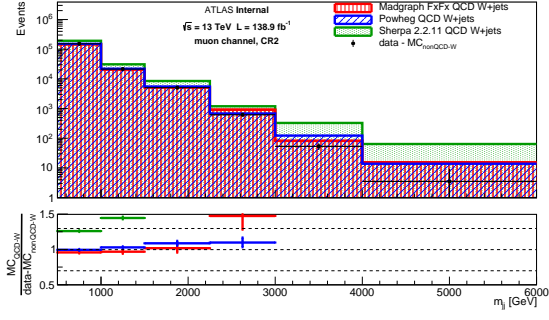
(a) CR2
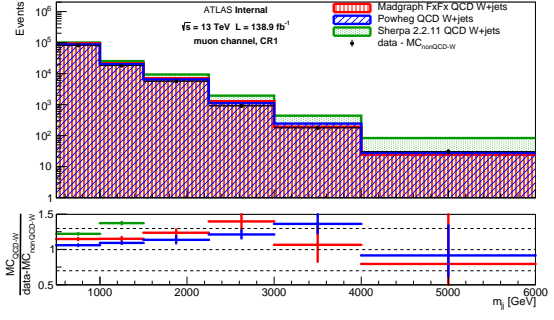
(b) CR1
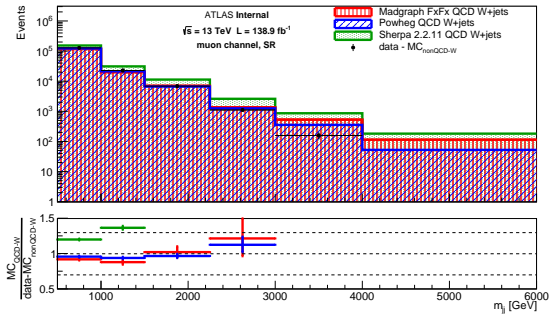
(c) SR
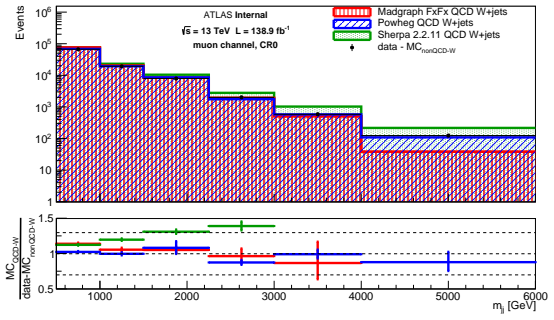
(d) CR0

Figure 6.10: Comparison of QCD-W samples with data in the M_{jj} distributions, muon channel, after the subtraction of other MC components. This is before any fitting or multijet estimate has been performed.

6.4.3 QCD Multijet and Fake Leptons

Though it is a small contribution in the fiducial phase space considered here (observed to be about a 10% effect), the fake contribution must be thoroughly addressed. Many different configurations of the data-driven multijet estimate were studied in order to constrain the contribution of this background and its associated systematic uncertainties. The primary method of estimating this background is the template-fit method. This method defines two more control regions: a template construction region and a fit region.

The template construction region is orthogonal to the fiducial volume and defines the shape of the multijet estimate as a function of a given observable. This region is defined by requiring that the leading lepton in the event fulfill the requirements of the "multijet" column in Table 6.1 or Table 6.2.

The fit region is defined to determine the normalization of the template via binned profile likelihood fit. It need not be orthogonal to the fiducial volume, but any cuts which are relaxed must be only in the fitted distribution, so that the distribution can be integrated from the fiducial cut value. Then the result is then logically consistent in both the fit region and fiducial region. The baseline choice of fit region is the same as the fiducial region, except with the $E_{\mathrm{T}}^{\mathrm{miss}}$ cut relaxed. Then the $E_{\mathrm{T}}^{\mathrm{miss}}$ distribution is fitted, where the bulk of the multijet contribution resides – at low $E_{\mathrm{T}}^{\mathrm{miss}}$ values. The binning and range of the fit is determined to keep the fit convergence stable given the statistics available. A systematic uncertainty is estimated to cover the variance in multijet yield observed due to this choice in each lepton channel and in each kinematic region.

For the electron channel, the fit is also be performed as a function of a given observable by fitting the same range of $E_{\mathrm{T}}^{\mathrm{miss}}$ but now binned in terms of another observable. This turns out to be more effective at modeling the shape of the multijet background than simply deriving one flat normalization for the entire range of an observable. In the muon channel, the contribution to the total background is observed to be about three times smaller than in the electron channel. As a result, determining the multijet normalization in the muon channel as a function of an observable suffers from fit convergence problems, due to lack of multijet events in the extremes of some distributions. Thus, in the muon channel, one normalization factor is used per region for all observables. As a shorthand, the technique where the normalization is determined as a function of each observable is

given the name "multi-bin fit", and the technique using only one normalization factor is given the name "flat fit."

During this fit, the QCD-W normalization is allowed to vary as well. The template and its detector systematic variations are then scaled to their post fit values, and this is taken as the multijet/fake lepton estimate. The QCD-W normalization determined from this fit is used only as a cross-check because it is allowed to vary in the signal extraction fit as well. The QCD-W normalization is observed to converge to a value close to 1 in these multijet fits. Technical details of the binned profile likelihood fit in the context of EWK-W signal extraction are described in Appendix C. The results of the multi-bin as a function of electron p_T are shown below in Figure 6.11. And the results of the muon channel flat fits in each region are shown in Figure 6.12.

(a) CR2

(b) CR1

(c) SR

(d) CR0
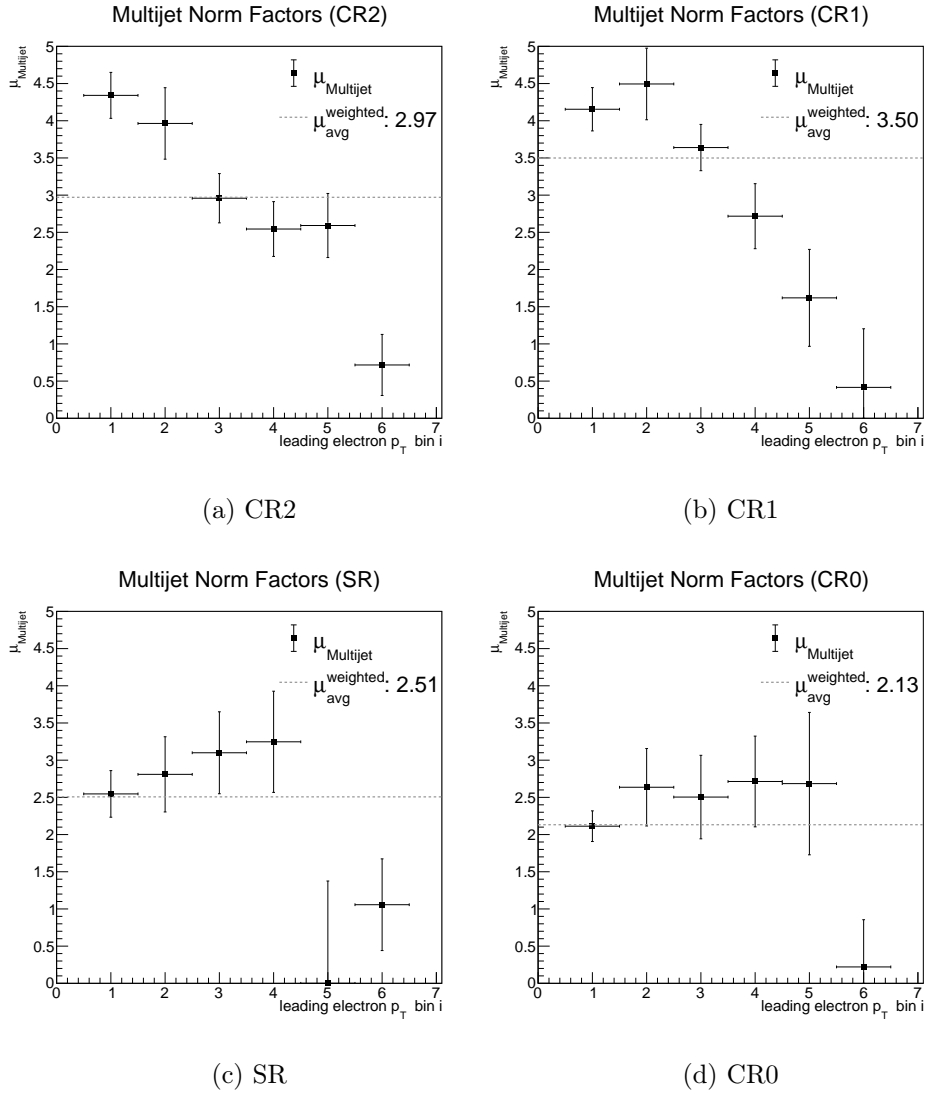
Figure 6.11: Multijet template normalization factors determined as a function of electron p_{T} in each region. The dashed line represents the weighted average of these values, where each value is weighted by the inverse square of its uncertainty.
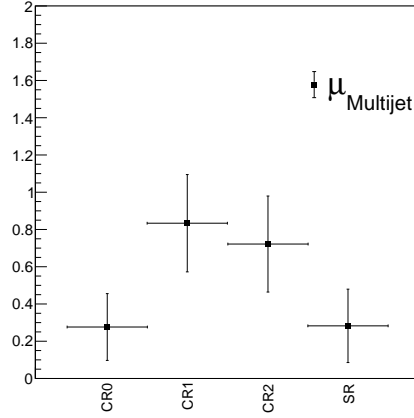
Figure 6.12: Multijet template normalization factors determined for each region in the muon channel.

Systematic uncertainties are estimated due to the choice of fit range, fit binning, multijet lepton isolation requirements, and the multijet normalization as a function of each observable of interest. These uncertainties are tabulated in subsection 6.5.5. The nominal choice of these parameters is taken to be that which gives the best post-fit agreement in the control regions. In the cases where the parameters perform similarly, then the one which gives smallest post-fit uncertainty is used. The uncertainty on the normalization coming from the fit is propagated to the statistical uncertainty on the multijet template.

6.4.4 Other Backgrounds

The remaining backgrounds are modelled using purely the MC prediction given by the relevant generators and PDF sets listed below.

- **Z+jets:** QCD-Z production analogous to the previously discussed QCD-W production, modeled by `Sherpa 2.2.11` using the `NNPDF30NNLO` PDF set

- **Top:** $t\bar{t}$ and single top (s and t-channel) production, modeled by `Powheg+Pythia`

with the `A14` generator tune

- **Diboson:** WW, ZZ, and WZ events, where at least one of the bosons decays leptonically, modeled by `Powheg+Pythia` with the `AZNLO CTEQ6L1` generator tune

- **Other electroweak:** electroweak Z production as well as the electroweak W production where the W decays into a τ-lepton, modeled primarily with `Sherpa`

A complete list of the MC samples used in this analysis, broken down by physics process, can be found in Appendix E. This list also contains the generator cross-sections, k-factors, and generator filter efficiencies for each sample.

6.5 Results

6.5.1 Detector-Level Distributions: Pre-Fit

The detector level distribution of M_{jj}, lepton p_{T}, and the $|\Delta y|$ between the two highest p_{T} jets, for each lepton channel is shown below, as well as the combined channel. This is after the multijet estimation, but before any signal extraction fit. The pre-fit distributions of each observable in each region are found to be in reasonable agreement with the Standard Model prediction within uncertainty. There is tension between data and prediction in the signal region at high M_{jj}. The other distributions are in agreement with the prediction within uncertainties, both pre- and post-fit. The large uncertainty in several lepton p_{T} distributions at high lepton p_{T} arises from the multijet uncertainty.
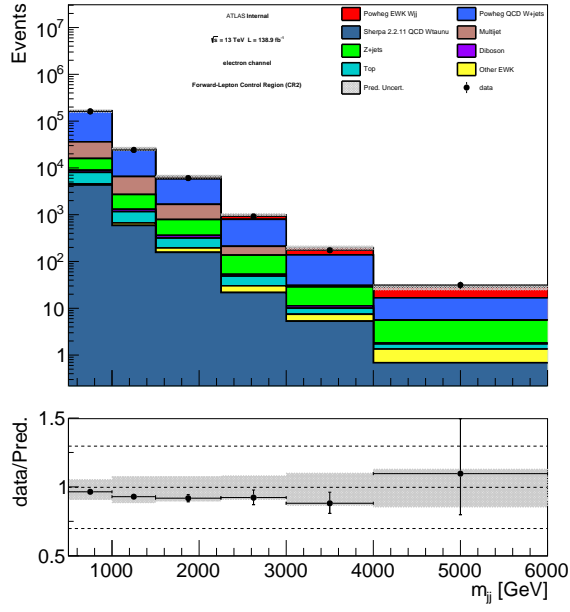
(a) CR2
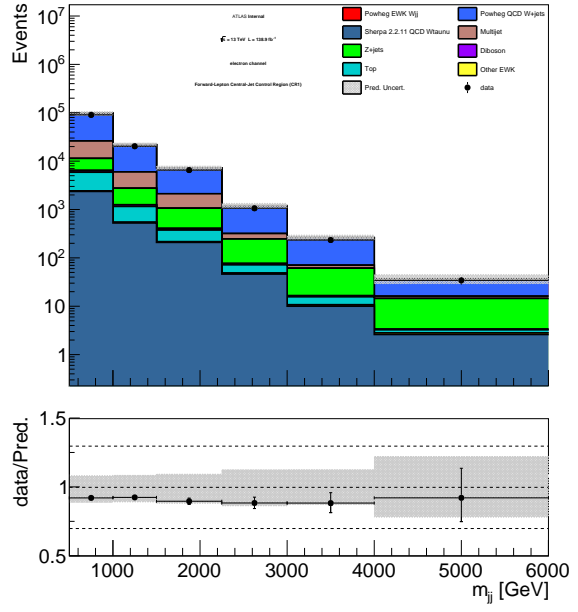
(b) CR1
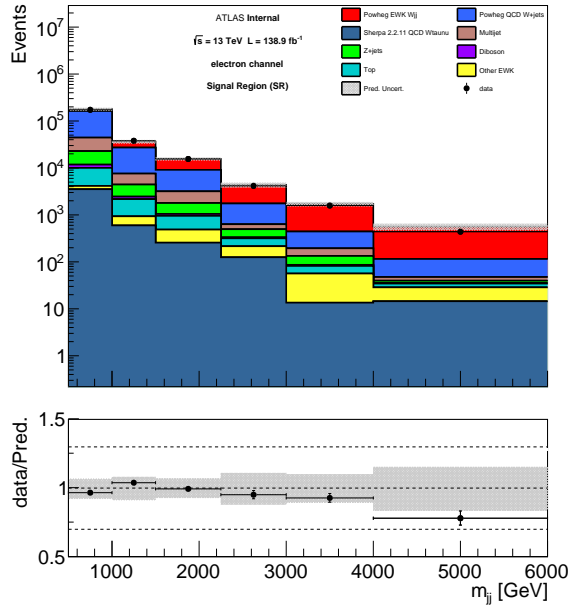
(c) SR
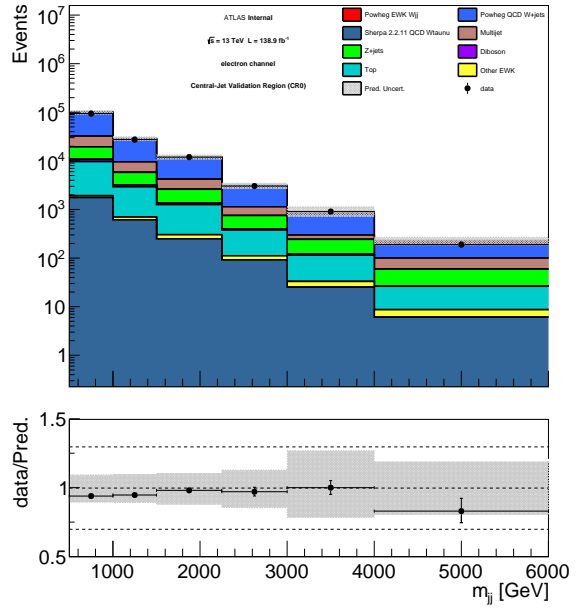
(d) CR0

Figure 6.13: Pre-fit detector-level M_{jj} distributions in the electron channel
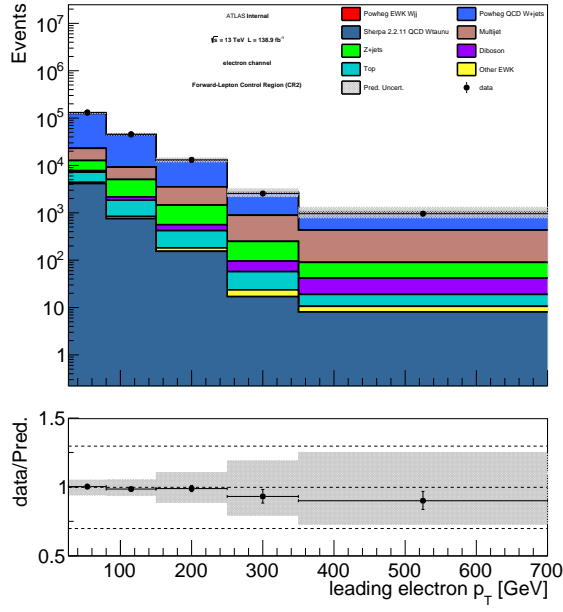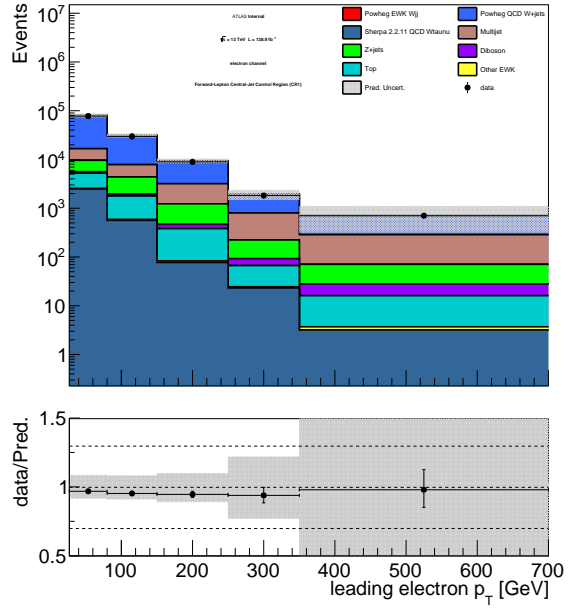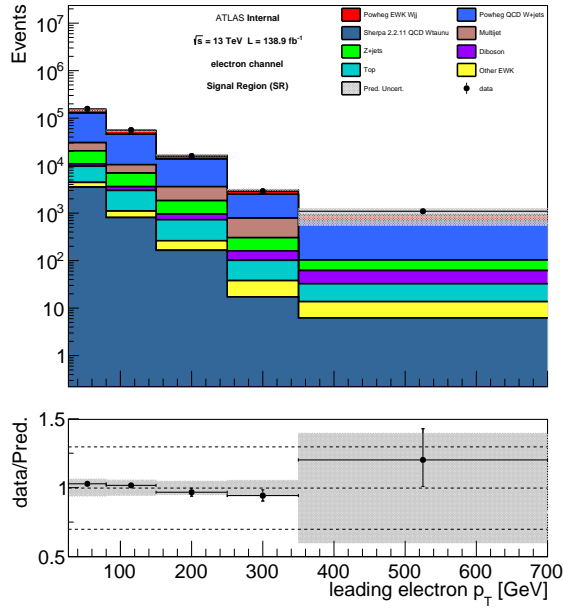
(a) CR2

(b) CR1

(c) SR
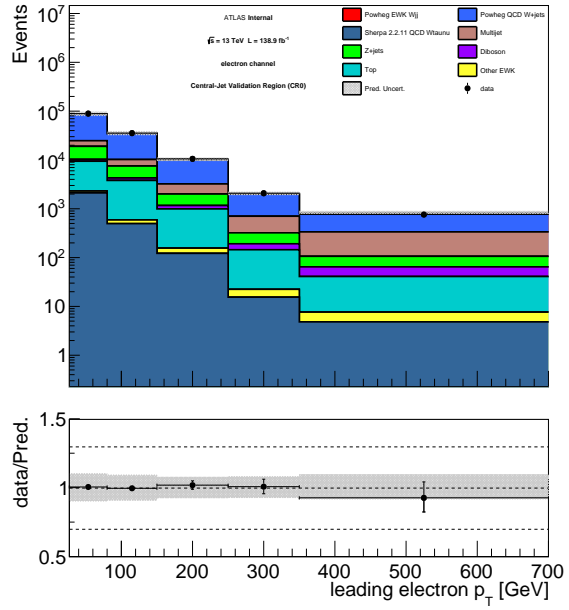
(d) CR0

Figure 6.14: Pre-fit detector-level leading electron p_T distributions
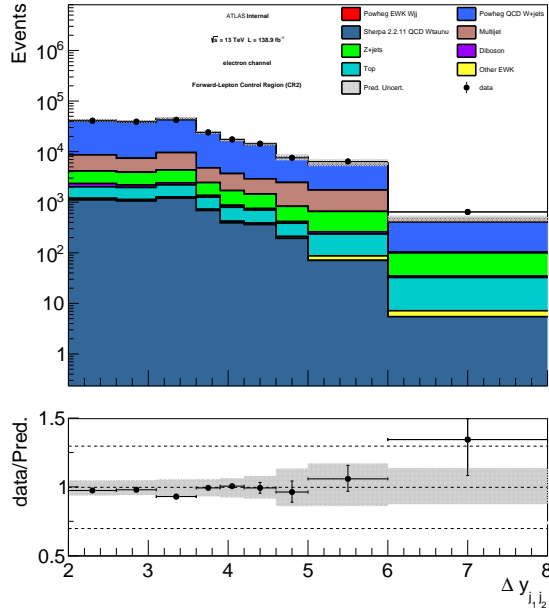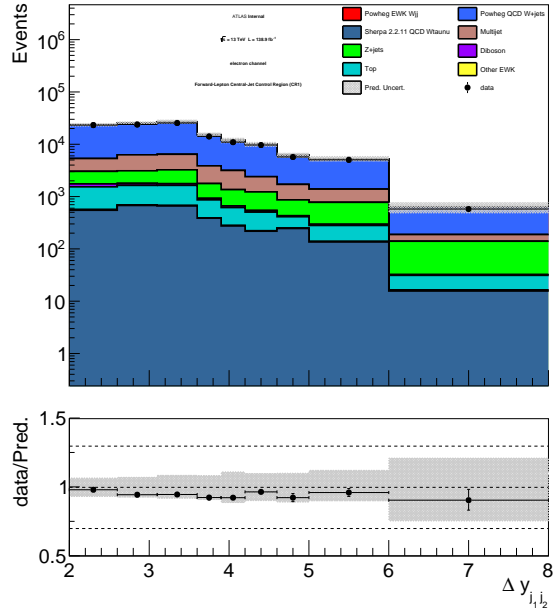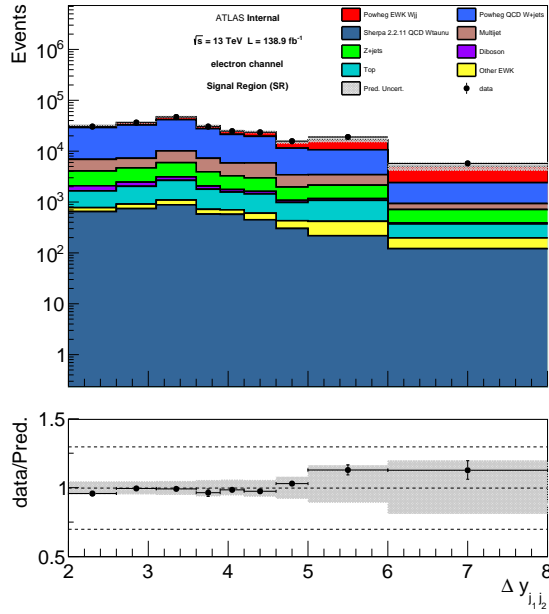
(a) CR2

(b) CR1

(c) SR
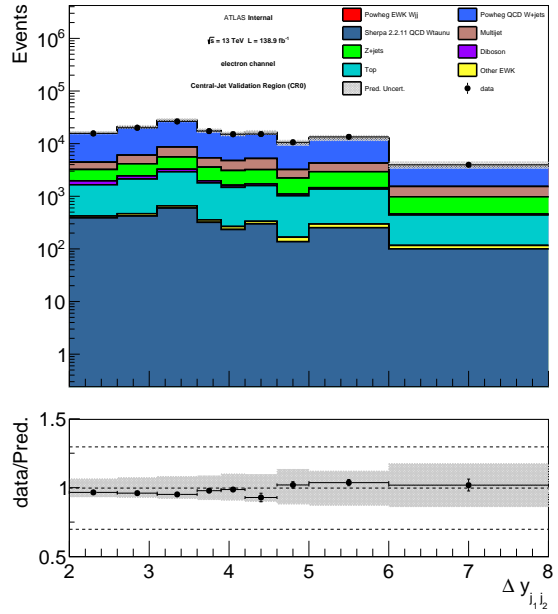
(d) CR0

Figure 6.15: Pre-fit detector-level distributions of $|\Delta y|$ between the two highest p_{T} jets in the electron channel
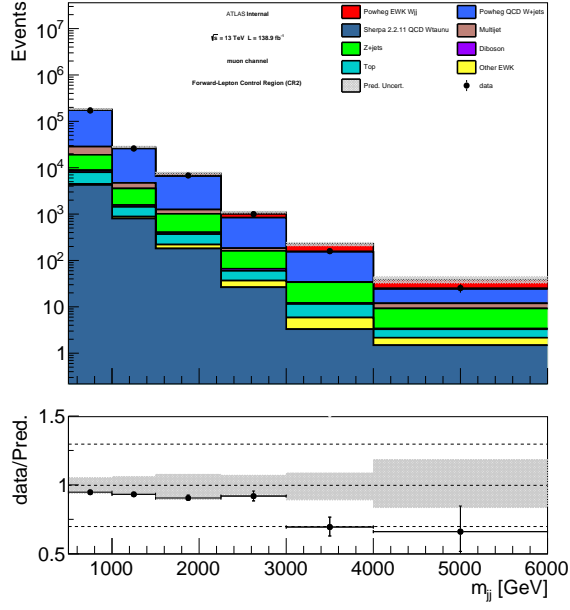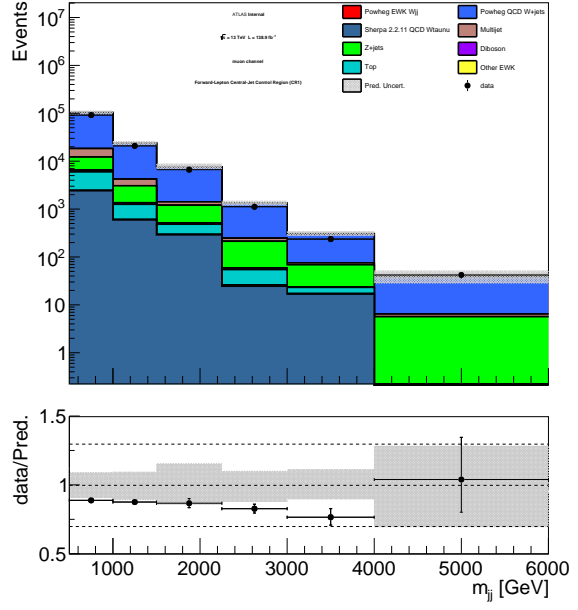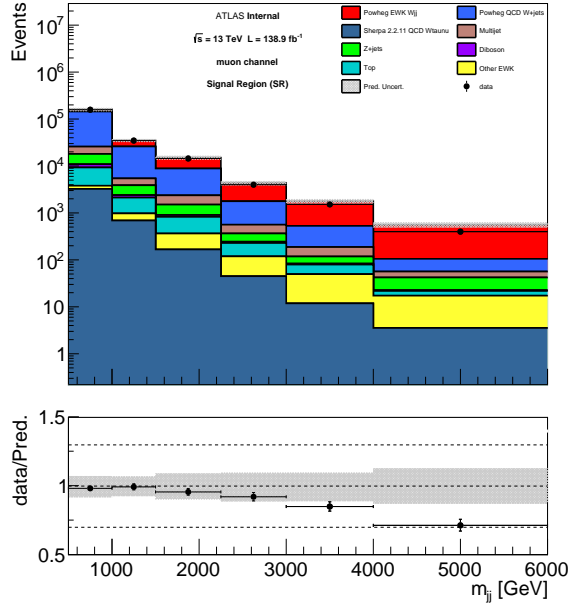
(a) CR2

(b) CR1

(c) SR
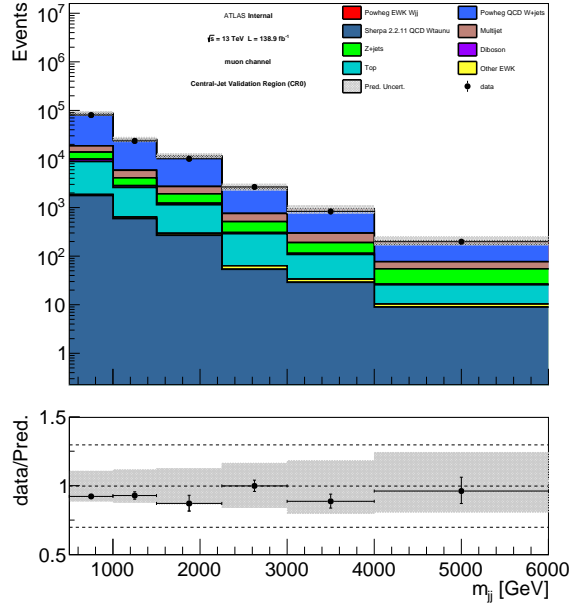
(d) CR0

Figure 6.16: Pre-fit detector-level M_{jj} distributions in the muon channel
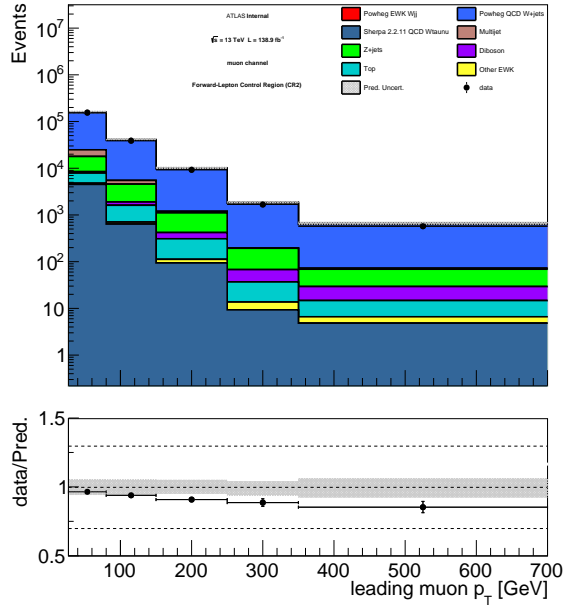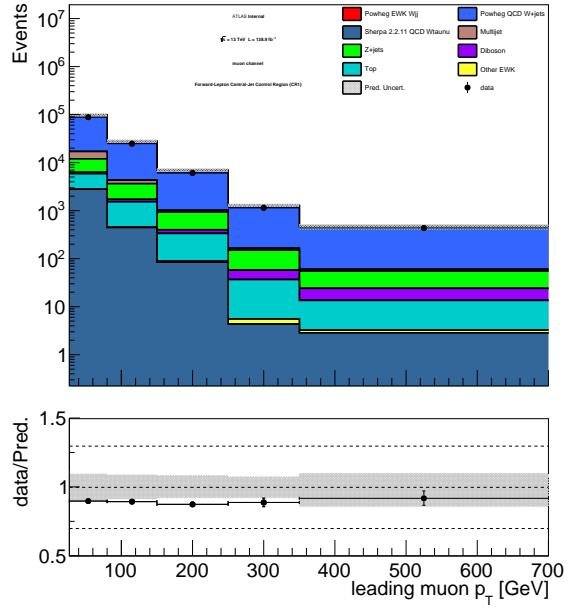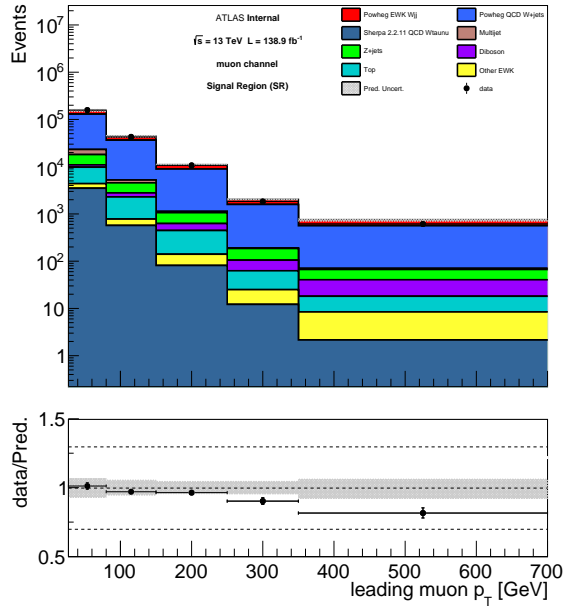
(a) CR2

(b) CR1

(c) SR
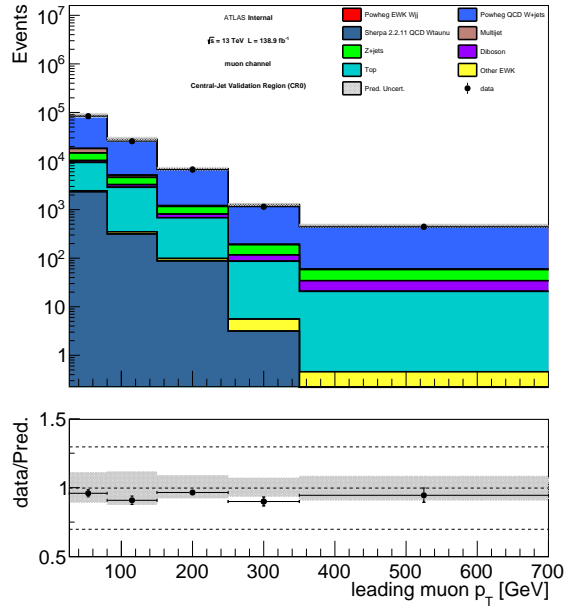
(d) CR0

Figure 6.17: Pre-fit detector-level leading muon p_T distributions
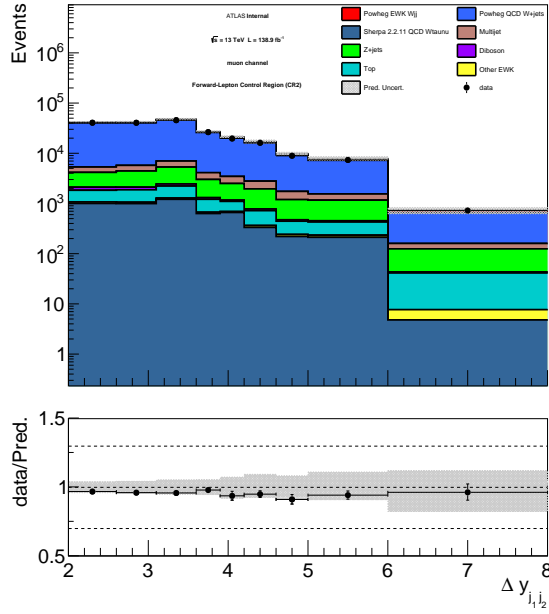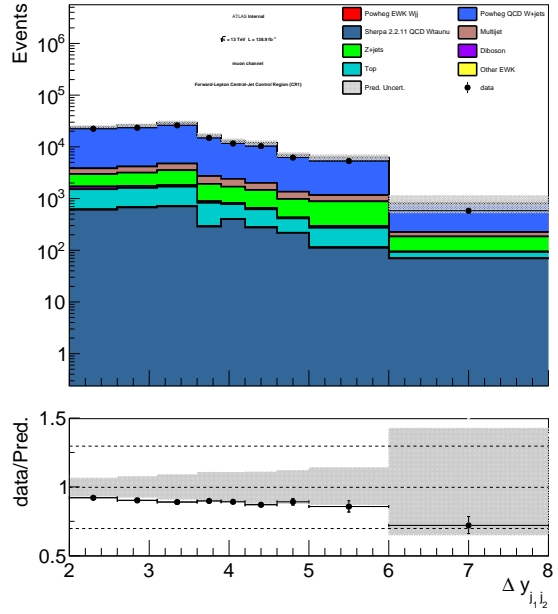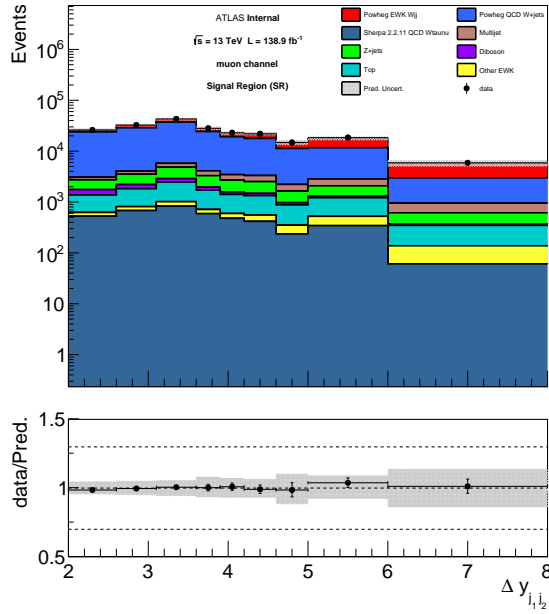
(a) CR2

(b) CR1

(c) SR
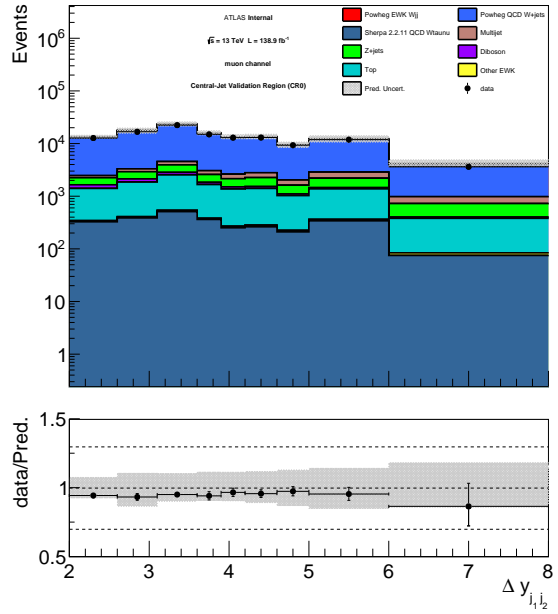
(d) CR0

Figure 6.18: Pre-fit detector-level distributions of $|\Delta y|$ between the two highest p_{T} jets in the muon channel
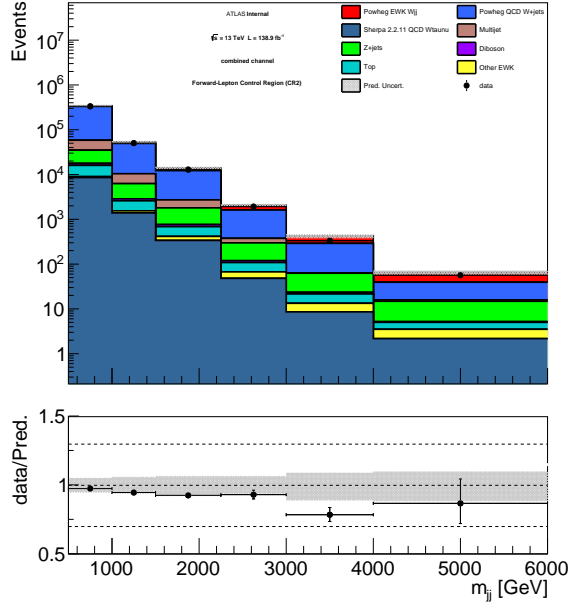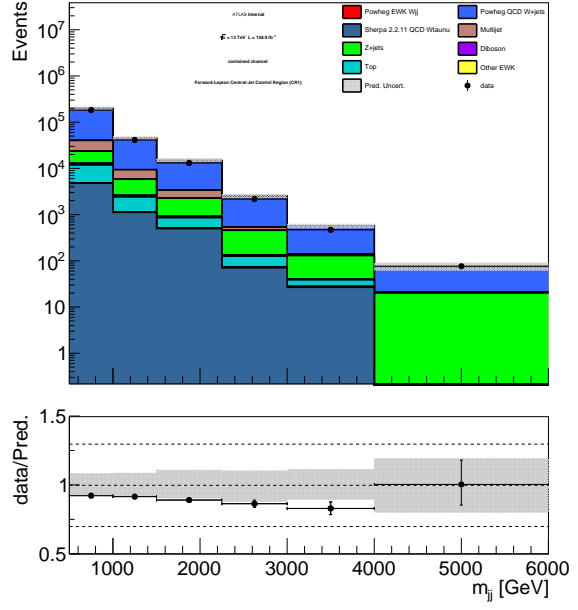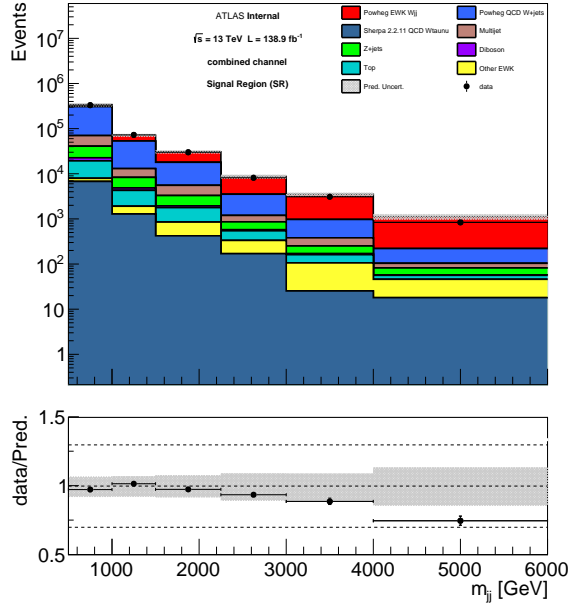
(a) CR2

(b) CR1

(c) SR
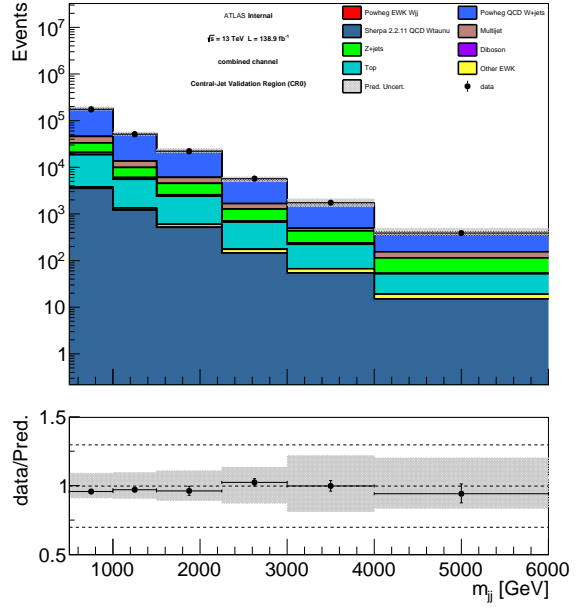
(d) CR0

Figure 6.19: Pre-fit detector-level M_{jj} distributions in the combined $W \to \ell\nu$ channel
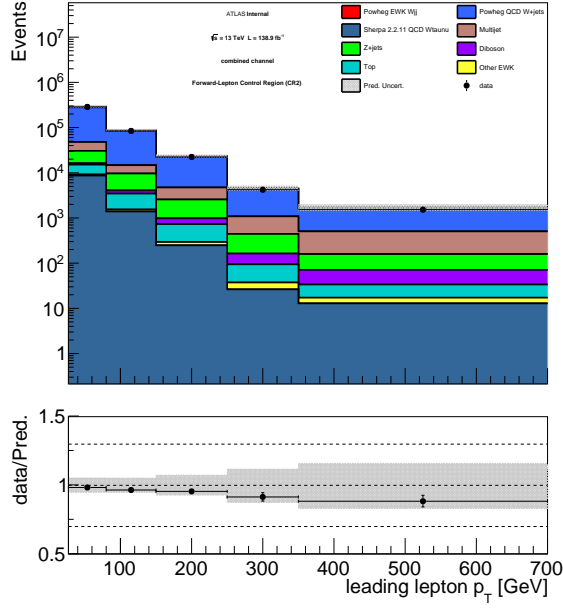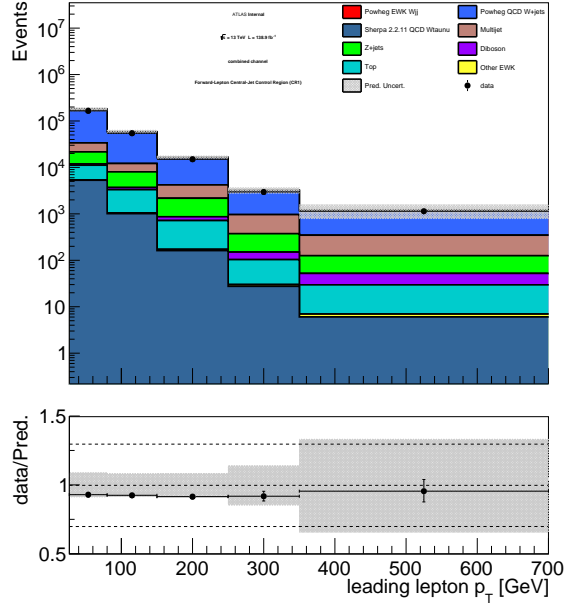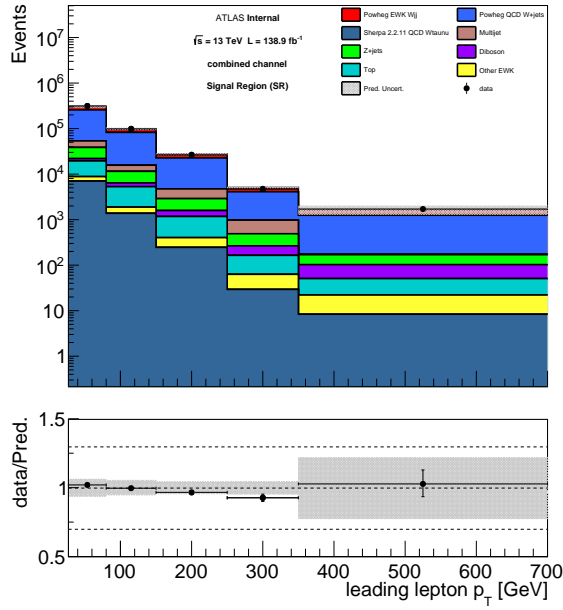
(a) CR2

(b) CR1

(c) SR
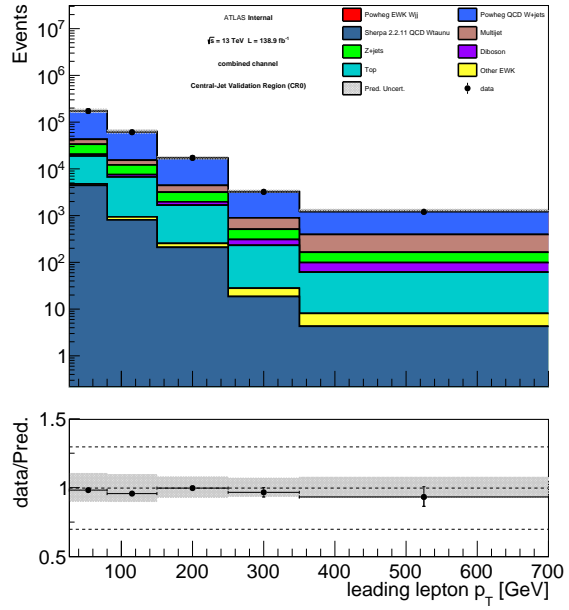
(d) CR0

Figure 6.20: Pre-fit detector-level leading lepton p_{T} distributions in the combined combined $W \to \ell\nu$ channel
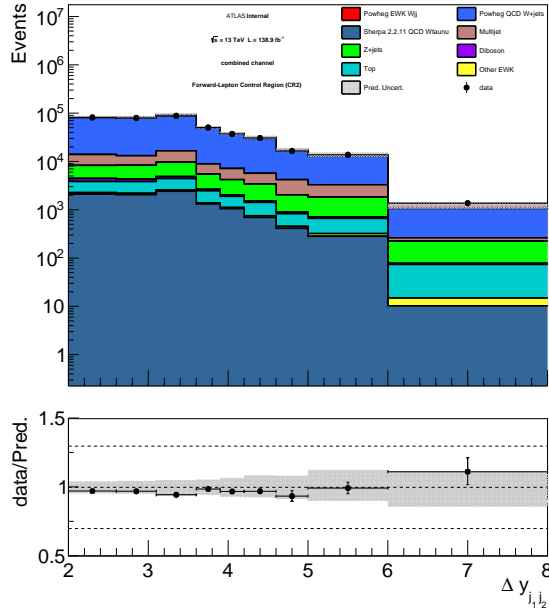
(a) CR2
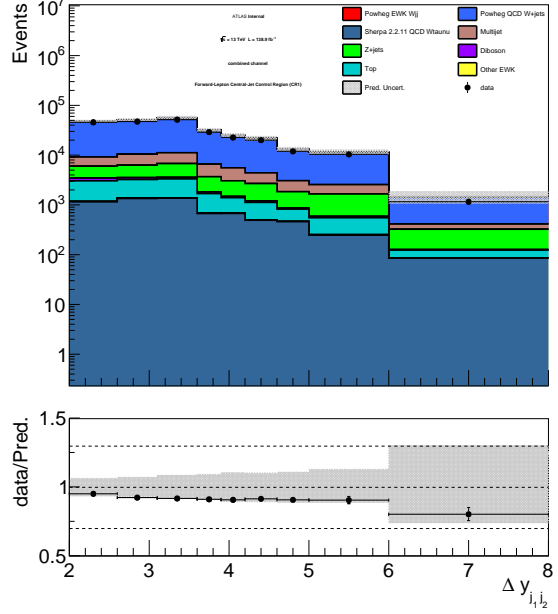
(b) CR1
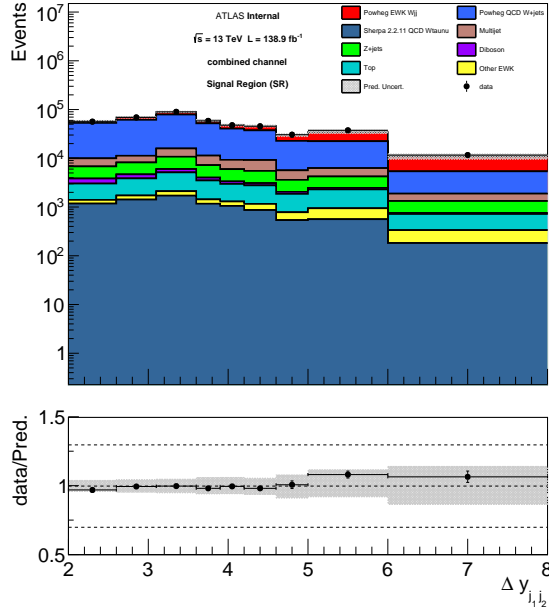
(c) SR
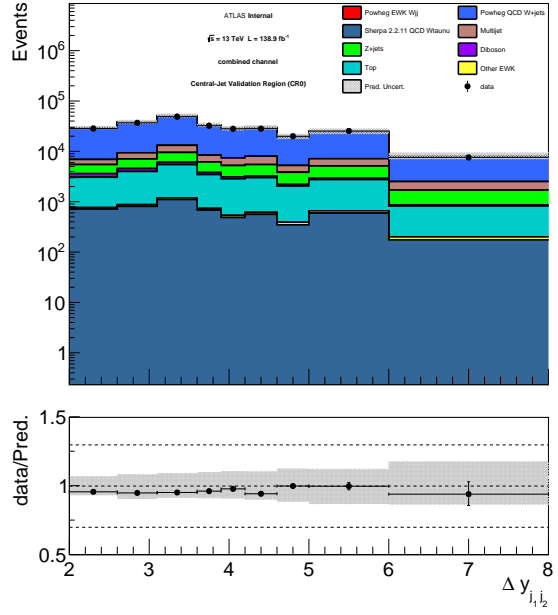
(d) CR0

Figure 6.21: Pre-fit detector-level distributions of $|\Delta y|$ between the two highest p_T jets in the combined $W \to \ell\nu$ channel

6.5.2 Signal Extraction Binned Profile Likelihood Fit

To determine the signal strength μ_{Ewk}, a binned profile likelihood fit of the leading lepton p_{T} is performed, similar to the technique employed to determine the multijet normalization. In this case, the QCD-W normalization μ_{QcdW} is determined by simultaneously fitting CR1, CR2, and SR regions, along with the EWK-W normalization, μ_{EWK}, which is determined from fitting SR. The CR0 region is not fitted, and it is used as a validation region. This choice of excluding CR0 from the fit regions arises from the fact that the top background is notably more prominent here, and large flavor tagging dependencies were observed when including this region in the determination of μ_{QcdW}. Also, using CR0 as a validation region adds a valuable cross-check of the fit result. As an additional cross-check, the $|\Delta y|$ distribution between the leading p_{T} jets is fitted and compared to the leading lepton p_{T} result.

The electron and muon channels are fitted separately to assess their agreement. To combine these channels, the distributions of the combined set of events are fitted, to profit from the profile likelihood treatment of the correlation structure of the combined nuisance parameters. `MINOS` minimization is used in each case to find the configuration of nuisance parameters which minimize the negative log-likelihood of the fit model.

The pre- and post-fit distributions are shown below for each region in the combined $W \to \ell\nu$ channel. The bin contents are allowed to fluctuate within their uncertainty, obeying the nuisance parameter correlation structure, and the profiled uncertainty is plotted in the post fit distributions, and the χ^2/ndf value displayed takes into account only the number of bins in the displayed region – the total number of μ parameters in the fit is not subtracted since their determination uses information from multiple regions. This metric is used only for qualitatively gauging the difference in pre-/post-fit agreement

141

within each region. In the extraction of the fiducial cross-section, the Standard Model predictions for the QCD-W and EWK-W are taken to be the associated μ values obtained in the fit multiplied by the prediction given by MC. Post-fit distributions for several kinematic variables with these μ applied are shown in subsection 6.5.3. More technical details of the binned profile likelihood fit machinery are described in Appendix C.

| (a) CR0 (pre-fit) | (b) CR1 (pre-fit) | (c) CR2 (pre-fit) | (d) SR (pre-fit) |

| (e) CR0 (post-fit) | (f) CR1 (post-fit) | (g) CR2 (post-fit) | (h) SR (post-fit) |
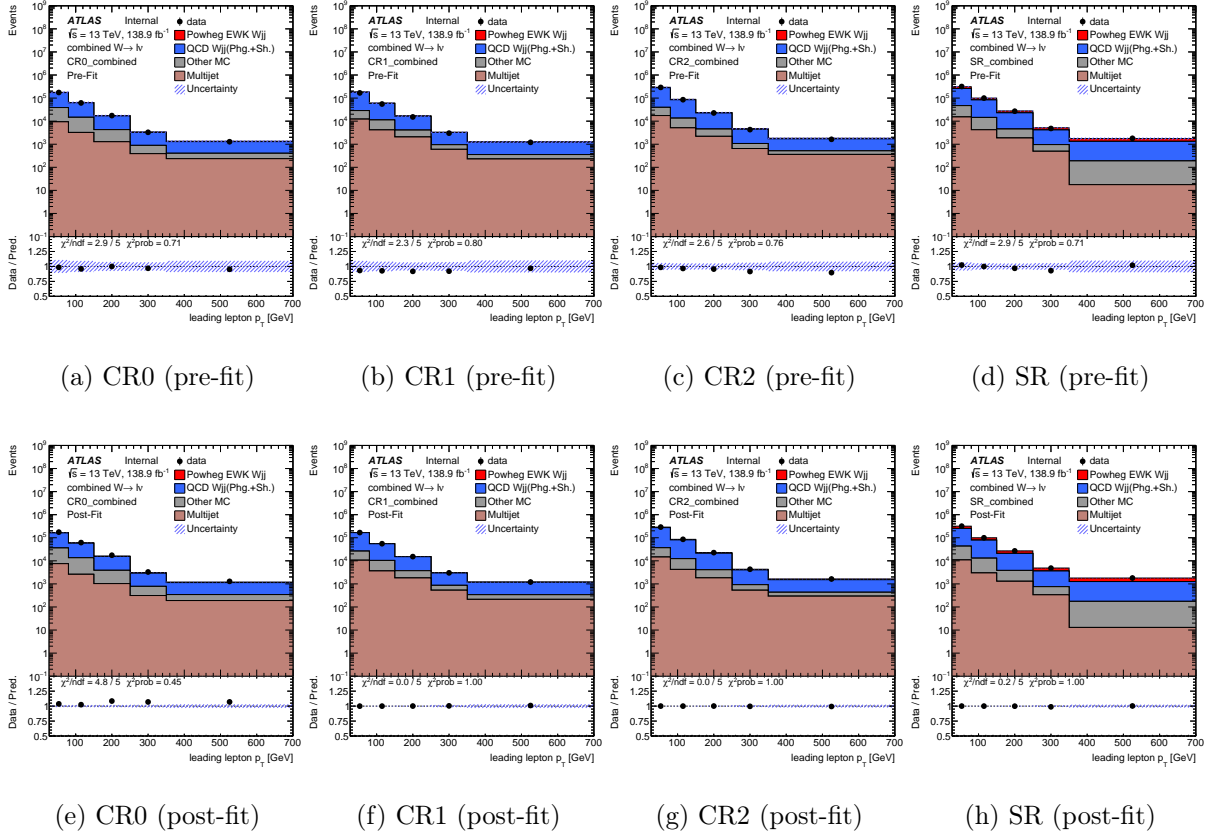
Figure 6.22: Signal extraction fit results pre- and post-fit - combined $W \rightarrow \ell\nu$ channel, fitting p_T^ℓ

(a) electron channel (b) muon channel (c) combined
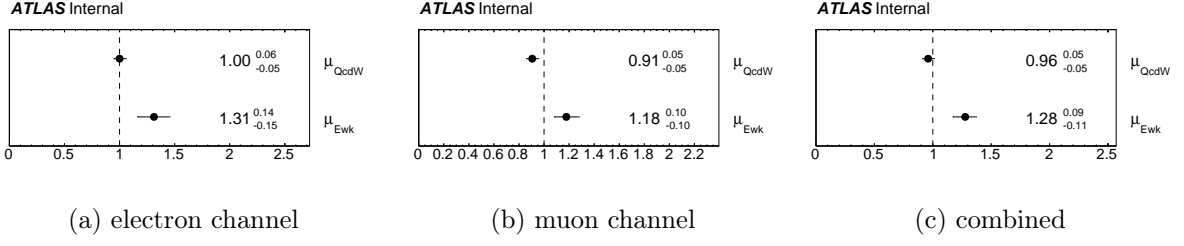
Figure 6.23: Signal extraction fit results: normalization factors derived from fitting the leading lepton p_{T} distribution in the electron, muon, and combined channels.

(a) CR0 (pre-fit) (b) CR1 (pre-fit) (c) CR2 (pre-fit) (d) SR (pre-fit)

(e) CR0 (post-fit) (f) CR1 (post-fit) (g) CR2 (post-fit) (h) SR (post-fit)
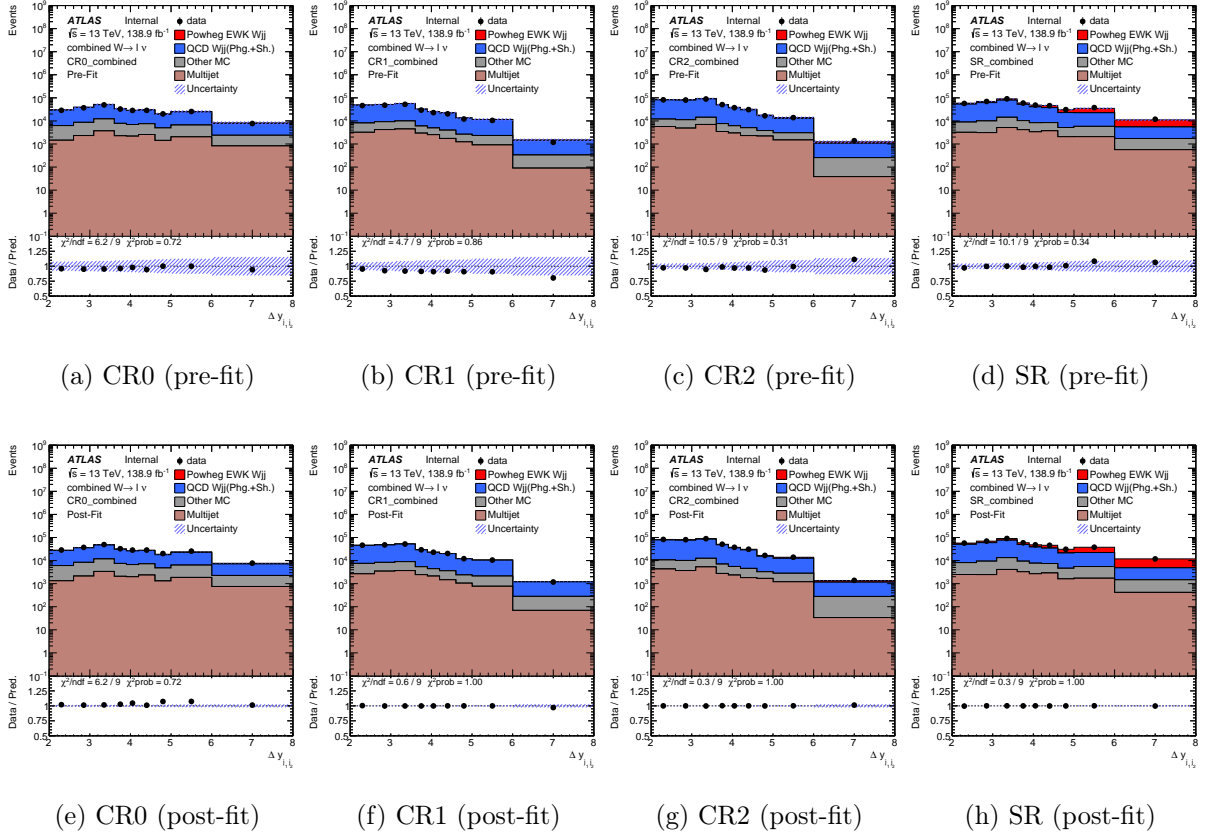
Figure 6.24: Alternative signal extraction fit results, pre- and post-fit - combined $W \to \ell\nu$ channel, fitting $|\Delta y_{jj}|$

0.96 $^{0.05}_{-0.05}$ μ_{QcdW}

1.13 $^{0.10}_{-0.10}$ μ_{Ewk}

0 0.2 0.4 0.6 0.8 1 1.2 1.4 1.6 1.8 2 2.2

(a) electron channel

0.97 $^{0.05}_{-0.05}$ μ_{QcdW}

1.35 $^{0.10}_{-0.09}$ μ_{Ewk}

0 0.5 1 1.5 2 2.5

(b) muon channel

0.98 $^{0.05}_{-0.05}$ μ_{QcdW}

1.28 $^{0.09}_{-0.09}$ μ_{Ewk}

0 0.5 1 1.5 2 2.5
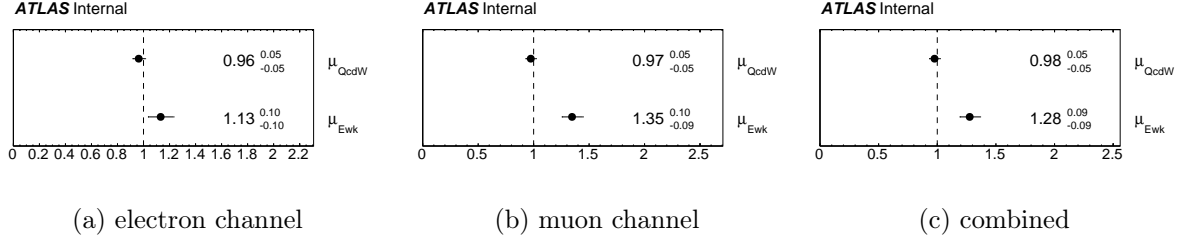
(c) combined

Figure 6.25: Signal extraction fit results: normalization factors derived from fitting the $|\Delta y_{jj}|$ distribution in the electron, muon, and combined channels.

The nuisance parameters with the largest impact are displayed for the combined channel in Figure 6.26. In general, the nuisance parameter impacts are reasonable. The full set of nuisance parameter pulls for the combined fit can be found in Appendix C in addition to the full correlation matrix. All nuisance parameter pulls are within 1-sigma bounds, except for the jet energy scale uncertainty due to pileup ρ topology, which takes on a best fit value of about -1.1-sigma away from the nominal best fit value. This is visible in the impact plot below (Figure 6.26), which shows the 10 most impactful parameters in the fit. The γ parameters represent nuisance parameters related to the finite statistics of the MC prediction in each bin.

(a) μ_{EWK}

(b) μ_{QCD}
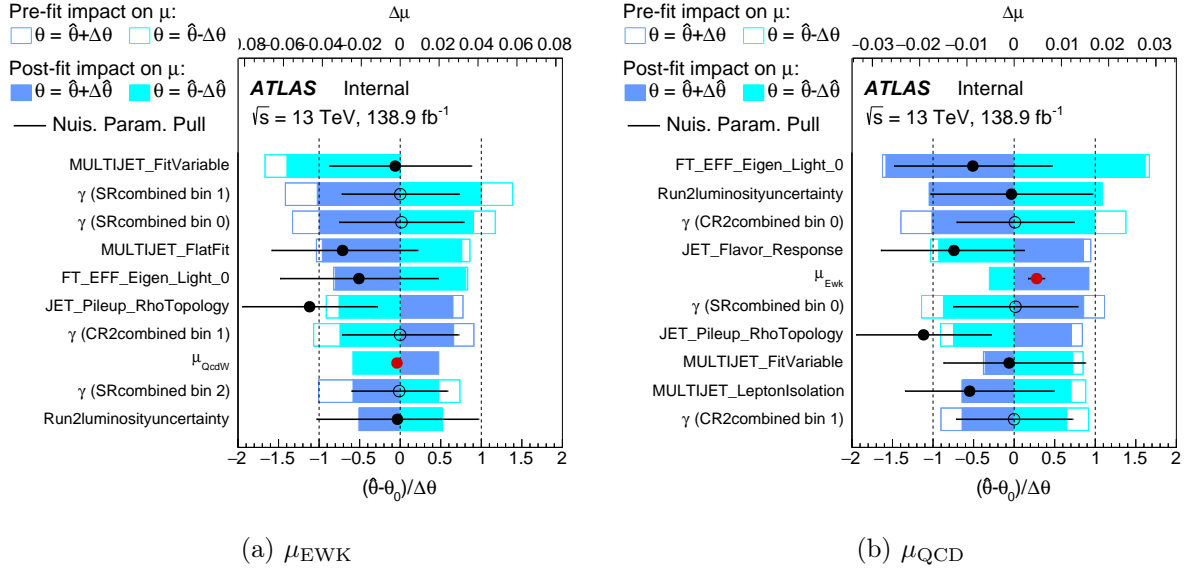
Figure 6.26: Nuisance parameter ranking - combined $W \rightarrow \ell\nu$ channel

To assess the convergence of the fit to the final μ values, the negative log-likelihood is evaluated at 30 points in the range $0 < \mu < 2$, for each μ. The minimization procedure relies on the fact that the negative log-likelihood should be parabolic near its minimum. For the combined fit, these scans are shown for each parameter of interest in Figure 6.27. Both distributions are reasonably parabolic, with no kinks or false minima which would indicate convergence problems.
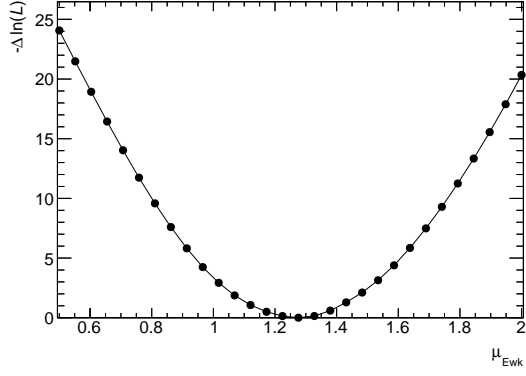
(a) Negative log likelihood scan for μ_{EWK}
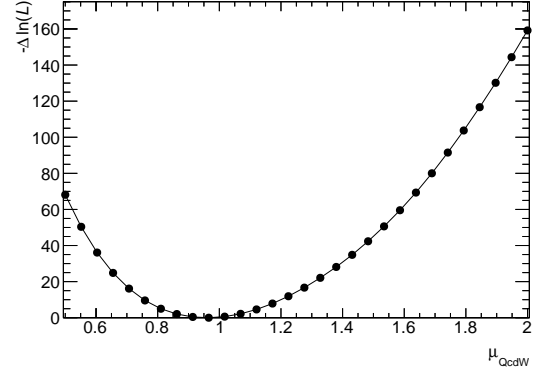
(b) Negative log likelihood scan for μ_{QCD}

Figure 6.27: Negative log likelihood scan for the signal extraction fit normalization factors - combined $W \to \ell\nu$ channel

The comparison with the saturated fit model is used as the overall goodness-of-fit figure of merit [19]. For the fits to leading lepton p_{T}, the χ^2 probability of agreement with the saturated model is given below in Table 6.7. Details of this test statistic can be found in Appendix C.

	Electron	**Muon**	**Combined**
$-\ln L_0$	604965.240913	600585.971981	1205316.883728
$-\ln L$	604968.526764	600599.329820	1205323.661920
ΔNLL	13	13	13
$N_{\text{d.o.f.}}$	3.285851	13.357839	6.778192
$\frac{2\Delta\text{NLL}}{N_{\text{d.o.f.}}}$	0.505515	2.055052	1.042799
Probability	0.922855	0.013605	0.405810

Table 6.7: Signal extraction goodness-of-fit metrics: the negative log-likelihood of the saturated model ($-\ln L_0$), the fit model used to fit the combined lepton p_{T} ($-\ln L$), their difference (ΔNLL), the total number of degrees of freedom in the fit ($N_{\text{d.o.f.}}$), and finally the χ^2 probability that the model used agrees with the saturated model.

The pre-fit event yields are shown in Table 6.8, and the final post-fit event yields per-region are enumerated below in Table 6.9, and additional material related to this signal extraction fit can be found in Appendix C.

Sample	**CR0**	**CR1**	**CR2**	**SR**
Sherpa 2.2.11 QCD $W \to \tau\nu$	5564 ± 648	6599 ± 751	10505 ± 744	8826 ± 809
Other EWK	502 ± 55	128 ± 12	695 ± 36	2533 ± 133
Top	21734 ± 4190	8815 ± 1672	8512 ± 1418	15171 ± 2480
Diboson	2993 ± 310	1331 ± 130	2100 ± 124	4152 ± 248
Z+jets	19389 ± 2312	15868 ± 1628	22142 ± 1501	23669 ± 2075
Multijet	14526 ± 4154	19305 ± 5059	25819 ± 7463	21822 ± 7301
Powheg QCD $W \to \ell\nu$	192239 ± 21150	207198 ± 20699	326344 ± 19510	295868 ± 20292
Powheg EWK $W \to \ell\nu$	6989 ± 736	1739 ± 167	16375 ± 716	73011 ± 3421
Total Prediction	263937 ± 33555	260982 ± 30118	412492 ± 31512	445053 ± 36759
Data	258548 ± 508	242738 ± 493	403267 ± 635	450896 ± 671

Table 6.8: Combined $W \to \ell\nu$ channel pre-fit event yields, rounded to the nearest whole number in the case of MC.

Sample	CR0	CR1	CR2	SR
`Sherpa 2.2.11` QCD $W \to \tau\nu$	5341 ± 165	6335 ± 185	10084 ± 281	8473 ± 334
Other EWK	502 ± 31	128 ± 7	695 ± 33	2533 ± 109
Top	21734 ± 3886	8815 ± 1555	8512 ± 1386	15171 ± 2402
Diboson	2993 ± 144	1331 ± 69	2100 ± 100	4152 ± 183
Z+jets	19389 ± 1300	15868 ± 934	22142 ± 1319	23669 ± 1413
Multijet	14526 ± 2840	19305 ± 2772	25819 ± 4532	21822 ± 5303
`Powheg` QCD $W \to \ell\nu$	184549 ± 3453	198910 ± 3111	313289 ± 4881	284032 ± 6320
`Powheg` EWK $W \to \ell\nu$	8929 ± 693	2222 ± 169	20920 ± 1397	93274 ± 6231
Total Prediction	257964 ± 12512	252912 ± 8802	403561 ± 13928	453127 ± 22295
Data	258548 ± 508	242738 ± 493	403267 ± 635	450896 ± 671

Table 6.9: Combined $W \to \ell\nu$ channel post-fit event yields derived from the fit to lepton p_{T}, rounded to the nearest whole number in the case of MC

6.5.3   Detector-Level Distributions: Post-Fit

The detector level distribution of M_{jj}, lepton p_{T}, and the $|\Delta y|$ between the two highest p_{T} jets, for each lepton channel is shown below, as well as the combined channel. The values of μ_{EWK} and μ_{QcdW} determined from the signal extraction fit are applied to the QCD-W and EWK-W predictions, respectively. The unprofiled statistical and systematic uncertainties are displayed in each plot.
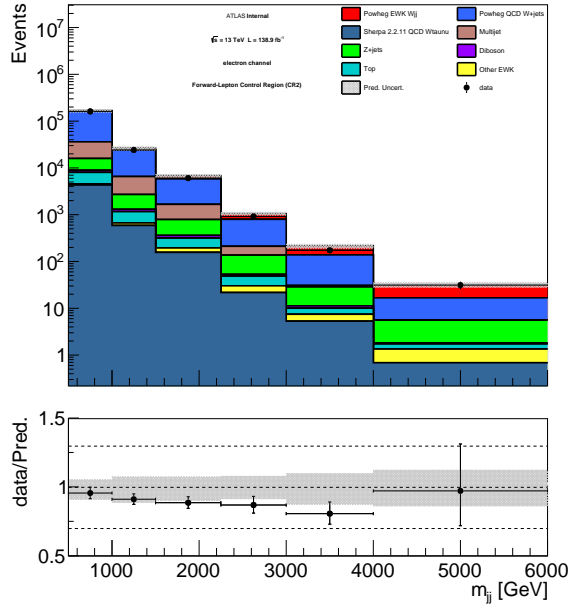
(a) CR2
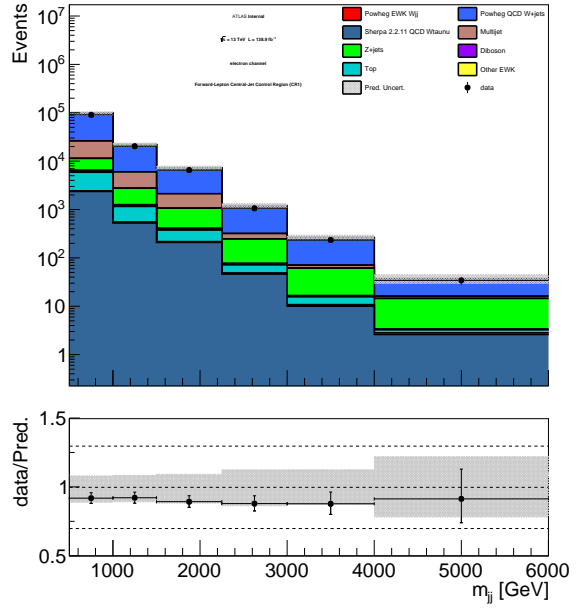
(b) CR1
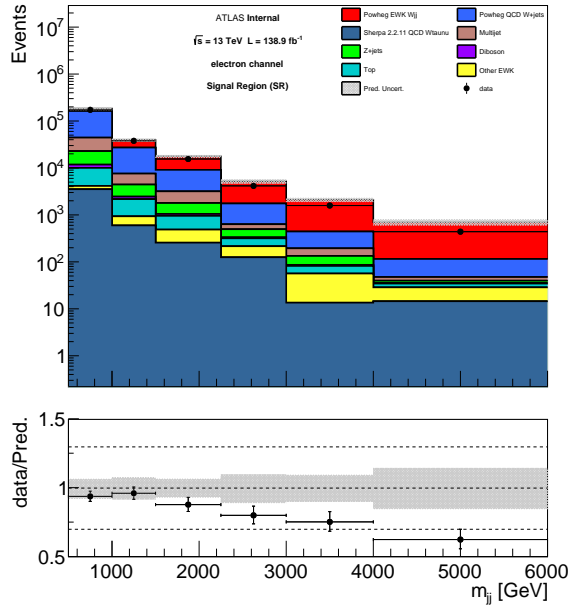
(c) SR
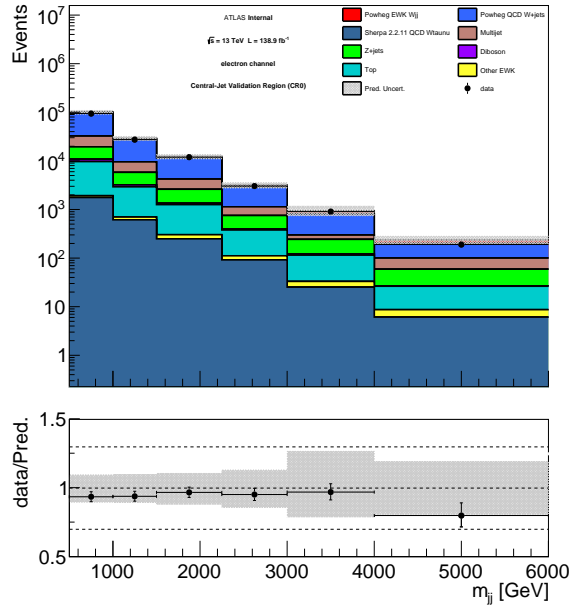
(d) CR0

Figure 6.28: Post-fit detector-level M_{jj} distributions in the electron channel
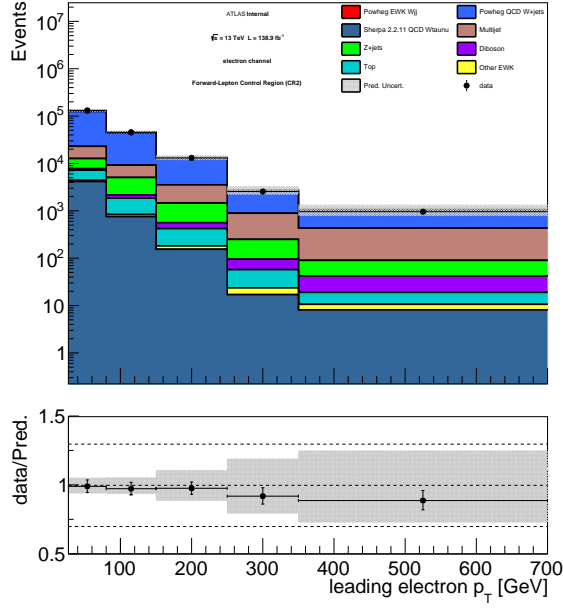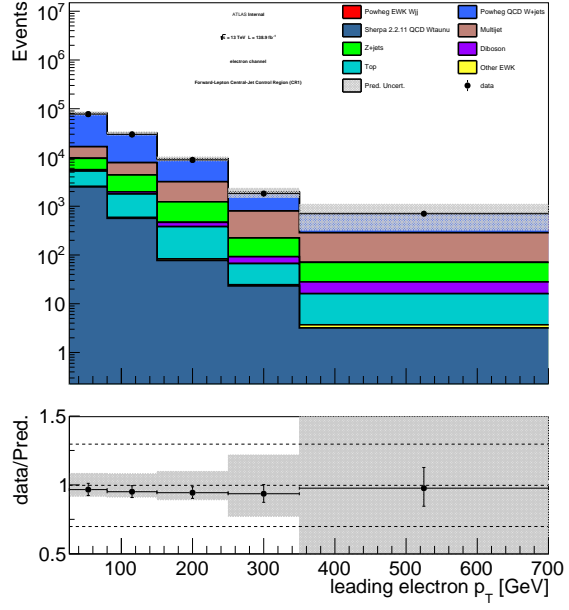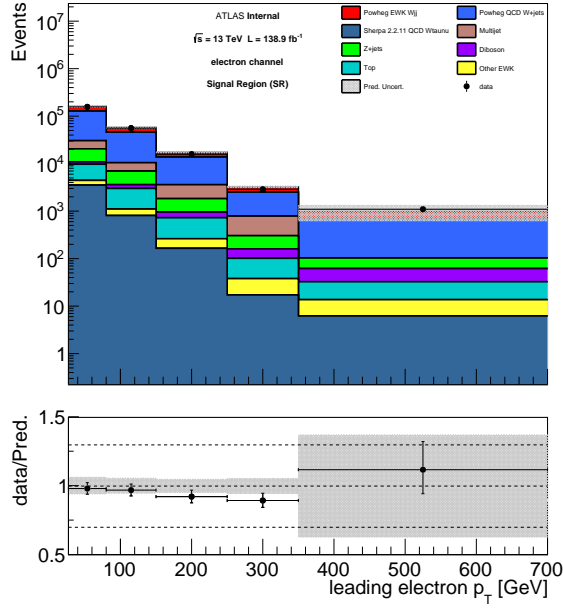
(a) CR2

(b) CR1

(c) SR
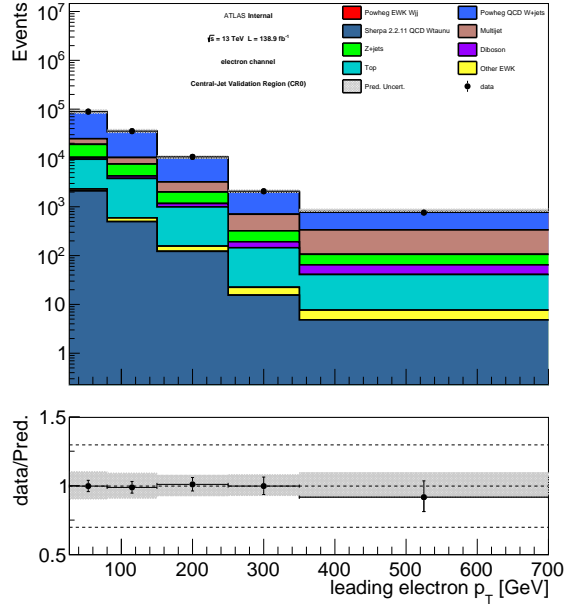
(d) CR0

Figure 6.29: Post-fit detector-level leading electron p_{T} distributions
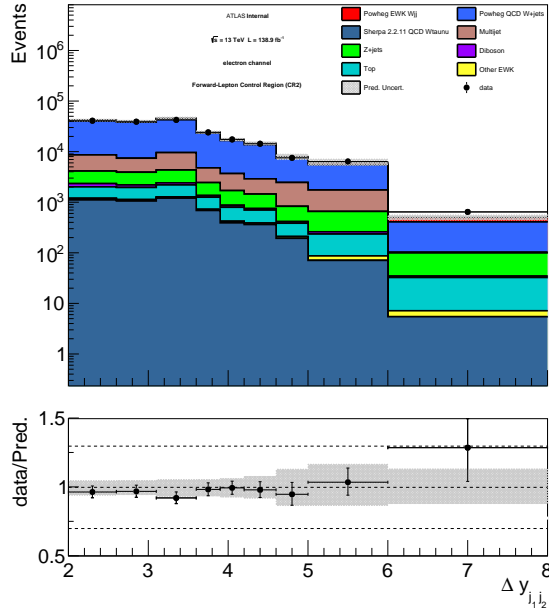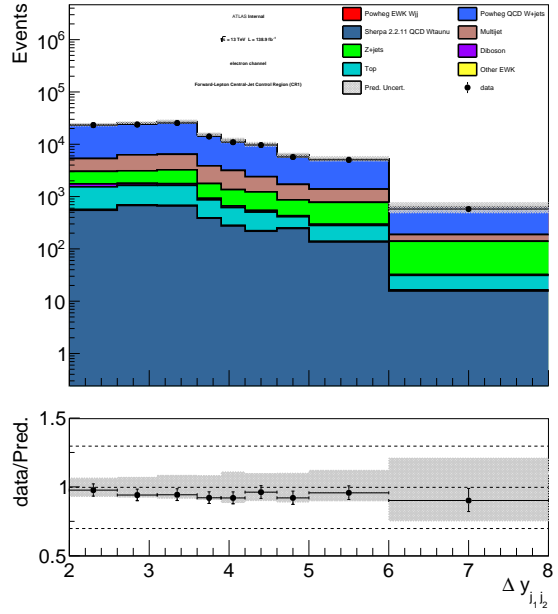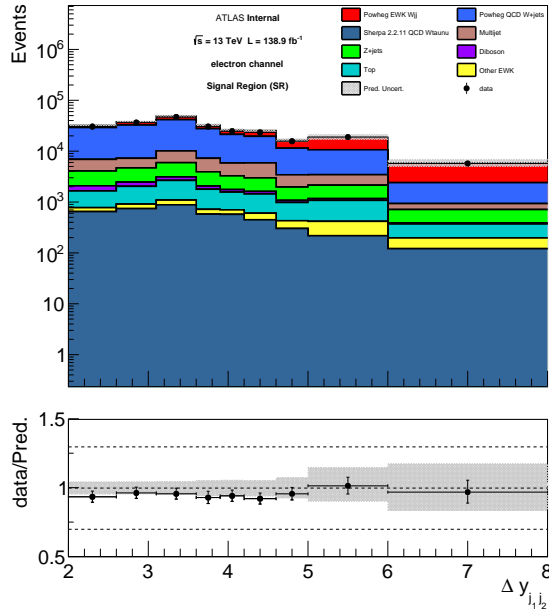
(a) CR2

(b) CR1

(c) SR
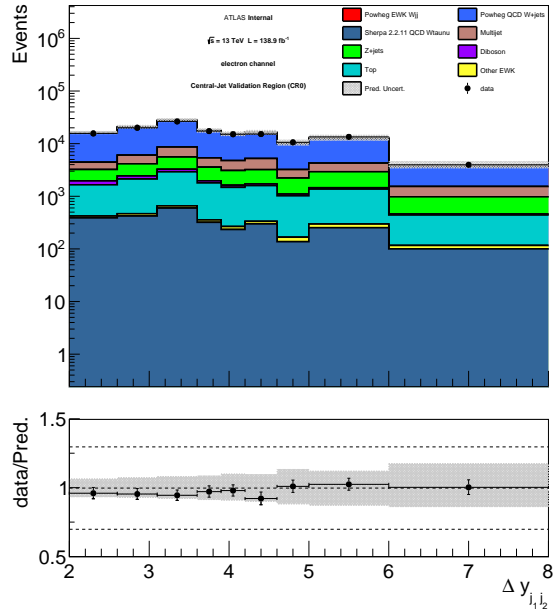
(d) CR0

Figure 6.30: Post-fit detector-level distributions of $|\Delta y|$ between the two highest p_{T} jets in the electron channel
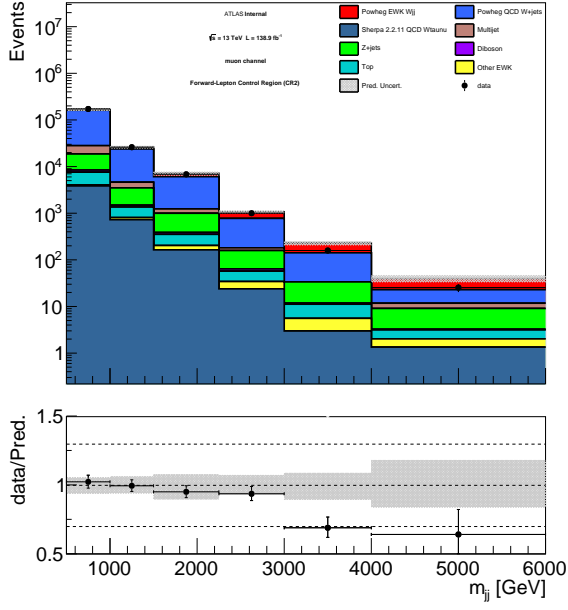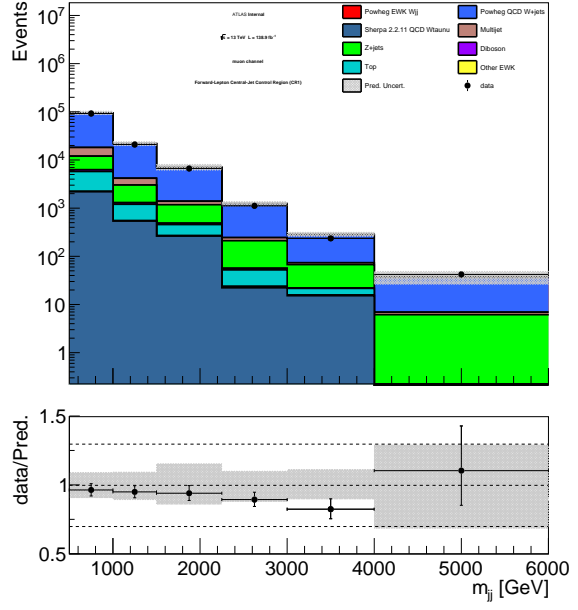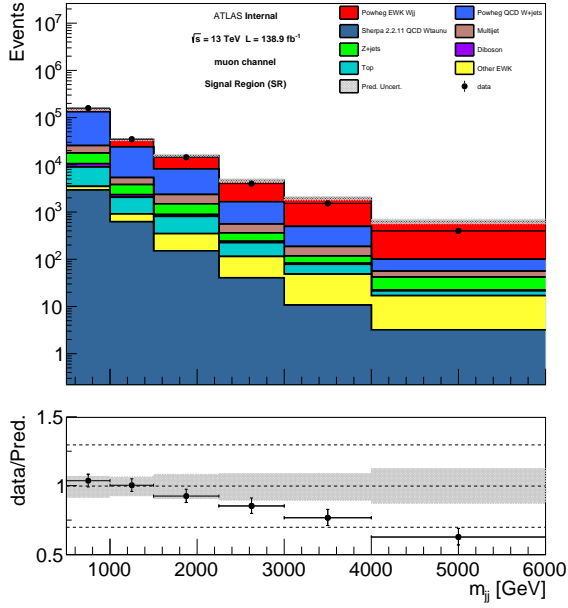
(a) CR2

(b) CR1

(c) SR
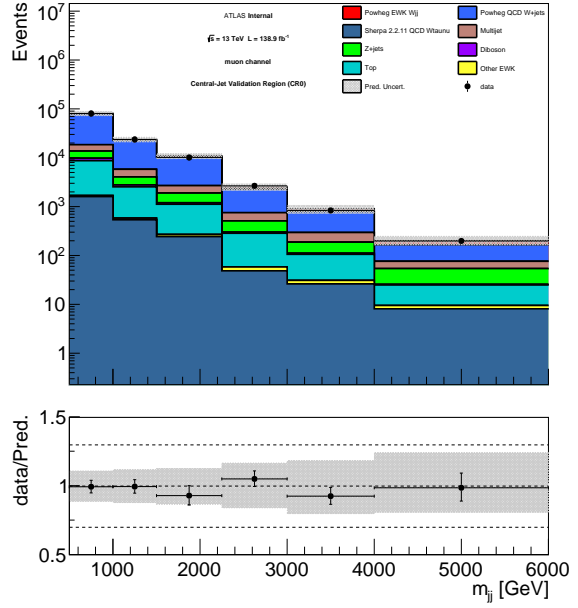
(d) CR0

Figure 6.31: Post-fit detector-level M_{jj} distributions in the muon channel
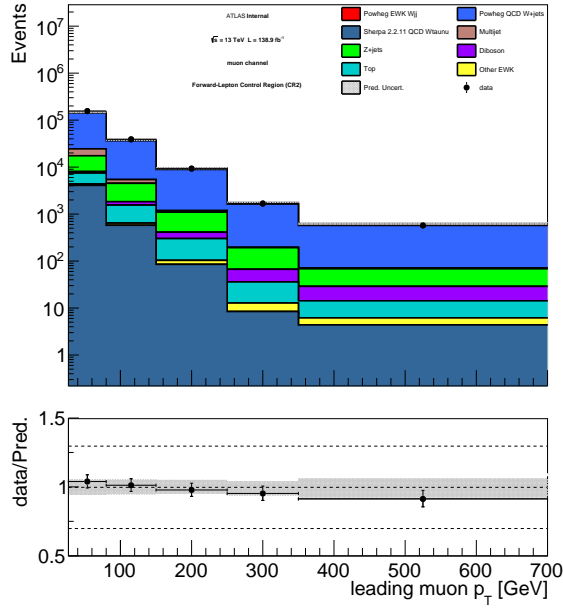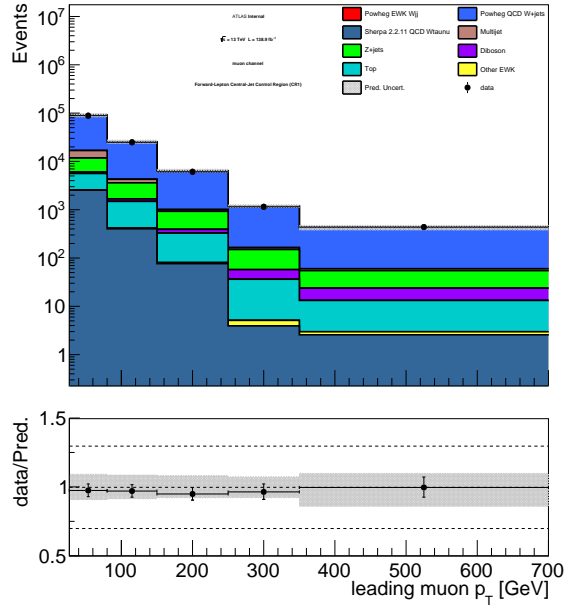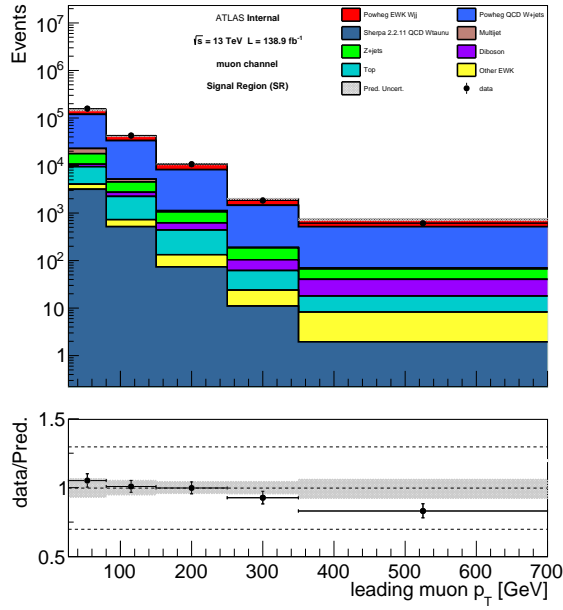
(a) CR2

(b) CR1

(c) SR
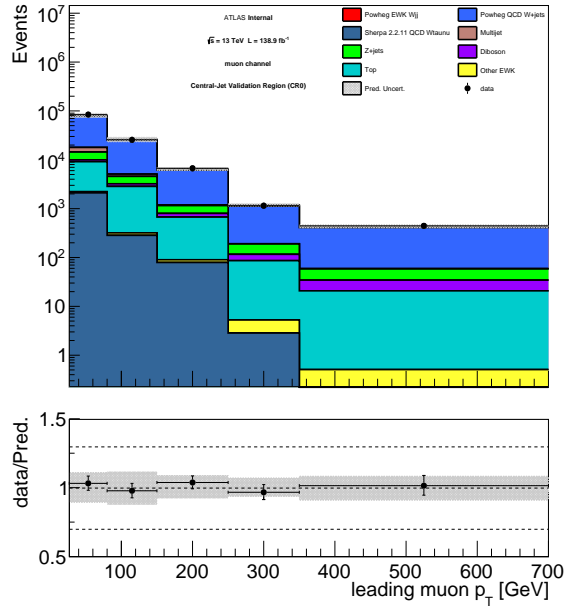
(d) CR0

Figure 6.32: Post-fit detector-level leading muon p_{T} distributions
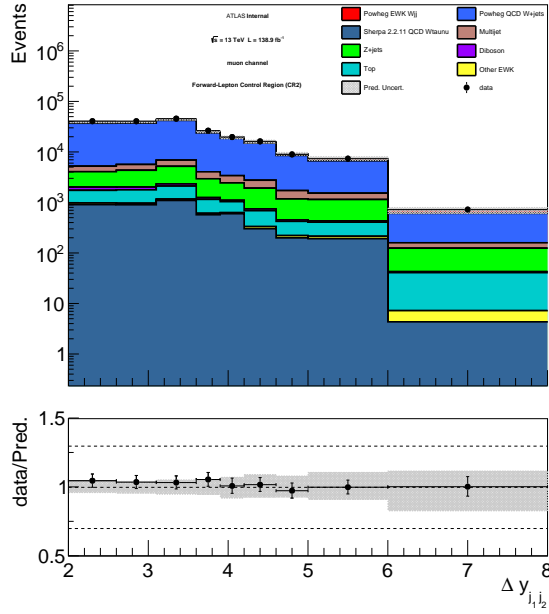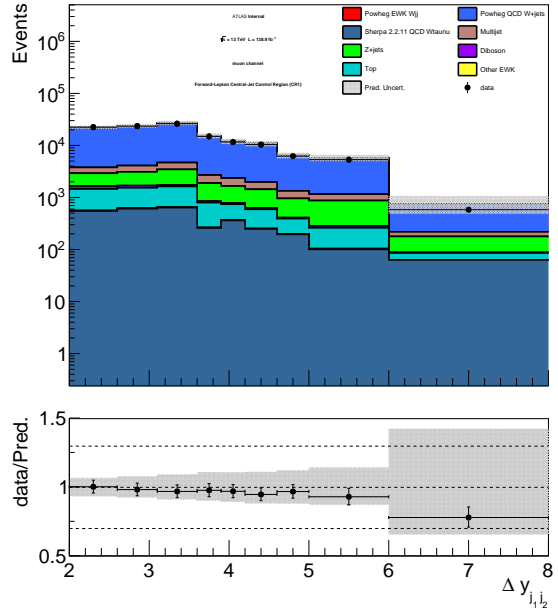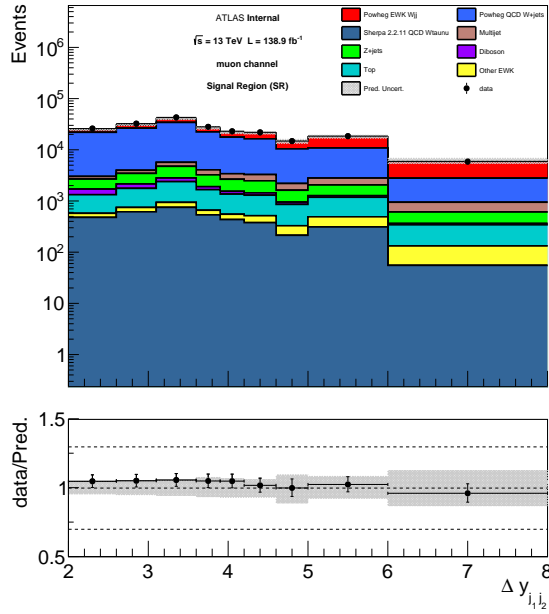
(a) CR2

(b) CR1

(c) SR
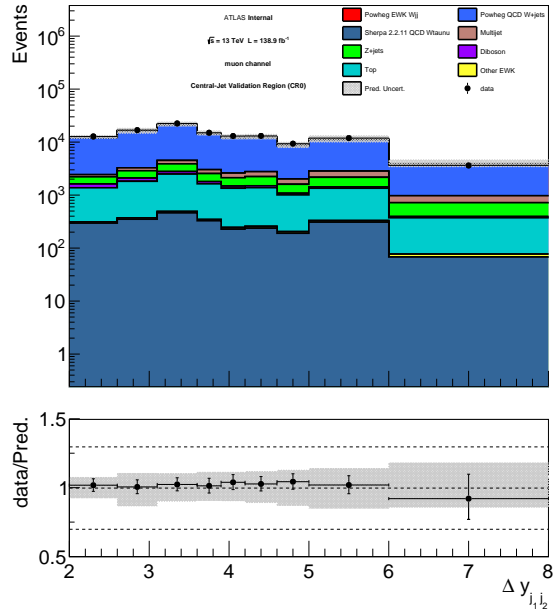
(d) CR0

Figure 6.33: Post-fit detector-level distributions of $|\Delta y|$ between the two highest p_{T} jets in the muon channel
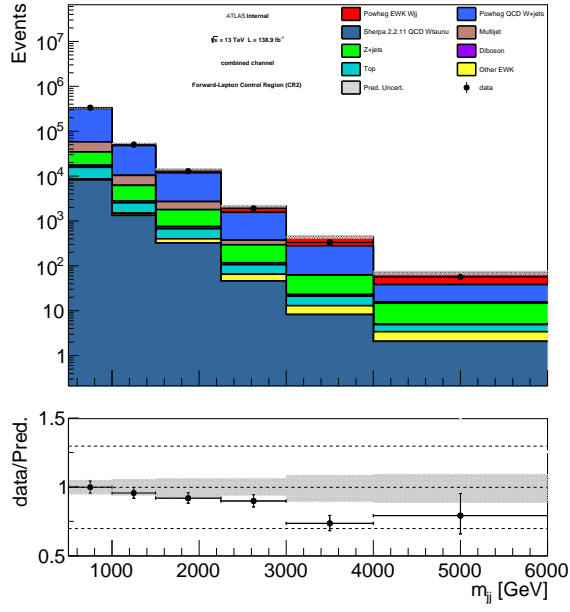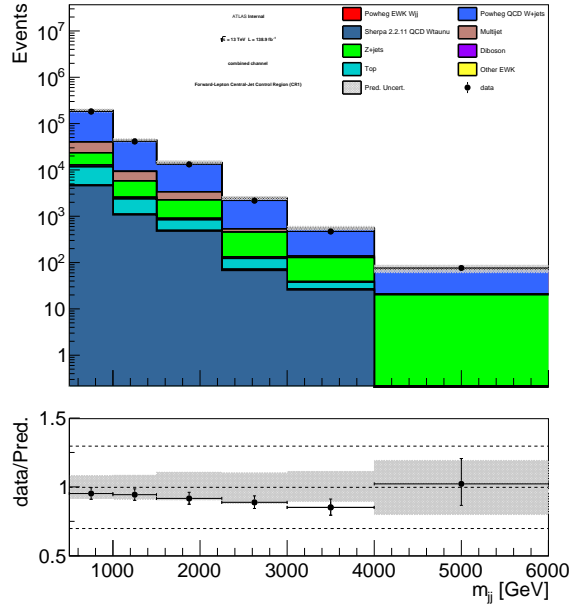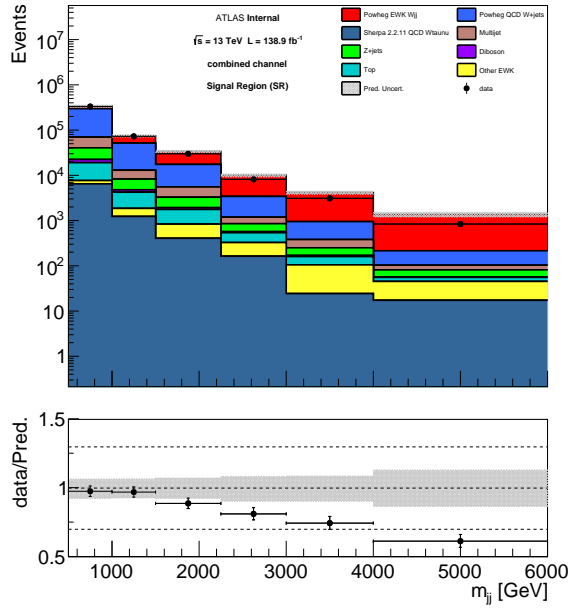
(a) CR2

(b) CR1

(c) SR
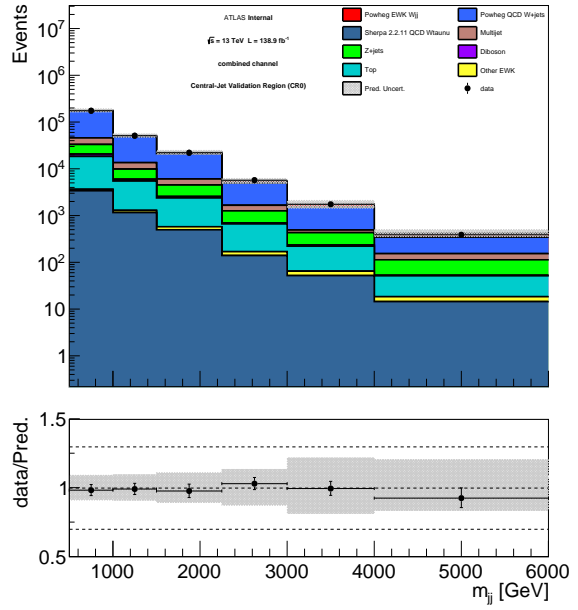
(d) CR0

Figure 6.34: Post-fit detector-level M_{jj} distributions in the combined $W \to \ell\nu$ channel
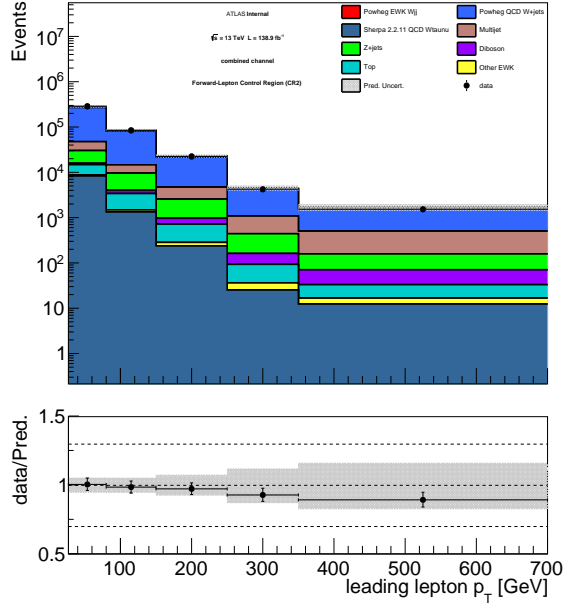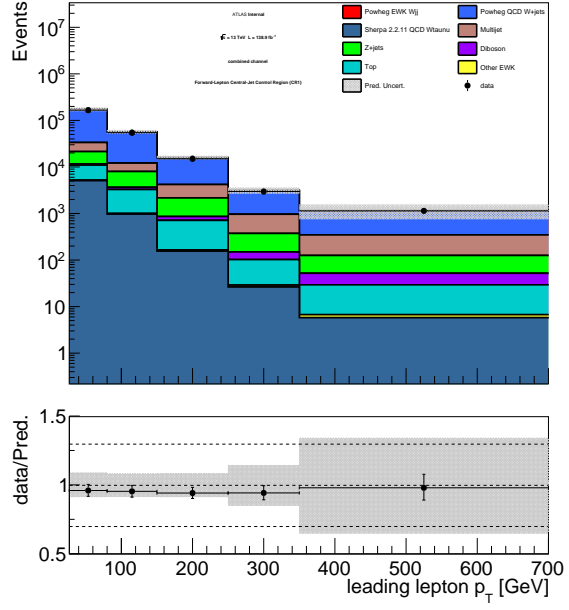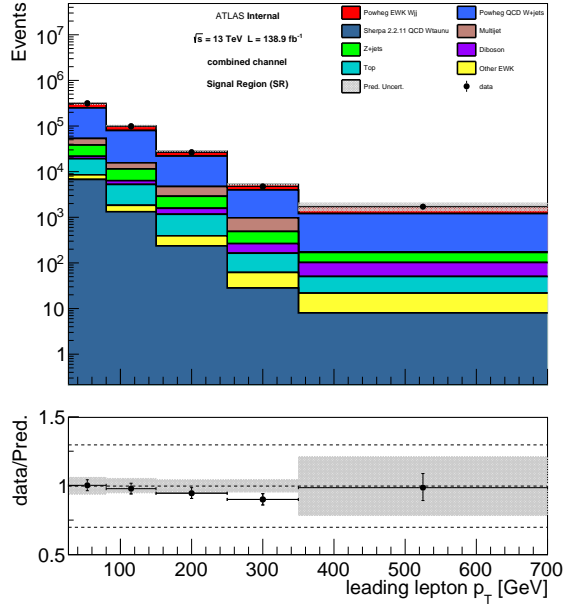
(a) CR2

(b) CR1

(c) SR
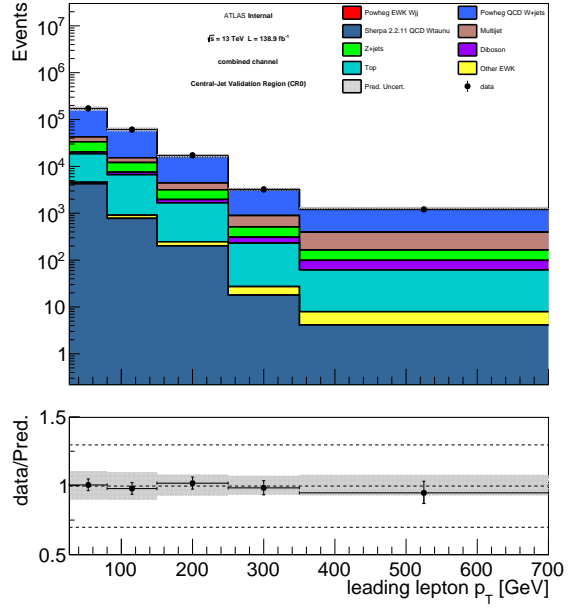
(d) CR0

Figure 6.35: Post-fit detector-level leading lepton p_{T} distributions in the combined $W \to \ell\nu$ channel.
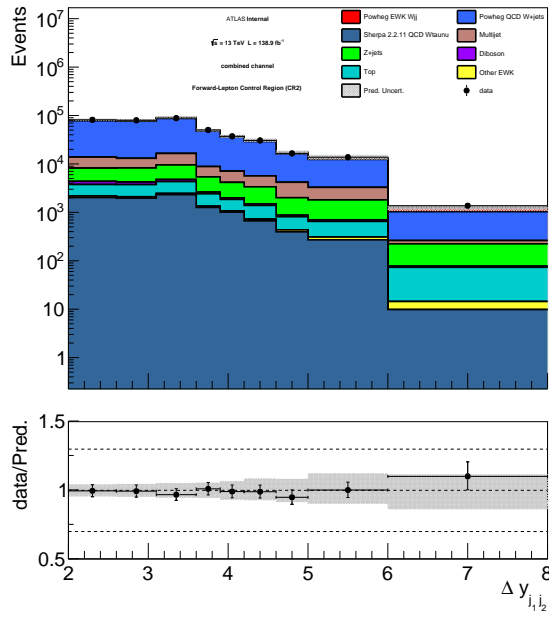
(a) CR2
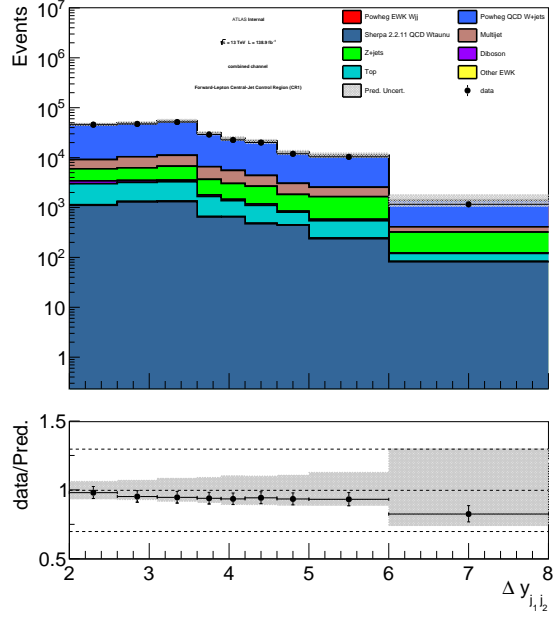
(b) CR1
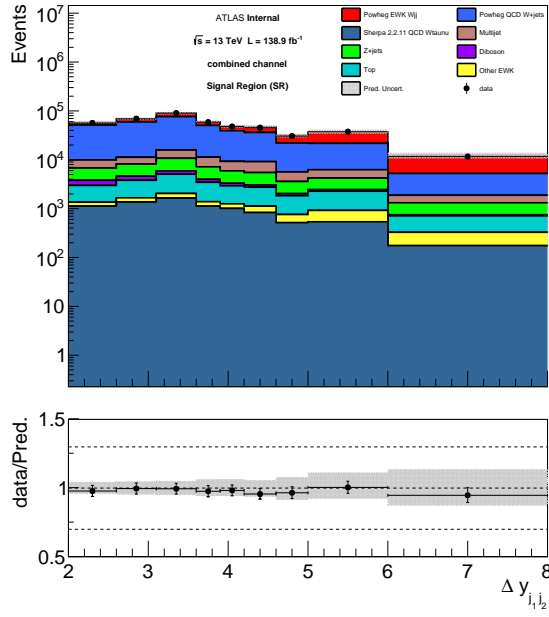
(c) SR
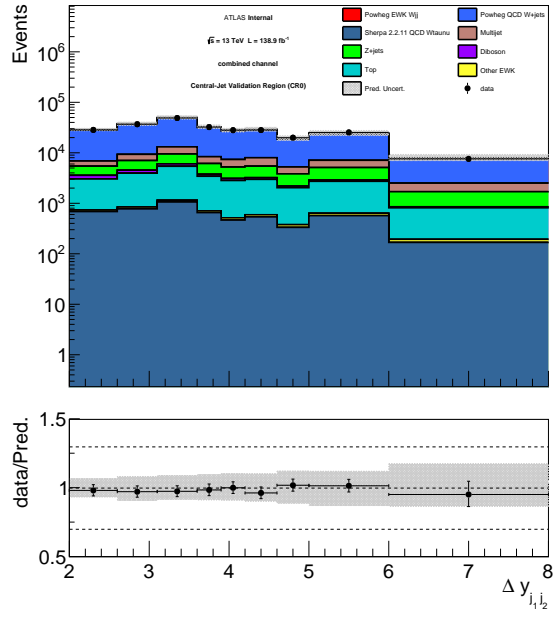
(d) CR0

Figure 6.36: Post-fit detector-level distributions of $|\Delta y|$ between the two highest p_{T} jets in the combined $W \to \ell\nu$ channel

6.5.4 Theory Uncertainties

For the EWK-W sample, the factorization and renormalization scale uncertainty is estimated by varying both scales, taking the envelope of prediction's deviation from $(\mu_R, \mu_F) = (1,1)$ in the case of the six combinations: $\mu_R \times \mu_F = \{0.5, 2\} \times \{0.5, 2\}$ in each parameter. This is the recommendation in [37]. This is included in the profile likelihood fit, and is given the name `SCALE_UNCERTAINTY` in the impact plots and tables.

The generator and PDF uncertainties on the EWK-W `Powheg+Pythia8` component are estimated by comparing the `Herwig7` prediction. The predicted event yields given by these two samples are found to be in agreement within $\mathcal{O}(7\%)$.

The QCD-W theory uncertainties are estimated by comparing the baseline `Powheg + Pythia8` to the `Madgraph FxFx`. The `Sherpa 2.2.11` samples are not included in this estimation due to known issues with `Sherpa 2` in this topology. The resulting cross-sections calculated using `Powheg` and `Madgraph FxFx` QCD-W are found to be in agreement. The post-fit impact of exchanging `Powheg` for `Madgraph FxFx` on the measured EWK-W cross-section is estimated by taking the difference in central values for the measured and predicted cross-sections. The effect on the central value of the measured cross-section is found to be $\mathcal{O}(9\%)$ in the combined channel, and the effect on the post-fit predicted cross-section is found to be $\mathcal{O}(12\%)$. These estimates, evaluated in the combined channel, are applied to the individual electron and muon channels as well and are quoted as theory uncertainties, abbreviated 'th.' in several places.

These types of two-point uncertainties are not profiled in the likelihood fit, and instead, added to the uncertainty on the cross-sections computed using the values in Table 6.9. Several improvements on the handling of these theory uncertainties are suggested in section 6.6

6.5.5 Detector and Analysis-Based Systematic Uncertainties

The uncertainties arising from detector effects and analysis choices along with their impact on pre-fit prediction and data are tabulated individually in Appendix D. The explanation of several sources of analysis-based systematic uncertainties are described in more detail below.

For the multijet estimate in the muon channel, the flat fit is used as the nominal estimate due to the simplicity and low multijet contribution. In the electron channel, the multi-bin estimate is used as the nominal, with the flat fit taken as a systematic variation, labeled: `MULTIJET_FlatFit`.

The choice of binning and fit range was also studied for the multijet fit. Covering the same range using half the number of bins, and separately, adjusting the fit range from 0-140 GeV to 0-100 GeV. This is taken as a symmetric systematic uncertainty, labeled: `MULTIJET_FitBinning`.

The tuning of the (anti)isolation requirements which define the multijet template are also accompanied by systematic uncertainty, labeled: `MULTIJET_LeptonIsolation`. This represents the variation in scanning several different ATLAS-recommended isolation working points, as well as several custom isolation definitions.

There is also choice in which observable to fit in order to determine the multijet normalization. Several choices were considered, and the envelope of the fit variables which appear to describe data well in the control regions is taken as the uncertainty estimate. This is tagged with the name: `MULTIJET_FitVariable`.

The impact of the choice of fitting the leading lepton p_{T} distribution is assessed by also considering fitting the Δy_{jj} distribution. This amounts to an 11% difference in the central values of the measured cross-section in the combined channel and is covered by the post-

fit statistical+systematic uncertainty. The M_{jj} distribution was also considered, but this fit suffers from large dependence on jet energy scale and also flavor tagging uncertainties, and several instabilities in the fit arise from this.

Finally, the uncertainties on the post fit yields are treated as uncorrelated in the calculation of the EWK-W cross-section. This is a choice made to more conservatively estimate the uncertainty on the cross-section and reduce the complexity and effects of the fitter correlating uncertainties across MC samples, which may have similar biases or assumptions not accurately estimated using the current generator and showering uncertainty estimates.

6.5.6 Fiducial Cross-Section

The fiducial cross-section in the signal region is calculated in two steps. First, the visible cross-section is calculated as in Equation 6.11, where N_{obs} is the number of data events minus the background prediction. The acceptance factor, C_{EWKW}, is then calculated to correct for the fraction of predicted EWK-W events at truth particle level which pass the reconstruction selection. Then the fiducial cross-section is extracted from the visible cross-section as given in Equation 6.12.

$$\sigma_{\mathrm{visible}}^{\mathrm{EWKW}} = \frac{N_{\mathrm{obs}}}{L} \tag{6.11}$$

$$\sigma_{\mathrm{fiducial}}^{\mathrm{EWKW}} = \frac{N_{\mathrm{obs}}}{C_{\mathrm{EWKW}} \cdot L} \tag{6.12}$$

$$C_{\mathrm{EWKW}} = \frac{N_{\mathrm{reco}}}{N_{\mathrm{truth}}} \tag{6.13}$$

The results of the cross-section measurements in the signal region are shown below in Table 6.10. These results are in good agreement with the Standard Model predictions. The predictions for the visible cross-sections ($\sigma_{\text{visible}}^{\text{EWKW}}$) in the electron, muon, and combined channels are $350 \pm 36(\text{stat+syst}) \pm 42(\text{th.})$ fb, $306 \pm 26(\text{stat+syst}) \pm 37(\text{th.})$ fb, and $671 \pm 45(\text{stat+syst}) \pm 81(\text{th})$ fb respectively.

	$\sigma_{\text{visible}}^{\text{EWKW}}$ [fb]	C_{EWKW}	$\sigma_{\text{fiducial}}^{\text{EWKW}}$ [fb]
Electron Channel	306 ± 85 (stat+syst) ± 28 (th.)	0.73	419 ± 116 (stat+syst) ± 38 (th.)
Muon Channel	368 ± 57 (stat+syst) ± 33 (th.)	0.67	549 ± 85 (stat+syst) ± 49 (th.)
Combined	655 ± 120 (stat+syst) ± 59 (th.)	0.70	936 ± 171 (stat+syst) ± 84 (th.)

Table 6.10: Fiducial cross-section of EWK-W production in the signal region

6.6 Discussion

The measured $\sigma_{\text{fiducial}}^{\text{EWKW}}$ values presented here are in agreement with the Standard Model predictions for each of the electron muon and combined channels. There is slight tension between the central values of the measured cross-sections in the electron and muon channels. This comes from the difference in post fit yield for the QCD-W component between the two channels, which in the muon channel appears to be coming from the gaussian constraint term in the fit model corresponding to the uncertainty on multijet estimate due to choice of fit variable. Also, a first estimate of the theory uncertainty is presented in the previous section, which can likely be improved. Suggestions for these improvements, and several avenues to increase the scope of this analysis are presented below.

To build upon the presented result, the fiducial cross-section can be used to place limits on the dimension-6 operators described in section 2.3 by generating EWK-W MC with

non-zero Wilson coefficients for these operators, using this modified EWK-W prediction to repeat the measurement of the fiducial cross-section, and analyzing the compatibility with data, either measuring discovery significance or placing limits on Wilson coefficients using the CL_s method [66]. This is not yet complete, and will be a welcome addition to improve the physical interpretation of the cross-section measurement presented in this chapter.

Another future improvement, is to measure the cross-section, differential in one or more kinematic observables. These distributions would then be unfolded – this procedure attempts to remove the effects of the ATLAS detector, transforming the measured distribution to the distribution at the particle level. The unfolded differential cross-section can be used to more powerfully constrain BSM physics by giving additional degrees of freedom to test the compatibility of the measured distributions at particle level with any non-zero Wilson coefficients in the EFT approach.

There are several areas where the estimation of uncertainties can be improved. First, the theory uncertainty can be more precisely quantified, and perhaps constrained, by preparing the PDF, and α_s in accordance with the recommendations in [37]. The PDF uncertainties are estimated using the prediction generated with 100 variations of the PDF eigenvectors, combined using the prescription outlined in [37]. Also, α_s should be varied in correlation with the PDF variations and the resulting uncertainty added in quadrature. In addition, performing the factorization and renormalization scale uncertainty estimation for larger background processes in addition to the signal is needed. Also, the effects due to showering are most likely underestimated in the current form of this analysis. This can be improved by producing a `Powheg` QCD-W sample with alternative showering scheme (such as `Herwig`). The showering uncertainty can be factorized from the uncertainty on

the matrix element generation.

In addition, the uncertainty due to the jet energy resolution can be more accurately estimated using the simplest technique. This is MC-only smearing, where the variations are symmetrized by reflecting $\frac{|\sigma_{\mathrm{up}} - \sigma_{\mathrm{down}}|}{2}$ about the nominal prediction. This changes the correlation structure of the jet energy resolution uncertainties. A more precise method involves smearing the jet energy resolution effects in both pseudo-data and MC in order to more accurately constrain this effect on the data versus the MC.

The multijet estimate, in general, is also an area which has room for improvement. Each choice involved in the methodology requires an analysis of the associated uncertainty, and there are several of these choices: choice of lepton isolation bounds, choice of fit variable, etc. A good way to reduce the impact of these systematic uncertainties is to extract the EWK-W signal in a region with very little multijet contribution, such as requiring $M_{jj} > 1$ TeV or further tuning of lepton isolation requirements. The slight tension between cross-sections measured in the electron and muon channels likely arises from the multijet estimate. The goodness of fit test using the saturated model approach results in a lower p-value in the muon channel compared to the electron and combined channels. This is interpreted as the fit model in the muon channel lacking expressiveness. Referencing the nuisance parameter pull plot in Figure C.1, a good starting place to improve the fit model in th muon channel would be to reassess the multijet estimate and its systematic uncertainties. When profiting from the correlations in the combined channel, this effect becomes less impactful.

Chapter 7

Conclusion

This document has detailed the development of the ATLAS gFEX calorimeter trigger system and also a measurement of electroweak W production cross-section in association with jets in proton-proton collision data at $\sqrt{s} = 13$ TeV using 139 fb^{-1} collected by the ATLAS detector. A fiducial cross-section in the combined $W \to \ell\nu$ channel of $\sigma_{\text{fiducial}}^{\text{EWKW}} = 936 \pm 171(\text{stat} + \text{syst}) \pm 84(\text{th.})$ fb is measured using a cut-based analysis and fit to leading lepton momentum. This measurement is in good agreement with the Standard Model prediction of $959 \pm 64(\text{stat} + \text{syst}) \pm 116(\text{th.})$ fb, though the absence of a rigorous assessment of the parton showering theory uncertainties leaves this component of the uncertainty likely under constrained. Several different configurations and associated uncertainties on the data driven template-fit estimate of the QCD multijet fake lepton background were detailed, as well as analysis of the signal extraction fit. Improvements on this analysis were identified, and future outlook considered.

Also described herein, is the installation and commissioning of the ATLAS L1Calo gFEX system and development of software tools for system operation. The system is functional inside the ATLAS detector environment with control and monitoring software functioning well, with the jet trigger items enabled. The $E_{\text{T}}^{\text{miss}}$ triggers have undergone validation in the production system and will soon be activated as well.

Prospects for both the physics reach of the gFEX system and the further measurement of the EWK-W processes at the LHC are bright. Perhaps there is even some synergy between the two efforts, given that the gFEX has an insight into the level 1 transverse

energy depositions that could be used to form a dedicated EWK-W trigger. As the LHC pushes to slightly higher energy and much higher luminosity, resolving the decay products of energetic bosons, especially $W^\pm$, will only become more challenging, and so the gFEX will become another tool to probe these interesting electroweak phenomena.

The full nature of the spacetime symmetries manifest in our universe remains to be seen. High energy proton collisions at the LHC are one of the best places to look for hints of new physics. And as every new collision rolls in, at 40 million times per second, I'm even more excited to see what shows up.

References

[1] U. Baur and D. Zeppenfeld. Measuring three vector boson couplings in q q —> q q W at the SSC. In *Workshop on Physics at Current Accelerators and the Supercollider*, 9 1993.

[2] M Begel, D W Miller, and G Stark. Turn-on curves and pile-up subtraction for global feature extraction (gFEX) jet trigger for the Phase I Upgrade. Technical report, CERN, Geneva, 2014. `https://cds.cern.ch/record/1749167`.

[3] Daniele Bertolini, Tucker Chan, and Jesse Thaler. Jet Observables Without Jet Algorithms. *JHEP*, 04:013, 2014.

[4] Carsten Burgard and David Galbraith. Standard model diagram. `https://texample.net/tikz/examples/model-physics/`.

[5] Matteo Cacciari, Gavin P. Salam, and Gregory Soyez. The anti-k_t jet clustering algorithm. *JHEP*, 04:063, 2008.

[6] John M. Campbell, R. Keith Ellis, Paolo Nason, and Giulia Zanderighi. W and Z Bosons in Association with Two Jets Using the POWHEG Method. *JHEP*, 08:005, 2013.

[7] LHCb Collaboration. Test of lepton universality in beauty-quark decays. *Nature Physics*, 18(3):277–282, mar 2022.

[8] The ATLAS Collaboration. *ATLAS liquid-argon calorimeter: Technical Design Report*. Technical design report. ATLAS. CERN, Geneva, 1996.

[9] The ATLAS Collaboration. *ATLAS tile calorimeter: Technical Design Report*. Technical design report. ATLAS. CERN, Geneva, 1996.

[10] The ATLAS Collaboration. *ATLAS inner detector: Technical Design Report, 1*. Technical design report. ATLAS. CERN, Geneva, 1997.

[11] The ATLAS Collaboration. The ATLAS experiment at the CERN large hadron collider. *Journal of Instrumentation*, 3(08):S08003–S08003, aug 2008.

[12] The ATLAS Collaboration. Technical Design Report for the Phase-I Upgrade of the ATLAS TDAQ System. Technical report, CERN, 2013. Final version presented to December 2013 LHCC.

[13] The ATLAS Collaboration. Measurement of the electroweak production of dijets in association with a z-boson and distributions sensitive to vector boson fusion in proton-proton collisions at $\sqrt{s} = 8$ tev using the atlas detector. *Journal of High Energy Physics*, 2014(4), apr 2014.

[14] The ATLAS Collaboration. ATLAS simulation of boson plus jets processes in Run 2. Technical report, CERN, Geneva, 2017.

[15] The ATLAS Collaboration. Measurement of the cross-section for electroweak production of dijets in association with a z boson in pp collisions at $\sqrt{s} = 13$ tev with the atlas detector. *Physics Letters B*, 775:206–228, December 2017.

[16] The ATLAS Collaboration. Measurements of electroweak wjj production and constraints on anomalous gauge couplings with the atlas detector. *The European Physical Journal C*, 77(474), 2017.

[17] The ATLAS Collaboration. Standard Model Summary Plots February 2022. Technical report, CERN, Geneva, 2022. `https://atlas.web.cern.ch/Atlas/GROUPS/PHYSICS/PUBNOTES/ATL-PHYS-PUB-2022-009`.

[18] The ATLAS Collaboration. Atlas metadata interface, 2023. `https://ami.in2p3.fr`.

[19] Robert D. Cousins. Generalization of chisquare goodness-of-fit test for binned data using saturated models, with application to histograms. Technical report, UCLA, 2013. `https://www.physics.ucla.edu/~cousins/stats/cousins_saturated.pdf`.

[20] Glen Cowan, Kyle Cranmer, Eilam Gross, and Ofer Vitells. Asymptotic formulae for likelihood-based tests of new physics. *Eur. Phys. J. C*, 71:1554, 2011. [Erratum: Eur.Phys.J.C 73, 2501 (2013)].

[21] Tomas Dado, Alexander Held, and Michele Pinamonti. Top-related experiment (TREx) fitter, 2023. `https://trexfitter-docs.web.cern.ch/trexfitter-docs/`.

[22] Aaboud et al. Jet reconstruction and performance using particle flow with the ATLAS Detector. *Eur. Phys. J. C*, 77(7):466, 2017.

[23] Aaboud et al. Object-based missing transverse momentum significance in the ATLAS detector. Technical report, CERN, Geneva, 2018.

[24] Aaboud et al. Performance of missing transverse momentum reconstruction with the ATLAS detector using proton-proton collisions at $\sqrt{s} = 13$ TeV. *Eur. Phys. J. C*, 78(11):903, 2018.

[25] Aaboud et al. Electron reconstruction and identification in the ATLAS experiment

using the 2015 and 2016 LHC proton-proton collision data at $\sqrt{s} = 13$ TeV. *Eur. Phys. J. C*, 79(8):639, 2019.

[26] Aad et al. Electron and photon performance measurements with the ATLAS detector using the 2015–2017 LHC proton-proton collision data. *JINST*, 14(12):P12006, 2019.

[27] Aad et al. Differential cross-section measurements for the electroweak production of dijets in association with a Z boson in proton–proton collisions at ATLAS. *Eur. Phys. J. C*, 81(2):163, 2021.

[28] Aad et al. Jet energy scale and resolution measured in proton–proton collisions at $\sqrt{s} = 13$ TeV with the ATLAS detector. *Eur. Phys. J. C*, 81(8):689, 2021.

[29] Aad et al. Muon reconstruction and identification efficiency in ATLAS using the full Run 2 pp collision data set at $\sqrt{s} = 13$ TeV. *Eur. Phys. J. C*, 81(7):578, 2021.

[30] Aad et al. ATLAS LAr Calorimeter trigger electronics phase I upgrade: LATOME Firmware Specification. Technical report, CERN, Geneva, 2022.

[31] Adams et al. Recommendations of the Physics Objects and Analysis Harmonisation Study Groups 2014. Technical report, CERN, Geneva, 2014.

[32] Aleksa et al. ATLAS Liquid Argon Calorimeter Phase-I Upgrade: Technical Design Report. Technical report, CERN, 2013. Final version presented to December 2013 LHCC.

[33] Begel et al. Global Feature Extractor of the Level-1 Calorimeter Trigger: AT-LAS TDAQ Phase-I Upgrade gFEX Final Design Report. Technical report, CERN, Geneva, 2016.

[34] Bierwagen et al. Level-1 Topological Processor (L1Topo) ATLAS TDAQ Phase-I Upgrade - Hardware Specifications. Technical report, CERN, Geneva, 2019.

[35] Bothmann et al. Event Generation with Sherpa 2.2. *SciPost Phys.*, 7(3):034, 2019.

[36] Bruce et al. Reaching record-low β^* at the cern large hadron collider using a novel scheme of collimator settings and optics. *Nuclear Instruments and Methods in Physics Research Section A: Accelerators, Spectrometers, Detectors and Associated Equipment*, 848:2, 12 2016.

[37] Butterworth et al. PDF4LHC recommendations for LHC Run II. *J. Phys. G*, 43:023001, 2016.

[38] Hayden et al. Fibre Optic Exchange (FOX) design and production. Technical report, CERN, Geneva, 2017.

[39] Khachatryan et al. Differential Cross Section Measurements for the Production of a W Boson in Association with Jets in Proton–Proton Collisions at $\sqrt{s} = 7$ TeV. *Phys. Lett. B*, 741:12–37, 2015.

[40] Khachatryan et al. Measurement of electroweak production of two jets in association with a Z boson in proton-proton collisions at $\sqrt{s} = 8$ TeV. *Eur. Phys. J. C*, 75(2):66, 2015.

[41] Khachatryan et al. Measurement of electroweak production of a W boson and two forward jets in proton-proton collisions at $\sqrt{s} = 8$ TeV. *JHEP*, 11:147, 2016.

[42] Mendez et al. CERN-IPMC solution for AdvancedTCA blades. *PoS*, TWEPP-17:053, 2018.

[43] Oliver Sim Brüning et al. *LHC Design Report*. CERN Yellow Reports: Monographs. CERN, Geneva, 2004.

[44] Sirunyan et al. Electroweak production of two jets in association with a Z boson in proton–proton collisions at $\sqrt{s} = 13$ TeV. *Eur. Phys. J. C*, 78(7):589, 2018.

[45] Sirunyan et al. Measurement of electroweak production of a W boson in association with two jets in proton–proton collisions at $\sqrt{s} = 13$ TeV. *Eur. Phys. J. C*, 80(1):43, 2020.

[46] Muon $g - 2$ Collaboration. Measurement of the positive muon anomalous magnetic moment to 0.46 ppm. *Phys. Rev. Lett.*, 126:141801, Apr 2021.

[47] ATLAS FELIX Group. FELIX User Manual. Technical report, CERN, Geneva, 2020.

[48] B. Grzadkowski, M. Iskrzyński, M. Misiak, and J. Rosiek. Dimension-six terms in the standard model lagrangian. *Journal of High Energy Physics*, 2010(10), oct 2010.

[49] KIP Heidelberg. ATLAS LAr Calorimeter trigger electronics phase I upgrade: LATOME Firmware Specification. Technical report, KIP Heidelberg, 2020.

[50] Serguei Kolos, Gordon Crone, and William P. Vazquez. New software-based readout driver for the atlas experiment. *IEEE Transactions on Nuclear Science*, 68(8):1811–1817, 2021.

[51] Sascha Mehlhase. ATLAS detector slice (and particle visualisations). `https://cds.cern.ch/record/2770815`, 2021.

[52] Esma Mobs. The CERN accelerator complex in 2019. Complexe des accélérateurs du CERN en 2019. `https://cds.cern.ch/record/2684277`, 2019.

[53] Paolo Nason and Carlo Oleari. Generation cuts and Born suppression in POWHEG. `https://arxiv.org/abs/1303.3922v1`, 2013.

[54] E. Noether. Invariante variationsprobleme. *Nachrichten von der Gesellschaft der Wissenschaften zu Göttingen, Mathematisch-Physikalische Klasse*, 1918:235–257, 1918.

[55] Carlo Oleari and Dieter Zeppenfeld. QCD corrections to electroweak nu(l) j j and l+ l- j j production. *Phys. Rev. D*, 69:093004, 2004.

[56] Abraham Pais. *Inward Bound.* Oxford University Press, 1986.

[57] Joao Pequenao. Computer Generated image of the ATLAS calorimeter. `https://cds.cern.ch/record/1095927`, 2008.

[58] Joao Pequenao. Computer generated image of the ATLAS inner detector. `https://cds.cern.ch/record/1095926`, 2008.

[59] Joao Pequenao. Computer generated image of the ATLAS Muons subsystem. `https://cds.cern.ch/record/1095929`, 2008.

[60] Joao Pequenao. Computer generated image of the whole ATLAS detector. `https://cds.cern.ch/record/1095924`, 2008.

[61] Michael E. Peskin and Daniel V. Schroeder. *An Introduction to Quantum Field Theory.* Westview Press, 1995.

[62] Antonio Pich. The Standard Model of Electroweak Interactions; rev. version. *CERN - CLAF School of High-Energy Physics*, 2008.

[63] Weiming Qian. Electromagnetic Feature Extractor (eFEX) ATLAS TDAQ Phase-I Upgrade Final Design Report. Technical report, CERN, Geneva, 2017.

[64] Qian, Weiming and Gonnella, Francesco and Brawn, Ian. Technical Specification - ATLAS Level-1 Calorimeter Trigger Upgrade - Electromagnetic Feature Extractor (eFEX). Technical report, CERN, 2021.

[65] Giorgia Rauco. Distinguishing quark and gluon jets at the LHC. In *Parton radiation and fragmentation from LHC to FCC-ee*, pages 73–78, 2 2017.

[66] Alexander L. Read. Presentation of search results: The CL_s technique. *J. Phys. G*, 28:2693–2704, 2002.

[67] Franziska Schissler and Dieter Zeppenfeld. Parton Shower Effects on W and Z Production via Vector Boson Fusion at NLO QCD. *JHEP*, 04:057, 2013.

[68] Mark Srednicki. *Quantum Field Theory*. University of California, Santa Barbara, 2006.

[69] R. L. Workman and Others. Review of Particle Physics. *PTEP*, 2022:083C01, 2022.

Appendix A

FEX Calorimeter Input Data Formats

W #	31	30	29	28	27	26	25	24	23	22	21	20	19	18	17	16	15	14	13	12	11	10	9	8	7	6	5	4	3	2	1	0
0	BCID[4:3]		DATA1[9:0]										DATA0[9:0]										BCID[6:5]		K28.5							
1	DATA19[9:8]		DATA4[9:0]										DATA3[9:0]										DATA2[9:0]									
2	DATA19[7:6]		DATA7[9:0]										DATA6[9:0]										DATA5[9:0]									
3	DATA19[5:4]		DATA10[9:0]										DATA9[9:0]										DATA8[9:0]									
4	DATA19[3:2]		DATA13[9:0]										DATA12[9:0]										DATA11[9:0]									
5	DATA19[1:0]		DATA16[9:0]										DATA15[9:0]										DATA14[9:0]									
6	CRC[8:0]									BCID[2:0]			DATA18[9:0]										DATA17[9:0]									

(a) LATOME data format

W #	31	30	29	28	27	26	25	24	23	22	21	20	19	18	17	16	15	14	13	12	11	10	9	8	7	6	5	4	3	2	1	0
0	LATOME_ID[7:0]								FEX_ID[1:0]		FIBER_ID[5:0]						K28.0								K28.5							
1	LATOME_SRC_ID[31:0]																															
2																																
3																																
4																																
5																																
6	CRC[8:0]																	BCID[11:0]														

(b) LATOME alignment data format

W #	b 31	b 30	b 29	b 28	b 27	b 26	b 25	b 24	b 23	b 22	b 21	b 20	b 19	b 18	b 17	b 16	b 15	b 14	b 13	b 12	b 11	b 10	b 9	b 8	b 7	b 6	b 5	b 4	b 3	b 2	b 1	b 0
0	BC [4:3]		DATA1 [9:0]										DATA0 [9:0]										BC [6:5]		K28.5							
1			DATA4 [9:0]										DATA3 [9:0]										DATA2 [9:0]									
2			DATA7 [9:0]										DATA6 [9:0]										DATA5 [9:0]									
3			DATA10 [9:0]										DATA9 [9:0]										DATA8 [9:0]									
4			DATA13 [9:0]										DATA12 [9:0]										DATA11 [9:0]									
5													DATA15 [9:0]										DATA14 [9:0]									
6	CRC								BCID [2:0]										BCID [11:0]													

(c) TREX data format

W #	b 31	b 30	b 29	b 28	b 27	b 26	b 25	b 24	b 23	b 22	b 21	b 20	b 19	b 18	b 17	b 16	b 15	b 14	b 13	b 12	b 11	b 10	b 9	b 8	b 7	b 6	b 5	b 4	b 3	b 2	b 1	b 0
0	TREX_ID [7:0]								FEX_ID [1:0]		FIBER_ID [5:0]						K28.0								K28.5							
1	TREX_SRC_ID [31:0]																															
2																																
3																																
4																																
5																																
6	CRC																		BCID [11:0]													

(d) TREX alignment data format

Figure A.1: Calorimeter input data formats for eFEX

174

(a) LATOME data format

Bit header: W # | 31 30 29 28 27 26 25 24 | 23 22 21 20 19 18 17 16 | 15 14 13 12 11 10 9 8 | 7 6 5 4 3 2 1 0

W #	bits 31–24	bits 23–12	bits 11–0
0	DATA2[7:0]	DATA1[11:0]	DATA0[11:0]
1	DATA5[11:8] / DATA2[11:8]	DATA4[11:0]	DATA3[11:0]
2	DATA5[7:0]	DATA7[11:0]	DATA6[11:0]
3	DATA10[7:0]	DATA9[11:0]	DATA8[11:0]
4	DATA13[11:8] / DATA10[11:8]	DATA12[11:0]	DATA11[11:0]
5	DATA13[7:0]	DATA15[11:0]	DATA14[11:0]
6	CRC[8:0]	BCID[6:0]	SATUR[15:8]	SATUR[7:0] / K28.5

(b) LATOME alignment data format

W #	bits 31–24	bits 23–22	bits 21–16	bits 11–0
0	LATOME_ID[7:0]	FEX_ID[1:0]	FIBER_ID[5:0]	BCID[11:0]
1	LATOME_SRC_ID[31:0]			
2				
3				
4				
5				
6	CRC[8:0]	BCID[6:0]	K28.0	K28.5

(c) TREX data format

Bit header: W # | b31 b30 b29 b28 b27 b26 b25 b24 | b23 b22 b21 b20 b19 b18 b17 b16 | b15 b14 b13 b12 b11 b10 b9 b8 | b7 b6 b5 b4 b3 b2 b1 b0

W #	bits 31–24	bits 23–12	bits 11–0
0	DATA2 [7:0]	DATA1 [11:0]	DATA0 [11:0]
1	DATA5 [11:8] / DATA2 [11:8]	DATA4 [11:0]	DATA3 [11:0]
2	DATA5 [7:0]	DATA7 [11:0]	DATA6 [11:0]
3	DATA10 [7:0]	DATA9 [11:0]	DATA8 [11:0]
4	DATA13 [11:8] / DATA10 [11:8]	DATA12 [11:0]	DATA11 [11:0]
5	DATA13 [7:0]	DATA15 [11:0]	DATA14 [11:0]
6	CRC	BCID_LOW [6:0]	BCID_HIGH [11:7]	K28.5

(d) TREX alignment data format

W #	bits 31–24	bits 23–22	bits 21–16	bits 11–0
0	TREX_ID [7:0]	FEX_ID [1:0]	FIBER_ID [5:0]	BCID [11:0]
1	TREX_SRC_ID [31:0]			
2				
3				
4				
5				
6	CRC	BCID_LOW [6:0]	K28.0	K28.5

Figure A.2: Calorimeter input data formats for jFEX

(a) LATOME EMB/EMEC data format

W #	31	30	29	28	27	26	25	24	23	22	21	20	19	18	17	16	15	14	13	12	11	10	9	8	7	6	5	4	3	2	1	0
0	POS1[3:0]				DATA1[11:0]												POS0[3:0]				DATA0[11:0]											
1																																
2	POS3[3:0]				DATA3[11:0]												POS2[3:0]				DATA2[11:0]											
3																	POS4[3:0]				DATA4[11:0]											
4	POS6[3:0]				DATA6[11:0]												POS5[3:0]				DATA5[11:0]											
5																	POS7[3:0]				DATA7[11:0]											
6	CRC[8:0]									BCID[6:0]							SATUR[7:0]								K28.5							

(a) LATOME EMB/EMEC data format

(b) LATOME EMEC/HEC and FCAL data format

W #	31	30	29	28	27	26	25	24	23	22	21	20	19	18	17	16	15	14	13	12	11	10	9	8	7	6	5	4	3	2	1	0
0	DATA2[7:0]								DATA1[11:0]												DATA0[11:0]											
1	DATA5[3:0]				DATA4[11:0]								DATA3[11:0]												DATA2[11:8]							
2	DATA7[11:0]												DATA6[11:0]								DATA5[11:4]											
3	DATA10[7:0]								DATA9[11:0]												DATA8[11:0]											
4	DATA13[3:0]				DATA12[11:0]								DATA11[11:0]												DATA10[11:8]							
5	DATA15[11:0]												DATA14[11:0]								DATA13[11:4]											
6	CRC[8:0]									BCID[6:0]							SATUR[15:8] OR SATUR[7:0]								K28.5							

(b) LATOME EMEC/HEC and FCAL data format

(c) TREX data format

W #	b31	b30	b29	b28	b27	b26	b25	b24	b23	b22	b21	b20	b19	b18	b17	b16	b15	b14	b13	b12	b11	b10	b9	b8	b7	b6	b5	b4	b3	b2	b1	b0
0	DATA2 [7:0]								DATA1 [11:0]												DATA0 [11:0]											
1	DATA5 [3:0]				DATA4 [11:0]								DATA3 [11:0]												DATA2 [11:8]							
2	DATA7 [11:0]												DATA6 [11:0]								DATA5 [11:4]											
3	DATA10 [7:0]								DATA9 [11:0]												DATA8 [11:0]											
4	DATA13 [3:0]				DATA12 [11:0]								DATA11 [11:0]												DATA10 [11:8]							
5	DATA15 [11:0]												DATA14 [11:0]								DATA13 [11:4]											
6	CRC								BCID_LOW [6:0]								BCID_HIGH [11:7]								K28.5							

(c) TREX data format

Figure A.3: Calorimeter input data formats for gFEX. The alignment data frame format for gFEX is the same as that which is used for jFEX, pictured above.

Appendix B

gFEX Naming and Labeling Conventions
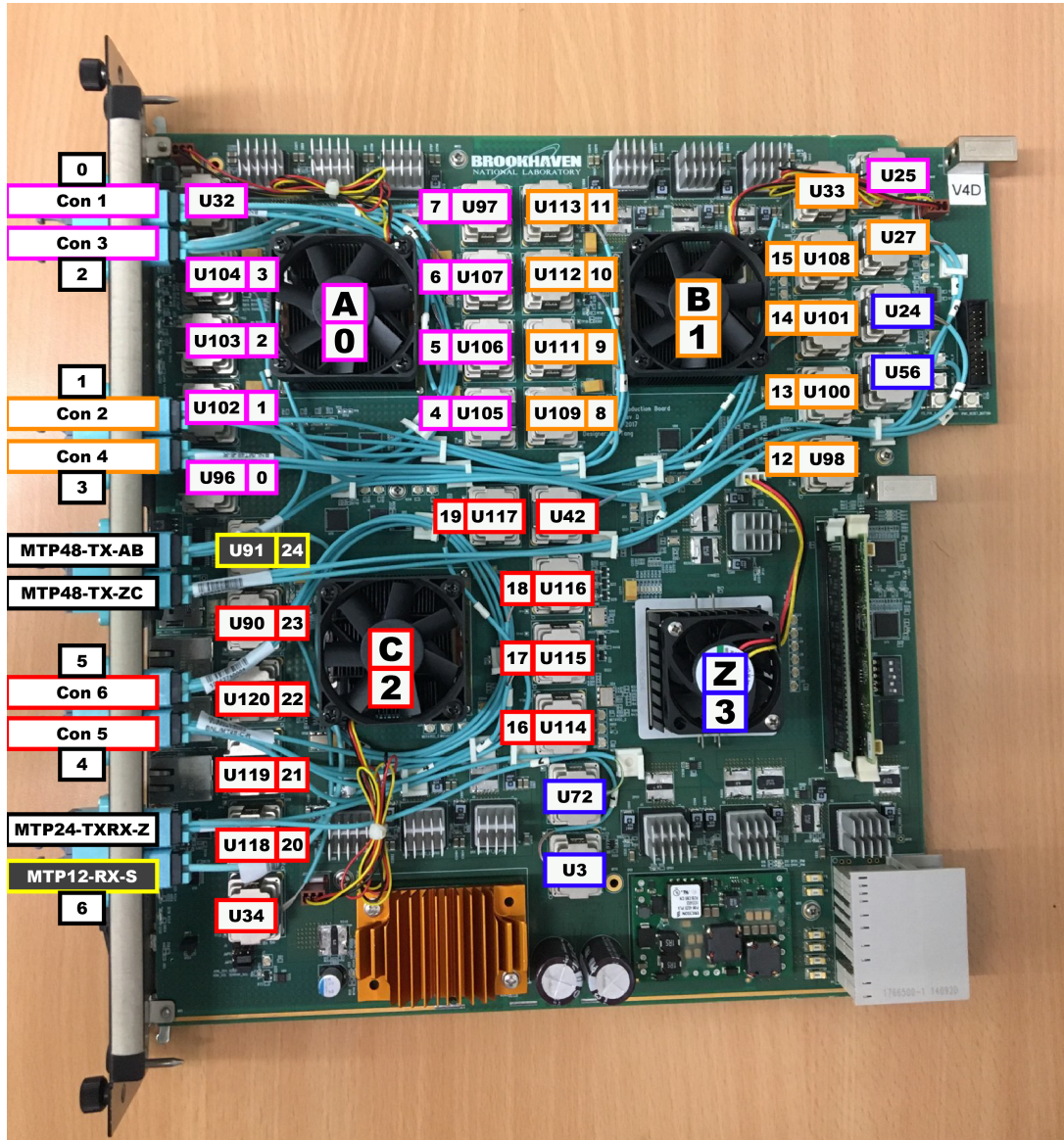
Figure B.1: Different naming and numbering schemes in the gFEX online software and documentation super-imposed on the physical board
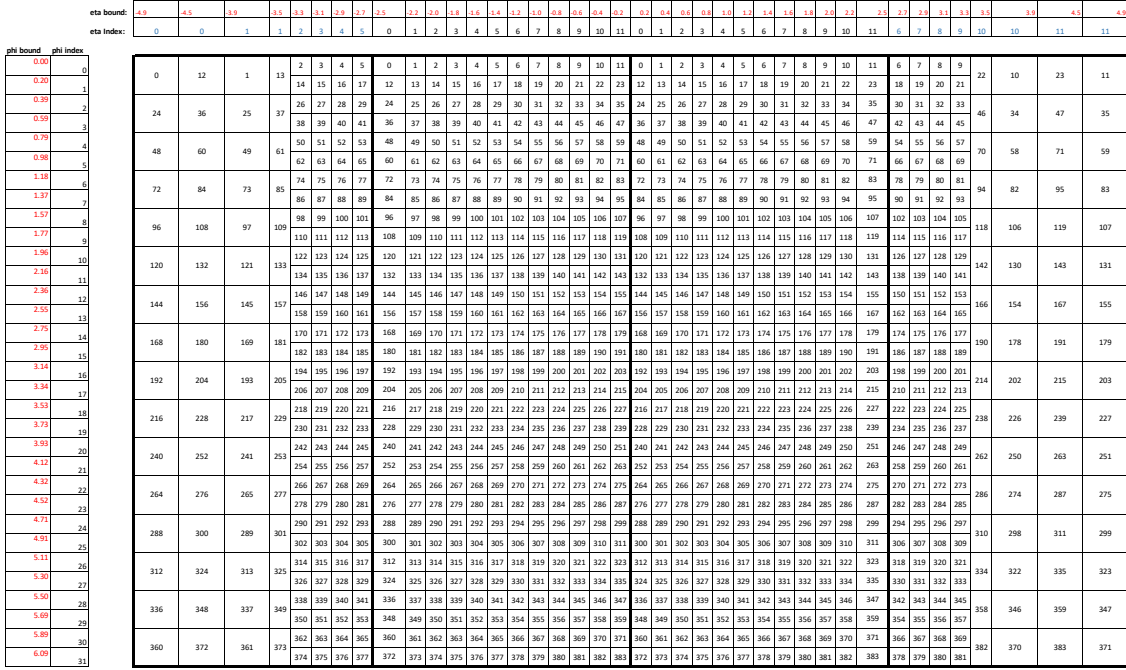
Figure B.2: gTower numbers within each processor FPGA

eta, phi index per tower:

Figure B.3: gTower (η, ϕ) bin indices within each processor FPGA

Figure B.4: Special gTower indices within each processor FPGA corresponding to the extended gTowers near $|\eta| \in [2.4, 2.5]$ and the overlap region near $|\eta| \sim 1.6$ where the liquid argon hadronic end-cap overlaps with the Tile calorimeter
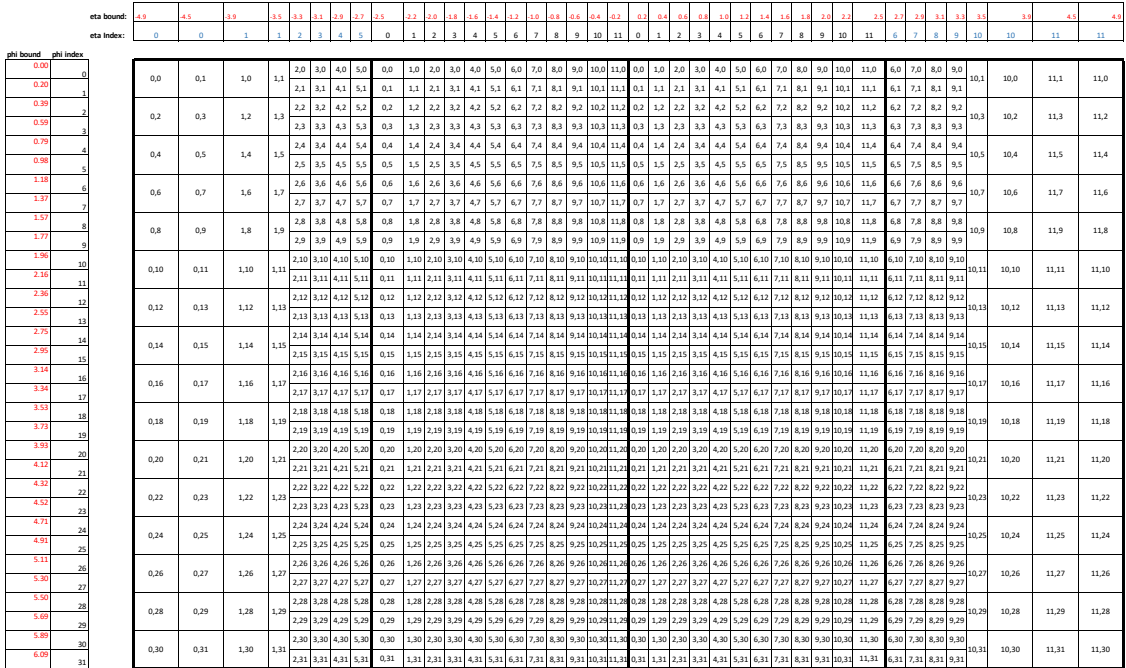
Appendix C

Binned Profile Likelihood Fit

C.1 Overview

The likelihood is generally defined as the probability of a model, given data. In the context of the analysis presented in chapter 6, the likelihood is Poisson distributed signal and background predictions in relation to measured data. In addition to the prediction and data, there are systematic uncertainties that arise from imperfect detector performance, theory, and other analysis considerations. These systematic uncertainties are considered "nuisance parameters" (NPs) which impact the determination of parameters of interest (POI), such as signal strength μ, in the profile likelihood fit. The `TRExFitter` software tool is used to carry out the binned profile likelihood fitting for this analysis [21].

C.1.1 The Likelihood Function

The likelihood function is constructed as shown in Equation C.1. It is a function of the measured values ($\vec{n}$), given the POI ($\vec{\mu}$) and nuisance parameters ($\vec{\theta}$). The $\nu_i(\vec{\mu}, \vec{\theta})$ is the total prediction in the ith bin, and the jth $c_j(\theta_j^0|\theta_j)$ are gaussian constraint terms introduced into the likelihood, which penalize the likelihood value in the event that a nuisance parameter takes on a value too far from the nominal value of θ_j^0.

$$L(\vec{n}|\vec{\mu}, \vec{\theta}) = \prod_{i \in bins} P(n_i|\nu_i(\vec{\mu}, \vec{\theta})) \times \prod_{j \in syst} c_j(\theta_j^0|\theta_j) \qquad (C.1)$$

The fit is performed by minimizing the negative log-likelihood, the expression for which

is given in Equation C.2. The $L(\vec{n}|\vec{\mu}, \vec{\theta}'')$ term is the maximum likelihood estimator, and $L(\vec{n}|\vec{\mu}, \vec{\theta}')$ is the maximum unconditional likelihood [20]. Minimizing this test statistic allows for the fitter to seek the optimum configuration of NPs and POIs provided the model adheres to the assumptions that the NPs are gaussian distributed.

$$t_\mu = -2\ln\left(\frac{L(\vec{n}|\vec{\mu}, \vec{\theta}'')}{L(\vec{n}|\vec{\mu}, \vec{\theta}')}\right) \quad (C.2)$$

C.1.2 The Correlation Matrix

The correlation matrix encapsulates the influence of the undetermined parameters in the mode in relation to one another. The definition of this correlation matrix is given in Equation C.3. The n and m indices denote pairs of nuisance parameters. The x_i are the post fit nominal predictions in the ith bin. The $\delta_{ij}x_i$ is the square of the statistical uncertainty. And the ρ_{nm} are the correlation coefficients: the normalized covariance of nuisance parameter n with nuisance parameter m.

$$C_{ij} = \sum_n \sum_m (x_{i,n} - x_i)\, \rho_{nm}\, (x_{j,m} - x_j) + \delta_{ij}x_i \quad (C.3)$$

C.1.3 Goodness of Fit

One measure of the compatibility of data given a fit model is the χ^2 value. Equation C.4 defines this quantity as it pertains to the analysis in chapter 6. Most often, the χ^2 divided by the number of degrees of freedom is quoted as a goodness of fit estimator. If the uncertainties reflect the true spread of the data, minus any freedom for the model to fluctuate, the χ^2/ndf will be close to 1 – put more simply, fluctuations observed in data are about the size of one standard deviation from the nominal prediction on average.

$$\chi^2 = \sum_i \sum_j \left(d_i - x_i\right) C_{ij}^{-1} \left(d_j - x_j\right) \qquad \text{(C.4)}$$

Another, more thorough evaluation of the goodness of fit uses a comparison of the nominal model to the so-called "saturated model" [19]. The saturated model is a model that uses many free parameters to *exactly* fit the data. According to Wilks' theorem, the ratio of the likelihoods of these two models follows a χ^2 distribution. And so the compatibility of the nominal model can be compared to the saturated model, and a χ^2-based probability can be calculated which is used to gauge the proximity of the nominal model to the arbitrary perfect fit model.

C.2 Supplementary Material to the EWK-W Signal Extraction Fit

(a) electron channel   (b) muon channel   (c) combined channel
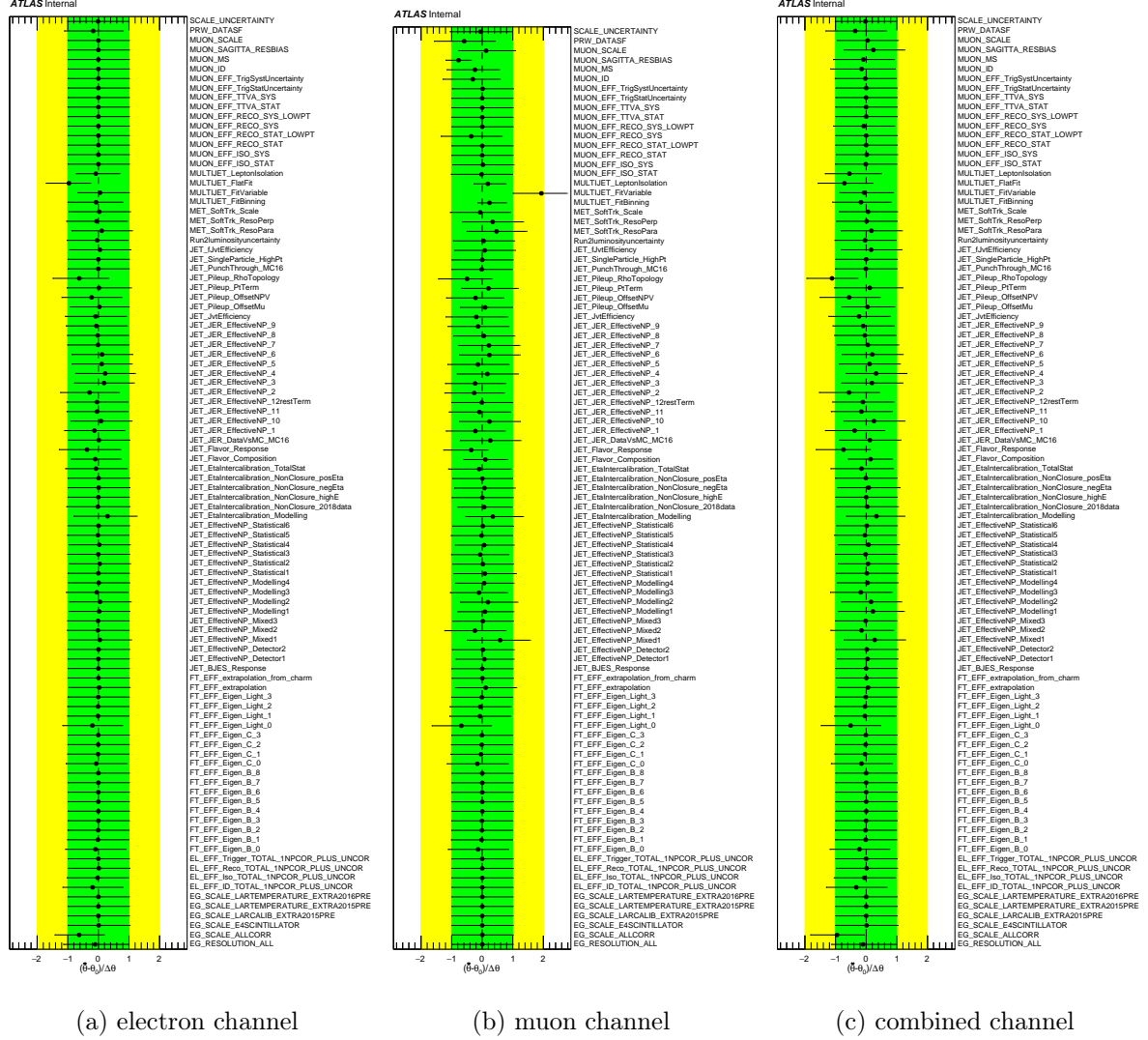
Figure C.1: Signal extraction fit nuisance parameter pulls
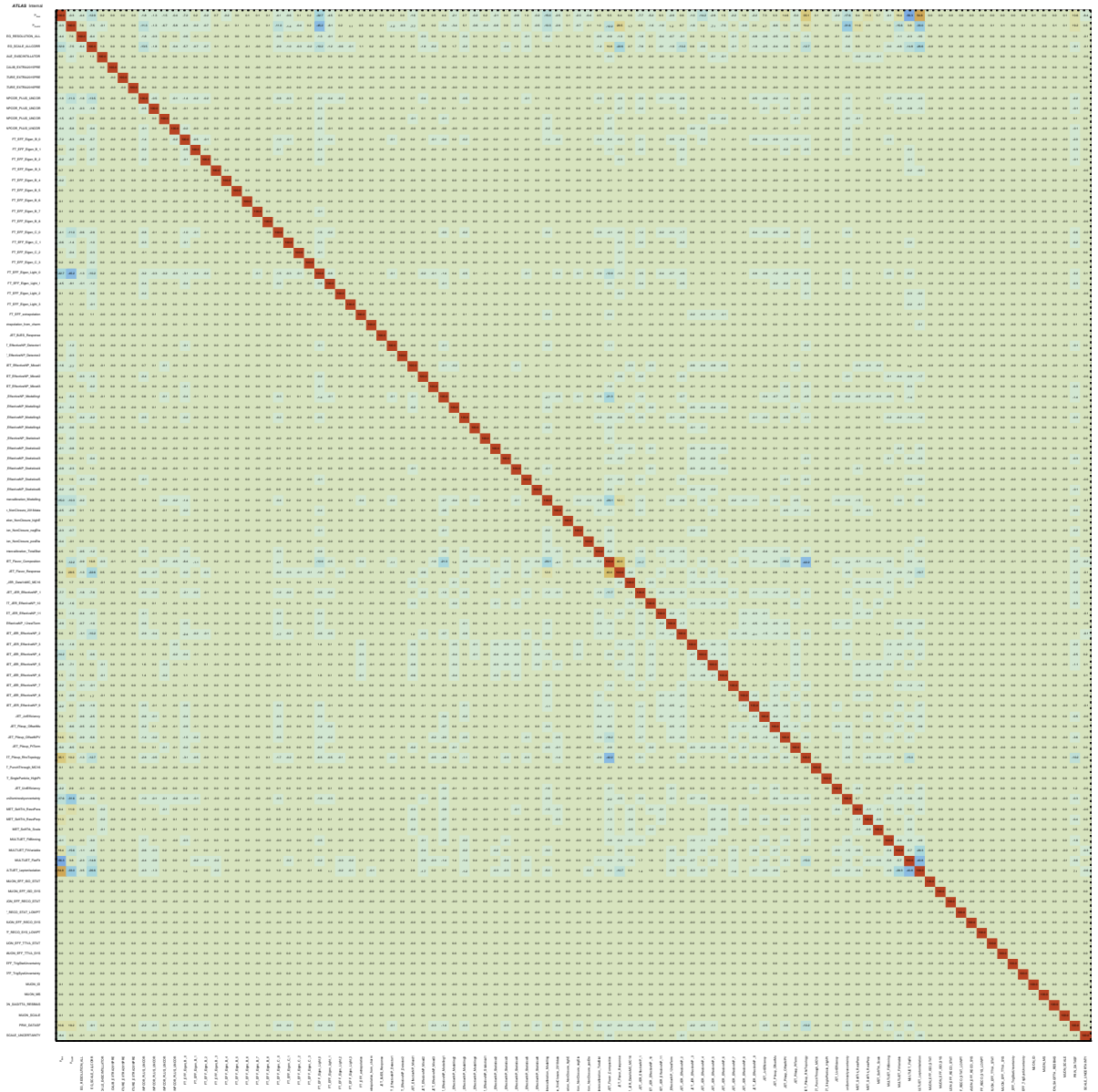
Figure C.2: Signal extraction fit correlation matrix for the electron channel

.

Figure C.3: Signal extraction fit correlation matrix for the muon channel

.
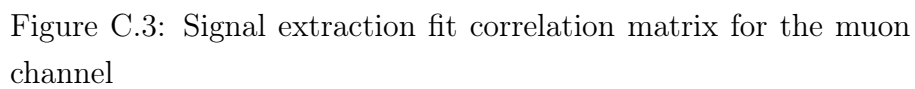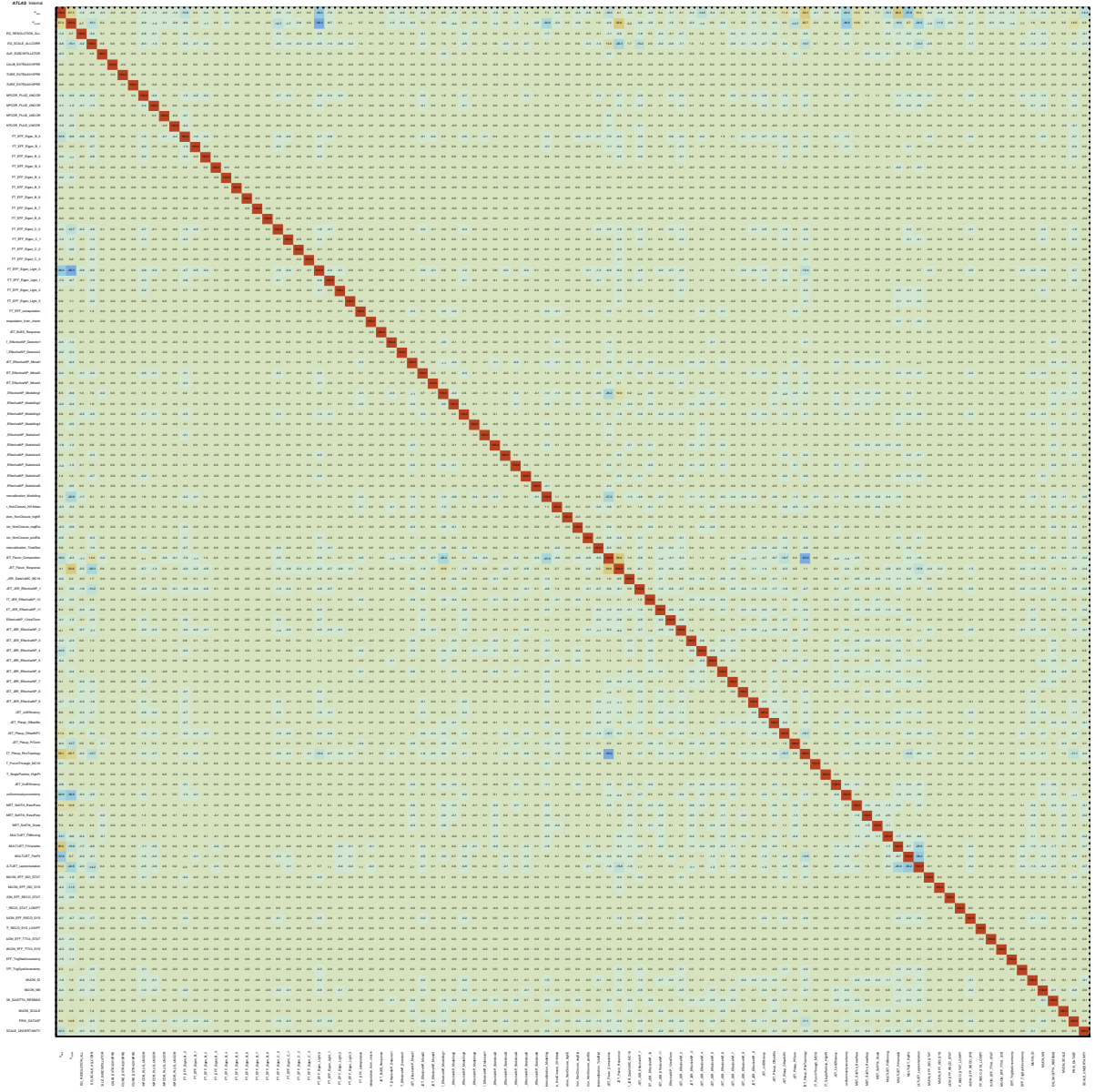
Figure C.4: Signal extraction fit correlation matrix for the combined $W \to \ell\nu$ channel

Appendix D

Electroweak W Production Analysis Systematic Breakdown

The relative uncertainty on the visible cross-section for the combined $W \to \ell\nu$ channel is shown below, broken down by systematic component, region, and sample.

	Sherpa 2.2.11 QCD $W \to \tau\nu$	Other EWK	Top	Diboson	Z+jets	Multijet	Powheg QCD $W \to \ell\nu$	Powheg EWK $W \to \ell\nu$
EL_EFF_Trigger_TOTAL_1NPCOR_PLUS_UNCOR	0.00116 / -0.00116	0.00127 / -0.00127	0.0012 / -0.0012	0.00135 / -0.00135	0.00179 / -0.00179	1.66e-08 / 1.66e-08	0.00122 / -0.00122	0.00118 / -0.00118
FT_EFF_Eigen_Light_2	-0.000317 / 0.000318	-6.58e-05 / 6.59e-05	-0.000378 / 0.000378	-0.000234 / 0.000234	-0.000441 / 0.000441	0.000345 / -0.000345	-0.000339 / 0.000339	-9.34e-05 / 9.34e-05
JET_JvtEfficiency	-0.002 / 0.00133	-0.00271 / 0.00199	-0.00419 / 0.0029	-0.00208 / 0.00135	-0.004 / 0.0029	0.000809 / -0.000396	-0.00137 / 0.000843	-0.000789 / 0.00056
EG_SCALE_LARTEMPERATURE_EXTRA2015PRE	4.4e-08 / 4.4e-08	2.94e-09 / 2.94e-09	2.02e-08 / 2.02e-08	3.64e-08 / 3.64e-08	1.27e-08 / 1.27e-08	1.66e-08 / 1.66e-08	8.63e-09 / 8.63e-09	4.39e-08 / 4.39e-08
MUON_EFF_RECO_SYS	4.4e-08 / 4.4e-08	2.94e-09 / 2.94e-09	2.02e-08 / 2.02e-08	3.64e-08 / 3.64e-08	1.27e-08 / 1.27e-08	1.66e-08 / 1.66e-08	8.63e-09 / 8.63e-09	4.39e-08 / 4.39e-08
EG_SCALE_LARCALIB_EXTRA2015PRE	4.4e-08 / 4.4e-08	2.94e-09 / 2.94e-09	2.02e-08 / 2.02e-08	3.64e-08 / 3.64e-08	1.27e-08 / 1.27e-08	1.66e-08 / 1.66e-08	8.63e-09 / 8.63e-09	4.39e-08 / 4.39e-08
JET_Pileup_PtTerm	0.0053 / -0.0167	0.00258 / -0.00226	0.00702 / -0.0051	0.00644 / -0.00377	0.00497 / -0.00462	-0.0079 / 0.00371	0.00493 / -0.00492	0.00185 / -0.00198
EG_SCALE_ALLCORR	0.00125 / -0.00125	0.00266 / -0.00266	0.00115 / -0.00114	0.00232 / -0.0029	0.00304 / -0.0039	-0.000275 / 0.000256	0.00176 / -0.00175	0.0016 / -0.00159
JET_EffectiveNP_Detector2	5.49e-05 / 6.68e-05	5.44e-05 / -0.000136	0.00135 / -0.000153	0.000236 / -0.000236	6.06e-05 / -0.000292	-7.44e-05 / 3.49e-05	0.000219 / -0.000221	6.54e-05 / -9.11e-05
JET_EtaIntercalibration_Modelling	0.0125 / -0.0303	0.00857 / -0.00789	0.0112 / -0.0111	0.0176 / -0.0146	0.021 / -0.0222	-0.0272 / 0.0183	0.0179 / -0.0164	0.00975 / -0.00985
EG_SCALE_E4SCINTILLATOR	5.38e-06 / -3.24e-05	-7.02e-05 / 6.87e-05	-2.32e-05 / -1.6e-05	-3.45e-05 / 0.000101	-0.000153 / 0.000113	-0.000127 / 2.55e-05	-4.6e-05 / 3.11e-05	-3.44e-05 / 2.56e-05
JET_BJES_Response	4.4e-08 / 4.4e-08	2.94e-09 / 2.94e-09	2.02e-08 / 2.02e-08	3.64e-08 / 3.64e-08	3.58e-06 / 3.58e-06	1.66e-08 / 1.66e-08	8.63e-09 / 8.63e-09	4.39e-08 / 4.39e-08
MUON_EFF_TrigStatUncertainty	0.000679 / -0.000705	0.000693 / -0.000716	0.000749 / -0.000773	0.000727 / -0.00075	0.000487 / -0.000506	-0.000236 / 0.000243	0.000736 / -0.00076	0.000777 / -0.000801
FT_EFF_Eigen_B_1	9.77e-05 / -0.000103	-1.87e-05 / 1.81e-05	0.0201 / -0.0202	0.000267 / -0.000275	6.62e-05 / -6.74e-05	-0.000706 / 0.000706	-3.26e-05 / 3.18e-05	-2.82e-05 / 2.81e-05
MUON_SCALE	-0.00366 / 0.000604	-0.00141 / 0.0108	-0.000873 / 0.000891	-0.000786 / 0.00107	-0.000634 / 0.00198	0.0016 / -0.00218	-0.00106 / 0.000776	-0.000965 / 0.000726
MUON_EFF_RECO_STAT	0.000363 / -0.000363	0.000356 / -0.000356	0.00037 / -0.00037	0.000358 / -0.000358	0.000299 / -0.000299	-8.12e-05 / 8.12e-05	0.000381 / -0.000381	0.000378 / -0.000378
JET_JER_EffectiveNP_7	-0.001 / 0.001	-0.00162 / 0.00162	-0.000649 / 0.000649	-0.000296 / 0.000296	0.000553 / -0.000553	0.00562 / -0.00562	-0.000242 / 0.000242	-0.000239 / 0.000239
JET_Pileup_OffsetMu	0.00514 / -0.0157	0.00515 / -0.00352	0.00636 / -0.00444	0.00819 / -0.00417	0.0111 / -0.013	-0.0153 / 0.00866	0.00837 / -0.0085	0.00538 / -0.00417
FT_EFF_Eigen_Light_3	-0.000554 / 0.000555	-0.000498 / 0.000499	-0.000527 / 0.000528	-0.000511 / 0.000512	-0.000594 / 0.000594	0.000531 / -0.000532	-0.000553 / 0.000553	-0.000484 / 0.000485
JET_JER_EffectiveNP_1	-0.000898 / 0.000898	-0.000897 / 0.000897	-0.000825 / 0.000825	-0.000463 / 0.000463	-0.00301 / 0.00301	-0.00616 / 0.00616	-0.00144 / 0.00144	-0.000366 / 0.000366
MUON_EFF_ISO_SYS	0.00597 / -0.00597	0.00505 / -0.00505	0.00453 / -0.00453	0.00358 / -0.00358	0.00412 / -0.00412	1.69e-08 / 1.63e-08	0.00461 / -0.00461	0.00449 / -0.00449
JET_EffectiveNP_Mixed2	-0.00607 / 0.000187	-0.000953 / 0.00101	-0.00191 / 0.0021	-0.00162 / 0.0035	-0.00255 / 0.0021	0.00239 / -0.00217	-0.00249 / 0.00252	-0.00122 / 0.00124
JET_EffectiveNP_Mixed1	0.00297 / -0.00497	0.0015 / -0.00142	0.00276 / -0.00274	0.00348 / -0.00271	0.00198 / -0.00308	-0.00278 / 0.00293	0.0303 / -0.00301	0.00122 / -0.00126
JET_JER_EffectiveNP_1	0.000819 / -0.000819	-0.000294 / 0.000294	0.000123 / -0.000123	0.00166 / -0.00166	0.000697 / -0.000697	-0.00539 / 0.00539	0.000681 / -0.000681	0.000377 / -0.000377
JET_PunchThrough_MC16	-3.13e-05 / 0.000139	-5.61e-05 / 4.72e-05	0.000123 / -0.000109	4.52e-05 / 2.37e-07	2.42e-05 / -1.26e-05	-4.55e-06 / 0.000102	2.28e-05 / -2.24e-05	5.33e-07 / -1.37e-05
FT_EFF_Eigen_B_7	-3.99e-07 / 3.76e-07	-1.89e-07 / 1.95e-07	-1.03e-05 / 1.02e-05	-4.33e-07 / 5.07e-07	-4.83e-07 / 4.25e-07	6.43e-07 / -6.1e-07	-4.14e-07 / 4.31e-07	-1.7e-07 / 1.51e-07
EG_SCALE_LARTEMPERATURE_EXTRA2016PRE	4.4e-08 / 4.4e-08	2.94e-09 / 2.94e-09	2.02e-08 / 2.02e-08	3.64e-08 / 3.64e-08	1.27e-08 / 1.27e-08	1.66e-08 / 1.66e-08	8.63e-09 / 8.63e-09	4.39e-08 / 4.39e-08
JET_EffectiveNP_Modelling4	0.000375 / -0.000267	7.21e-05 / -0.000189	0.000382 / -0.000171	0.000628 / -0.000143	0.000241 / -0.000383	-0.000331 / 0.00044	0.000464 / -0.000367	0.000153 / -0.000196
JET_Flavor_Composition	0.02 / -0.042	0.0148 / -0.0144	0.0129 / -0.0105	0.0225 / -0.0222	0.0392 / -0.0385	-0.0362 / 0.0283	0.0334 / -0.0274	0.0177 / -0.0174
JET_EffectiveNP_Statistical2	-0.00342 / 0.00047	-0.000603 / 0.000259	0.000754 / -0.000242	-9.09e-05 / 0.000948	-0.000485 / 0.000299	-5.87e-06 / 0.000362	-0.00024 / 0.000204	-0.000349 / 0.000384
PRW_DATASF	0.00556 / 0.00512	-0.00289 / 0.00375	-0.00482 / 0.0062	-0.00373 / 0.00378	-1.11e-08 / -0.000253	-0.018 / 0.0133	-0.0035 / 0.00264	-0.00455 / 0.00431
JET_Pileup_RhoTopology	0.0261 / -0.0236	0.00464 / -0.00456	-0.0116 / 0.0116	0.00402 / -0.00409	0.00622 / -0.00626	-0.00367 / 0.00403	0.0056 / -0.00563	0.00572 / -0.00572
FT_EFF_Eigen_B_2	0.000167 / -0.000167	0.000144 / -0.000143	-0.0047 / 0.00465	0.0021 / -0.0021	0.000229 / -0.000229	-1.49e-05 / 1.44e-05	0.000268 / -0.000267	0.000122 / -0.000122
JET_JER_EffectiveNP_2	0.00626 / -0.00621	0.00731 / -0.00725	0.0022 / -0.00219	0.00176 / -0.00175	0.00748 / -0.00742	-0.0179 / 0.0181	0.0019 / -0.00189	0.000314 / -0.000312
JET_EffectiveNP_Statistical6	0.000724 / -0.00287	0.00014 / -0.000319	0.000347 / -9.67e-05	0.000246 / -8.58e-05	0.000238 / -0.000377	-0.000186 / 0.000611	0.000279 / -0.000355	0.000142 / -0.000156
FT_EFF_Eigen_Light_1	0.00492 / -0.00489	0.00433 / -0.0043	0.00486 / -0.00482	0.00467 / -0.00464	0.00517 / -0.00513	-0.0046 / 0.00456	0.00482 / -0.00479	0.00409 / -0.00406
JET_EffectiveNP_Statistical1	-0.000192 / -0.000186	1.24e-05 / -0.000126	6.79e-05 / 6.08e-05	0.000194 / 6.98e-05	-9.42e-05 / -0.000101	-2.02e-05 / 0.000138	0.000141 / -5.99e-05	2.81e-05 / -5.64e-05
EL_EFF_ID_TOTAL_1NPCOR_PLUS_UNCOR	0.00208 / -0.00208	0.00245 / -0.00245	0.00227 / -0.00227	0.00269 / -0.00268	0.00354 / -0.00353	-0.00206 / 0.00206	0.00231 / -0.00231	0.00228 / -0.00228
JET_JER_EffectiveNP_9	-0.00535 / 0.00535	0.000646 / -0.000646	0.0004 / -0.0004	0.0105 / -0.0105	0.00152 / -0.00152	-0.00253 / 0.00253	0.00233 / -0.00233	7.06e-05 / -7.06e-05
JET_EffectiveNP_Detector1	0.00131 / -0.00352	0.000426 / -0.000662	0.000832 / -0.000409	-0.00055 / 0.00055	0.000994 / -0.000894	-0.00728 / 0.00105	0.001 / -0.001	0.000499 / -0.000499
JET_Pileup_OffsetNPV	0.0104 / -0.0193	0.0253 / -0.00225	-0.00281 / 0.00343	0.0235 / -0.0014	0.00573 / -0.00645	-0.00595 / 0.00239	0.00349 / -0.00274	0.00295 / -0.0027
FT_EFF_Eigen_B_8	-6.66e-08 / 4.4e-08	2.93e-09 / 2.96e-09	-8.8e-07 / 9.21e-07	-8.08e-08 / 3.68e-08	-6.99e-08 / 1.27e-08	1.66e-08 / -7.29e-08	8.85e-09 / 8.58e-09	-6.31e-08 / 4.39e-08
FT_EFF_Eigen_B_6	2.37e-06 / -2.39e-06	1.35e-06 / -1.34e-06	5.16e-05 / -5.16e-05	3.33e-06 / -3.25e-06	3.07e-06 / -3.04e-06	-3.65e-06 / 3.69e-06	2.96e-06 / -2.95e-06	1.11e-06 / -1.13e-06
JET_EffectiveNP_Modelling3	-0.00414 / 0.0015	-0.000939 / 0.000834	-0.00247 / 0.0029	-0.00126 / 0.00213	-0.00219 / 0.00205	0.00213 / -0.00142	-0.00225 / 0.00235	-0.000879 / 0.000871
JET_JER_DataVsMC_MC16	-0.00471 / 0.00471	-0.00351 / 0.00351	-0.00308 / 0.00308	-0.00471 / 0.00471	-0.00314 / 0.00314	0.0167 / -0.0167	-0.00175 / 0.00175	-0.000851 / 0.000851
EL_EFF_Iso_TOTAL_1NPCOR_PLUS_UNCOR	0.000352 / -0.000352	0.000402 / -0.000406	0.000369 / -0.000037	0.000441 / -0.000452	0.000477 / -0.00048	1.56e-08 / 1.75e-08	0.000369 / -0.000371	0.000377 / -0.000379
JET_JER_EffectiveNP_4	0.00962 / -0.0096	0.00423 / -0.00422	0.000863 / -0.000862	0.00409 / -0.00409	0.00232 / -0.00232	-0.00656 / 0.00657	0.00294 / -0.00293	0.00101 / -0.00101
JET_EffectiveNP_Modelling2	6.65e-05 / -0.00315	0.000212 / -0.000065	0.00192 / -0.00147	-0.00126 / 0.00499	0.000889 / -0.000728	-0.00103 / 0.0015	0.0127 / -0.00129	0.000405 / -0.000394
MUON_SAGITTA_RESBIAS	-0.0012 / -0.000334	0.00187 / 0.00147	0.0259 / 0.0169	0.00283 / 0.00134	0.0102 / 0.000596	-0.000261 / -0.000172	0.0165 / 0.0159	0.0174 / 0.0016
JET_EtaIntercalibration_NonClosure_2018data	0.00225 / -0.0109	0.00162 / -0.00111	0.00135 / -0.000237	-0.00237 / -0.00236	0.00286 / -0.00165	-0.00440 / -0.00165	0.00318 / -0.00323	0.0012 / -0.00118
JET_JvtEfficiency	-0.00169 / 0.00205	-0.000169 / 0.000427	0.000189 / 0.000323	-0.00046 / 0.0079	-0.00337 / 0.00384	0.000507 / -0.000527	0.0035 / -0.00108	0.0023 / -0.00217
JET_EtaIntercalibration_NonClosure_highE	-2.84e-06 / 1.71e-05	5.9e-05 / -7.11e-05	-1.15e-06 / -1.07e-05	3.65e-08 / 3.64e-08	1.07e-06 / -1.03e-05	3.87e-06 / 7.5e-07	-1.35e-06 / 7.5e-06	-1.36e-06 / 1.86e-06
JET_EffectiveNP_Statistical3	-0.000346 / 7.51e-05	-2.28e-05 / -2.3e-05	-0.000189 / 0.000219	2.62e-05 / 0.000299	-3.66e-05 / -5.67e-05	0.000297 / -0.000229	-0.000214 / 0.000216	-5.85e-05 / 4.09e-05
JET_JER_EffectiveNP_1	-0.00943 / 0.00943	0.0018 / -0.0018	0.00324 / -0.000324	0.00093 / -0.000869	0.00087 / -0.000869	0.0105 / -0.0105	0.00179 / -0.00179	0.00148 / -0.000148
FT_EFF_Eigen_B_0	0.00457 / -0.00436	0.00219 / -0.0021	0.158 / -0.144	0.00593 / -0.00559	0.00542 / -0.00518	-0.00856 / 0.008	0.0048 / -0.00456	0.00171 / -0.00165
MET_SoftTrk_ResoPara	-0.00924 / 0.00925	-0.0149 / 0.0149	-0.00155 / 0.00155	-0.00341 / 0.00341	-0.0224 / 0.0225	-0.00106 / 0.00106	-0.00387 / 0.00388	-0.0022 / 0.00221
MUON_EFF_RECO_SYS	0.00123 / -0.00123	0.00132 / -0.00131	0.00134 / -0.00133	0.00134 / -0.00133	0.00128 / -0.00128	-0.000223 / 0.000222	0.00145 / -0.00145	0.00139 / -0.00139
MUON_EFF_ISO_STAT	0.000332 / -0.000332	0.000434 / -0.000434	0.000483 / -0.000483	0.000638 / -0.000638	0.000365 / -0.000365	1.64e-08 / 1.68e-08	0.000509 / -0.000509	0.000523 / -0.000523
MUON_EFF_RECO_STAT	4.4e-08 / 4.4e-08	2.94e-09 / 2.94e-09	2.02e-08 / 2.02e-08	3.64e-08 / 3.64e-08	1.27e-08 / 1.27e-08	1.66e-08 / 1.66e-08	8.63e-09 / 8.63e-09	4.39e-08 / 4.39e-08
JET_EffectiveNP_Mixed3	0.00037 / 0.000439	0.00017 / -0.000357	0.000198 / 0.000193	0.000397 / -0.000494	0.00033 / -0.000343	0.000102 / 0.000345	0.00017 / -0.000259	0.000216 / -0.00021
FT_EFF_Eigen_C_0	0.00903 / -0.00893	0.00721 / -0.00714	0.012 / -0.0118	0.0131 / -0.013	0.00686 / -0.00675	-0.00638 / 0.0063	0.00778 / -0.00768	0.00478 / -0.00473
FT_EFF_Eigen_Light_0	0.0291 / -0.0281	0.0266 / -0.0257	0.0269 / -0.026	0.028 / -0.0271	0.0311 / -0.03	-0.0255 / 0.0252	0.0287 / -0.0277	0.0255 / -0.0247
FT_EFF_Eigen_B_3	-0.000282 / 0.000284	-0.000121 / 0.000121	-0.00098 / 0.01	-0.000369 / 0.000371	-0.0035 / 0.000351	0.000555 / -0.000558	-0.000291 / 0.000292	-0.000101 / 0.000101
FT_EFF_Eigen_C_2	0.000146 / -0.000146	0.000161 / -0.000161	0.000176 / -0.000176	0.000122 / -0.000122	0.000182 / -0.000182	-6.12e-05 / 6.11e-05	5.18e-05 / -5.18e-05	1.35e-05 / -1.34e-05
FT_EFF_extrapolation	-0.00246 / 0.00246	-0.0028 / 0.0028	-0.00355 / 0.0036	-0.00393 / 0.00396	-0.00182 / 0.00183	0.000441 / -0.00044	-3.79e-06 / 3.8e-06	-1.99e-06 / 1.97e-06
MET_SoftTrk_ResoPerp	-0.015 / 0.015	-0.0105 / 0.0105	-0.0014 / 0.0014	-0.00244 / 0.00244	-0.0184 / 0.0184	0.00227 / -0.00227	-0.0036 / 0.0036	-0.00199 / 0.00199
FT_EFF_Eigen_C_1	0.000345 / -0.000346	0.000658 / -0.000658	0.000264 / -0.000265	0.000883 / -0.00884	5.42e-05 / -5.43e-05	-0.000342 / 0.000342	0.000629 / -0.000629	0.000664 / -0.000664
FT_EFF_Eigen_B_4	6.11e-05 / -6.11e-05	2.29e-05 / -2.29e-05	0.00238 / -0.00238	8.33e-05 / -8.32e-05	7.68e-05 / -7.68e-05	-0.000128 / 0.000128	6.18e-05 / -6.18e-05	2.01e-05 / -2.01e-05
JET_EtaIntercalibration_TotalStat	-4.41e-05 / -0.00547	0.000663 / -0.00103	-0.000121 / 0.000114	0.00019 / 0.00114	0.0019 / -0.00152	-8.06e-05 / 0.00082	0.00132 / -0.00101	0.00128 / -0.00121
JET_JER_EffectiveNP_3	0.00451 / -0.00451	0.00078 / -0.000781	-0.00698 / 0.000698	0.00449 / -0.00449	-0.000479 / 0.000479	0.00795 / -0.00795	-0.000997 / 0.000958	0.000434 / -0.000434
MET_SoftTrk_Scale	-0.0127 / 0.0102	-0.0128 / 0.0131	-0.00171 / 0.00178	-0.00302 / 0.00348	-0.0208 / 0.0196	0.0018 / -0.00406	-0.00378 / 0.00444	-0.00208 / 0.00207
MUON_ID	-0.0013 / -0.00265	-0.000903 / 5.48e-05	-0.00466 / 0.00037	-0.00419 / 0.00128	0.000571 / 0.0011	-1.8e-05 / -0.000131	-0.00104 / 0.000361	-0.00102 / 0.000378
JET_EffectiveNP_Modelling1	0.00628 / -0.032	0.00514 / -0.00634	0.00444 / -0.00379	0.0114 / -0.0102	0.012 / -0.0137	-0.0124 / 0.0118	0.012 / -0.0122	0.00667 / -0.00727
JET_EtaIntercalibration_NonClosure_posEta	0.000883 / -0.0083	-0.000154 / 0.000266	0.000497 / -0.000539	0.000441 / -0.000191	0.001 / -0.000402	-0.00274 / 0.000406	0.000623 / -0.000456	0.000207 / -0.000181
FT_EFF_Eigen_B_5	-1.07e-05 / 1.07e-05	-5.57e-06 / 5.58e-06	-0.000261 / 0.000261	-1.57e-05 / 1.57e-05	-1.49e-05 / 1.49e-05	1.91e-05 / -1.9e-05	-1.39e-05 / 1.39e-05	-5.09e-06 / 5.07e-06
MUON_EFF_TTVA_STAT	0.000109 / -0.00011	0.000118 / -0.000119	0.000127 / -0.000127	0.000148 / -0.000148	9.45e-05 / -9.46e-05	-2.84e-05 / 2.83e-05	0.000137 / -0.000137	0.000136 / -0.000136
MUON_EFF_TrigSystUncertainty	-0.00309 / 0.0015	-0.00299 / 0.00304	-0.00306 / 0.00312	-0.00299 / 0.0034	-0.00274 / 0.0028	0.00107 / -0.00109	-0.00322 / 0.00328	-0.00311 / 0.00317
JET_JER_EffectiveNP_6	0.00109 / -0.00109	-0.00348 / 0.00348	-0.000662 / 0.000663	-0.00134 / 0.00134	-0.00242 / 0.00242	0.00572 / -0.00572	-0.00209 / 0.0021	-7.48e-05 / 7.48e-05
JET_SingleParticle_HighPt	4.4e-08 / 4.4e-08	2.94e-09 / 2.94e-09	2.02e-08 / 2.02e-08	3.64e-08 / 3.64e-08	3.58e-06 / 3.58e-06	1.66e-08 / 1.66e-08	8.63e-09 / 8.63e-09	4.39e-08 / 4.39e-08
JET_JER_EffectiveNP_8	0.00378 / -0.00378	-0.00104 / 0.00104	-0.000105 / 0.000105	-0.000481 / 0.000481	-0.000163 / 0.000163	0.000649 / -0.000649	-0.000821 / 0.000821	-0.000158 / 0.000158
JET_EtaIntercalibration_NonClosure_negEta	0.00123 / -0.00252	0.000232 / -0.000467	0.00166 / -0.00156	0.000139 / -0.000486	0.0035 / -0.00125	-0.0011 / 0.000781	0.0103 / -0.00131	0.000495 / -0.000533
JET_EffectiveNP_Statistical5	-0.000565 / -0.00112	-0.000318 / 0.000326	-0.000774 / 0.00112	-0.000602 / 0.000877	-0.000942 / 0.000967	0.000748 / -9.72e-05	-0.000796 / 0.000832	-0.000417 / 0.000363
MUON_EFF_TTVA_SYS	0.000138 / -0.000131	0.000152 / -0.000141	0.000171 / -0.000157	0.000114 / -0.000116	0.000129 / -0.00012	-3e-05 / 2.87e-05	0.000183 / -0.000168	0.00018 / -0.000165
FT_EFF_Eigen_C_3	-0.00015 / 0.0015	-0.000114 / 0.000114	-0.000164 / 0.000164	-0.000164 / 0.000164	-0.000111 / 0.000111	0.000108 / -0.000108	-0.000127 / 0.000127	-7.36e-05 / 7.36e-05
JET_JER_EffectiveNP_1	0.00855 / -0.00849	0.00943 / -0.00935	0.00549 / -0.00455	0.0605 / -0.006	0.0126 / -0.0124	-0.0327 / 0.0328	0.0533 / -0.00529	0.00169 / -0.00168
JET_JER_EffectiveNP_5	0.00669 / -0.00669	-0.00174 / 0.00174	-0.00117 / 0.00117	-0.000729 / 0.000729	-0.00264 / 0.00264	0.0081 / -0.0081	-0.000538 / 0.000538	-0.000523 / 0.000523
FT_EFF_extrapolation	-0.000139 / 0.00014	-0.000268 / 0.000268	-0.000355 / 0.000355	-0.000355 / 0.000366	-6.86e-05 / 6.88e-05	7.93e-05 / -7.94e-05	-0.000151 / 0.000151	-0.0002 / 0.0002
JET_Flavor_Response	-0.0225 / 0.0187	-0.0098 / 0.0101	-0.0137 / 0.0146	-0.0201 / 0.0217	-0.0208 / 0.0221	0.0282 / -0.03	-0.0245 / 0.0263	-0.0118 / 0.0124
JET_EffectiveNP_Statistical4	0.00102 / -0.00362	0.000311 / -0.000455	0.00112 / -0.000498	0.000652 / -0.000513	0.000652 / -0.000513	0.000881 / -0.000829	0.00031 / -0.000322	
EL_EFF_Reco_TOTAL_1NPCOR_PLUS_UNCOR	0.00161 / -0.00161	0.00156 / -0.00156	0.00157 / -0.00157	0.00153 / -0.00153	0.00216 / -0.00216	-0.00174 / 0.00174	0.00152 / -0.00152	0.0015 / -0.0015
MUON_MS	-0.00119 / -0.00349	-0.000352 / 0.000326	-0.000439 / 0.000555	-1.62e-05 / 0.000876	0.000437 / 0.000437	-5.1e-05 / 1.31e-06	-0.000479 / 0.000365	-0.000437 / 0.000443
EG_RESOLUTION_ALL	0.00167 / 0.00132	0.000638 / 0.000583	-0.00023 / -0.000183	-1.04e-05 / -0.000701	-3.4e-06 / -0.000648	0.0101 / 0.000289	-0.000209 / -1.71e-05	-0.0001 / -3.63e-05
Run2luminosityuncertainty	0.017 / -0.017	0.017 / -0.017	0.017 / -0.017	0.017 / -0.017	0.017 / -0.017	0.017 / -0.017	0.017 / -0.017	0.017 / -0.017
MULTIJET_LeptonIsolation	0 / 0	0 / 0	0 / 0	0 / 0	0 / 0	0.207 / -0.189	0 / 0	0 / 0
MULTIJET_FitBinning	0 / 0	0 / 0	0 / 0	0 / 0	0 / 0	0.0637 / -0.123	0 / 0	0 / 0
MULTIJET_FitVariable	0 / 0	0 / 0	0 / 0	0 / 0	0 / 0	0.0953 / -0.0561	0 / 0	0 / 0
MULTIJET_FlatFit	0 / 0	0 / 0	0 / 0	0 / 0	0 / 0	0.29 / -0.224	0 / 0	0 / 0
SCALE_UNCERTAINTY	0 / 0	0 / 0	0 / 0	0 / 0	0 / 0	0 / 0	0 / 0	0.00876 / -0.00876
gamma_stat_SR_combined_bin_0	0.00935 / -0.00936	0.00835 / -0.00835	0.00831 / -0.00831	0.00697 / -0.00697	0.00833 / -0.00833	0.00809 / -0.0081	0.00812 / -0.00812	0 / 0
gamma_stat_SR_combined_bin_1	0.00138 / -0.00137	0.00175 / -0.00174	0.00196 / -0.00195	0.00233 / -0.00232	0.00188 / -0.00187	0.00169 / -0.00168	0.00197 / -0.00196	0 / 0
gamma_stat_SR_combined_bin_2	0.000353 / -0.000349	0.000757 / -0.000749	0.000617 / -0.000611	0.0122 / -0.0121	0.000675 / -0.000668	0.0106 / -0.00106	0.000745 / -0.000737	0 / 0
gamma_stat_SR_combined_bin_3	6.66e-05 / -6.58e-05	0.000249 / -0.000246	0.000125 / -0.000123	0.000461 / -0.000455	0.00178 / -0.000176	0.000444 / -0.000439	0.000202 / -0.000199	0 / 0
gamma_stat_SR_combined_bin_4	4.63e-05 / -4.4e-05	0.00025 / -0.000237	8.37e-05 / -7.95e-05	0.000583 / -0.000554	0.000128 / -0.000121	3.79e-05 / -3.6e-05	0.00017 / -0.000161	0 / 0
μ_{QcdW}	0.0537 / -0.0513	0 / 0	0 / 0	0 / 0	0 / 0	0 / 0	0.0537 / -0.0513	0 / 0
μ_{Ewk}	0 / 0	0 / 0	0 / 0	0 / 0	0 / 0	0 / 0	0 / 0	0.0729 / -0.0826

Table D.1: Relative post-fit uncertainty on event yields due to each nuisance parameter in SR

188

	Sherpa 2.2.11 QCD $W \to \tau\nu$	Other EWK	Top	Diboson	Z+jets	Multijet	Powheg QCD $W \to \ell\nu$	Powheg EWK $W \to \ell\nu$
EL_EFF_Trigger_TOTAL_1NPCOR_PLUS_UNCOR	0.00128 / -0.00128	0.00152 / -0.00152	0.0013 / -0.0013	0.00165 / -0.00165	0.00151 / -0.00151	-9.55e-09 / -9.58e-09	0.00135 / -0.00135	0.0013 / -0.0013
FT_EFF_Eigen_Light_2	-0.000267 / 0.000268	6.81e-05 / -6.79e-05	-0.000336 / 0.000336	-0.000149 / 0.000149	-0.00033 / 0.00033	0.000447 / -0.000448	-0.000266 / 0.000266	3.18e-05 / -3.16e-05
JET_JvtEfficiency	-0.00121 / 0.00062	-0.00257 / 0.00186	-0.00344 / 0.00219	-0.00207 / 0.00124	-0.00397 / 0.00281	0.00159 / -0.000919	-0.00112 / 0.000614	-0.000777 / 0.000516
EG_SCALE_LARTEMPERATURE_EXTRA2015PRE	2.09e-08 / 2.09e-08	6.48e-09 / 6.48e-09	-2.34e-08 / -2.34e-08	-5.37e-08 / -5.37e-08	3.99e-08 / 3.99e-08	-9.57e-09 / -9.57e-09	3.18e-09 / 3.18e-09	-1.53e-08 / -1.53e-08
MUON_EFF_RECO_SYS	2.09e-08 / 2.09e-08	6.48e-09 / 6.48e-09	-2.34e-08 / -2.34e-08	-5.37e-08 / -5.37e-08	3.99e-08 / 3.99e-08	-9.57e-09 / -9.57e-09	3.18e-09 / 3.18e-09	-1.53e-08 / -1.53e-08
EG_SCALE_LARCALIB_EXTRA2015PRE	2.09e-08 / 2.09e-08	6.48e-09 / 6.48e-09	-2.34e-08 / -2.34e-08	-5.37e-08 / -5.37e-08	3.99e-08 / 3.99e-08	-9.57e-09 / -9.57e-09	3.18e-09 / 3.18e-09	-1.53e-08 / -1.53e-08
JET_Pileup_PtTerm	0.00541 / 0.000579	0.000167 / -0.00242	0.0497 / -0.0462	0.0067 / -0.00542	0.00661 / -0.00495	-0.00672 / 0.00762	0.00565 / -0.00391	0.00215 / -0.00208
EG_SCALE_ALLCORR	0.00202 / -0.00201	0.00335 / -0.00332	0.00108 / -0.00108	0.00171 / -0.00172	0.00326 / -0.00326	0.000315 / -0.000307	0.00188 / -0.00187	0.00154 / -0.00154
JET_EffectiveNP_Detector2	7.74e-05 / -2.82e-06	2.34e-05 / -5.74e-05	0.000167 / -0.00018	0.00013 / -2.71e-05	0.000298 / -5.51e-05	-0.000292 / 0.00039	0.000198 / -0.000189	9.96e-05 / -8.94e-05
JET_EtaIntercalibration_Modelling	0.0202 / -0.0176	0.00641 / -0.00601	0.0101 / -0.00925	0.0145 / -0.0148	0.0169 / -0.0122	-0.0184 / 0.0174	0.0166 / -0.015	0.00828 / -0.0082
EG_SCALE_E4SCINTILLATOR	-0.000101 / -1.32e-05	-3.09e-05 / -5.53e-05	5.77e-06 / -1.09e-05	-0.000108 / 3.36e-05	-8.33e-05 / 0.00011	-9.79e-05 / 5.8e-05	-4.68e-05 / 3.67e-05	-3.78e-05 / 3.23e-05
JET_BJES_Response	2.09e-08 / 2.09e-08	6.48e-09 / 6.48e-09	-2.34e-08 / -2.34e-08	-5.37e-08 / -5.37e-08	-4.86e-08 / -4.86e-08	-9.57e-09 / -9.57e-09	9.64e-07 / 9.64e-07	-1.53e-08 / -1.53e-08
MUON_EFF_TrigStatUncertainty	0.0006 / -0.000625	0.000681 / -0.000705	0.000728 / -0.000754	0.000649 / -0.000672	0.00072 / -0.000744	-0.000391 / 0.000406	0.000683 / -0.000709	0.000719 / -0.000744
FT_EFF_Eigen_B_1	6.18e-05 / -6.22e-05	4.89e-06 / -5.57e-06	0.0259 / -0.0259	0.000247 / -0.000254	0.000118 / -0.000119	-0.000742 / 0.000744	-3.37e-05 / 3.28e-05	-3.02e-05 / 3e-05
MUON_SCALE	-0.0019 / -0.00198	-0.0017 / 0.00169	-0.00102 / 0.000836	-0.000381 / 0.000844	-0.00121 / 0.00179	0.000792 / -0.000325	-0.00135 / 0.00123	-0.00126 / 0.00115
MUON_EFF_RECO_STAT	0.00037 / -0.00037	0.000375 / -0.000375	0.000383 / -0.000383	0.000365 / -0.000365	0.000437 / -0.000437	-0.000159 / 0.000159	0.000402 / -0.000402	0.000397 / -0.000397
JET_JER_EffectiveNP_7	0.000961 / -0.000961	-0.00123 / 0.00123	-0.000895 / 0.000895	-0.00151 / 0.00151	-0.00223 / 0.00223	0.00345 / -0.00345	-0.000419 / 0.000419	-0.000298 / 0.000298
JET_Pileup_OffsetMu	0.0116 / -0.0273	0.00311 / -0.00132	0.00463 / -0.00303	0.00674 / -0.00914	0.00904 / -0.00393	-0.0135 / 0.00766	0.00974 / -0.00553	0.0399 / -0.00289
FT_EFF_Eigen_Light_3	-0.000599 / 0.0006	-0.000477 / 0.000478	-0.000516 / 0.000517	-0.000504 / 0.000504	-0.000589 / 0.000589	0.000768 / -0.000768	-0.000552 / 0.000552	-0.000474 / 0.000474
JET_JER_EffectiveNP_1	-0.00407 / 0.00407	-0.00176 / 0.00176	-0.00104 / 0.00104	-0.00221 / 0.00221	-0.00308 / 0.00308	0.00354 / -0.00354	-0.00101 / 0.00101	-0.000579 / 0.000579
MUON_EFF_ISO_SYS	0.00671 / -0.00671	0.00529 / -0.00529	0.0465 / -0.0465	0.00367 / -0.00367	0.00538 / -0.00538	-9.73e-09 / -9.4e-09	0.00507 / -0.00507	0.005 / -0.005
JET_EffectiveNP_Mixed2	0.00474 / 0.00145	-0.00141 / 0.000882	-0.0018 / 0.0167	-0.00122 / 0.00199	-0.0015 / 0.00315	0.00373 / -0.00317	-0.0025 / 0.00262	-0.00136 / 0.00149
JET_EffectiveNP_Mixed1	0.00285 / -3.65e-05	0.00174 / -0.00162	0.0299 / -0.00289	0.00367 / -0.00234	0.00353 / -0.00205	-0.00405 / 0.005	0.00333 / -0.00331	0.00161 / -0.00158
JET_JER_EffectiveNP_1	-0.00299 / 0.00299	-0.000733 / 0.000733	-0.000965 / 0.000965	-0.00138 / 0.00138	0.000223 / -0.000223	-0.0043 / 0.0043	0.00101 / -0.00101	-3.06e-05 / 3.06e-05
JET_PunchThrough_MC16	0.000674 / -5.69e-06	-6.38e-05 / 0.000118	5.48e-05 / -1.78e-05	1.93e-05 / 3.57e-05	1.56e-05 / 0.000825	1.66e-05 / -2.06e-05	9.8e-06 / -3.18e-05	-1.33e-05 / -5e-05
FT_EFF_Eigen_B_7	-3.51e-07 / 2.99e-07	-1.69e-07 / 1.82e-07	-1.14e-05 / 1.13e-05	-4.02e-07 / 4.11e-07	-4.01e-07 / 3.92e-07	9.74e-07 / -9.93e-07	-4.76e-07 / 4.82e-07	-1.94e-07 / 1.64e-07
EG_SCALE_LARTEMPERATURE_EXTRA2016PRE	2.09e-08 / 2.09e-08	6.48e-09 / 6.48e-09	-2.34e-08 / -2.34e-08	-5.37e-08 / -5.37e-08	3.99e-08 / 3.99e-08	-9.57e-09 / -9.57e-09	3.18e-09 / 3.18e-09	-1.53e-08 / -1.53e-08
JET_EffectiveNP_Modelling4	0.000321 / 0.000126	5.35e-05 / -0.000106	0.000293 / -0.000347	0.000493 / -3.39e-05	0.000499 / -0.000314	-0.000529 / 0.000609	0.000431 / -0.000393	0.000258 / -0.000223
JET_Flavor_Composition	0.0183 / -0.034	0.0129 / -0.0112	0.011 / -0.0068	0.0227 / -0.0203	0.0216 / -0.0175	-0.0265 / 0.0261	0.0242 / -0.0217	0.0138 / -0.0135
JET_EffectiveNP_Statistical2	-0.00121 / 0.000767	-0.000537 / 0.000228	0.000649 / -0.000737	0.000852 / -0.000685	0.000131 / 0.00123	0.000382 / -0.000574	-0.000138 / 0.000121	-0.000342 / 0.000372
PRW_DATASF	-0.011 / -0.00147	-0.0033 / 0.00688	-0.00562 / 0.0068	-0.00278 / 0.00376	0.0058 / -0.00241	-0.0303 / 0.0358	-0.00333 / 0.003	-0.00372 / 0.00448
JET_Pileup_RhoTopology	0.00597 / -0.00522	0.0024 / -0.00256	-0.0122 / 0.0122	0.00193 / -0.00193	-0.000182 / -0.000117	-0.0037 / 0.00371	0.00355 / -0.00363	0.00447 / -0.00449
FT_EFF_Eigen_B_2	0.000175 / -0.000175	0.000149 / -0.000149	-0.00527 / 0.00524	0.000185 / -0.000186	0.000219 / -0.000218	-0.000254 / 0.000254	0.000302 / -0.0003	0.000165 / -0.000165
JET_JER_EffectiveNP_2	0.000169 / -0.000168	0.0101 / -0.01	0.00521 / -0.00518	0.00375 / -0.00372	0.00985 / -0.00976	-0.0246 / 0.0248	0.0154 / -0.0154	0.000467 / -0.000465
FT_EFF_Eigen_Light_1	0.00539 / -0.00533	0.00442 / -0.00439	0.00481 / -0.00478	0.00483 / -0.0048	0.00528 / -0.00524	-0.0067 / 0.00664	0.0048 / -0.00477	0.00418 / -0.00415
JET_EffectiveNP_Statistical1	6.86e-05 / 0.000171	0.000198 / -0.00012	0.000137 / -9.03e-05	-0.000155 / -7.13e-05	6.03e-05 / 7.18e-06	-0.000317 / 0.000186	0.000141 / -0.000101	0.000129 / -7.77e-05
EL_EFF_ID_TOTAL_1NPCOR_PLUS_UNCOR	0.00248 / -0.00247	0.00304 / -0.00304	0.00251 / -0.0025	0.00338 / -0.00337	0.00316 / -0.00316	-0.00317 / 0.00317	0.00272 / -0.00272	0.0259 / -0.0259
JET_JER_EffectiveNP_9	-0.00192 / 0.00192	0.00182 / -0.00182	0.00175 / -0.00175	0.00167 / -0.00167	0.0019 / -0.0019	0.00151 / -0.00151	0.000672 / -0.000672	0.000354 / -0.000354
JET_EffectiveNP_Detector1	0.00121 / 0.000819	1.15e-05 / -0.000819	0.000518 / -0.000737	6.31e-05 / -0.00021	0.00194 / -0.000714	-0.00148 / 0.00167	0.000097 / -0.00095	0.000589 / -0.000595
JET_Pileup_OffsetNPV	0.00478 / -0.00486	0.00146 / -0.000872	-0.00347 / 0.00451	0.00285 / -0.00423	0.002 / -0.000911	-0.00327 / 0.00315	0.00318 / -0.00225	0.00257 / -0.00221
FT_EFF_Eigen_B_8	-7.21e-08 / 2.07e-08	6.35e-09 / 6.42e-09	-8.26e-07 / 8.94e-07	-5.35e-08 / 6.27e-08	-4.83e-08 / 3.98e-08	6.61e-08 / -8.52e-08	3.27e-09 / 3.15e-09	-1.53e-08 / 4.43e-08
FT_EFF_Eigen_B_6	2.06e-06 / -2.12e-06	1.41e-06 / -1.4e-06	6.38e-05 / -6.39e-05	3.08e-06 / -3.19e-06	2.95e-06 / -2.96e-06	-6.29e-06 / 6.27e-06	3.16e-06 / -3.16e-06	1.48e-06 / -1.45e-06
JET_EffectiveNP_Modelling3	0.000228 / 0.001	-0.00125 / 0.000576	-0.00255 / 0.0053	-0.00248 / 0.00325	-0.00196 / 0.00326	0.00286 / -0.00243	-0.00218 / 0.00218	-0.000915 / 0.000948
JET_JER_DataVsMC_MC16	-0.0058 / 0.0058	-0.00357 / 0.00357	-0.00345 / 0.00345	-0.00559 / 0.00559	-0.00607 / 0.00607	0.0138 / -0.0138	-0.00154 / 0.00154	-0.000578 / 0.000579
EL_EFF_Iso_TOTAL_1NPCOR_PLUS_UNCOR	0.000358 / -0.000359	0.000426 / -0.000436	0.000367 / -0.000368	0.000502 / -0.000527	0.000379 / -0.000386	-8.97e-09 / -1.01e-08	0.000365 / -0.000369	0.000375 / -0.000381
JET_JER_EffectiveNP_4	0.00281 / -0.00281	0.00521 / -0.0052	-4.66e-05 / 4.65e-05	0.00295 / -0.00295	0.00581 / -0.0058	-0.0167 / 0.0167	0.00151 / -0.00151	0.00125 / -0.00125
MUON_SAGITTA_RESBIAS	-0.00287 / -0.00324	-0.00101 / 0.000854	0.00228 / 0.00138	0.00473 / 0.000339	0.00824 / 0.000807	-1.15e-05 / 1.94e-05	0.00235 / 0.00146	0.00202 / 0.00104
JET_EtaIntercalibration_NonClosure_2018data	0.00222 / -0.00122	0.00129 / -0.00119	0.00194 / -0.00121	0.002 / -0.00325	0.0047 / -0.00318	-0.00482 / 0.0035	0.00292 / -0.00268	0.00184 / -0.00166
JET_JvtEfficiency	-0.00891 / 0.00897	-0.00262 / 0.0285	-0.000701 / 0.00114	-0.00218 / 0.00231	-0.00509 / 0.0567	0.00113 / -0.0013	0.00116 / 6.55e-05	0.000349 / -0.000238
JET_EtaIntercalibration_NonClosure_highE	4.82e-05 / -7.34e-06	-7.66e-09 / -5.5e-05	-2.25e-05 / 4.93e-06	-5.37e-08 / 6.25e-08	9.2e-06 / 2.49e-05	-3.42e-06 / -1.48e-05	-1.27e-05 / 1.11e-06	-1.47e-05 / -2.11e-05
JET_EffectiveNP_Statistical3	0.000816 / -4.44e-05	0.000243 / 0.000127	-0.000363 / 0.000157	-6.31e-05 / -4.59e-05	-7.73e-05 / 0.000167	0.000367 / -0.000253	-0.000207 / 0.000291	-0.000111 / 0.0002
JET_JER_EffectiveNP_1	0.00247 / -0.00247	0.00266 / -0.00266	0.00159 / -0.00158	0.000964 / -0.00964	0.000694 / -0.000694	0.000729 / -0.000729	0.00078 / -0.00078	0.000151 / -0.000151
FT_EFF_Eigen_B_0	0.00391 / -0.00366	0.00219 / -0.00214	0.161 / -0.147	0.00526 / -0.00497	0.00494 / -0.0047	-0.0109 / 0.0103	0.00496 / -0.0047	0.00204 / -0.00196
MET_SoftTrk_ResoPara	-0.00891 / 0.0089	-0.0166 / 0.0166	-0.00135 / 0.00135	-0.00133 / 0.00133	-0.0212 / 0.0212	0.00132 / -0.00132	-0.00323 / 0.00323	-0.00201 / 0.00202
MUON_EFF_RECO_SYS	0.00152 / -0.00151	0.00169 / -0.00168	0.00153 / -0.00153	0.00158 / 0.00178	0.00221 / -0.0022	-0.000534 / 0.000532	0.00178 / -0.00177	0.00168 / -0.00168
MUON_EFF_ISO_STAT	0.000321 / -0.000321	0.000487 / -0.000487	0.000505 / -0.000505	0.000713 / -0.000713	0.000599 / -0.000599	-9.45e-09 / -9.69e-09	0.000521 / -0.000521	0.000538 / -0.000538
MUON_EFF_RECO_STAT	2.09e-08 / 2.09e-08	6.48e-09 / 6.48e-09	-2.34e-08 / -2.34e-08	-5.37e-08 / -5.37e-08	3.99e-08 / 3.99e-08	-9.57e-09 / -9.57e-09	3.18e-09 / 3.18e-09	-1.53e-08 / -1.53e-08
JET_EffectiveNP_Mixed3	0.0011 / 0.000538	-8.52e-05 / -0.000258	2.48e-05 / 4.11e-05	-0.00011 / 0.000323	0.0015 / -0.000215	-0.000314 / 0.000395	0.000236 / -0.00018	0.000163 / -0.00018
FT_EFF_Eigen_C_0	0.00832 / -0.00821	0.00713 / -0.00705	0.0126 / -0.0124	0.0138 / -0.0136	0.00705 / -0.00695	-0.00874 / 0.00863	0.00737 / -0.00727	0.00494 / -0.00489
FT_EFF_Eigen_Light_0	0.0311 / -0.0299	0.0272 / -0.0263	0.0276 / -0.0267	0.0294 / -0.0284	0.0318 / -0.0307	-0.0369 / 0.0366	0.0285 / -0.0275	0.0256 / -0.0248
FT_EFF_Eigen_B_3	-0.000253 / 0.000254	-0.00012 / 0.00012	-0.0107 / 0.0107	-0.000315 / 0.000315	-0.000318 / 0.000319	0.000772 / -0.000775	-0.000316 / 0.000317	-0.000119 / 0.000119
FT_EFF_Eigen_C_2	0.000248 / -0.000248	0.000215 / -0.000215	0.000174 / -0.000174	0.000278 / -0.000278	0.000207 / -0.000207	-0.000151 / 0.000151	0.000129 / -0.000129	9.21e-05 / -9.2e-05
FT_EFF_extrapolation	-0.00208 / 0.00208	-0.00261 / 0.00262	-0.00401 / 0.00402	-0.00511 / 0.00515	-0.00206 / 0.00206	0.00574 / -0.00578	-3.82e-06 / 3.73e-06	-2.28e-06 / 2.31e-06
MET_SoftTrk_ResoPerp	-0.00754 / 0.00754	-0.0139 / 0.0139	-0.000434 / 0.000434	-0.00264 / 0.00264	-0.0168 / 0.0168	0.000999 / -0.000999	-0.00281 / 0.00281	-0.00194 / 0.00194
FT_EFF_Eigen_C_1	0.000438 / -0.000438	0.000868 / -0.000868	0.000443 / -0.000443	0.000905 / -0.000906	0.000146 / -0.000147	-0.000525 / 0.000525	0.000631 / -0.000631	0.000797 / -0.000797
FT_EFF_Eigen_B_4	5.39e-05 / -5.39e-05	2.19e-05 / -2.19e-05	0.00203 / -0.00203	7.22e-05 / -7.21e-05	6.39e-05 / -6.39e-05	-0.000144 / 0.000144	6.71e-05 / -6.7e-05	2.32e-05 / -2.32e-05
JET_EtaIntercalibration_TotalStat	0.000684 / -0.00238	0.000261 / -0.0016	-0.000353 / 0.000777	0.00098 / 8.01e-05	0.00169 / 8.1e-05	-0.00152 / 0.00177	0.00142 / -0.00101	0.00116 / -0.000998
JET_JER_EffectiveNP_3	0.00419 / -0.00419	0.00606 / -0.00606	-0.00259 / 0.00259	0.00418 / -0.00419	0.000245 / -0.000245	-0.00177 / 0.00177	0.000265 / -0.000265	0.0093 / -0.0093
MET_SoftTrk_Scale	-0.00626 / 0.0084	-0.0127 / 0.0112	-0.00128 / 0.00212	-0.00181 / 0.00351	-0.0185 / 0.0186	0.00196 / -0.00204	-0.0033 / 0.00335	-0.00201 / 0.00212
MUON_ID	-0.000148 / -0.00329	-0.000532 / 0.000145	-0.00109 / 0.000531	-0.00025 / 0.00135	-0.00059 / 0.00136	-9.14e-06 / -0.000148	-0.000647 / 0.00102	-0.000665 / 0.000659
JET_EffectiveNP_Modelling1	0.00622 / -0.0123	0.00563 / -0.00444	0.0032 / -0.00359	0.00853 / -0.00933	0.01 / -0.00662	-0.0151 / 0.0141	0.0115 / -0.0114	0.00648 / -0.0069
JET_EtaIntercalibration_NonClosure_posEta	0.0011 / 3.06e-07	0.0036 / 0.000179	0.000289 / -0.00016	0.000812 / 0.000608	0.000506 / -0.000297	0.000299 / 0.000309	0.000309 / -0.000204	8.52e-05 / -0.000152
FT_EFF_Eigen_B_5	-9.64e-06 / 9.68e-06	-5.7e-06 / 5.71e-06	-0.000203 / 0.000203	-1.45e-05 / 1.45e-05	-1.32e-05 / 1.32e-05	2.22e-05 / -2.22e-05	-1.5e-05 / 1.5e-05	-6.04e-06 / 6.07e-06
MUON_EFF_TTVA_STAT	9.73e-05 / -9.73e-05	0.000123 / -0.000123	0.000129 / -0.000129	0.000157 / -0.000157	0.000146 / -0.000146	-5.54e-05 / 5.54e-05	0.000131 / -0.000131	0.000133 / -0.000133
MUON_EFF_TrigSystUncertainty	-0.00344 / 0.00351	-0.00339 / 0.00346	-0.00334 / 0.0034	-0.00319 / 0.00325	-0.00413 / 0.00421	0.00242 / -0.00247	-0.00368 / 0.00375	-0.00352 / 0.0359
JET_JER_EffectiveNP_6	0.00248 / -0.00248	-0.00367 / 0.00367	-0.0025 / 0.0025	-0.00233 / 0.00233	-0.00368 / 0.00368	0.00376 / -0.00376	-0.000725 / 0.000725	-0.000539 / 0.000539
JET_SingleParticle_HighPt	2.09e-08 / 2.09e-08	6.48e-09 / 6.48e-09	-2.34e-08 / -2.34e-08	-5.37e-08 / -5.37e-08	-4.87e-08 / -4.87e-08	-9.57e-09 / -9.57e-09	9.64e-07 / 9.64e-07	-1.53e-08 / -1.53e-08
JET_JER_EffectiveNP_8	-0.00213 / 0.00213	-0.000858 / 0.000858	-0.000412 / 0.000412	-0.00493 / 0.00493	-0.0005 / 0.0005	0.0104 / -0.0104	-0.000817 / 0.000817	-9.69e-05 / 9.69e-05
JET_EtaIntercalibration_NonClosure_negEta	0.00187 / 0.000402	-0.000209 / -0.000815	0.00439 / -0.000643	0.00149 / -0.00128	0.00146 / -0.00128	-0.00172 / 0.00154	0.0083 / -0.00078	0.000363 / -0.000285
JET_EffectiveNP_Statistical5	-0.00043 / 0.00184	-0.000357 / 0.000338	-0.000647 / 0.000708	-0.000249 / 0.000707	-0.000664 / 0.00201	0.000689 / -0.000709	-0.000677 / 0.000683	-0.000232 / 0.000271
MUON_EFF_TTVA_SYS	0.00013 / -0.00012	0.00017 / -0.000159	0.000171 / -0.000157	0.00022 / -0.000201	0.000206 / -0.000193	-6.36e-05 / 6.15e-05	0.000174 / -0.000162	0.000177 / -0.000163
FT_EFF_Eigen_C_3	-0.000141 / 0.000141	-8.37e-05 / 8.37e-05	-0.00015 / 0.00015	0.000122 / -0.000123	-0.000106 / 0.000106	0.000138 / -0.000138	-0.000114 / 0.000114	-6.34e-05 / 6.34e-05
JET_JER_EffectiveNP_1	0.00203 / -0.00202	0.0113 / -0.0113	0.00641 / -0.00686	0.0691 / -0.0686	0.0125 / -0.0124	-0.0288 / 0.0288	0.00422 / -0.00419	0.00164 / -0.00163
JET_JER_EffectiveNP_5	-0.00664 / 0.00664	-0.0027 / 0.0027	-0.00125 / 0.00125	0.000279 / -0.000279	-0.000467 / 0.000467	0.00817 / -0.00817	-0.00088 / 0.00088	-0.00054 / 0.00054
FT_EFF_extrapolation	-0.000184 / 0.000184	-0.00044 / 0.000441	-0.000526 / 0.000528	-0.000505 / 0.000505	-0.000131 / 0.000131	0.000168 / -0.000169	-0.000174 / 0.000175	-0.00031 / 0.000311
JET_Flavor_Response	-0.0161 / 0.0165	-0.00935 / 0.0099	-0.0132 / 0.0142	-0.0192 / 0.0208	-0.0181 / 0.0197	0.027 / -0.0276	-0.0222 / 0.0239	-0.0122 / 0.0129
JET_EffectiveNP_Statistical4	0.000795 / 0.000813	6.87e-05 / -0.00024	0.000806 / -0.000484	0.00122 / -0.000403	0.000972 / -0.000596	-0.000887 / 0.000945	0.000836 / -0.000847	0.000387 / -0.000348
EL_EFF_Reco_TOTAL_1NPCOR_PLUS_UNCOR	0.00161 / -0.00161	0.00173 / -0.00173	0.0164 / -0.0164	0.00167 / -0.00167	0.00162 / -0.00162	-0.0024 / 0.0024	0.0164 / -0.00164	0.00159 / -0.00159
MUON_MS	-0.000527 / 0.000165	-0.000658 / 0.000556	-0.000634 / 0.000476	-0.000377 / 0.000993	-6.98e-05 / 0.000581	0.000113 / 5.71e-05	-0.000365 / 0.000772	-0.000403 / 0.000402
EG_RESOLUTION_ALL	0.000998 / 0.000525	-0.000741 / 0.000184	-0.000239 / 9.96e-05	0.000351 / -0.000453	0.000315 / 9.37e-05	0.000862 / -0.00234	-0.000149 / 0.00136	-2.72e-05 / 6.3e-05
Run2luminosityuncertainty	0.017 / -0.017	0.017 / -0.017	0.017 / -0.017	0.017 / -0.017	0.017 / -0.017	0.017 / -0.017	0.017 / -0.017	0.017 / -0.017
MULTIJET_LeptonIsolation	0 / 0	0 / 0	0 / 0	0 / 0	0 / 0	0.238 / -0.159	0 / 0	0 / 0
MULTIJET_FitBinning	0 / 0	0 / 0	0 / 0	0 / 0	0 / 0	0.0271 / -0.0823	0 / 0	0 / 0
MULTIJET_FitVariable	0 / 0	0 / 0	0 / 0	0 / 0	0 / 0	0.0801 / -0.177	0 / 0	0 / 0
MULTIJET_FlatFit	0 / 0	0 / 0	0 / 0	0 / 0	0 / 0	0.0989 / -0.0872	0 / 0	0 / 0
SCALE_UNCERTAINTY	0 / 0	0 / 0	0 / 0	0 / 0	0 / 0	0 / 0	0 / 0	0.00794 / -0.00794
gamma_stat_CR2_combined_bin_0	0.00639 / -0.00632	0.00538 / -0.00533	0.00541 / -0.00536	0.00413 / -0.00409	0.00507 / -0.00502	0.00518 / -0.00512	0.0055 / -0.00544	0 / 0
gamma_stat_CR2_combined_bin_1	0.000945 / -0.00094	0.00147 / -0.00146	0.00161 / -0.0016	0.00205 / -0.00204	0.00177 / -0.00176	0.0014 / -0.00139	0.00145 / -0.00149	0 / 0
gamma_stat_CR2_combined_bin_2	0.000227 / -0.000226	0.000612 / -0.000609	0.000496 / -0.000493	0.00113 / -0.00112	0.00658 / -0.00654	0.000804 / -0.000799	0.000509 / -0.000506	0 / 0
gamma_stat_CR2_combined_bin_3	4.61e-05 / -4.55e-05	0.000273 / -0.000269	0.000125 / -0.000123	0.000578 / -0.00057	0.000216 / -0.000213	0.000455 / -0.000449	0.000179 / -0.000177	0 / 0
gamma_stat_CR2_combined_bin_4	3.48e-05 / -3.41e-05	0.000176 / -0.000173	5.73e-05 / -5.61e-05	0.000498 / -0.000488	0.000103 / -0.000101	0.000384 / -0.000376	9.47e-05 / -9.27e-05	0 / 0
μ_{QcdW}	0.0537 / -0.0513	0 / 0	0 / 0	0 / 0	0 / 0	0 / 0	0.0537 / -0.0513	0 / 0
μ_{Ewk}	0 / 0	0 / 0	0 / 0	0 / 0	0 / 0	0 / 0	0 / 0	0.0729 / -0.0826

Table D.2: Relative post-fit uncertainty on event yields due to each nuisance parameter in CR2

	Sherpa 2.2.11 QCD $W \to \tau\nu$	Other EWK	Top	Diboson	Z+jets	Multijet	Powheg QCD $W \to \ell\nu$	Powheg EWK $W \to \ell\nu$
EL_EFF_Trigger_TOTAL_1NPCOR_PLUS_UNCOR	0.00134 / -0.00134	0.00188 / -0.00188	0.00139 / -0.00139	0.00158 / -0.00158	0.00178 / -0.00178	-1.98e-08 / -1.98e-08	0.0014 / -0.0014	0.00136 / -0.00136
FT_EFF_Eigen_Light_2	-0.000367 / 0.000368	-8.41e-05 / 8.43e-05	-0.000449 / 0.000449	-0.000234 / 0.000234	-0.000421 / 0.000421	0.000506 / -0.000507	-0.000372 / 0.000373	-8.61e-05 / 8.63e-05
JET_JvtEfficiency	0.00459 / -0.00157	-0.000334 / -0.000367	-0.000332 / -0.00107	0.00123 / -0.00187	-0.000363 / -0.000760	-0.00173 / 0.00235	0.00175 / -0.00228	0.000996 / -0.00142
EG_SCALE_LARTEMPERATURE_EXTRA2015PRE	-1.89e-08 / -1.89e-08	2.4e-08 / 2.4e-08	3.64e-08 / 3.64e-08	-2.47e-08 / -2.47e-08	2.51e-08 / 2.51e-08	-1.98e-08 / -1.98e-08	-2.84e-09 / -2.84e-09	-6.44e-09 / -6.44e-09
MUON_EFF_RECO_SYS	-1.89e-08 / -1.89e-08	2.4e-08 / 2.4e-08	3.64e-08 / 3.64e-08	-2.47e-08 / -2.47e-08	2.51e-08 / 2.51e-08	-1.98e-08 / -1.98e-08	-2.84e-09 / -2.84e-09	-6.44e-09 / -6.44e-09
EG_SCALE_LARCALIB_EXTRA2015PRE	-1.89e-08 / -1.89e-08	2.4e-08 / 2.4e-08	3.64e-08 / 3.64e-08	-2.47e-08 / -2.47e-08	2.51e-08 / 2.51e-08	-1.98e-08 / -1.98e-08	-2.84e-09 / -2.84e-09	-6.44e-09 / -6.44e-09
JET_Pileup_PtTerm	0.00076 / -0.00442	0.00503 / -0.00509	0.00524 / -0.00569	0.00806 / -0.00463	0.00396 / -0.00302	-0.00886 / 0.00876	0.00456 / -0.00514	0.00326 / -0.00512
EG_SCALE_ALLCORR	0.00143 / -0.00146	0.00423 / -0.00415	0.00148 / -0.00148	0.00124 / -0.00124	0.00359 / -0.00362	0.000548 / -0.000557	0.00182 / -0.00181	0.0017 / -0.00169
JET_EffectiveNP_Detector2	-1.64e-05 / -1.02e-05	-3.98e-07 / 8.07e-07	0.000293 / -4.25e-05	0.000451 / -4.14e-05	0.000148 / -0.000183	-0.000145 / 0.000347	0.000126 / -0.000153	0.000201 / -0.000202
JET_EtaIntercalibration_Modelling	0.0087 / -0.0223	0.0173 / -0.0193	0.0156 / -0.0156	0.0267 / -0.0239	0.021 / -0.0208	-0.0267 / 0.0269	0.0237 / -0.0248	0.0212 / -0.0229
EG_SCALE_E4SCINTILLATOR	-1.95e-05 / -2.72e-05	-0.000288 / 1.78e-06	-7.94e-05 / -2.52e-05	-4.96e-07 / 2.08e-05	-0.000133 / 0.000204	-0.000129 / -5.29e-05	-6.94e-05 / 3.58e-05	7.89e-07 / 7.88e-05
JET_BJES_Response	-1.89e-08 / -1.89e-08	2.4e-08 / 2.4e-08	3.64e-08 / 3.64e-08	-2.47e-08 / -2.47e-08	-5.88e-07 / -5.88e-07	-1.98e-08 / -1.98e-08	-1.43e-06 / -1.43e-06	-6.44e-09 / -6.44e-09
MUON_EFF_TrigStatUncertainty	0.000573 / -0.000594	0.000547 / -0.000565	0.000692 / -0.000718	0.000657 / -0.000681	0.000618 / -0.000639	-0.000377 / 0.000391	0.000664 / -0.000689	0.000683 / -0.000707
FT_EFF_Eigen_B_1	0.000264 / -0.000263	-5.04e-05 / 5.6e-05	0.0281 / -0.0278	0.000307 / -0.000308	0.0019 / -0.000191	-0.000124 / 0.000127	8.21e-05 / -8.31e-05	3.34e-05 / -3.23e-05
MUON_SCALE	-0.00317 / -0.00192	-0.000647 / 0.00213	-0.000925 / 0.00102	-0.00114 / 0.00175	-0.000873 / 0.0165	0.000229 / -0.000591	-0.00139 / 0.00126	-0.00111 / 0.00103
MUON_EFF_RECO_STAT	0.000378 / -0.000379	0.000325 / -0.000325	0.000381 / -0.000381	0.000376 / -0.000376	0.000389 / -0.000389	-0.000155 / 0.000155	0.000402 / -0.000402	0.000393 / -0.000394
JET_JER_EffectiveNP_7	-0.00166 / 0.00166	0.00365 / -0.00365	-0.000264 / 0.000264	-0.00221 / 0.00221	-0.00169 / 0.00169	0.00144 / -0.00144	-0.000379 / 0.000379	0.00128 / -0.00128
JET_Pileup_OffsetMu	0.00367 / -0.0171	0.0127 / -0.00621	0.0089 / -0.00471	0.0169 / -0.0062	0.0127 / -0.00888	-0.0144 / 0.015	0.013 / -0.0107	0.0132 / -0.0105
FT_EFF_Eigen_Light_3	-0.000495 / 0.000496	-0.000467 / 0.000467	-0.000483 / 0.000483	-0.000459 / 0.000459	-0.000535 / 0.000536	0.000623 / -0.000623	-0.000502 / 0.000503	-0.000467 / 0.000467
JET_JER_EffectiveNP_1	-0.00109 / 0.00109	-0.000226 / 0.000226	0.000352 / -0.000352	-0.00108 / 0.00108	-0.00157 / 0.00157	0.000127 / -0.000157	-5.25e-05 / 5.25e-05	0.00198 / -0.00198
MUON_EFF_ISO_SYS	0.00616 / -0.00617	0.00401 / -0.00401	0.00417 / -0.00417	0.0037 / -0.0037	0.00447 / -0.00447	-2.01e-08 / -1.94e-08	0.0049 / -0.0049	0.00462 / -0.00462
JET_EffectiveNP_Mixed2	-0.00281 / 0.00201	-0.000145 / -0.000288	-0.00196 / 0.00217	-0.00241 / 0.00272	-0.00249 / 0.00259	0.00424 / -0.00238	-0.00287 / 0.0028	-0.0026 / 0.00206
JET_EffectiveNP_Mixed1	0.00213 / -0.00338	0.0108 / -0.000276	0.00294 / -0.00235	0.00402 / -0.00134	0.00165 / -0.00184	-0.00228 / 0.00343	0.00255 / -0.00265	0.00166 / -0.00207
JET_JER_EffectiveNP_1	-0.00501 / 0.00501	-0.00686 / 0.00686	-0.000773 / 0.000773	-0.0017 / 0.0017	-0.00395 / 0.00395	-0.000754 / 0.000754	-0.00132 / 0.00132	-0.00142 / 0.00142
JET_PunchThrough_MC16	-6.33e-05 / 8.91e-05	-0.00031 / 0.000582	6.07e-05 / -7.12e-05	6.11e-05 / -0.000762	-6.03e-05 / 1.26e-05	-5.03e-05 / 8.61e-06	2.26e-05 / -1.45e-05	0.00012 / -0.000104
FT_EFF_Eigen_B_7	-4.63e-07 / 4.99e-07	-3.35e-07 / 3.23e-07	-1.09e-05 / 1.1e-05	-3.01e-07 / 3.42e-07	-5.29e-07 / 5.18e-07	9.92e-07 / -1.03e-06	-4.55e-07 / 5.25e-07	-2.87e-07 / 2.74e-07
EG_SCALE_LARTEMPERATURE_EXTRA2016PRE	-1.89e-08 / -1.89e-08	2.4e-08 / 2.4e-08	3.64e-08 / 3.64e-08	-2.47e-08 / -2.47e-08	2.51e-08 / 2.51e-08	-1.98e-08 / -1.98e-08	-2.84e-09 / -2.84e-09	-6.44e-09 / -6.44e-09
JET_EffectiveNP_Modelling4	0.000181 / 4.16e-05	-0.000224 / 0.000379	0.000558 / -0.000114	0.000477 / 0.000233	0.000132 / -0.000264	-0.000201 / 0.000517	0.00036 / -0.000327	0.000492 / -0.000359
JET_Flavor_Composition	0.0505 / -0.0589	0.0431 / -0.0378	0.0295 / -0.0264	0.0492 / -0.0415	0.0459 / -0.0411	-0.0492 / 0.0486	0.0484 / -0.046	0.0448 / -0.0445
JET_EffectiveNP_Statistical2	-0.00279 / 0.00179	0.000234 / 0.00164	-0.000319 / 0.000361	-0.00164 / 0.00254	-0.00193 / 0.0017	0.00357 / -0.0012	-0.00152 / 0.00153	-0.00165 / 0.0015
PRW_DATASF	0.00395 / 0.000978	0.00653 / 0.00745	-0.00193 / -0.00155	0.00873 / -0.00214	0.006 / -0.00335	-0.036 / 0.0207	0.00118 / -0.00112	0.00444 / -0.00165
JET_Pileup_RhoTopology	0.0303 / -0.0292	0.0218 / -0.0214	0.0036 / -0.00381	0.016 / -0.0164	0.0221 / -0.0217	-0.0248 / 0.0256	0.0249 / -0.0243	0.0263 / -0.0256
FT_EFF_Eigen_B_2	0.000113 / -0.000111	0.000282 / -0.000279	-0.00794 / 0.00797	5.55e-05 / -5.53e-05	0.000181 / -0.00018	0.000138 / -0.00014	0.000225 / -0.000224	0.000172 / -0.00017
JET_JER_EffectiveNP_2	0.0131 / -0.0129	0.0177 / -0.0174	0.0685 / -0.0068	0.0103 / -0.0102	0.0171 / -0.0169	-0.0262 / 0.0265	0.0618 / -0.00614	0.00743 / -0.00737
JET_EffectiveNP_Statistical6	6.98e-05 / 0.000417	0.000961 / -7.28e-06	0.000549 / -0.000256	0.000519 / 0.000256	0.000242 / -0.000392	-0.000386 / 0.000433	0.000406 / -0.000421	0.000498 / -0.000487
FT_EFF_Eigen_Light_1	0.00519 / -0.00516	0.00492 / -0.00488	0.00507 / -0.00504	0.00486 / -0.00483	0.00555 / -0.00551	-0.00614 / 0.00609	0.00503 / -0.00499	0.0048 / -0.00476
JET_EffectiveNP_Statistical1	-4.16e-05 / -0.000529	-0.000785 / 0.000816	0.000364 / 0.000121	0.000235 / 0.000739	0.000166 / 6.59e-05	-0.00011 / 0.000382	0.000157 / -0.000211	0.000226 / -0.000133
EL_EFF_ID_TOTAL_1NPCOR_PLUS_UNCOR	0.00258 / -0.00258	0.00374 / -0.00373	0.0027 / -0.00269	0.00334 / -0.00334	0.00377 / -0.00376	-0.00266 / 0.00265	0.00282 / -0.00281	0.00271 / -0.00271
JET_JER_EffectiveNP_9	0.0018 / -0.0018	0.0103 / -0.0103	0.00193 / -0.00193	0.00378 / -0.00378	0.00477 / -0.00477	-0.0038 / 0.0038	0.00176 / -0.00176	0.00141 / -0.00141
JET_EffectiveNP_Detector1	0.00107 / -0.0021	0.000683 / -0.000553	0.000939 / -0.000507	0.0013 / -0.00109	0.00149 / -0.00138	-0.00114 / 0.00189	0.0012 / -0.00132	0.00117 / -0.00103
JET_Pileup_OffsetNPV	0.0176 / -0.0164	0.00988 / -0.00902	0.0043 / -0.00366	0.0132 / -0.0082	0.0139 / -0.0117	-0.0175 / 0.0154	0.0141 / -0.0129	0.0148 / -0.0135
FT_EFF_Eigen_B_8	-1.89e-08 / 5.51e-08	-3.59e-08 / 2.41e-08	-8.5e-07 / 8.12e-07	-2.47e-08 / 6.67e-08	-3.66e-08 / 2.49e-08	8.14e-08 / -1.21e-07	-2.68e-09 / 7.26e-08	-6.44e-09 / -6.44e-09
FT_EFF_Eigen_B_6	3.24e-06 / -3.2e-06	3.07e-06 / -3.09e-06	7.75e-05 / -7.76e-05	2.82e-06 / -2.78e-06	3.59e-06 / -3.61e-06	-6.9e-06 / 6.86e-06	3.54e-06 / -3.55e-06	2.17e-06 / -2.11e-06
JET_EffectiveNP_Modelling3	-0.00101 / -0.000288	0.000591 / 0.000346	-0.00205 / 0.0018	0.000416 / 0.0013	-0.000944 / 0.000973	0.0214 / -0.00134	-0.00134 / 0.00126	-0.00115 / 0.00108
JET_JER_DataVsMC_MC16	0.00601 / -0.00602	-0.00541 / 0.00541	-0.00317 / 0.00317	-0.00705 / 0.00705	-0.00638 / 0.00639	0.00751 / -0.00751	-0.00301 / 0.00301	-0.00196 / 0.00196
EL_EFF_Iso_TOTAL_1NPCOR_PLUS_UNCOR	0.00374 / -0.000375	0.000503 / -0.000524	0.000385 / -0.000388	0.000491 / -0.000517	0.000448 / -0.000458	-1.86e-08 / -2.08e-08	0.00037 / -0.000381	0.000394 / -0.000403
JET_JER_EffectiveNP_4	0.00337 / -0.00337	-0.00604 / 0.00604	-0.000912 / 0.000912	-0.00331 / 0.00331	-0.000292 / 0.000232	0.0069 / -0.00689	-0.00212 / 0.00212	-0.00583 / 0.00583
JET_EffectiveNP_Modelling2	0.00518 / 0.000891	-0.000638 / 0.00174	0.00078 / -0.00081	0.00539 / 0.00885	-0.000318 / -1.99e-05	-0.000266 / 0.00014	0.00258 / -0.00195	0.000206 / 1.28e-05
MUON_SAGITTA_RESBIAS	0.00806 / 0.00416	0.00571 / 0.00189	0.00294 / 0.00165	0.00429 / -0.000586	0.00199 / 0.000712	0.00153 / -0.000948	0.00282 / 0.00158	0.00201 / 0.0014
JET_EtaIntercalibration_NonClosure_2018data	0.00479 / -0.0101	0.00169 / -0.00812	0.00334 / -0.00313	0.00486 / -0.00355	0.0049 / -0.00555	-0.00696 / 0.00385	0.00415 / -0.00437	0.00234 / -0.00408
JET_JvtEfficiency	-0.00326 / 0.00343	-0.00162 / 0.00179	-0.000981 / 0.00161	-8.58e-05 / 0.000289	-0.00325 / 0.000372	-4.9e-05 / -0.000607	0.000645 / -0.000434	-0.000465 / -0.00041
JET_EtaIntercalibration_NonClosure_highE	3.18e-05 / 1.39e-05	-0.000299 / 0.000289	1.68e-05 / 2.54e-05	8.97e-05 / -0.000387	2.05e-05 / -5.76e-06	6.09e-05 / -8.84e-06	-5.42e-06 / 4.97e-06	-5.91e-05 / -1.85e-05
JET_EffectiveNP_Statistical3	-0.000646 / 0.000232	0.000743 / -0.000788	0.000106 / 0.000172	0.0007 / 0.000172	0.00374 / -0.0002	0.000323 / -0.000142	-0.000156 / 0.00018	-6.66e-05 / 0.000185
JET_JER_EffectiveNP_1	-0.0016 / 0.0016	0.00668 / -0.00667	0.00201 / -0.00201	0.000285 / -0.000285	0.00421 / -0.00421	-0.0045 / 0.0045	0.00157 / -0.00157	0.00117 / -0.00117
FT_EFF_Eigen_B_0	0.00555 / -0.00512	0.00441 / -0.00417	0.18 / -0.162	-0.00492 / -0.00468	0.0063 / -0.00596	-0.0136 / 0.0127	0.00583 / -0.00551	0.00336 / -0.00319
MET_SoftTrk_ResoPara	-0.0102 / 0.0102	-0.0124 / 0.0124	-0.00223 / 0.00224	-2.22e-05 / 2.22e-05	-0.0193 / 0.0194	0.00181 / -0.00181	-0.00309 / 0.00309	-0.00279 / 0.00279
MUON_EFF_RECO_SYS	0.00159 / -0.00159	0.00155 / -0.00154	0.00162 / -0.00161	0.00181 / -0.00181	0.00202 / -0.00202	-0.000542 / 0.000545	0.00184 / -0.00184	0.00173 / -0.00172
MUON_EFF_ISO_STAT	0.000375 / -0.000375	0.000462 / -0.000462	0.000561 / -0.000561	0.000705 / -0.000705	0.000582 / -0.000582	-1.96e-08 / -2e-08	0.000547 / -0.000547	0.000573 / -0.000573
MUON_EFF_RECO_STAT	-1.89e-08 / -1.89e-08	2.4e-08 / 2.4e-08	3.64e-08 / 3.64e-08	-2.47e-08 / -2.47e-08	2.51e-08 / 2.51e-08	-1.98e-08 / -1.98e-08	-2.84e-09 / -2.84e-09	-6.44e-09 / -6.44e-09
JET_EffectiveNP_Mixed3	0.000289 / -0.000566	0.000993 / 0.000618	0.000203 / -6.17e-05	0.000985 / -0.000366	0.000827 / -0.00102	-0.000599 / 0.000641	0.000599 / -0.00062	0.000666 / -0.000524
FT_EFF_Eigen_C_0	0.0102 / -0.01	0.0112 / -0.011	0.0173 / -0.017	0.015 / -0.0148	0.00928 / -0.00911	-0.0102 / 0.0101	0.00948 / -0.00931	0.00812 / -0.008
FT_EFF_Eigen_Light_0	0.0353 / -0.034	0.0335 / -0.0322	0.0332 / -0.032	0.0331 / -0.0319	0.0377 / -0.0362	-0.0374 / 0.037	0.0339 / -0.0326	0.0323 / -0.0311
FT_EFF_Eigen_B_3	-0.000291 / 0.000292	-0.000209 / 0.00021	-0.000859 / 0.00862	-0.00016 / 0.000217	-0.000319 / 0.00019	0.000712 / -0.000715	-0.000302 / 0.000303	-0.000164 / 0.000164
FT_EFF_Eigen_C_2	0.000148 / -0.000148	0.000122 / -0.000122	-6.43e-05 / 6.42e-05	-0.000118 / 0.000118	0.000139 / -0.000139	-7.48e-05 / 7.48e-05	5.88e-05 / -5.88e-05	1.6e-05 / -1.59e-05
FT_EFF_extrapolation	-0.00126 / 0.00126	-0.00431 / 0.00434	-0.00462 / 0.00462	-0.00417 / 0.00422	-0.00218 / 0.00219	0.000838 / -0.00084	-5.36e-06 / 5.43e-06	-1.9e-06 / 1.89e-06
MET_SoftTrk_ResoPerp	-0.00922 / 0.00922	-0.0147 / 0.0147	-0.00214 / 0.00214	-0.00479 / 0.00479	-0.016 / 0.016	0.00079 / -0.00079	-0.00351 / 0.00351	-0.00371 / 0.00371
FT_EFF_Eigen_C_1	0.00041 / -0.00041	0.00112 / -0.00112	0.000519 / -0.000519	0.00124 / -0.00124	0.000164 / -0.000164	-0.000154 / 0.000154	0.000617 / -0.000617	0.0097 / -0.00097
FT_EFF_Eigen_B_4	6.58e-05 / -6.58e-05	4.54e-05 / -4.54e-05	0.00183 / -0.00183	6.14e-05 / -6.14e-05	7e-05 / -7e-05	-0.000154 / 0.000154	6.92e-05 / -6.92e-05	3.47e-05 / -3.46e-05
JET_EtaIntercalibration_TotalStat	0.00437 / -0.0674	0.00166 / -0.00144	0.00191 / -0.00199	0.0039 / -0.00293	0.0045 / -0.00393	-0.00386 / 0.00578	0.00418 / -0.00406	0.00373 / -0.00419
JET_JER_EffectiveNP_3	-0.00121 / 0.00121	-0.00653 / 0.00653	-0.00416 / 0.00416	-0.00463 / 0.00464	-0.00512 / 0.00513	0.0141 / -0.0141	-0.00256 / 0.00256	-0.00512 / 0.00512
MET_SoftTrk_Scale	-0.0114 / 0.0109	-0.0132 / 0.0192	-0.00196 / 0.00246	-0.00193 / 0.00431	-0.0182 / 0.0176	0.00194 / -0.00161	-0.00327 / 0.0032	-0.00268 / 0.0151
MUON_ID	-0.00117 / 0.00026	-0.00096 / -0.000339	-0.00109 / 0.00012	0.000104 / 0.0026	-0.000386 / 0.000592	-0.000373 / -0.000434	-0.000477 / 0.000852	-0.000901 / 0.000301
JET_EffectiveNP_Modelling1	0.0141 / -0.0194	0.0149 / -0.0191	0.0122 / -0.0118	0.0212 / -0.014	0.0182 / -0.0195	-0.0196 / 0.0229	0.0197 / -0.0217	0.0175 / -0.0205
JET_EtaIntercalibration_NonClosure_posEta	0.00207 / 0.000643	0.000751 / -0.000978	0.000477 / -0.000305	0.00131 / -0.000387	0.000495 / -0.000683	-0.000567 / 0.000336	0.000783 / -0.000535	0.000714 / -0.000442
FT_EFF_Eigen_B_5	-1.49e-05 / 1.49e-05	-1.59e-05 / 1.6e-05	-0.000275 / 0.000275	-1.13e-05 / 1.13e-05	-1.56e-05 / 1.56e-05	2.66e-05 / -2.66e-05	-1.62e-05 / 1.62e-05	-8.5e-06 / 8.49e-06
MUON_EFF_TTVA_STAT	0.000105 / -0.000105	0.000113 / -0.000113	0.000137 / -0.000137	0.000156 / -0.000157	0.000139 / -0.000139	-5.52e-05 / 5.51e-05	0.000135 / -0.000135	0.000137 / -0.000137
MUON_EFF_TrigSystUncertainty	-0.00354 / 0.00361	-0.00294 / 0.003	-0.00336 / 0.00343	-0.00326 / 0.00333	-0.0037 / 0.00377	0.00239 / -0.00243	-0.00371 / 0.00378	-0.00349 / 0.00355
JET_JER_EffectiveNP_6	-0.000127 / 0.000127	-0.0105 / 0.0105	-0.00247 / 0.00247	-0.00642 / 0.00642	-0.00646 / 0.00647	0.0163 / -0.0164	-0.00261 / 0.00261	-0.00316 / 0.00316
JET_SingleParticle_HighPt	-1.89e-08 / -1.89e-08	2.4e-08 / 2.4e-08	3.64e-08 / 3.64e-08	-2.47e-08 / -2.47e-08	-5.9e-07 / -5.88e-07	-1.98e-08 / -1.98e-08	-1.43e-06 / -1.43e-06	-6.44e-09 / -6.44e-09
JET_JER_EffectiveNP_8	-0.00242 / 0.00242	0.00142 / -0.00142	-0.000124 / 0.000124	0.00272 / -0.00272	-0.00179 / 0.00179	-0.00481 / 0.00481	0.00023 / -0.00023	0.00146 / -0.00146
JET_EtaIntercalibration_NonClosure_negEta	0.000754 / -0.000165	-0.000731 / -0.00076	0.00049 / -0.000252	0.000399 / -3.59e-05	0.000873 / -0.00119	-0.00192 / 0.00207	0.000918 / -0.00112	0.000631 / -0.000661
JET_EffectiveNP_Statistical5	-0.00058 / 0.000296	-0.000273 / 0.000634	-0.000391 / 0.000691	-0.000141 / 0.000941	-0.0071 / 0.000812	0.000484 / -0.000683	-0.000533 / 0.000459	-0.000372 / 0.000537
MUON_EFF_TTVA_SYS	0.000122 / -0.000113	0.000154 / -0.00014	0.000184 / -0.000169	0.0002008 / -0.000195	0.000196 / -0.000183	-6.26e-05 / 6.06e-05	0.000181 / -0.000165	0.000185 / -0.000171
FT_EFF_Eigen_C_3	-9.88e-05 / 9.88e-05	-6.66e-05 / 6.66e-05	0.000122 / 0.000122	-6.81e-05 / 6.82e-05	-8.45e-05 / 8.46e-05	9.03e-05 / -9.03e-05	-8.56e-05 / 8.57e-05	-4.21e-05 / 4.22e-05
JET_JER_EffectiveNP_1	-0.000766 / 0.000762	0.0204 / -0.0202	0.00836 / -0.00883	0.0163 / -0.0162	0.0179 / -0.0177	-0.0269 / 0.0269	0.00807 / -0.00801	0.0101 / -0.00997
JET_JER_EffectiveNP_5	-0.00441 / 0.00442	-0.00274 / 0.00274	-0.00179 / 0.0179	-0.00405 / 0.00405	-0.00528 / 0.00528	0.00235 / -0.00235	-0.00125 / 0.00125	-0.00038 / 0.00038
FT_EFF_extrapolation	-0.000263 / 0.000264	-0.000564 / 0.000565	-0.00063 / 0.000632	-0.00063 / 0.000531	-0.000201 / 0.000202	0.000202 / -0.000203	-0.000238 / 0.000238	-0.000447 / 0.000448
JET_Flavor_Response	-0.0362 / 0.0385	-0.0231 / 0.0243	-0.0225 / 0.0243	-0.0319 / 0.0351	-0.0285 / 0.0308	0.0374 / -0.0379	-0.0317 / 0.0343	-0.0278 / 0.0296
JET_EffectiveNP_Statistical4	0.000435 / -0.000331	-0.000216 / 0.000421	0.000905 / -0.000599	0.000674 / -0.000236	4.6e-05 / -0.000132	-0.000709 / 0.000593	0.000544 / -0.000539	0.0007 / -0.000535
EL_EFF_Reco_TOTAL_1NPCOR_PLUS_UNCOR	0.00159 / -0.00159	0.00197 / -0.00197	0.0166 / -0.00166	0.00166 / -0.00166	0.00191 / -0.00191	-0.00196 / 0.00196	0.00167 / -0.00167	0.00158 / -0.00158
MUON_MS	0.00128 / -0.00499	-0.000848 / 0.00124	-0.000243 / 0.00054	0.000336 / -0.00044	0.000125 / 0.000131	-0.00019 / -0.000543	-0.00373 / 0.00395	-0.000362 / 0.000738
EG_RESOLUTION_ALL	-0.00116 / 0.000247	0.00192 / -0.000378	1.9e-05 / 6.22e-05	0.000442 / -9.71e-05	1.49e-05 / 0.000983	0.00177 / 0.0007	-9.73e-05 / 0.000139	-7.53e-05 / -2.28e-05
Run2luminosityuncertainty	0.017 / -0.017	0.017 / -0.017	0.017 / -0.017	0.017 / -0.017	0.017 / -0.017	0.017 / -0.017	0.017 / -0.017	0.017 / -0.017
MULTIJET_LeptonIsolation	0 / 0	0 / 0	0 / 0	0 / 0	0 / 0	0.208 / -0.135	0 / 0	0 / 0
MULTIJET_FitBinning	0 / 0	0 / 0	0 / 0	0 / 0	0 / 0	0.0506 / 0.00331	0 / 0	0 / 0
MULTIJET_FitVariable	0 / 0	0 / 0	0 / 0	0 / 0	0 / 0	0.00802 / -0.165	0 / 0	0 / 0
MULTIJET_FlatFit	0 / 0	0 / 0	0 / 0	0 / 0	0 / 0	0.102 / -0.0895	0 / 0	0 / 0
SCALE_UNCERTAINTY	0 / 0	0 / 0	0 / 0	0 / 0	0 / 0	0 / 0	0 / 0	0.00988 / -0.00988
gamma_stat_CR1_combined_bin_0	0.00621 / -0.00618	0.00492 / -0.00489	0.00509 / -0.00506	0.0413 / -0.00411	0.00476 / -0.00474	0.00482 / -0.0048	0.00536 / -0.00533	0 / 0
gamma_stat_CR1_combined_bin_1	0.00114 / -0.00113	0.00183 / -0.00182	0.0019 / -0.00189	0.00207 / -0.00206	0.002 / -0.002	0.00157 / -0.00157	0.00164 / -0.00163	0 / 0
gamma_stat_CR1_combined_bin_2	0.000237 / -0.000235	0.000731 / -0.000724	0.000582 / -0.000577	0.00109 / -0.00108	0.000769 / -0.000762	0.00101 / -0.001	0.000545 / -0.00054	0 / 0
gamma_stat_CR1_combined_bin_3	8.79e-05 / -8.59e-05	0.000395 / -0.000386	0.000168 / -0.000165	0.000742 / -0.000725	0.000286 / -0.000279	0.000639 / -0.000624	0.000217 / -0.000212	0 / 0
gamma_stat_CR1_combined_bin_4	3.42e-05 / -3.16e-05	0.000247 / -0.000228	9.47e-05 / -8.75e-05	0.0007 / -0.000646	0.000164 / -0.000152	0.000421 / -0.000389	0.000143 / -0.000132	0 / 0
μ_{QcdW}	0.0537 / -0.0513	0 / 0	0 / 0	0 / 0	0 / 0	0 / 0	0.0537 / -0.0513	0 / 0
μ_{Ewk}	0 / 0	0 / 0	0 / 0	0 / 0	0 / 0	0 / 0	0 / 0	0.0729 / -0.0826

Table D.3: Relative post-fit uncertainty on event yields due to each nuisance parameter in CR1

190

	Sherpa 2.2.11 QCD $W \to \tau\nu$	Other EWK	Top	Diboson	Z+jets	Multijet	Powheg QCD $W \to \ell\nu$	Powheg EWK $W \to \ell\nu$
EL_EFF_Trigger_TOTAL_1NPCOR_PLUS_UNCOR	0.00114 / -0.00114	0.00182 / -0.00182	0.00127 / -0.00127	0.0014 / -0.0014	0.00203 / -0.00203	2.26e-09 / 2.27e-09	0.00123 / -0.00123	0.00122 / -0.00122
FT_EFF_Eigen_Light_2	-0.00459 / 0.00046	-0.000256 / 0.000256	-0.000509 / 0.000509	-0.000365 / 0.000365	-0.000597 / 0.000597	0.00411 / -0.00411	-0.000483 / 0.000483	-0.000255 / 0.000256
JET_JvtEfficiency	0.00052 / 0.00134	-0.000446 / -0.000265	-0.000559 / 0.000829	0.00115 / -0.0018	-0.000574 / -0.000541	-0.000982 / 0.00145	0.0018 / -0.00233	0.000989 / -0.00137
EG_SCALE_LARTEMPERATURE_EXTRA2015PRE	2.58e-08 / 2.58e-08	-2.21e-08 / -2.21e-08	1.38e-08 / 1.38e-08	2.1e-08 / 2.1e-08	8.15e-09 / 8.15e-09	2.26e-09 / 2.26e-09	-2.97e-08 / -2.97e-08	-2.37e-08 / -2.37e-08
MUON_EFF_RECO_SYS	2.58e-08 / 2.58e-08	-2.21e-08 / -2.21e-08	1.38e-08 / 1.38e-08	2.1e-08 / 2.1e-08	8.15e-09 / 8.15e-09	2.26e-09 / 2.26e-09	-2.97e-08 / -2.97e-08	-2.37e-08 / -2.37e-08
EG_SCALE_LARCALIB_EXTRA2015PRE	2.58e-08 / 2.58e-08	-2.21e-08 / -2.21e-08	1.38e-08 / 1.38e-08	2.1e-08 / 2.1e-08	8.15e-09 / 8.15e-09	2.26e-09 / 2.26e-09	-2.97e-08 / -2.97e-08	-2.37e-08 / -2.37e-08
JET_Pileup_PtTerm	0.0102 / 0.00165	0.00662 / -0.0033	0.00533 / -0.00402	0.00216 / -0.00324	0.00361 / -0.00317	-0.00418 / 0.00676	0.00586 / -0.00766	0.00294 / -0.00303
EG_SCALE_ALLCORR	0.00279 / -0.0027	0.00454 / -0.00452	0.00124 / -0.00123	0.000903 / -0.000953	0.00391 / -0.00389	-0.000477 / 0.000461	0.00148 / -0.00148	0.00144 / -0.00143
JET_EffectiveNP_Detector2	-1.52e-05 / -0.000355	-2.5e-05 / -0.00188	0.000197 / -0.000205	0.0044 / -0.000159	0.000281 / -8.39e-05	-9.45e-05 / 0.000123	0.000142 / -0.000162	9.6e-05 / -0.000112
JET_EtaIntercalibration_Modelling	0.0345 / -0.0255	0.0286 / -0.0255	0.0205 / -0.0182	0.0263 / -0.0271	0.0313 / -0.0291	-0.017 / 0.0225	0.0269 / -0.0283	0.0268 / -0.0265
EG_SCALE_E4SCINTILLATOR	-0.000136 / -2.36e-05	3.03e-06 / 0.000482	7.37e-06 / 1.63e-05	-2.03e-05 / 0.00031	-0.0013 / 0.000132	2.54e-05 / 4.51e-06	-2.1e-05 / 4.2e-05	-4.67e-05 / -4.15e-06
JET_BJES_Response	2.58e-08 / 2.58e-08	-2.21e-08 / -2.21e-08	1.38e-08 / 1.38e-08	2.1e-08 / 2.1e-08	8.16e-09 / 8.16e-09	2.26e-09 / 2.26e-09	-2.97e-08 / -2.97e-08	-2.37e-08 / -2.37e-08
MUON_EFF_TrigStatUncertainty	0.000651 / -0.000674	0.000481 / -0.000496	0.00074 / -0.000763	0.000715 / -0.000738	0.000381 / -0.000395	-0.000204 / 0.000211	0.000707 / -0.00073	0.000738 / -0.000761
FT_EFF_Eigen_B_1	6e-05 / -6e-05	4.26e-05 / -4.13e-05	0.0224 / -0.0223	0.000417 / -0.000417	0.000165 / -0.000166	-0.00159 / 0.00158	3.62e-05 / -3.7e-05	5.99e-05 / -6.07e-05
MUON_SCALE	-0.000743 / 0.00194	-0.000825 / 0.00169	-0.00069 / 0.000555	-0.000391 / 0.000542	-0.000672 / 0.0063	0.00115 / -0.000164	-0.000951 / 0.000862	-0.000989 / 0.000737
MUON_EFF_RECO_STAT	0.000371 / -0.000371	0.000261 / -0.000261	0.000361 / -0.000361	0.000356 / -0.000356	0.000238 / -0.000238	-7.33e-05 / 7.33e-05	0.000377 / -0.000377	0.000374 / -0.000374
JET_JER_EffectiveNP_7	0.00696 / -0.0696	-0.00104 / 0.00104	0.000275 / -0.000275	-4.5e-05 / 4.5e-05	-0.0009 / 0.0009	0.00316 / -0.00316	0.0015 / -0.0015	0.000786 / -0.000786
JET_Pileup_OffsetMu	0.0237 / -0.017	0.0186 / -0.0126	0.0111 / -0.00609	0.0109 / -0.0106	0.0212 / -0.015	-0.0129 / 0.014	0.0154 / -0.0129	0.0159 / -0.0126
FT_EFF_Eigen_Light_3	-0.000499 / 0.000499	-0.000518 / 0.000519	-0.000491 / 0.000491	-0.000479 / 0.000479	-0.00055 / 0.00055	0.000419 / -0.00042	-0.000519 / 0.000519	-0.000497 / 0.000497
JET_JER_EffectiveNP_1	-0.00185 / 0.00185	-0.00231 / 0.00231	-0.000208 / 0.000208	0.00036 / -0.00036	-0.00115 / 0.00115	-0.00139 / 0.00139	-0.00146 / 0.00146	0.00114 / -0.00114
MUON_EFF_ISO_SYS	0.00602 / -0.00602	0.00323 / -0.00323	0.00377 / -0.00377	0.00358 / -0.00358	0.00292 / -0.00292	2.3e-09 / 2.22e-09	0.00444 / -0.00444	0.00421 / -0.00421
JET_EffectiveNP_Mixed2	0.000701 / 0.00362	-0.00173 / 0.00148	-0.0022 / 0.00227	-0.00284 / 0.003	-0.00276 / 0.00238	0.00444 / -0.00214	-0.00461 / 0.00317	-0.00233 / 0.00194
JET_EffectiveNP_Mixed1	0.00214 / -9.25e-05	0.00159 / -0.00107	0.00265 / -0.0026	0.00311 / -0.00277	0.00186 / -0.00199	-0.00185 / 0.00366	0.0027 / -0.00421	0.00118 / -0.00139
JET_JER_EffectiveNP_1	0.00135 / -0.00135	-0.00292 / 0.00292	0.000957 / 0.000957	-0.000653 / 0.000653	-0.00105 / 0.00105	0.0017 / -0.0017	-0.00265 / 0.00266	-0.00195 / 0.00195
JET_PunchThrough_MC16	2.29e-05 / 0.0005	0.00014 / -5.24e-05	6.44e-06 / -3.31e-05	-7.21e-06 / -0.000127	1.65e-05 / 2.9e-05	-6.78e-07 / 4.64e-05	2.51e-05 / 8.59e-06	-3.49e-06 / -4.96e-05
FT_EFF_Eigen_B_7	-4.13e-07 / 3.77e-07	-3.26e-07 / 2.82e-07	-1.04e-05 / 1.03e-05	-3.87e-07 / 4.29e-07	-4.96e-07 / 5.12e-07	9.43e-07 / -9.39e-07	-4.36e-07 / 4.58e-07	-2.33e-07 / 2.56e-07
EG_SCALE_LARTEMPERATURE_EXTRA2016PRE	2.58e-08 / 2.58e-08	-2.21e-08 / -2.21e-08	1.38e-08 / 1.38e-08	2.1e-08 / 2.1e-08	8.15e-09 / 8.15e-09	2.26e-09 / 2.26e-09	-2.97e-08 / -2.97e-08	-2.37e-08 / -2.37e-08
JET_EffectiveNP_Modelling4	2.69e-05 / 0.00231	0.000275 / -0.000552	0.000467 / -0.000406	0.000883 / -0.000235	0.000395 / -0.000437	-0.000402 / 0.00244	0.000368 / -0.0049	0.000283 / -0.000291
JET_Flavor_Composition	0.0665 / -0.0489	0.0536 / -0.0447	0.0337 / -0.0286	0.0495 / -0.0501	0.0613 / -0.0539	-0.0427 / 0.0447	0.0525 / -0.0529	0.052 / -0.0495
JET_EffectiveNP_Statistical2	0.00157 / 0.000785	-0.00127 / 0.00223	-0.000444 / 0.000363	-0.00176 / 0.00116	-0.00179 / 0.0016	0.00387 / -0.00107	-0.00157 / 0.00193	-0.00186 / 0.00189
PRW_DATASF	-0.00141 / -0.00821	0.00884 / -0.0179	-4.52e-05 / 0.00125	-0.00109 / -0.00563	0.00839 / -0.00565	-0.0164 / 0.0159	0.0021 / -0.00179	0.00563 / -0.00555
JET_Pileup_RhoTopology	0.0263 / -0.0252	0.0193 / -0.0197	0.00272 / -0.00303	0.0263 / -0.0254	0.0203 / -0.0201	-0.0208 / 0.021	0.028 / -0.0271	0.0286 / -0.0279
FT_EFF_Eigen_B_2	0.000208 / -0.000209	0.000139 / -0.000138	-0.00956 / 0.00959	5.54e-05 / -5.46e-05	0.000141 / -0.000141	0.000543 / -0.000548	0.000225 / -0.000225	0.00012 / -0.000119
JET_JER_EffectiveNP_2	0.0132 / -0.013	0.0226 / -0.0223	0.0605 / -0.0601	0.004 / -0.00397	0.0139 / -0.0137	-0.0227 / 0.0229	0.0602 / -0.0597	0.00639 / -0.00634
JET_EffectiveNP_Statistical6	0.000168 / 0.00195	0.000458 / -0.000311	0.000344 / -0.000367	0.000994 / -0.00019	0.000405 / -0.000364	-0.000388 / 0.00254	0.000709 / -0.000514	0.000381 / -0.000356
FT_EFF_Eigen_Light_1	0.00511 / -0.00507	0.0051 / -0.00506	0.00507 / -0.00504	0.00507 / -0.00503	0.00547 / -0.00543	-0.0114 / 0.00412	0.00512 / -0.00508	0.00486 / -0.00482
JET_EffectiveNP_Statistical1	0.000205 / -0.000326	-0.0001 / -0.00064	0.000181 / -0.00024	0.000446 / -4.72e-05	3.68e-05 / -9.31e-05	-0.000267 / 8.66e-05	0.00017 / -0.000217	9.06e-05 / -0.000112
EL_EFF_ID_TOTAL_1NPCOR_PLUS_UNCOR	0.00214 / -0.00214	0.00351 / -0.0035	0.00239 / -0.00239	0.00278 / -0.00278	0.00402 / -0.00401	-0.00177 / 0.00177	0.00236 / -0.00236	0.00235 / -0.00235
JET_JER_EffectiveNP_9	0.00597 / -0.00597	0.0058 / -0.0058	0.00213 / -0.00213	-0.000549 / 0.000549	0.00343 / -0.00343	-0.000557 / 0.000557	0.0108 / -0.0108	0.00284 / -0.00284
JET_EffectiveNP_Detector1	0.000234 / 0.00155	0.00131 / -0.00133	0.0098 / -0.000884	0.00152 / -0.000729	0.00123 / -0.00104	-0.000845 / 0.00037	0.00157 / -0.00317	0.00105 / -0.00118
JET_Pileup_OffsetNPV	0.0204 / -0.0116	0.0165 / -0.014	0.00419 / -0.00268	0.0111 / -0.0111	0.0139 / -0.0126	-0.015 / 0.0148	0.0161 / -0.0152	0.0167 / -0.015
FT_EFF_Eigen_B_8	-6.2e-08 / 2.58e-08	-2.21e-08 / 3.87e-08	-7.95e-07 / 8.23e-07	-6.06e-08 / 2.1e-08	8.15e-08 / -6.5e-08	6.95e-08 / -6.5e-08	-2.97e-08 / 5.15e-08	-2.37e-08 / 4.62e-08
FT_EFF_Eigen_B_6	3.62e-06 / -3.66e-06	1.98e-06 / -1.97e-06	6.91e-05 / -6.91e-05	2.79e-06 / -2.83e-06	3.43e-06 / -3.42e-06	-6.18e-06 / 6.19e-06	3.38e-06 / -3.36e-06	1.79e-06 / -1.77e-06
JET_EffectiveNP_Modelling3	0.00144 / 0.00144	-9.2e-05 / 0.000131	-0.00185 / 0.0021	-0.00176 / 0.00247	-0.00135 / 0.0015	0.00281 / -0.00087	-0.00285 / 0.00138	-0.000744 / 0.000677
JET_JER_DataVsMC_MC16	-0.00272 / 0.00273	-0.00808 / 0.00809	-0.00332 / 0.00333	-0.0018 / 0.0018	-0.00742 / 0.00743	0.0111 / -0.0111	-0.00176 / 0.00176	-0.0017 / 0.00017
EL_EFF_Iso_TOTAL_1NPCOR_PLUS_UNCOR	0.00348 / -0.00035	0.00055 / -0.00556	0.000389 / -0.000389	0.00458 / -0.000464	0.000542 / -0.000547	2.12e-09 / 2.38e-09	0.000375 / -0.000377	0.000393 / -0.000396
JET_JER_EffectiveNP_4	0.00305 / -0.00305	-0.00388 / 0.00389	-0.0022 / 0.0022	-0.00133 / 0.00133	0.000782 / -0.000782	0.00624 / -0.00623	-0.00199 / 0.00199	-0.00534 / 0.00535
JET_EffectiveNP_Modelling2	0.00123 / 0.00159	-0.000407 / 0.000636	0.00119 / -0.00093	0.0011 / -0.000482	0.000282 / -0.000324	0.000398 / 0.00212	0.000345 / -6.69e-05	-0.000152 / 0.000209
MUON_SAGITTA_RESBIAS	0.00397 / 0.00195	0.000477 / 0.000306	0.0031 / 0.0017	0.00122 / -2.46e-05	0.000237 / 8.87e-06	-0.000107 / 9.31e-05	0.0222 / 0.00224	0.0176 / 0.00171
JET_EtaIntercalibration_NonClosure_2018data	0.00472 / 0.00303	0.00593 / -0.00352	0.0225 / -0.00185	0.00598 / -0.00401	0.00201 / -0.00201	-0.00236 / 0.00256	0.0045 / -0.00413	0.00286 / -0.00316
JET_fJvtEfficiency	0.0047 / -0.0027	-0.00044 / 0.000678	0.0008 / -0.000266	0.000843 / -0.000566	-0.000806 / 0.0013	0.000295 / -0.000511	0.000813 / -0.000613	0.0018 / -0.00164
JET_EtaIntercalibration_NonClosure_highE	-3.87e-05 / 2.06e-05	-2.21e-08 / -2.21e-08	8.38e-06 / 1.03e-05	-1.65e-05 / 8.67e-06	5.12e-07 / -1.91e-06	6.05e-07 / -9.34e-06	2.16e-06 / -4.01e-06	-9.24e-06 / 2.79e-05
JET_EffectiveNP_Statistical3	-0.000296 / 0.000854	-0.000116 / -0.000287	-0.000211 / 0.000104	-0.000294 / 0.000751	0.000105 / -0.000165	0.000165 / -0.000152	-9.07e-05 / 0.000189	-5.4e-06 / 5.67e-05
JET_JER_EffectiveNP_1	0.00127 / -0.00127	0.00472 / -0.00471	0.00171 / -0.00171	0.00135 / -0.00135	0.00211 / -0.00211	0.00277 / -0.00277	-0.000165 / 0.000165	0.00217 / -0.00216
FT_EFF_Eigen_B_0	0.00457 / -0.00439	0.00362 / -0.00339	0.183 / -0.165	0.00548 / -0.00518	0.00632 / -0.006	-0.015 / 0.014	0.00565 / -0.00534	0.00303 / -0.00289
MET_SoftTrk_ResoPara	-0.0139 / 0.0139	-0.0164 / 0.0164	-0.00164 / 0.00164	-0.00349 / 0.00349	-0.0223 / 0.0224	0.00262 / -0.00262	-0.00355 / 0.00356	-0.00268 / 0.00269
MUON_EFF_RECO_SYS	0.0013 / -0.0013	0.000999 / -0.000995	0.00135 / -0.00135	0.00148 / -0.00148	0.00105 / -0.00105	-0.000206 / 0.000204	0.00147 / -0.00146	0.00142 / -0.00142
MUON_EFF_ISO_STAT	0.000357 / -0.000357	0.0035 / -0.0035	0.000545 / -0.000545	0.00062 / -0.00062	0.000336 / -0.000336	2.23e-09 / 2.29e-09	0.000528 / -0.000528	0.000541 / -0.000541
MUON_EFF_RECO_STAT	2.58e-08 / 2.58e-08	-2.21e-08 / -2.21e-08	1.38e-08 / 1.38e-08	2.1e-08 / 2.1e-08	8.15e-09 / 8.15e-09	2.26e-09 / 2.26e-09	-2.97e-08 / -2.97e-08	-2.37e-08 / -2.37e-08
JET_EffectiveNP_Mixed3	0.000151 / 0.00216	0.000623 / -0.000556	0.000369 / -0.000455	0.000645 / -0.000251	0.00067 / -0.000558	-0.000495 / 0.00285	0.000898 / -0.000764	0.000716 / -0.000667
FT_EFF_Eigen_C_0	0.0101 / -0.00991	0.0105 / -0.0104	0.017 / -0.0168	0.0153 / -0.015	0.00895 / -0.00879	-0.00794 / 0.00781	0.00989 / -0.00972	0.00812 / -0.00801
FT_EFF_Eigen_Light_0	0.035 / -0.0336	0.0337 / -0.0324	0.0327 / -0.0315	0.0327 / -0.0315	0.0372 / -0.0357	-0.0256 / 0.0252	0.0342 / -0.0329	0.0325 / -0.0313
FT_EFF_Eigen_B_3	-0.0027 / 0.0027	-0.000179 / 0.000179	-0.0067 / 0.00672	-0.000289 / 0.00029	-0.000321 / 0.000322	0.000634 / -0.000637	-0.000295 / 0.000296	-0.00015 / 0.00015
FT_EFF_Eigen_C_2	9.33e-05 / -9.33e-05	-1.32e-05 / 1.32e-05	-8.41e-05 / 8.4e-05	-0.000152 / 0.000152	9.27e-05 / -9.27e-05	2.44e-05 / -2.44e-05	-6.03e-05 / 6.04e-05	-9.96e-05 / 9.97e-05
FT_EFF_extrapolation	-0.00142 / 0.00142	-0.00489 / 0.0049	-0.00451 / 0.00451	-0.00374 / 0.00379	-0.00223 / 0.00224	0.000645 / -0.000648	-4.99e-06 / 5.01e-06	-5.05e-06 / 5.08e-06
MET_SoftTrk_ResoPerp	-0.000593 / 0.000593	-0.0152 / 0.0152	-0.0013 / 0.0013	-0.00298 / 0.00298	-0.0215 / 0.0215	0.00218 / -0.00218	-0.00329 / 0.00329	-0.00147 / 0.00147
FT_EFF_Eigen_C_1	0.000292 / -0.000293	0.000914 / -0.000915	0.0027 / -0.00027	0.001 / -0.001	6.06e-05 / -6.06e-05	-0.000243 / 0.000244	0.000553 / -0.000553	0.0008 / -0.0008
FT_EFF_Eigen_B_4	5.36e-05 / -5.36e-05	4.12e-05 / -4.12e-05	0.00217 / -0.00217	7.23e-05 / -7.23e-05	7.72e-05 / -7.72e-05	-0.0019 / 0.0019	6.74e-05 / -6.73e-05	3.26e-05 / -3.26e-05
JET_EtaIntercalibration_TotalStat	0.00387 / 0.000195	0.00496 / -0.00328	0.0209 / -0.00176	0.00402 / -0.00396	0.00438 / -0.00453	-0.00349 / 0.00578	0.00488 / -0.00606	0.00461 / -0.00478
JET_JER_EffectiveNP_3	-0.00428 / 0.00428	-0.00684 / 0.00685	-0.00437 / 0.00438	-0.00244 / 0.00244	-0.00451 / 0.00451	0.0605 / -0.0605	-0.000921 / 0.000921	-0.00601 / 0.00602
MET_SoftTrk_Scale	-0.0117 / 0.00896	-0.0182 / 0.0196	-0.002 / 0.00174	-0.00376 / 0.00258	-0.0222 / 0.021	0.0173 / -0.0136	-0.00388 / 0.00389	-0.00226 / 0.0024
MUON_ID	-0.00241 / -0.00143	0.000959 / 0.000568	-0.00117 / 0.000801	-0.00213 / 0.000611	-0.000785 / -0.000176	9.54e-05 / -0.000158	-0.000358 / 0.00115	-0.00107 / 0.000574
JET_EffectiveNP_Modelling1	0.0121 / -0.0192	0.0178 / -0.0158	0.0116 / -0.0092	0.0102 / -0.0247	0.0177 / -0.0189	-0.0131 / 0.0199	0.0216 / -0.0245	0.0198 / -0.0217
JET_EtaIntercalibration_NonClosure_posEta	0.00134 / -0.00133	0.00118 / 0.000271	0.00061 / -0.000612	0.000931 / -0.000604	0.000906 / -0.000537	-0.000504 / 0.00277	0.000897 / -0.000767	0.000765 / -0.000707
FT_EFF_Eigen_B_5	-1.37e-05 / 1.36e-05	-9.32e-06 / 9.34e-06	-0.000348 / 0.000348	-1.23e-05 / 1.23e-05	-1.63e-05 / 1.63e-05	3.24e-05 / -3.24e-05	-1.53e-05 / 1.53e-05	-7.78e-06 / 7.8e-06
MUON_EFF_TTVA_STAT	9.7e-05 / -9.7e-05	9.45e-05 / -9.46e-05	0.000139 / -0.000139	0.000153 / -0.000154	8.34e-05 / -8.34e-05	-2.6e-05 / 2.6e-05	0.000138 / -0.000138	0.000142 / -0.000143
MUON_EFF_TrigSystUncertainty	-0.00324 / 0.00331	-0.00216 / 0.00219	-0.00297 / 0.00303	-0.00295 / 0.003	-0.003 / 0.00217	-0.00221 / 0.0101 / -0.00103	-0.00323 / 0.00329	-0.00308 / 0.00313
JET_JER_EffectiveNP_6	-0.0086 / 0.00861	-0.00807 / 0.00808	-0.00286 / 0.00286	-0.00213 / 0.00213	-0.00555 / 0.00555	0.0258 / -0.00258	-0.00151 / 0.00151	-0.00371 / 0.00371
JET_SingleParticle_HighPt	2.58e-08 / 2.58e-08	-2.21e-08 / -2.21e-08	1.38e-08 / 1.38e-08	2.1e-08 / 2.1e-08	8.16e-09 / 8.16e-09	2.26e-09 / 2.26e-09	-2.97e-08 / -2.97e-08	-2.37e-08 / -2.37e-08
JET_JER_EffectiveNP_8	-0.00245 / 0.00245	0.00118 / -0.00118	0.000399 / -0.000399	0.00237 / -0.00237	-0.00117 / 0.00117	-0.00477 / 0.00477	0.00154 / -0.00154	0.000473 / -0.000473
JET_EtaIntercalibration_NonClosure_negEta	0.00614 / 0.000397	0.00127 / -0.00121	0.00114 / -0.00123	0.00202 / -8.78e-05	0.00113 / -0.00172	-0.00141 / 0.000593	0.00139 / -0.00137	0.00125 / -0.00103
JET_EffectiveNP_Statistical5	0.00178 / 1.18e-05	0.000264 / 6.81e-05	0.000816 / 0.000769	-0.000153 / 0.000537	-0.00103 / 0.000927	0.00244 / -0.000291	-0.000585 / 0.00061	-0.000448 / 0.000515
MUON_EFF_TTVA_SYS	0.000112 / -0.000195	0.00125 / -0.000115	0.000189 / -0.000172	0.00204 / -0.00186	0.000113 / -0.000105	-2.77e-05 / 2.66e-05	0.000178 / -0.000163	0.000179 / -0.000162
FT_EFF_Eigen_C_3	-0.000115 / 0.000115	-8.28e-05 / 8.28e-05	-0.000126 / 0.000126	-8.69e-05 / 8.69e-05	-8.59e-05 / 8.59e-05	6.64e-05 / -6.64e-05	-9.54e-05 / 9.54e-05	-5.61e-05 / 5.6e-05
JET_JER_EffectiveNP_1	0.00873 / -0.00866	0.0258 / -0.0255	0.00858 / -0.00855	0.00743 / -0.00737	0.0173 / -0.0171	-0.0282 / 0.0283	0.00734 / -0.00728	0.0113 / -0.0112
JET_JER_EffectiveNP_5	-0.00378 / 0.00378	-0.00316 / 0.00316	-0.00102 / 0.00102	-0.00213 / 0.00213	-0.00324 / 0.00324	0.0176 / -0.00176	-0.000768 / 0.000768	-0.00128 / 0.00128
FT_EFF_extrapolation	-0.000187 / 0.000187	-0.000319 / 0.000319	-0.000372 / 0.000373	-0.00406 / 0.000407	-0.00105 / 0.000105	0.000108 / -0.000108	-0.000175 / 0.000175	-0.000381 / 0.000281
JET_Flavor_Response	-0.0375 / 0.0411	-0.0329 / 0.029	-0.021 / 0.0228	-0.0319 / 0.0342	-0.0284 / 0.0307	0.0265 / -0.0265	-0.0345 / 0.0372	-0.0299 / 0.0323
JET_EffectiveNP_Statistical4	0.0064 / 0.003	-0.000141 / -0.00023	0.0008 / -0.000625	0.00128 / -0.00486	0.000431 / -0.00381	-0.0029 / 0.00239	0.000641 / -0.000566	0.000363 / -0.000249
EL_EFF_Reco_TOTAL_1NPCOR_PLUS_UNCOR	0.00149 / -0.00149	0.00208 / -0.00208	0.00158 / -0.00158	0.00155 / -0.0015	0.00246 / -0.00246	-0.00148 / 0.00148	0.00154 / -0.00154	0.00149 / -0.00149
MUON_MS	0.000147 / 0.000683	0.000439 / -7.84e-05	-0.00467 / 0.000629	-0.00066 / -0.000808	-0.000227 / -8.37e-05	0.000293 / 6.97e-05	-0.000355 / 0.000522	-0.000358 / 0.00055
EG_RESOLUTION_ALL	-0.00255 / 0.00526	0.00063 / 0.000182	0.000145 / -6.86e-06	3.87e-05 / -3.25e-05	0.00016 / -0.000101	0.00219 / -7.83e-05	-3.83e-05 / 4.76e-05	-0.000224 / 0.000216
Run2luminosityuncertainty	0.017 / -0.017	0.017 / -0.017	0.017 / -0.017	0.017 / -0.017	0.017 / -0.017	0.017 / -0.017	0.017 / -0.017	0.017 / -0.017
MULTIJET_LeptonIsolation	0 / 0	0 / 0	0 / 0	0 / 0	0 / 0	0.155 / -0.125	0 / 0	0 / 0
MULTIJET_FitBinning	0 / 0	0 / 0	0 / 0	0 / 0	0 / 0	0.126 / 0.0081	0 / 0	0 / 0
MULTIJET_FitVariable	0 / 0	0 / 0	0 / 0	0 / 0	0 / 0	0.108 / 0.00279	0 / 0	0 / 0
MULTIJET_FlatFit	0 / 0	0 / 0	0 / 0	0 / 0	0 / 0	0.236 / -0.189	0 / 0	0 / 0
SCALE_UNCERTAINTY	0 / 0	0 / 0	0 / 0	0 / 0	0 / 0	0 / 0	0 / 0	0.00912 / -0.00912
gamma_stat_CR0_combined_bin_0	0.0117 / -0.0117	0.00907 / -0.00907	0.00947 / -0.00947	0.00836 / -0.00836	0.00995 / -0.00995	0.00933 / -0.00933	0.00981 / -0.00981	0 / 0
gamma_stat_CR0_combined_bin_1	0.00258 / -0.00258	0.00449 / -0.00449	0.00466 / -0.00498	0.00498 / -0.00498	0.00413 / -0.00413	0.00389 / -0.00389	0.00423 / -0.00423	0 / 0
gamma_stat_CR0_combined_bin_2	0.000682 / -0.000682	0.00157 / -0.00157	0.00117 / -0.00117	0.00175 / -0.00175	0.00109 / -0.00109	0.00157 / -0.00157	0.00112 / -0.00112	0 / 0
gamma_stat_CR0_combined_bin_3	0.000105 / -0.000105	0.000564 / -0.000564	0.000287 / -0.000287	0.000757 / -0.000757	0.000313 / -0.000313	0.000822 / -0.000822	0.0036 / -0.00036	0 / 0
gamma_stat_CR0_combined_bin_4	5.71e-05 / -5.71e-05	0.000536 / -0.000536	0.00017 / -0.00017	0.000852 / -0.000852	0.000231 / -0.000231	0.00112 / -0.00112	0.0003 / -0.0003	0 / 0
μ_{QcdW}	0.0537 / -0.0513	0 / 0	0 / 0	0 / 0	0 / 0	0 / 0	0.0537 / -0.0513	0 / 0
μ_{Ewk}	0 / 0	0 / 0	0 / 0	0 / 0	0 / 0	0 / 0	0 / 0	0.0729 / -0.0826

Table D.4: Relative post-fit uncertainty on event yields due to each nuisance parameter in CR0

191

Appendix E

Electroweak W Production Analysis MC Datasets

The tables below contain the ATLAS Dataset Identifier (DSID), generator-level cross-section, k-factor, and filter efficiency for each MC sample used in th EWK-W analysis.

Powheg EWK-W ($W \rightarrow \ell\nu$)

DSID	Cross-section [nb]	k-Factor	Generator Filter Efficiency
600931	3.1329E-03	1.0	1.0000E+00
600932	3.1329E-03	1.0	1.0000E+00
600933	3.1329E-03	1.0	1.0000E+00
600934	4.4832E-03	1.0	1.0000E+00
600935	4.4832E-03	1.0	1.0000E+00
600936	4.4832E-03	1.0	1.0000E+00

Table E.1: Powheg EWK-W ($W \rightarrow \ell\nu$) datasets used in the ATLAS EWK-W measurement.

Herwig7 EWK-W

DSID	Cross-section [nb]	k-Factor	Generator Filter Efficiency
363237	8.1172E-03	1.0	1.0000E+00
830006	8.0575E-03	1.0	1.0000E+00
363239	8.1393E-03	1.0	1.0000E+00

Table E.2: Herwig7 EWK-W datasets used in the ATLAS EWK-W measurement.

Powheg QCD-W ($W \to \ell\nu$ with $|w_{\mathrm{MC}}| < 400 \times 10^3$)

DSID	Cross-section [nb]	k-Factor	Generator Filter Efficiency
601231	1.3847	1.0	1.0000E+00
601232	1.3847	1.0	1.0000E+00
601233	1.7816	1.0	1.0000E+00
601234	1.7817	1.0	1.0000E+00

Table E.3: `Powheg` QCD-W ($W \to \ell\nu$ datasets used in the ATLAS EWK-W measurement.

Sherpa 2.2.11 QCD-W

DSID	Cross-section [nb]	k-Factor	Generator Filter Efficiency
700338	2.1742E+01	1.0	9.3902E-03
700339	2.1742E+01	1.0	1.4699E-01
700340	2.1742E+01	1.0	8.4360E-01
700341	2.1806E+01	1.0	9.2214E-03
700342	2.1806E+01	1.0	1.4722E-01
700343	2.1806E+01	1.0	8.4355E-01
700344	7.6800E+00	1.0	9.0177E-03
700345	7.6800E+00	1.0	1.4343E-01
700346	7.6800E+00	1.0	8.4747E-01
700347	1.4126E+01	1.0	9.1596E-03
700348	1.4126E+01	1.0	1.4335E-01
700349	1.4126E+01	1.0	8.4746E-01

Table E.4: `Sherpa 2.2.11` QCD-W datasets considered in the ATLAS EWK-W measurement.

Madgraph FxFx QCD-W ($W \rightarrow \ell\nu$)

DSID	Cross-section [nb]	k-Factor	Generator Filter Efficiency
508979	2.2155E+01	1.0	7.6416E-03
508980	2.2098E+01	1.0	1.5372E-01
508981	2.2084E+01	1.0	8.3866E-01
508982	2.2242E+01	1.0	7.5108E-03
508983	2.2198E+01	1.0	1.5336E-01
508984	2.2117E+01	1.0	8.3901E-01

Table E.5: `Madgraph FxFx` QCD-W ($W \rightarrow \ell\nu$) datasets used in the ATLAS EWK-W measurement.

Sherpa 2.2.11 Z+jets

DSID	Cross-section [nb]	k-Factor	Generator Filter Efficiency
700320	2.2212E+00	1.0	2.4945E-02
700321	2.2212E+00	1.0	1.2905E-01
700322	2.2212E+00	1.0	8.4607E-01
700323	2.2213E+00	1.0	2.4427E-02
700324	2.2213E+00	1.0	1.2937E-01
700325	2.2213E+00	1.0	8.4635E-01
700326	2.7533E-01	1.0	2.4289E-02
700327	2.7533E-01	1.0	1.2540E-01
700328	2.7533E-01	1.0	8.5036E-01
700329	1.0132E+00	1.0	2.4395E-02
700330	1.0132E+00	1.0	1.2542E-01
700331	1.0132E+00	1.0	8.5022E-01
700332	9.3253E-01	1.0	2.4585E-02
700333	9.3253E-01	1.0	1.2536E-01
700334	9.3253E-01	1.0	8.5004E-01

Table E.6: `Sherpa 2.2.11` Z+jets datasets used in the ATLAS EWK-W measurement.

Sherpa 2.2.11 EWK-W

DSID	Cross-section [nb]	k-Factor	Generator Filter Efficiency
700362	8.5022E-03	1.0	1.0000E+00
700363	8.5027E-03	1.0	1.0000E+00
700364	8.5013E-03	1.0	1.0000E+00

Table E.7: `Sherpa 2.2.11` EWK-W datasets considered in the ATLAS EWK-W measurement.

Powheg Diboson

DSID	Cross-section [nb]	k-Factor	Generator Filter Efficiency
361600	1.0636E-02	1.0	1.0000E+00
361601	4.5106E-03	1.0	1.0000E+00
361602	2.7781E-03	1.0	1.0000E+00
361603	1.2663E-03	1.0	1.0000E+00
361604	9.2303E-04	1.0	1.0000E+00
361605	5.4900E-04	1.0	1.0000E+00
361606	4.4176E-02	1.0	1.0000E+00
361607	3.2882E-03	1.0	1.0000E+00
361608	5.7747E-03	1.0	1.0000E+00
361609	1.0095E-02	1.0	1.0000E+00
361610	2.2759E-03	1.0	1.0000E+00
361611	3.9441E-03	1.0	1.0000E+00

Table E.8: `Powheg` Diboson datasets used in the ATLAS EWK-W measurement.

Powheg $t\bar{t}$

DSID	Cross-section [nb]	k-Factor	Generator Filter Efficiency
410470	7.2977E-01	1.13975636159	5.4384E-01
410501	7.3017E-01	1.13913198296	5.4383E-01

Table E.9: `Powheg` $t\bar{t}$ datasets used in the ATLAS EWK-W measurement.

Powheg Single-Top

DSID	Cross-section [nb]	k-Factor	Generator Filter Efficiency
410658	3.6995E-02	1.1935	1.0000E+00
410659	2.2173E-02	1.1849	1.0000E+00
410644	0.002027	1.0170	1.0000E+00
410645	1.2674E-03	1.0167	1.0000E+00
410646	3.7936E-02	0.9450	1.0000E+00
410647	3.7905E-02	0.9457	1.0000E+00

Table E.10: `Powheg` Single-Top datasets used in ATLAS EWK-W measurement.

<div align="center">**Curriculum Vitae**</div>

<div align="center"># Gregory Myers</div>

Education

Indiana University   August 2017 – August 2023

PhD Physics   *Bloomington, IN*

Florida State University   August 2012 – July 2014

MS Physics   *Tallahassee, FL*

Indiana University   August 2008 – May 2012

BS Physics   *Bloomington, IN*

BS Mathematics

Minor Latin

Research Experience

Research Assistant   May 2018 – Present

Indiana University   *Bloomington, IN (based at CERN)*

- Integral in the ATLAS Global Feature Extractor installation and commissioning

  - Physically installed the gFEX board and connected I/O for Run 3

  - Helped maintain the gFEX board in the L1Calo surface test facility

  - Organized and validated documentation on the gFEX I/O channel mapping

  - Validated the low-level firmware functionality of the gFEX $E_{\mathrm{T}}^{\mathrm{miss}}$ algorithm

  - Ran myriad tests of new firmware features on hardware

- ATLAS Level 1 Calorimeter Trigger control and monitoring software development

  - Wrote the majority of the run control and online I/O mapping software for gFEX

  - Developed the gFEX status panel in the ATLAS run control GUI

  - Created scripts for L1Calo to automate FELIX setup

- ATLAS physics analysis: electroweak W boson production in association with jets
  - Performed fake lepton estimation via profile likelihood fit
  - Extended fitting tools from fake lepton estimate to perform a signal extraction fit
  - Implemented and maintained tools for checking data/MC agreement

Research Assistant December 2013 – July 2014

Florida State University *Tallahassee, FL*
- CMS physics analysis: quark contact interaction search
  - Studied the impact of PDF choice, factorization scale, and renormalization scale on inclusive jet p_T spectrum

Professional Experience

Mathematician June, 2015 – July, 2017

Scientific Games Corperation *Cedar Falls, IA*
- Gameplay and architecture development in C# and ActionScript environments
  - Worked with game designers, artists, and programmers to build games
  - Collaboratively developed foundation for server-side calculations of game outcomes
- Mathematical solution of game design and proof of odds for Class III games
  - Solved for the expected value of 4 custom IP games and proved convergence
  - Translated $\sim$100 existing game designs into C# and ActionScript models
- Training of new developers and mathematicians

Teaching Experience

Indiana University *Bloomington, IN*
- Introductory Physics Discussion Instructor - Spring 2018
- Introductory Physics Lab Instructor - Fall 2017
- Math tutor in IU Academic Support Center, 10-20 hours per week - 2009-2012

Florida State University *Tallahassee, FL*
- Introductory Physics Studio Instructor - Spring 2014
- Intermediate Physics Lab Instructor - Fall 2013
- Introductory Physics Lab Instructor - Summer 2013
- Introductory Astronomy Lab Instructor - Fall 2012 and Spring 2013

Research Presentations

- *Commissioning Status of gFEX* – ATLAS Weekly Meeting, September 6th, 2022

- *The Phase 1 Upgrade of the ATLAS Level 1 Calorimeter Trigger* – 9th Annual Conference on Large Hadron Collider Physics, June 10th, 2021

Awards

- IU Dept. of Physics: Outstanding Graduate Student in Research – April 26, 2023

Specialized Skills

Programming Languages: Python (intermediate), C++ (intermediate), C# (intermediate), ActionScript (intermediate), LaTeX (intermediate), bash scripting (beginner), java (beginner), SQLite (beginner), VHDL (beginner)

Electronics Experience: ATCA blade handling, fiber optic cable management, Pigeon Point ATCA shelf manager (beginner), Xilinx FPGA firmware development tools

Physics Outreach: ATLAS underground tour guide

Other: Game development in Unity environment, Agile/Scrum software development and group management

Other Interests

Music: Drums, guitar, audio signal processing and sound engineering, CERN Music Club member since 2019

Technical: Breadboard hobbyist, video game development (Unity and Pygame)

Woodworking: Hand tools (beginner)

Cooking (and Eating): Knife skills (expert), braising (expert), sautée (intermediate), fermentation (intermediate), baking (beginner)